ADVERTIMENT. L'accés als continguts d'aquesta tesi doctoral i la seva utilització ha de respectar els drets de la persona autora. Pot ser utilitzada per a consulta o estudi personal, així com en activitats o materials d'investigació i docència en els termes establerts a l'art. 32 del Text Refós de la Llei de Propietat Intel·lectual (RDL 1/1996). Per altres utilitzacions es requereix l'autorització prèvia i expressa de la persona autora. En qualsevol cas, en la utilització dels seus continguts caldrà indicar de forma clara el nom i cognoms de la persona autora i el títol de la tesi doctoral. No s'autoritza la seva reproducció o altres formes d'explotació efectuades amb finalitats de lucre ni la seva comunicació pública des d'un lloc aliè al servei TDX. Tampoc s'autoritza la presentació del seu contingut en una finestra o marc aliè a TDX (framing). Aquesta reserva de drets afecta tant als continguts de la tesi com als seus resums i índexs.

ADVERTENCIA. El acceso a los contenidos de esta tesis doctoral y su utilización debe respetar los derechos de la persona autora. Puede ser utilizada para consulta o estudio personal, así como en actividades o materiales de investigación y docencia en los términos establecidos en el art. 32 del Texto Refundido de la Ley de Propiedad Intelectual (RDL 1/1996). Para otros usos se requiere la autorización previa y expresa de la persona autora. En cualquier caso, en la utilización de sus contenidos se deberá indicar de forma clara el nombre y apellidos de la persona autora y el título de la tesis doctoral. No se autoriza su reproducción u otras formas de explotación efectuadas con fines lucrativos ni su comunicación pública desde un sitio ajeno al servicio TDR. Tampoco se autoriza la presentación de su contenido en una ventana o marco ajeno a TDR (framing). Esta reserva de derechos afecta tanto al contenido de la tesis como a sus resúmenes e índices.

WARNING. The access to the contents of this doctoral thesis and its use must respect the rights of the author. It can be used for reference or private study, as well as research and learning activities or materials in the terms established by the 32nd article of the Spanish Consolidated Copyright Act (RDL 1/1996). Express and previous authorization of the author is required for any other uses. In any case, when using its content, full name of the author and title of the thesis must be clearly indicated. Reproduction or other forms of for profit use or public communication from outside TDX service is not allowed. Presentation of its content in a window or frame external to TDX (framing) is not authorized either. These rights affect both the content of the thesis and its abstracts and indexes.

Measurement of refractive index in non-planar surfaces with a conoscopic Mueller microscope

Irene Estévez Caride

Submitted in fulfillment of

the requirements for the degree of

Doctor of Physics

Thesis supervisors:

Dr. Juan Campos

Dr. Angel Lizana

Departament de Física

Universitat Autònoma de Barcelona

Bellaterra, 2018

A mis padres, a mi hermano y a Sergi

This work has been financed by the following research projects:

i) Development of systems and methods for the surface metrology and polarimetric characterization based on liquid crystals modulators. FIS2012-39158-C02-01. Ministerio de Economía y Competitividad.

ii) Development of advanced optical instrumentation for applications in image polarimetry and surface metrology by fringe deflectometry. FIS2015-66328-C3-1-R. Ministerio de Economía y Competitividad.

I. Estévez thanks the Ministerio de Economía y Competitividad for the grant "*Ayudas para contratos predoctorales para la formación de doctores 2013*". BES-2013-064046

Agradecimientos

Las primeras líneas son para todos aquellos que, de alguna manera, me habéis acompañado durante este proceso y que habéis llenado de buenos recuerdos estos inolvidables años. Gracias a todos vosotros por acompañarme en este camino hacia la persona que soy ahora mismo.

A mis directores de tesis, por todo lo que me habéis aportado en estos cuatro años, por haber tenido siempre vuestra puerta abierta para escucharme, aconsejarme y ayudarme.

A Juan, por invitarme a formar parte del grupo, y por permitirme desarrollarme como científica. Por la aventura que empezamos el 2 de septiembre de 2013, cuando contestaste al correo que te envié solicitando una beca de doctorado para unirme a tu grupo. Contigo he aprendido todo lo que sé ahora como investigadora, a trabajar en el laboratorio, a programar, a diseñar en 3D... Tu confianza y constante lucha por este proyecto me ha permitido llegar hasta aquí y enfrentarme a cada uno de los imprevistos que surgían con este montaje.

A Ángel, por tu positivismo, tu paciencia y tu constante ayuda en cada pequeño paso que hemos dado para llegar hasta aquí. En especial te agradezco todos los momentos en los que me has animado y escuchado mientras *hacíamos* un café. También agradezco cada uno de los consejos que me has dado cuando más los necesitaba, las charlas en nuestras vueltas a casa en tren y todas las veces que te has sentado conmigo para entender lo que para mí era inentendible, aunque estuviésemos en una cola y fuesen las 6.00h de la mañana.

Al grupo de óptica, por acogerme desde el primer momento y por todo lo que hemos vivido juntos. En especial...

A Marifí, por compartir toda tu experiencia conmigo, así como con todos los que empezamos en el mundo de la investigación. Por tu preocupación por cada uno de nosotros y por mostrarme la importancia y la necesidad de visibilizar que las mujeres también podemos ser científicas. Ahora esta también es mi lucha. A Juan Carlos, por toda tu ayuda en la preparación de los laboratorios de prácticas, sin tus explicaciones todo hubiese sido caótico. Mis primeros recuerdos en el mundo de la docencia universitaria son contigo. A Jordi y Verónica, por vuestra cercanía, consejos y ayuda durante estos años. A Francesc, por permitirme explorar la divulgación científica, un mundo que me ha apasionado y que no voy a dejar de lado. A Gaspar, por tu ayuda en la docencia en el máster.

A mis compañeros de despacho, por todos los ratos de descanso compartidos, después de horas delante del ordenador. A Alba por estar siempre dispuesta a ayudarme, incluso antes de conocerme (que me fueras a buscar al aeropuerto cuando llegué a Barcelona me hizo tener menos miedo a esa nueva etapa que empezaba), y por enseñarme todo lo necesario en mis inicios en la Autònoma. A Claudio, por acompañarme durante mis primeros meses en Barcelona haciendo planes culturales por toda la ciudad. Gracias a ti no me he sentido sola. A Haolin y Albert, por haberme acompañado en mi recta final, llenando el despacho de diversión, bromas, vídeos, debates y consejos que me han animado cuando tenía algún día duro y largo. Tengo que confesar que gracias a vosotros llego todavía antes al despacho por las mañanas, me gusta poneros difícil que lleguéis los primeros.

A los exdoctorandos cuánticos, Alexiño y Joan, por hacerme sentir mejor en los momentos difíciles, aunque sólo fuera con una conversación sincera. Por ayudarme a liberar presiones y, en general, por hacer que mi estancia en la UAB haya sido fantástica. A los actuales cuánticos: Gerard Pelegrí, Gerard Queraltó, Josep, JuanLu (Poeta Cuántico) y Dani, por hacerme un huequito a vuestro lado cada día a las 13.00h para comer juntos (café incluido) y conversar de todo un poco. Así se nos da por un debate trascendental sobre nuestro futuro, como por el vídeo más gracioso de YouTube. A todos, gracias por ayudarme a desconectar un ratiño cada día.

A todos los que habéis pasado pequeñas temporadas con nosotros durante estos años. A Tania, Wiam, Fabián, Marcela y Víctor, por enseñarme nuevas culturas, nuevas comidas, nuevos paisajes y nueva música.

Al “Laboratoire de Physique des Interfaces et des Couches Minces” de la “Ecole Polytechnique”, así como a todos mis compañeros de estancia. En especial...

A Enric, por tu cálido recibimiento en París, por permitirme trabajar contigo y por enseñarme a desenvolverme en otro grupo de investigación donde seguir creciendo como científica. Cada una de las ideas, los consejos y las conversaciones que hemos mantenido me han ayudado a construir el modelo matemático que soporta mi tesis. Al sincrotrón “Soleil”, y a Freddie, por permitirme aplicar mis conocimientos de microscopía y ayudaros en el diseño de un nuevo microscopio de infrarrojo.

A todo lo vivido con mi gente de Barcelona en estos cuatro años. En especial...

A Marina, por estar siempre ahí con tu sonrisa y tu sabiduría, porque Barcelona no es lo mismo desde que te fuiste. A Noè, por los karaokes, las cenas, los juegos y por abrirme las puertas de tu casa cuando más lo necesitaba. A Mafe, a Natalia, por hacerme disfrutar los momentos compartidos en nuestro pisiño. A Elio, por las maravillosas conversaciones que hemos compartido.

Al grupo de físicos *Hangouts*, por ayudarme a desconectar cada viernes con cervezas y risas, por las cenas improvisadas entre semana, domingos de *calçotada*, esquiadas, findes en Bonastre y en Martinet, deliciosas paellas en el Delta, y especialmente por nuestra aventura veraniega Santiago 2020.

A mi nueva familia de Vilassar de Mar, por haberme recibido con todo vuestro cariño y con los brazos abiertos. A Marisa y a Martín, por todo vuestro afecto y por el apoyo que me habéis dado desde el primer momento. A Lluïsa y a Joan, por invitarme a los domingos familiares a *Can Giol* y por compartir conmigo vuestras historias sobre Galicia. A Joan y a Paula, por vuestra frescura, juventud y sinceridad en cada una de nuestras conversaciones. *A tots, moltes gràcies per fer-me sentir de la família!*

A todas las personas del Colegio de España. En especial...

A Elena, por cada una de nuestras charlas *tesistenciales*. A Emilio, por tu paciencia, por tus consejos médicos y por nuestras locuras canario-gallegas. A Jorge, por amenizar con grandes debates mis viajes a la "Ecole". A Manu, Samuel y Sara, por seguirme en todas de mis locuras turísticas (en realidad me contuve). A Soraya, por toda la alegría que me transmites y por los ánimos que me das cada día. Gracias a todos por hacer inolvidable mi estancia en París y porque, pese a la distancia, seguís siendo parte de mi vida.

A mi gente de Galicia, porque seguís a mi lado, aunque hayan pasado cuatro años y viva a mil kilómetros. Porque cuando nos vemos, todo sigue igual y me hacéis sentir en casa, como si nunca me hubiese ido. En especial...

A Luci, a Nieves y a Javi, por todos y cada uno de nuestros planes juntos, nuestras cenas, desayunos, y tardes de piscina, que me hacen desconectar de todo y ser verdaderamente feliz. A Bea, a Irene y a Jessy, por animarme y apoyarme a lo largo de tantos años. Gracias por todo el cariño que me dais. A mis *velliñas* físicas, Aniña, Lau y Raqui, porque gracias a vosotras dejé atrás todo lo malo y volví a ser yo misma. Que comenzara este proyecto es, también, mérito vuestro. A Manu, por tu espontaneidad, tu alegría y tu cercanía desde que nos conocimos en la facultad. Y por seguir acompañándome desde entonces. A Angelillo, por sacarme mil sonrisas cada día con nuestros chistecillos, que alegran mis mañanas y me ayudan a comenzar con fuerzas mi día. A María, por tu apoyo constante y por ser mi símbolo de perseverancia y paciencia. A Ferran, a Rafa, y a nuestro señor Pato Macho, por todos los grandes momentos que me dais, sois mi fuente de risa inagotable.

A mi familia, por creer siempre en mí y por hacérmelo saber en todo momento, habéis sido la fuerza que necesitaba en más momentos de los que imagináis, gracias. Porque de verdad que cualquier cosa que pueda escribir en estas líneas es ridículamente insuficiente y jamás reflejará todo lo que os quiero decir en realidad. A vosotros, Sisis y Enris, por estar

a mi lado en cada paso que he dado para llegar hasta aquí. Por escucharme, aconsejarme y por animarme siempre a perseguir mis sueños. Vosotros siempre habéis sido mi modelo a seguir. A ti, Rus, por ser mi amigo además de mi hermano, por todos los años de juegos, de guitarra y poesía. Por recordarme, con tu actitud y con tus acciones, que nunca debemos rendirnos y que siempre debemos luchar por aquello que queremos. A vosotros, Merchi y Queipo, por vuestro cariño y atención durante toda mi vida. Por ser tan buenos conmigo y prestarme vuestra ayuda incondicional en todo momento. Porque siempre os he considerado mis segundos padres.

Y muy especialmente, a Sergi. Por acompañarme en este viaje dándome fuerzas cada día. Has sido el bastón y el apoyo que ha facilitado mi camino. Porque sin ti me faltaría la energía para enfrentarme a este gran reto. Por escucharme, aconsejarme y ser capaz de arrancarme una sonrisa en las situaciones más duras. En estas líneas no puedo reflejar todo lo que disfruto a tu lado, todos los momentos compartidos, porque contigo soy verdaderamente feliz. *Gràcies per caminar al meu costat.*

Abstract

Refractive index (RI) provides information about the propagation of light through a specimen and it is related with some optical and electrical properties of materials. In many cases, certain changes in matter can produce a modification of the refractive index, such as, for example, temperature variations, mechanical stress or changes in the chemical composition of the material. Other materials may present different RI values depending on light propagation direction, as is the case of anisotropic materials. Hence, there are multiple applications in different fields such as biology, pharmacology, mineralogy or material characterization, where the RI value can give interesting information. In this thesis, we have developed an optical method to characterize the RIs of dielectric isotropic samples and uniaxial anisotropic crystals. The particularity of our method is to measure, in a reflection configuration, solid or liquid phases and planar or non-planar surfaces, allowing to characterize optical elements already integrated in optical systems. In-situ characterization of the refractive index is nowadays an unsolved problem of interest for industry and research. Particularly, lenses integrated in optical systems are the major motivation of this work, because they may modify their RI value when inserted into devices.

Our proposal was to design, implement and use, for the first time, a conoscopic Mueller microscope working in reflection to measure the RIs of several samples with arbitrary surfaces. The working principle of our microscope is based on measuring the angle-resolved Mueller matrix of any dielectric specimen by using a complete Mueller matrix polarimeter and a high numerical aperture objective (HNAO). Under this scenario, a polarized incident light beam is highly focused over the studied sample, being the spot size smaller than the curvature of the sample surface, this allowing us to measure non-planar surfaces. The reflected cone of light passes through the same HNAO, being collimated and then, it is polarimetrically analyzed. Note that the incident and reflected light cones are formed by light rays with different angles of incidence and polarizations. As a consequence, the proposed conoscopic microscope is able to measure the angle-resolved Mueller matrix in reflection at numerous incident angles simultaneously, obtaining data redundancy without any mechanical motion of the set-up. A camera with high-resolution records the different intensity patterns that ultimately are used to calculate the Mueller matrix image. Data redundancy is function of the maximum angle of incidence of the HNAO and the number of pixels of the camera.

A mathematical model was developed to theoretically determine the Mueller matrix image. It is based on the Fresnel coefficients that describe the ratio of the reflected and transmitted electric fields to that of the incident beam on an interface between different optical media. These coefficients depend, on the one hand, on the angle of incidence, the polarization and the frequency (or wavelength) of the incident beam and, on the other hand, on the RIs of the media. The model was tested by performing a collection of

simulations and we analyzed the validity of the method by measuring the characteristics of different artificial samples.

The model parameters, such as the refractive indices can be calculated by fitting them with the experimental data measured with the conoscopic Mueller microscope. An iterative optimization routine was developed in order to find the best-fit parameters that minimize a merit function based on the Mean Squared Error (*MSE*) between both experimental and simulated Mueller matrix images. The conoscopic Mueller microscope was finally tested by measuring well-known polarimetric samples with different surface forms.

Resumen

El índice de refracción (RI) es un parámetro físico que proporciona información sobre la propagación de la luz a través de una muestra y está relacionado con algunas propiedades ópticas y eléctricas del medio. El RI es una propiedad intrínseca de los materiales, pero en muchos casos, cambios en la materia producidos por interacciones físicas o químicas, pueden producir una modificación de su valor, como, por ejemplo, debido a variaciones de temperatura, estrés mecánico o cambios en su composición química. Otros materiales pueden presentar diferentes valores de RI dependiendo de la dirección de propagación de la luz, como es el caso de los materiales anisótropos.

Existen múltiples aplicaciones en diferentes campos, como biología, farmacología, mineralogía o caracterización de materiales, donde el valor de RI puede proporcionar información de gran utilidad. En esta tesis, hemos desarrollado un método óptico para caracterizar los índices de refracción de muestras dieléctricas isótropas y cristales anisótropos uniáxicos. Una ventaja de nuestro método es que es capaz de medir el RI en materiales en fase sólida o líquida y superficies planas o no-planas, iluminando la muestra en reflexión. Esto nos permitiría caracterizar elementos ópticos ya integrados en sistemas ópticos. La caracterización del índice de refracción *in situ* es hoy en día un problema por resolver, de gran interés para la industria y la investigación. La principal motivación de este trabajo es caracterizar las lentes integradas en sistemas ópticos, para las que no existe un método estándar.

Hemos diseñado e implementado por primera vez, un microscopio conoscópico de Mueller que trabaja en reflexión para medir los RIs de varias muestras, independientemente de su superficie. En particular, medimos la matriz de Mueller de cualquier muestra dieléctrica mediante un polarímetro de Mueller completo y un objetivo de gran apertura numérica (HNAO). Como consecuencia, se obtiene un haz de luz polarizado y altamente focalizado que incide sobre la muestra, siendo el tamaño del punto focal más pequeño que la curvatura de la superficie de la muestra, lo que nos permite medir superficies no planas. Gracias al HNAO, el microscopio conoscópico propuesto mide simultáneamente la matriz de Mueller para un gran número de ángulos de incidencia (aquellos dentro del cono iluminando la muestra), sin ningún movimiento mecánico del sistema y obteniendo una gran redundancia de datos. Con una cámara de alta resolución se pueden registrar los diferentes patrones de intensidad correspondientes a distintas configuraciones polarimétricas, y utilizarlos para calcular la imagen de la matriz de Mueller. Hemos desarrollado el modelo matemático que nos permite determinar la matriz de Mueller teórica de la muestra. Éste se basa en los coeficientes de Fresnel, que describen la relación entre los campos eléctricos reflejado y transmitido con el haz incidente, en una interfaz entre diferentes medios. Estos coeficientes dependen, por un lado, del ángulo de incidencia, la polarización y la frecuencia del haz incidente y, por otro lado, de los índices de refracción de ambos medios. El modelo desarrollado se probó realizando una serie de simulaciones y

se validó midiendo las características ópticas de matrices de Mueller simulando materiales reales e incluyendo efectos experimentales (ruido, desalineamiento, etc.).

Finalmente, se ha utilizado el instrumento para medir la matriz de Mueller de materiales reales. Los diferentes parámetros ópticos del modelo pueden ser ajustados para que la matriz de Mueller teórica coincida con la experimental. Para tal fin, se ha desarrollado un programa de optimización para hallar el mejor ajuste entre simulación y datos experimentales, mediante la minimización de una función de mérito basada en el error cuadrático medio (MSE). El microscopio conoscópico de Mueller ha mostrado su potencial para caracterizar muestras dieléctricas independientemente de su superficie.

Contents

Chapter 1 Introduction 1
1.1 Motivation 2
1.1.1 Biological applications and pharmaceutical industry 2
1.1.2 Mineralogy and crystallography 3
1.1.3 Characterization of optical elements 4
1.2 Methods for the refractive index measurement 5
1.2.1 Minimum deviation method 5
1.2.2 The Abbe refractometer 6
1.2.3 Interferometric methods 8
1.2.4 Ellipsometry 8
1.2.5 Conoscopy 10
1.3 Proposed optical conoscopic microscope 11
1.3.1 Fresnel coefficients 12
1.3.2 Mueller polarimetry 13
1.3.3 High Numerical Aperture Objective (HNAO) 15
1.3.4 Conoscopic Mueller microscope 15
1.4 Main goals of this thesis 18
1.5 Structure of this thesis 19
Chapter 2 Mathematical formalism 21
2.1 Waves at planar boundaries 21
2.1.1 Maxwell Equations 21
2.1.2 Plane waves approximation 22
2.1.3 Crystal Optics 24
2.1.4 Polarization 27
2.1.5 Boundary conditions 29
2.2 Reflection and refraction of electromagnetic radiation at a crystal surface 31
2.2.1 Wave vectors of the incident, reflected and transmitted beams 31
2.2.2 Polarizations states 37
2.2.3 Fresnel coefficients 39

2.3 Approximations and considerations 43
2.4 Wave propagation inside the uniaxial anisotropic crystals and the emerging waves 43
2.5 Jones and Mueller Matrix formalisms 45
Chapter 3 Mueller conoscopy 49
3.1 Theoretical background of reflection conoscopy 49
3.1.1 General considerations on reflective Mueller matrices 49
3.1.2 Conoscopic illumination 51
3.1.3 Focusing light with a High Numerical Aperture Objective 54
3.2 Conoscopic Mueller microscope 56
3.2.1 Polarization transformations at high numerical aperture systems 58
3.2.2 Calculation of Mueller matrices after the high *NA* objective 60
3.2.3 Mueller matrices in the laboratory system 61
3.2.4 Polarimetric measurement matrix principle 63
3.3 Simulated conoscopic Mueller matrix images 67
3.3.1 Simulated Mueller matrix images of isotropic samples 68
3.3.2 Simulated Mueller matrix images of anisotropic samples 71
3.4 Polarimetric sensitivity 72
3.4.1 Maximum angle of incidence 73
3.4.2 Refractive indices 74
3.5 Constrained variational analysis method to obtain the optical parameters 79
3.6 Accuracy of the optimization program 83
3.6.1 Accuracy as a function of the maximum angle of incidence 85
3.6.2 Accuracy as a function of the refractive indices 88
3.6.3 Influence of noise 93
Chapter 4 Experimental implementation and calibration of the set-up 97
4.1 Experimental configuration of the microscope 97
4.1.1 PSG and PSA design 99
4.1.2 Illuminating arm 102
4.1.3 High *NA* Objective Focusing Systems (HNAOFS) 103
4.1.4 Detection Arm 107
4.2 Alignment method 108
4.2.1 Laser collimation and width measurement 108

4.2.2 Proper Alignment of the Microscope 113

4.2.3 High *NA* Microscope Objective aligning method 116

4.3 Calibration 117

4.3.1 Beam-splitter calibration 118

4.3.2 PSG and PSA calibration 120

4.3.3 CMOS camera calibration 125

Chapter 5 Results: Validation, applications and perspectives 127

5.1 Experimental validation of the reflective Mueller polarimeter 127

5.2 Improving experimental Mueller matrix images 132

5.2.1 Covariance filtering 134

5.2.2 Depolarization filtering 135

5.3 Measured Mueller matrix images of samples 136

5.3.1 High *NA* Objective calibration 136

5.3.2 High *NA* Objective alignment concerns 139

5.3.3 Correlation between model parameters 143

5.3.4 Mueller matrix images of unknown samples 144

5.3.5 Mueller matrix images of well-known glass prisms 152

5.3.6 Non-planar surfaces 157

5.4 Discussion and perspectives 159

Chapter 6 Conclusions 163

6.1 Summary and conclusions 163

6.1.1 Mathematical formalism 164

6.1.2 Mueller conoscopy 164

6.1.3 Experimental implementation of our conoscopic Mueller microscope 165

6.1.4 Results 167

6.2 Proposal for future research 169

List of acronyms 171

Bibliography 173

Chapter 1 Introduction

This thesis proposes an optical method to characterize optical properties of anisotropic crystals (refraction index (RI), crystal orientation, etc.), being isotropic materials a particular case. The developed instrumentation, a conoscopic Mueller microscope working in reflection configuration, is mainly devised to measure the refraction index of non-planar isotropic materials. In particular, lenses already integrated into optical devices are the major motivation. These integrated lenses may modify their value of the refraction index when inserted into the devices, due to mechanical stress. Therefore, the precise calibration of the RI for such optical elements, once they are already inserted into the optical instrumentation, becomes an unsolved problem of interest for industry and research. In this sense, well known transmissive methods for refraction index determination are somewhat invalid in numerous cases due to the in-shell configuration of the lenses. What is more, a standard method does not exist nowadays to calibrate the RI of such kind of optical samples. We want to emphasize that although the optical instrumentation presented in this thesis was mainly devised to find a solution for the above-stated scenario, the achieved conoscopic Mueller microscope, and the associated mathematical model we developed to describe its performance, are more general, and can also be applied to non-planar anisotropic dielectric materials with an arbitrary orientation of its anisotropic axis.

In this first chapter we perform an overview of the state of the art in refractive index characterization. In this sense, this introduction contextualizes this thesis and the research developed these last four years with the intent of describing the purpose of developing our conoscopic Mueller microscope.

First, to motivate this current thesis, a general description of some applications where the measurement of the refractive index is important, are introduced in section 1.1. Diverse examples in multidisciplinary fields, such as biology, mineralogy or material characterization, are described in this first section. Then, an overview of the most common methods for the measurement of the refractive index is given in section 1.2. Following, in section 1.3, the main research studies on which our proposed design is based are summarized. Finally, the main goals of this thesis (section 1.4) and the structure of this thesis (section 1.5) are detailed.

1.1 Motivation

The refractive index (RI), also called index of refraction (n), provides information about the propagation of light through a medium and about the propagation modification it suffers when changing from one medium to another. It is also directly related with some optical and electrical properties of materials. Thus, it is an important optical parameter that must be calibrated in multiple scenarios since it exhibits the optical properties of the material. Its value depends on the one hand, on the frequency (or the wavelength) of light, and, on the other hand, on the characteristics of the material, i.e. its density, chemical composition, electrical susceptibility, … [1, 2].

The thorough knowledge of a material RI value and dispersive characteristics are useful for the characterization of minerals, synthetic materials and specimens with linear or nonlinear refractive indices. In many cases, certain changes in matter can produce a modification of the RI, such as, for example, mechanical stress or a variation in the chemical composition of the material (e.g. by doping with impurities), or an increase (or decrease) in the temperature. Accordingly, there are many applications in many different fields where there is interesting to measure and study the RI to characterize a specimen. To motivate this thesis, and to show that the refractive index is an important optical property (not only significant in optics-related fields), some examples are introduced in the following.

1.1.1 Biological applications and pharmaceutical industry

In numerous biophysical, medicinal, chemical and pharmaceutical applications, the value of the refractive index can provide useful information. In this sense, since light is deflected as it enters a material, the characterization of RI and its distribution may be interesting to study biological and chemical complex media such as biological tissue. Note that the refractive index is a key parameter for image reconstruction and interpretation as well as for understanding sample properties, offering a non-invasive way to probe the structural information of living cells or tissues without using exogenous agents. To highlight the relevance of the study of refractive index in this area some examples are shown.

The refractive index plays an important role in bioimaging techniques, mainly due to the huge number of existing methods to characterize it and their versatility. As most tissue samples are optically turbid, highly scattering, and non-homogeneous, the measure of the RI can be used to improve bioimages, providing high-fidelity images [3–5] or generating 2D and 3D refractive index maps to visualize cells and tissues [6–8]. The non-invasive measure of the RI can also report a real time visualization of cellular and bacteria dynamics under study [9, 10].

In addition, most normal cells have a refractive index different than diseased cells. For this reason, various research studies have characterized the refractive index of healthy and diseased cells, aiming to better distinguish them to remove diseased tissues or to study their cell cycles. In particular, tumor tissue can be an example because exhibits higher refractive index variance than normal tissue [9, 11].

The refractive index is also used to determinate the concentration of a solute in an aqueous solution and to analyze chemical properties of dissolutions [12–16]. There exist a wide variety of implementations in very different areas relating the concentration of a solute in a solution with the local RI, as in atmospheric air pollution where the concentration and the chemical composition of particle pollution in air has to be measured [17–19]. Moreover, dissolution of sucrose and other sugars in an aqueous solution changes the optical properties, in particular its RI. Thus, the determination of pure sucrose content in soft drinks, fruit juices, tomato concentrates, etc. can be calculated from the RI measurement. BRIX refractometers [20, 21] are widely used in food and beverage industry. In medicine, the concentration measurement of different kind of cells or glucose in blood can be also of interest, for example for diabetes diseases [22, 23].

1.1.2 Mineralogy and crystallography

Another application where the characterization of the refractive index can also be important is crystallography. Note that the internal structure and the RI of minerals are related. In this respect, by using simple set-ups (as polariscopes, interference color charts, Becke line method, etc. [24–28]) the RIs of materials can be studied and related with the structure of the mineral (symmetries, axes, etc.). For this reason, in optical crystallography a specimen can be classified depending on how a light beam is propagated inside the material. We say that a crystal is isotropic when the refractive index is the same in all crystallographic directions and, anisotropic when the refractive index varies along different crystallographic directions. Furthermore, the RI of a particular mineral does not vary significantly from one mineral grain to another [26, 28]. As a result, the refractive index is particularly useful for rapid identification of most common minerals using tables and charts [29, 30], for distinction between natural and synthetic gemstones, for helping reveal the origin and evolution of a mineral [24, 25, 31, 32], among others.

When geologists try to identify minerals, at least two characteristics are taken into account, the chemical composition and the structure of the material. The main reason is that structural differences of a mineral can occur for the same chemical substance, as a function of external conditions, such as temperature or pressure. These minerals are called polymorphs and two clear well-known examples are diamond-graphite (C) and calcite-aragonite ($CaCO_3$) [26]. By analyzing the RI and the birefringence (the difference between the major and minor refractive indices of the specimen), structural information can be obtained and polymorphs can be differentiate [33].

Moreover, stress can temporary change the refractive index and introduce birefringence into the material or, in extreme cases, damage it. This case is called photoelasticity and it can be caused by variations in temperature, vibrations and shocks [34, 35]. Under this scenario, anisotropy is governed by the stress field and could not be necessarily constant throughout the sample (an example is given in Figure 1-1, where we show an image of a plastic CD case where the non-homogeneous stress-induced birefringence is observed by using a polarization based technique).

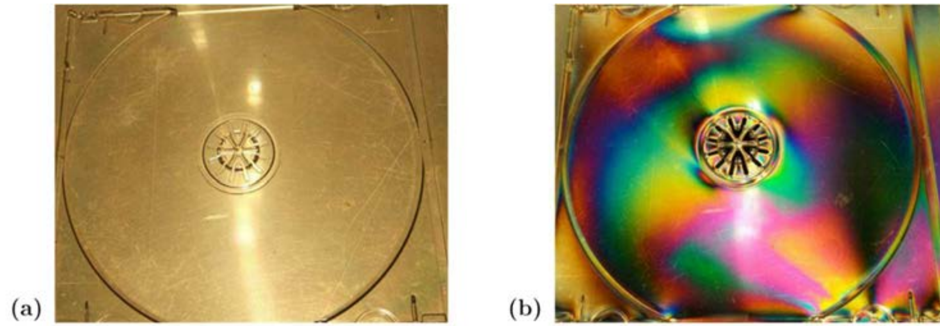

Figure 1-1. (a) Plastic CD case. (b) Stress-induced birefringence in the plastic CD case placed between two crossed polarizers and illuminated with white light. It can be observed that anisotropy is not constant over the entire sample.

Over the years, a number of photoelasticity based measurement techniques and commercial equipment have been developed for residual stress measurements in so many applications such as mineralogy [36–38]. However, the birefringence changes due to stress, temperature, or pressure can appear in other types of samples. Because of this, the study of photoelasticity has been extended to other research fields, such as in mechanical engineering [32, 39, 40], medical science [41, 42], among others.

1.1.3 Characterization of optical elements

Companies that manufacture optical materials are interested in characterizing the refractive index of the optical components in their designs in order to accurately define how light behaves when it passes through, or is reflected by, the different optical elements. To properly characterize the optical properties of any element, an accurate knowledge of the element profile as well as its RI value (which may be unique or related to a stack of different material layers with different RIs) must be ensured. Note that the knowledge of the refractive index profile of each element may help to design different complicated optical devices.

A lens is an example of an optical element that is used in a wide variety of applications such as, for example, the correction of visual impairments, in imaging systems as telescopes, microscopes or cameras, for light concentrators, etc. [1, 2]. When designing a lens to have a specific optical power, any change in the RI of the material has to be controlled, because it can affect the focal length of the optical system.

Another example are optical waveguides that are mostly used in communications [43, 44], sensors [45, 46], etc., and may become part of complex optical integrated circuits. The refractive index of an optical fiber enables to determine some properties as guiding mode propagation, cutoff wavelength, chromatic dispersion characteristics, and so on [47].

Some applications use high precision optical elements that must be studied after they are manufactured and placed at their final position. This is because during its manufacturing process or once they are placed on its holder, a change in temperature or

pressure can produce a slight defect in the element, making it completely ineffective for its intended purpose.

Nowadays, the two most common techniques used to manufacture optical elements, as lenses, are injection molding process [48, 49] and compression molding process [50, 51]. The benefits of both techniques are the low unit cost and the very high-volume production, but both imply strong temperature or pressure changes that may incur various defects on the used material, such as deformation, sink mark, birefringence, and aberrations. Despite rigorous control of the specimens during production processes, the quality of an optical product can be further reduced by introducing these defects in the refraction index of the specimen [52–54]. Such uncontrollable effects can be critical, requiring their precise characterization prior to use the optical elements in any device.

1.2 Methods for the refractive index measurement

In literature, one can find many books and scientific manuscripts studying different techniques to measure the refractive index of solids, liquids and gases. To evaluate the optical properties of a material, destructive or non-destructive approaches can be used. The first one analyzes the specimens by destroying a small number of them, while the second one allows samples to be characterized by several means without destroying them. Thus, non-destructive testing is a highly valuable technique because the analyzed sample is still available for other uses, tests, or simply can continue performing its current function. Note that when optical elements are already integrated in optical systems, non-destructive methods for RI determination are unique possible approaches.

Several types of non-destructive techniques have been developed for measuring the refractive index. In the next sub-sections some optical methods are briefly described, and their main advantages and disadvantages are commented.

1.2.1 Minimum deviation method

One of the most common techniques used to study transparent isotropic materials is based on the study of the angle of minimum deviation ($\delta_{\min}$) observed when a light beam passes through a prism [1, 2]. To determine the RI of any material with this method, the sample has to be cut with the geometry of a prism similar to the shown in Figure 1-2.

When a monochromatic beam passes through a prism, according to the Snell law, it is deviated from its original direction by an angle δ. In general, the deviation angle δ depends on the incident angle θ_{in} to the prism, except for very small prism refringence angles ϕ. In addition, the $\delta(\theta_{in})$ function presents a minimum, $\delta_{\min}$ for a given incident angle θ_{in}.

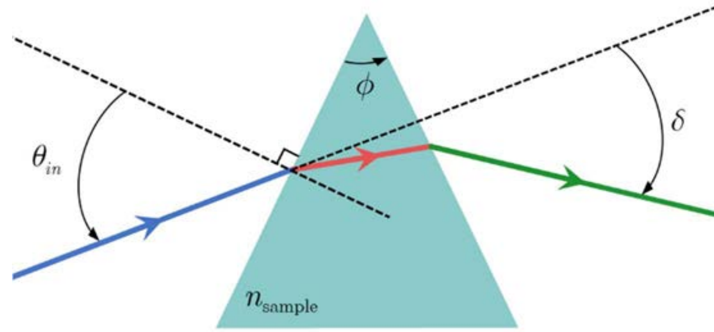

Figure 1-2. Scheme, showing the deviation angle δ, used to determine the refractive index n_{sample}.

The method of minimum deviation consists in finding the angle of minimum deviation δ_{min} for a particular wavelength (this value depends on the incident wavelength, due to the materials dispersion). The refractive index can be calculated from a measurement of the angle of minimum deviation δ_{min} [55, 56]

$$n_{\text{sample}} = \frac{\sin\left(\dfrac{\delta_{\text{min}} + \phi}{2}\right)}{\sin\left(\dfrac{\phi}{2}\right)} \tag{1.1}$$

where ϕ is the refringence angle of the prism (see Figure 1-2). Note that as the minimum deviation angle $\delta_{\text{min}}(\lambda)$ depends on the wavelength, the measured $n_{\text{sample}}(\lambda)$ also presents this dependence. Consequently, by calibrating the refringence of the fabricated prism ϕ and measuring the δ_{min} for a given wavelength, the n_{sample} is computed from Eq. (1.1) for such wavelength.

The prism minimum deviation technique is commonly used for extremely accurate measurements of bulk transparent glasses [2, 55–58] and also, liquid and gases can be optically characterized by using a hollow prism to contain the sample [55, 59].

Nevertheless, minimum deviation method presents a great disadvantage: users have to fabricate high-quality prism-shaped samples. Hence, this technique cannot be used with routinely produced samples, as lenses or waveguides, or specimens of different shapes, as biological tissues.

1.2.2 The Abbe refractometer

The Abbe refractometer can work in reflection and in transmission configurations (see Figure 1-3 (a) and (b), respectively). In both cases the material under study is placed between two prisms made of dense glass (also known as Flint glass) with high refractive indices (n_{prism}) that are well-known.

This refractometer is used to determine the refractive index of a sample by measuring the critical angle α_{cr} occurring at total internal reflection [60]

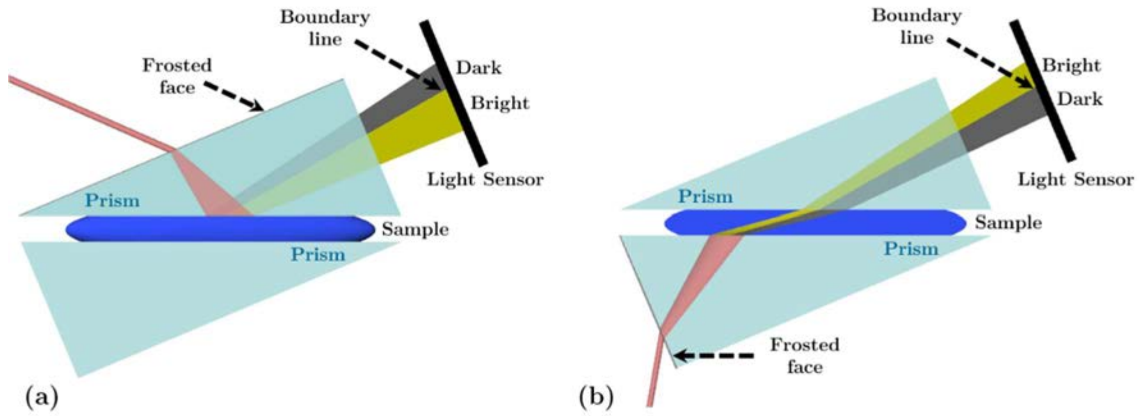

Figure 1-3. Scheme of two Abbe refractometers working (a) in reflection, and (b) in transmission configurations.

$$n = n_{\text{prism}} \sin \alpha_{\text{cr}} \tag{1.2}$$

where n is the RI of the sample to be studied.

The incident collimated beam is diffused by the first frosted face of the Abbe prism. The diffused light is propagated in all directions, passes through the prism and hits the interface of the specimen under different angles of incidence (see Figure 1-3). If the incident angle is above the value $\arcsin(n/n_{\text{prism}})$, then total reflection occurs at this interface, and no light is transmitted into the sample. On the other side, if the incident angle is below $\arcsin(n/n_{\text{prism}})$, light is transmitted through the sample. At the angle α_{cr}, at which the transition from transmission to total reflection occurs, the image displays a sharp separation between bright and dark ranges, similar to the scheme shown in Figure 1-4. By varying the observation angle, the angle of total reflection can be found when the boundary line is adjusted to the point of intersection of a reticle. The Abbe refractometer is calibrated to give the refractive index n, instead of the angle of total reflection (α_{cr}).

Abbe refractometers can work with monochromatic or white light. In non-monochromatic cases, each wavelength is dispersed in different directions, each one with a particular critical angle, and thus, the boundary line (see Figure 1-4) of white light light is not well defined. To correct this dispersive effect, two compensating Amici prisms are introduced into the refractometer.

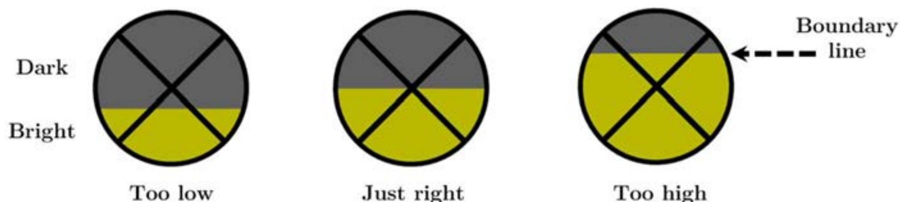

Figure 1-4. By simply aligning the boundary line of refraction at the cross intersections, the Abbe refractometer directly indicates the refractive index.

The Abbe refractometer can be used to measure RI of liquid or solid samples [60–67]. However, it is limited by the condition that $n < n_{\mathrm{prism}}$, i.e., it cannot measure refractive indices larger than that of their constitutive prisms. In this sense, depending on the sample under studio, Abbe refractometers based on prisms with different n_{prism} are built. The catalogue of [68] shows Abbe refractometers with different measurement ranges.

Note that the surfaces of the solids measured by Abbe refractometers have to be flat because an incomplete contact between the prisms and the sample increases the measured RI uncertainty. Thus, this kind of refractometer does not allow to characterize non-planar optical products, as lenses. In addition, samples must be optically isotropic, non-absorbing, and homogeneous to avoid refractive index errors [69].

1.2.3 Interferometric methods

Interferometry has been extensively used for RI characterization. By using this approach, interferences are created between two coherent beams, the reference beam and a second beam testing the sample. Spatial shifts of the interference pattern, caused by the introduction of the studied sample (which modifies the optical path of one of the beams), can be related with the RI of the studied specimen. There are several interferometric methods with completely different basic principles that provide a versatile way of obtaining the refractive indices of different materials, or other parameters, as the thicknesses of the sample.

Some examples of interferometers that make simultaneous measurements of RIs of optically transparent plates or multiple layers are: Michelson interferometers [70–72], Fabry Perot interferometers [73–75], Mach-Zehnder interferometers [76–78] and combinations of confocal microscopes and optical low-coherence interferometers [79–82], among others.

The interferometric methods present some advantages as they are sensitive to the phase or optical path differences and consequently, small relative shifts of the RIs can be measured interferometrically. Nonetheless, they usually require complex instrumentation and very accurate alignment processes. In addition, they are very sensitive to vibrations and air fluctuations (or they have to be built under void conditions), and the interferometer measurement is restricted by the available wavelength range of the existing laser.

A wide variety of interferometers is only able to characterize sample surfaces that are flat, parallel, and homogeneous. Nevertheless, when non-planar surfaces need to be optically characterized, other techniques have to be implemented.

1.2.4 Ellipsometry

Ellipsometry is an optical technique that enables to measure the change of polarization that occurs when a polarized beam is reflected by (or transmitted through) a material. By doing so, ellipsometers can simultaneously measure the modulus and phase of the polarization components of light [83–85].

By assuming an incident light beam that illuminates the sample to be analyzed, both reflection and refraction may occur at the interface sample-air. The Fresnel equations mathematically describe the ratio of the reflected (or transmitted) electric field to the incident beam. The ellipsometric values $\tan\Psi$ (corresponding to the amplitude ratio) and Δ (corresponding to the difference in phase shift) are defined from the ratio (ρ) of the complex Fresnel coefficients as [84]

$$\rho = \tan\Psi \exp\left(i\Delta\right) \tag{1.3}$$

Since these ratios are complex, the Fresnel coefficients and the ellipsometric angles (Ψ and Δ) describe not only the relative amplitudes, but also phase shifts between waves. Moreover, all these parameters are function of the optical characteristics of the sample, the illumination wavelength and the angle of incidence of the incident light beam. Therefore, by building proper physical models, the optical parameters of samples can be determined by fitting the model parameters to ellipsometric measurements.

The ellipsometer working principle is based on a controlled polarized beam that illuminates the sample. The polarization of this input beam, after reflection or transmission on the sample, is modified due to light-matter interaction, according to the specific ellipsometric angles Ψ and Δ. The corresponding exiting beam, function of Ψ and Δ, is analyzed with a controlled polarization analyzer. Finally, a radiometer is used to measure the irradiance corresponding to the projection of the unknown exiting polarization on a selected particular polarization analyzer. Figure 1-5 shows a schematic view of a simple ellipsometer working in reflection. By measuring the polarization changes after reflection or transmission, the parameters Ψ and Δ of the sample can be determined, from which optical characteristics may be deduced. Ellipsometers are very sensitive to any change in the optical response of incident beam, thus, they are useful to characterize composition, thickness, crystalline nature, doping concentration or optical parameters as RI. For that purpose, as stated before, a theoretical physical model is developed in order to simulate the experimental conditions. By comparing the model solutions with the experimental results, the optical parameters of the sample are obtained.

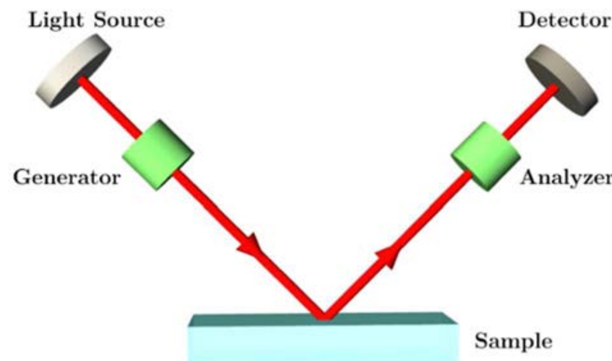

Figure 1-5. Scheme of a general ellipsometer working in reflection formed by two optical arms. The first arm comprises a polarization state generator coupled to a source of light. The second arm is used to determine the polarization of the reflected beam. It comprises a polarization state analyzer and a detector.

Apart from reflection and transmission configurations, ellipsometers can work in total internal reflection mode to determine the optical response of specimens [86]. By taking into account these three configurations, they are used to measure the RI and the thickness (ranging from few nanometers to hundreds of micrometers) of transparent or low-absorbing thin films [87–90]. The use of coherent light sources as lasers can considerably increase up to centimeters the maximum sample thickness measurable [90]. Consequently, ellipsometry is widely used to investigate different kinds of surfaces and thin-film materials, such as biological materials [91–93], microelectronic fabrication processes [94], or films at the nanoscale [95, 96].

Unfortunately, as ellipsometric measures cannot distinguish depolarization contributions and are insufficient to completely characterize polarization changes in time or space, "classical ellipsometry" applied to the measure of the RI on rough substrates, or other type of depolarizers, has generally proven to be very difficult [97]. That is to say, ellipsometric measurements require that the light beam remains completely polarized during the measurement process. Nevertheless, when the sample surface has significant roughness, "classical ellipsometry" is not adequate to describe reflected beams because it cannot take into account depolarization and cross polarization effects. For this reason, when light becomes partially polarized, by interacting with some element, it is necessary to use more "generalized ellipsometric" techniques, as the Mueller Ellipsometry (known as Polarimetry) [90, 98].

1.2.5 Conoscopy

Conoscopy is an optical technique, widely used in mineralogy, to obtain the orientation and the refractive indices of anisotropic crystals, i.e. materials where the RIs change with direction of propagation.

When light enters an arbitrary oriented uniaxial anisotropic crystal, if the propagation direction is not perpendicular or parallel to the crystal optical axis, it is split into two rays (ordinary and extraordinary rays) that vibrate perpendicular to each other and that have different velocities [2, 99]. Based on this phenomenon, a collimated light beam that passes in sequence through a polarizer, a microscope objective, the anisotropic crystal, an objective lens system (that re-collimates the transmitted beam) and an analyzer (that is crossed with respect to the first polarizer), generates a highly informative pattern of interference (see Figure 1-6). This interference pattern is not a magnification of the object itself, but instead, it is a propagation directions image mapping the directions that light takes through the sample. By using this scheme, the symmetries of the anisotropic crystal, the directions of its optical axes, its principal RIs, among other parameters, can be determined by analyzing the interference pattern obtained for a particular crystal. Note that the obtained interference figure depends on the thickness and the birefringence of the mineral under study. That is to say, different thicknesses of the same mineral may display different interference patterns.

The main feature of conoscopy is its feasible set-up. Because the figure is a wave-directions image, vertical displacements of the sample will not alter the observed interference figure. To increase the information about the sample under study, higher angles of incidence should be used, i.e. larger numerical aperture cones of light provided by higher numerical aperture objectives.

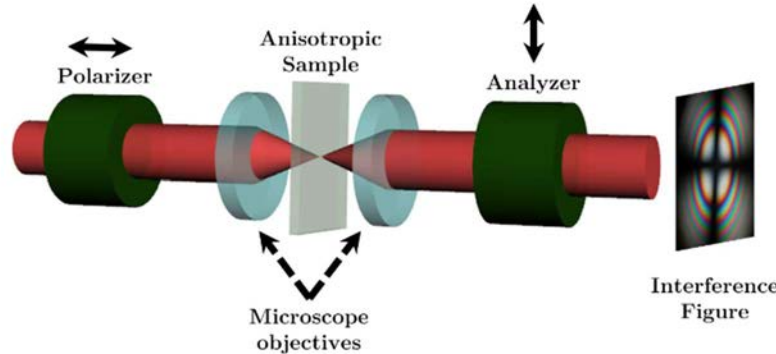

Figure 1-6. Scheme of a conoscopic set-up. A linearly polarized convergent light beam passes through the anisotropic sample and it is projected, at the exit, on a linear analyzer, generating an interference figure.

Several optical configurations of a conoscope can be found in literature, consisting in illuminating the anisotropic sample with a convergent or divergent cone of light, measuring the transmitted or the reflected beam, using a monochromatic or polychromatic illumination, etc. [25, 33].

Conoscopes are also used to characterize plane-parallel uniaxial plates such as wave retarders or polymers [100–102], and more complex anisotropic devices as liquid crystal displays [103–105].

Nevertheless, conoscopy presents the same disadvantage than other methods used for the characterization of RI, the sample under study must be reasonably homogeneous and planar across the region illuminated by the cone of light.

1.3 Proposed optical conoscopic microscope

As we can see, the great majority of methods shown in references present a configuration able to measure the refractive index of samples in transmission. Nevertheless, there are some situations where the only possibility to measure the RI is by using a reflective configuration. In particular, for the characterization of a sample that is not transparent, or an optical component already integrated into a device (for example, CCD camera lenses of a mobile phone). In such cases, the specimen cannot be characterized to guarantee the accuracy of the optical system.

In the same way, the previous described techniques are able to accurately characterize the RI when the sample surface is homogeneous and planar, either prisms or parallel-side

thin films. But, what happens when the specimen presents a significant curvature or certain roughness? Or what about if it presents local anisotropies?

Let us take as an example the possible anisotropies that appear in a curved lens during its manufacture, after the injection molding and compression molding processes. A possible solution is to analyze one portion of the material used to create the lens. A thin film or a prism can be made from the specimen before or after the molding processes and, it can be optically characterized. Then, the optical element can be considered invariant, i.e. it remains unchanged even if there is a variation in the density of the material due to temperature or stress changes or because of contact with another material. However, this assumption cannot be guaranteed, and degradation of optical systems associated to the above-stated external conditions, cannot be detected with the previously described techniques.

As stated above, it looks like there is not a technique that allows characterizing samples that are fixed in optical devices or whose surfaces are non-planar. In this thesis we propose a new method that could provide a solution to these situations of interest for industry and research applications. To this end, the following items have been taken into account.

1.3.1 Fresnel coefficients

The main goal of this thesis is to propose a general optical approach able to measure the RI of samples, including isotropic or anisotropic materials, and valid for planar and non-planar surfaces. In addition, the method must be devised in reflection configuration, in order to be able to measure optical components already integrated in optical systems. With all this in mind, from those methods presented in section 1.2, ellipsometric based systems seems to be a feasible approach to measure the RI in a reflective configuration. Consequently, we have proposed to design a polarimetric set-up that characterizes the Fresnel coefficients in reflection. As our idea is to analyze optical components, which may include birefringence effects, the calculus of the Fresnel coefficients has to consider not only isotropic materials, but also anisotropic samples.

Based on the theoretical models described in [106–108], the Fresnel coefficients in reflection can be calculated by measuring the polarization changes produced by a light beam interacting with the specimen under study. By assuming an optically controlled incident light beam that illuminates the sample and, by analyzing the reflected light beam, the material parameters can be obtained. It is important to note that to characterize the sample using the Fresnel coefficients, the angle of incidence and the illumination wavelength must be known.

To increase the number of measurements (redundancy data) and to reduce possible measurement errors, [109] and [110] propose to introduce a mechanical arm in the “classical ellipsometer” to variate the angle of incidence of light on the material. In this manner, a single polarized light beam interacts with the specimen under study at different angles of incidence. For each different angle of incidence, reflected and/or transmitted beams are

polarimetrically analyzed. A combination of the measurements at multiple angles of incidence and at several wavelengths gives additional information that can be used to measure multilayer thin films or to reduce correlations between parameters.

However, as has been previously commented, "classical ellipsometry" cannot analyze rough substrates because ellipsometric angles are insufficient to completely characterize depolarization contributions. The "generalized ellipsometry" uses the Mueller matrix based formalism [111] to determine the optical properties of more complex structures, and is valid to deal with depolarizing materials.

1.3.2 Mueller polarimetry

Let us focus in Mueller polarimetry. When an optical beam interacts with matter its polarization state can be changed by varying its amplitudes, its phase, its direction of the orthogonal field components, or reducing its degree of polarization. For these reasons, a mathematical formalism that describes not only polarized light, but also partially and unpolarized light is needed. The Mueller-Stokes formalism [85, 111, 112] is a valid approach to describe the above-stated situations. In such formalism, Stokes vectors, $\boldsymbol{S}$, describe the polarization state of light beams, this information being contained in 4 real magnitudes called Stokes parameters [111, 112]. From Stokes parameters, the degree of polarization of light beams can also be calculated. What is more, the Stokes parameters can be described from combinations of different radiometric measurements, and therefore, they can be experimentally determined from simple intensity measurements. By turn, Mueller matrices, $\boldsymbol{M}$, are 4×4 real matrices that represent the polarimetric transfer function of the system, and contain information related to all the polarization properties of samples (diattenuation, retardance and depolarization) [83, 84, 111, 112]. In this context, Mueller matrices relate the input and output polarization states ($\boldsymbol{S}_{in}$ and $\boldsymbol{S}_{out}$, respectively) by following the well-known linear relation

$$\boldsymbol{S}_{out} = \boldsymbol{M} \cdot \boldsymbol{S}_{in} \tag{1.4}$$

Thus, Mueller-Stokes formalism (and thereby Mueller polarimetry) is able to describe the polarization-altering characteristics of a sample, or a cascade of samples, being a powerful technique for an accurate determination of the polarization states of light beams, as well as the optical properties and geometric characteristics of materials, including its depolarizing capability.

Numerous papers and discussions have appeared in literature that use Mueller polarimeters to measure the refractive index of samples for a particular angle of incidence [90, 111, 113, 114]. For our particular goal, let us study the research developed by authors in Refs. [115] and [116].

Based on the idea of increasing the number of angles of incidence, Refs. [115] and [116] proposed to include two microscope objectives to construct a Mueller matrix imaging polarimeter that measures angle-resolved Mueller matrices of isotropic and anisotropic

substrates, single-layer thin films, or multi-layer structures. The special feature of their set-up is the use of two long working distance microscope objectives to measure the Mueller matrix image of samples and then, calculate their dielectric tensors. One microscope objective focuses the beam onto the sample and the other one collects the reflected beam exiting the sample (see Figure 1-7). Therefore, instead of measuring a single Mueller matrix per angle of incidence, the microscope objectives simultaneously generate and collect a large number of incident and reflected angles to finally obtain an angle-resolved Mueller matrix image.

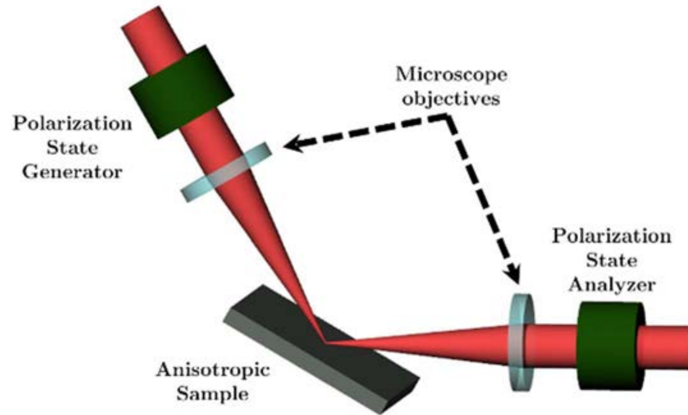

Figure 1-7. Diagram of the microscope objectives illuminating the anisotropic sample in reflection mode and collecting the reflected beam.

Moreover, the illumination arm and the sample stage can be rotated to change the angle of the illumination microscope objective axis to the sample surface and hence, select the proper set of angles of incidence and the azimuthal angles during the measure. In this way, by modulating the polarization of the focused illuminating beam and measuring the spatially varying reflected beam, the sixteen Mueller matrix elements are acquired at numerous angles of incidence. Thus, the polarization properties of the sample are obtained as a function of the set of incident and azimuthal angles point-by-point, represented in the Mueller matrix image. Selecting the illumination microscope optical axis by mechanically rotating the illumination arm, their designed Mueller polarimeter can operate either in transmission mode or in reflection mode.

Then, the dielectric tensor and the thickness of the measured sample are determined by an optimization routine that compares the measured Mueller matrix image to a Mueller matrix image obtained by a forward calculation using an initial estimation of the sample optical properties.

Their set-up and their developed model allow to determine the dielectric tensor of either isotropic or anisotropic samples, but the characterized samples must also be substrates or thin film layers. Even then, based on the methodology described in Refs. [115] and [116], we have proposed to use a Mueller polarimeter to characterize isotropic and uniaxial anisotropic crystals, but in our case avoiding any mechanical movement (and the consequent positioning errors).

For that purpose, we propose to build a polarimetric microscope based on a single high numerical aperture objective (HNAO) with its optical axis perpendicular to the sample surface. In this configuration, the microscope allows us to illuminate a very small specimen area (and therefore, non-planar surfaces can be locally approximated to planar surfaces). The same microscope is also used to collect the reflected beam. The small focus spot created by the HNAO allows as well minimizing the effects of any spatial non-uniformities in the sample.

1.3.3 High Numerical Aperture Objective (HNAO)

According to the Debye approximation [117, 118], high numerical aperture objectives decompose an incident light beam into a set of superposed plane waves whose propagation direction is within the geometrical focal cone. In addition, the reflected light cone is also formed by a combination of plane waves at different reflected angles.

Assuming the HNAO to be free from aberrations, its focusing properties can be modeled with a well-established angular distribution of plane waves and polarizations. Moreover, the size of the focal spot becomes very small (around microns). When the set of plane waves illuminates a non-planar surface placed at the focal plane of the HNAO, the boundary can be approximated to a planar interface when it is compared with the size of the focal spot, and in this approximation, the Fresnel equations still work. By taking into account the Fresnel coefficients, the reflectivity is different for light polarized in the plane of incidence and light polarized perpendicular to it. Furthermore, to focus a polarized beam, by a high numerical aperture objective, causes bending of the polarization vectors [119]. Accordingly, different polarization vectors illuminate the sample surface at different angles of incidence, which results in a set of reflected polarizations, clearly described by the Fresnel equations. Hence, a polarimetric image of the back focal plane of the HNAO lead to a certain intensity distribution image, from which significant information of the sample can be retrieved, when the reflected beam is projected on a linear analyzer [101].

1.3.4 Conoscopic Mueller microscope

In the literature, there are several works that used conoscopic microscopy to measure the Mueller matrix, most of them operating in transmission [120–123]. Nevertheless, the designed set-up constructed in our laboratory is based on the Mueller microscope working in reflection proposed in Refs. [124, 125]. Their designed microscope is made of two optical arms that share a unique HNAO. The first arm, at the entry, comprises a source of light coupled to a polarization state generator that generates any desired state of polarization. On the other side, the reflected arm comprises a polarization state analyzer and a pixelated detector that determine the polarization of the reflected beams. Their proposal uses a non-polarizing beam-splitter to steer the polarized incident beam to the HNAO as well as the reflected beam, collected by the HNAO, to the analyzer (see Figure 1-8). That is to say, the incident polarized beam, transmitted through the beam-splitter, passes through the

HNAO and is focused onto the sample. Then, the reflected beam is collected by the same HNAO and is steered, by the non-polarizing beam-splitter, to the polarization state analyzer. In addition, they use a system of lenses to eliminate the inhomogeneities of the source and to select the measurement modes, between conoscopic images and conventional microscopic images.

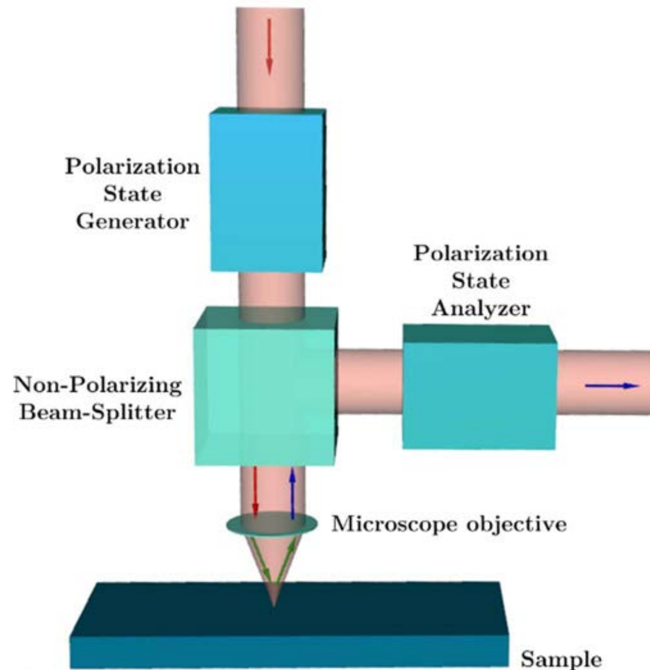

Figure 1-8. Diagram of the non-polarizing beam-splitter and the microscope objective. Polarized incident light is steered to the microscope objective and, the reflected beam is steered to the polarization state analyzer.

In the conoscopic mode, the Mueller microscope is able to measure angle-resolved Mueller matrices as a function of incident and azimuthal angles, represented point-by-point in the recorded image. They have used this Mueller microscope to characterize diffraction gratings and entomological structures in reflection.

Returning to the subject of optically characterizing non-planar surfaces, we have decided to modify and readapt the set-up proposed in Refs. [124] and [125] to measure the Mueller matrix image of isotropic and uniaxial anisotropic samples. As mentioned above, Mueller ellipsometry can be used to look at changes in reflected polarization states but, instead of measuring the specimen at several angles selected manually by changing the position of an optical arm, the HNAO is used to generate a larger set of angles of incidence that allows performing fast and accurate measurements without any mechanical movement. In addition, the use of a high numerical aperture microscope significantly reduces the size of the focal spot, which allows us to consider non-planar and inhomogeneous samples as planar and homogeneous at the illuminated region.

Although high numerical apertures are of interest for our goal, care must be taken in the alignment of the conoscopic Mueller microscope shown in Figure 1-8. Aberrations might

be caused by imperfections in the HNAO or by misalignments of any component of the system. For this reason, a free-aberration microscope objective ideal for polarizing applications has to be used. In addition, during the construction of the set-up, the misalignments introduced by the optical elements have to be corrected to avoid changes in the direction of propagation of light. The most sensitive part of the whole set-up is to achieve an overlap between the incident and reflected cones, so the optical axis of the HNAO and the illumination beam propagation direction have to be parallel between them and, at the same time, perpendicular to the sample surface.

Based on other research works [126, 127], we can see that the use of mechanically rotating elements may cause vibration and beam wander. In the proposed polarimetric microscope, they can affect the illumination of the back focal plane of the HNAO and therefore, light passing through the microscope objective. To avoid misalignments during measuring time, electrically addressable polarization elements (e.g. liquid crystal displays) are a suitable option to overcome this limitation. The used polarization state generator and analyzer can consist of a fixed linear polarizer and two electrically controlled variable retarders [128–131]. By electrically addressing pairs of voltages to the polarization state generator and analyzer and recording the intensity patterns with a pixelated camera, the angle-resolved Mueller matrix of the non-planar sample can be calculated from the Mueller-Stokes formalism [111, 112].

Since each pixel of the detector corresponds to a different pair of incidence-azimuthal angles and thus, to a different polarization transformation, the experimental Mueller matrix image consist of several single Mueller matrices. Notice that the HNAO provides large sample redundancy data because it is able to generate multiple polarized waves that simultaneously illuminate the dielectric sample. Hence, the number of measured data will depend, on the one hand on the numerical aperture of the HNAO and, on the other hand, on the number of pixels of the used sensor.

After measuring the characteristic Mueller matrix image of the sample, the optical parameters (RI and crystal orientation) can be determined by comparing experimental angle-resolved Mueller matrices with theoretical angle-resolved Mueller matrices obtained from an appropriate physical model (by using a developed anisotropic model based on the Fresnel coefficients for reflection). The calculus of these optical parameters requires an optimization program that minimizes the difference between simulated and experimental data. To find the optical parameters of the sample, Ref. [115] proposes to use as merit function the mean squared difference between each point of the calculated and measured Mueller matrices. From an approximate knowledge of the dielectric sample and by iteratively varying the model parameters, different Mueller matrix images are calculated. When the merit function is minimized, the desired RI and the orientation of the specimen are found.

1.4 Main goals of this thesis

Several optical techniques have been developed to measure the refractive indices of thin films and dielectric materials by analyzing the light transmitted or reflected by the sample (see section 1.2). Nevertheless, the surfaces of the analyzed samples are always planar, either as prisms or thin films. In this thesis, we provide the theoretical basis and the procedure followed in the laboratory to describe and implement a Mueller microscope that is able to measure in reflection the RI and the orientation of non-planar and non-transparent dielectric samples, such as curved lenses, minerals or liquid crystal displays.

In this context, we propose to use a high numerical aperture objective to generate a wide number of incident waves, each one with its characteristic angle of incidence, and, at the same time, to steer the reflected beam to a polarization analyzer system where the polarization changes can be studied, avoiding mechanical movements. The analysis is performed in the basis of the Mueller matrix formalism, to extract the complete polarimetric information of the sample. The technique discussed in this thesis extends the conoscopy process resumed in section 1.2.5 to the measure of isotropic and uniaxial anisotropic materials in reflection mode. The main goals of this thesis are:

i. Mathematical formalism: To develop a mathematical formalism describing the interaction of an incident electromagnetic plane wave propagating in air with an interface of an arbitrarily oriented uniaxial anisotropic media (or isotropic media as particular case), and fully determining the resulting reflected and transmitted plane waves (both ordinary and extraordinary waves in the last case). Starting in the Maxwell equations, the Fresnel reflection coefficients of a dielectric sample and its respective Mueller matrix have to be described.

ii. Conoscopic formalism: To extend the previous mathematical formalism in order to consider the polarization changes introduced by the HNAO working in reflection. The conoscopic formalism has to mathematically describe the angle-resolved Mueller matrix of the sample as a function of the angle of incidence, the refractive indices and the orientation of any isotropic or uniaxial anisotropic crystal.

iii. Mueller matrices simulations: To develop a MatLab program with the conoscopic isotropic-uniaxial anisotropic model of the goal ii, to simulate angle-resolved Mueller matrix images of anisotropic media. With this program, the viability of the conoscopic Mueller microscope can be studied analyzing some angle-resolved Mueller matrices of diverse samples with various RIs and orientations, as well as different numerical apertures microscope objectives. Therefore, the parameters of interest and the sensitivity of the method from simulated data can be studied.

iv. Iterative optimization program: To develop an iterative optimization routine that fits the calculated Mueller matrix image to the measured data. At the same time, to analyze the accuracy of the optimization routine by testing some calculated angle-resolved Mueller matrices.

v. Implementation: To carry out the experimental implementation of the conoscopic Mueller microscope. A proper alignment of the system is a very crucial issue, so to develop and describe a suitable experimental approach to perform this alignment with high accuracy. To calibrate the implemented system and to validate the suitability of the instrument by measuring the Mueller matrix of some known polarimetric materials.

vi. Samples measurements: To analyze the experimental measurements of different specimens (isotropic and uniaxial anisotropic crystals, planar and non-planar surfaces, etc.) and to discuss the suitability of the system in the framework of samples characterization.

1.5 Structure of this thesis

The outline of this thesis is as follows:

In Chapter 2, we explain in detail the mathematical formalism we developed to describe the performance of our conoscopic Mueller microscope. From well-known Maxwell equations we develop the mathematical model to finally obtain the relation between the incident and reflected-transmitted polarized waves, at different angles of incidence. Therefore, the Fresnel coefficients required to calculate the reflected-transmitted waves are determined. The developed mathematical formalism is valid for isotropic-isotropic and isotropic-uniaxial anisotropic interfaces and, it is valid for arbitrary orientations of the uniaxial optical axis. To conclude this chapter, Jones and Mueller formalism are introduced.

In Chapter 3 we describe the adaptation of the mathematical formalism of Chapter 2 to the conoscopic approximation, i.e., to describe the beam propagations related to the cone of light obtained after the light beam passes through the HNAO. The respective variations of the electromagnetic field components, due to the high focalization of the incident polarized beam, are also introduced in the model. After that, we show some simulated angle-resolved Mueller matrix images of uniaxial anisotropic and isotropic samples. From data obtained with these simulations, the dependence of the angle-resolved Mueller matrices with the maximum angle of incidence and the RIs of samples are analyzed. The last sections of the chapter are intended to explain the developed constrained optimization program used to obtain the parameters of interest of crystals: refractive indices (ordinary and extraordinary) and the optical axis orientation. In addition, the accuracy of this optimization routine is discussed.

Afterwards, Chapter 4 focuses on the design and experimental implementation of the conoscopic Mueller microscope. This chapter describes in detail the devised optical design for the instrument, the optical elements used in the final set-up and the proposed alignment process. It also shows the calibration methods we have applied in the laboratory for the tune-up of the instrument.

The last chapter, Chapter 5, is divided in four different subsections. In the first one we analyze the validity of the reflective Mueller polarimeter and we explain some filtering techniques that were used to improve the experimental results. Next, we introduce the calibration methods used in the laboratory to accurately characterize the HNAO. Afterward, some experimentally measured Mueller matrix images of isotropic and uniaxial anisotropic samples, with different shapes as prisms or non-planar surfaces, are shown. A discussion of the experimental characterization of samples is also provided. The sample parameters are fitted using the developed iterative optimization program to fit the simulated Mueller matrix image to the experimental measured data. To conclude the last chapter, a description of the instrument limitations is provided, and a discussion of some possible modifications that may enhance the instrument performance is also included.

Finally, the conclusions of the present work are summarized and a proposal for future research is presented in Chapter 6.

Chapter 2 Mathematical formalism

This chapter presents the mathematical formalism used in this thesis to describe the performance of the developed conoscopic Mueller microscope. Starting from well-known Maxwell equations, the light-matter interaction is studied for an isotropic-uniaxial anisotropic interface.

First of all, the concepts and notations needed to describe the behavior of planar electromagnetic waves at plane boundaries are introduced in section 2.1. Next, the description for wave vectors and polarization states of the incident, reflected and transmitted beams at isotropic-uniaxial anisotropic interfaces are introduced in section 2.2. In particular, the Fresnel coefficients required to characterize the reflected-transmitted waves are mathematically described for light beams with an arbitrary angle of incidence. Then, the model is simplified in section 2.3 to isotropic-isotropic interfaces when birefringence is very small. In section 2.4, the calculation of the amplitudes of the waves transmitted through the sample is briefly described. To conclude this chapter, in section 2.5, the proposed mathematical model is adapted to the Jones and Mueller matrix formalisms, they being well-known descriptions for polarimetric systems.

2.1 Waves at planar boundaries

2.1.1 Maxwell Equations

The well-known Maxwell equations are the fundamental equations of electrodynamics [132]. They can be represented as

$$\nabla \times \boldsymbol{E} + \frac{\partial \boldsymbol{B}}{\partial t} = 0 \tag{2.1}$$

$$\nabla \times \boldsymbol{H} - \frac{\partial \boldsymbol{D}}{\partial t} = \boldsymbol{J} \tag{2.2}$$

$$\nabla \cdot \boldsymbol{D} = \rho \tag{2.3}$$

$$\nabla \cdot \boldsymbol{B} = 0 \tag{2.4}$$

where $\boldsymbol{E}$ and $\boldsymbol{H}$ are the electric field vector and magnetic field vector, respectively, while $\boldsymbol{D}$ is the electric displacement and $\boldsymbol{B}$ the magnetic induction, and where ρ and $\boldsymbol{J}$ are the electric field charge density and the current density of free charges.

As the Maxwell equations present a hybrid notation ($\boldsymbol{E}$ and $\boldsymbol{D}$, $\boldsymbol{H}$ and $\boldsymbol{B}$), supplementary equations are needed to relate both pairs of parameters. The material equations (or constitutive relations) depend on the nature of the material [132]

$$\boldsymbol{D} = \varepsilon \boldsymbol{E} = \varepsilon_0 \boldsymbol{E} + \boldsymbol{P} \tag{2.5}$$

$$\boldsymbol{B} = \mu \boldsymbol{H} = \mu_0 \boldsymbol{H} + \boldsymbol{M} \tag{2.6}$$

where μ is the permeability tensor of the optical medium, μ_0 is the vacuum permeability ($\mu_0 = 4\pi \cdot 10^{-7}\ H/m$), ε is the electric permittivity tensor of the optical medium, ε_0 is the vacuum permittivity ($\varepsilon_0 = 8.854 \cdot 10^{-12}\ F/m$), $\boldsymbol{M}$ is the magnetization and $\boldsymbol{P}$ is the induced electric polarization. The relation between the material polarization and the electric field for a linear material is given by [132, 133]

$$\boldsymbol{P} = \varepsilon_0 \chi \boldsymbol{E} \tag{2.7}$$

where χ is the electric susceptibility tensor. As can be seen in Eq. (2.7), the material polarization $\boldsymbol{P}$ depends on the susceptibility of the studied material. Note that the polarization of light, direction of oscillation of $\boldsymbol{E}$, should not be confused with material polarization ($\boldsymbol{P}$).

The Poynting vector ($\boldsymbol{S}$) represents the directional energy flux, the energy transfer per unit area and time, of an electromagnetic field and it is normal to $\boldsymbol{E}$ and $\boldsymbol{H}$ [132, 134]

$$\boldsymbol{S} = \boldsymbol{E} \times \boldsymbol{H} = \frac{1}{\mu_0 \mu} \boldsymbol{E} \times \boldsymbol{B} \tag{2.8}$$

The Poynting vector magnitude changes with time due to the oscillation of the electric and magnetic fields. Its average over a time longer than the period of the wave is called the intensity $I = \left\langle \boldsymbol{S} \right\rangle$.

The energy density of the electromagnetic fields is [99, 133]

$$U = \frac{1}{2}\left(\boldsymbol{E} \cdot \boldsymbol{D} + \boldsymbol{B} \cdot \boldsymbol{H} \right) \tag{2.9}$$

2.1.2 Plane waves approximation

A monochromatic plane wave propagating along a general direction is going to be considered. Its electric field vector can be expressed as [99, 132]

$$\boldsymbol{E} = E_0 \exp\left[i\left(\omega t - \boldsymbol{k} \cdot \boldsymbol{r} \right) \right]\ \hat{u}_1 \tag{2.10}$$

where E_0 is the amplitude of the electric field that is constant in space and time, $\hat{u}_1$ is the unit vector that indicates the direction of the electric field, which is also called the polarization of the wave, $\boldsymbol{r}$ is the coordinate vector of any point in the space, ω is the angular frequency and $\boldsymbol{k}$ is the wave vector, given by [134]

$$\boldsymbol{k} = \omega \sqrt{\mu\varepsilon}\ \hat{k} \tag{2.11}$$

where $\hat{k}$ is the direction of propagation for uniform plane waves and can be expressed as $\hat{k} = \boldsymbol{k} / |\boldsymbol{k}|$.

One characteristic of uniform planar waves is that a surface with a constant phase ($\omega\, t - \boldsymbol{k} \cdot \boldsymbol{r} =$ constant phase) is a plane that moves along the direction of $\boldsymbol{k}$ with a velocity known as the phase velocity [99]. This velocity of the wave is given by

$$v = \frac{\omega}{|\boldsymbol{k}|} = \frac{1}{\sqrt{\mu\varepsilon}} \tag{2.12}$$

As v is function of the permittivity and permeability, it is easily seen that the phase velocity is characteristic for each medium. The phase velocity of an electromagnetic wave propagating in the vacuum is [132, 133]

$$c = \frac{1}{\sqrt{\mu_0\varepsilon_0}} = 2.998 \cdot 10^8\ \left(m/s \right) \tag{2.13}$$

The refractive index (RI) is defined as the ratio between the speed of light in vacuum and in a material media [132, 133]

$$n = \frac{c}{v} = \sqrt{\frac{\mu\varepsilon}{\mu_0\varepsilon_0}} \tag{2.14}$$

The magnetic field vector for a planar wave is [99, 132]

$$\boldsymbol{H} = H_0 \exp\left[i\left(\omega t - \boldsymbol{k} \cdot \boldsymbol{r} \right) \right]\ \hat{u}_2 \tag{2.15}$$

Where H_0 is the amplitude of the magnetic field and the unit vector $\hat{u}_2$ gives its specific vibration direction.

Optical media commonly used in classical optics, also refereed as optical medias [99, 133, 134], are uniform dielectric nonmagnetic materials with no free charges and no currents due to free charges, and neither amplifying nor absorbing materials. Thus, in those materials the following approximations can be conducted: $\boldsymbol{M} = 0$, $\mu = \mu_0$, $\rho = 0$ and $\boldsymbol{J} = 0$.

In view of the above, and operating with the constitutive equations $\boldsymbol{D} = \varepsilon \boldsymbol{E}$ and $\boldsymbol{B} = \mu_0\, \boldsymbol{H}$, the Maxwell equations (2.1) - (2.4) in the case of plane waves of the form (2.10) and (2.15) result in [99, 134]

$$\boldsymbol{k} \times \boldsymbol{E} = \omega\mu_0 \boldsymbol{H} = \omega \boldsymbol{B} \tag{2.16}$$

$$\boldsymbol{k} \times \boldsymbol{H} = -\omega\varepsilon \boldsymbol{E} = -\omega \boldsymbol{D} \tag{2.17}$$

$$\boldsymbol{k} \cdot \boldsymbol{D} = 0 \tag{2.18}$$

$$\boldsymbol{k} \cdot \boldsymbol{H} = 0 \tag{2.19}$$

From Eqs. (2.16) - (2.19), it is extracted that $\boldsymbol{k}$, $\boldsymbol{D}$ and $\boldsymbol{H}$ are a right handed orthogonal system and $\boldsymbol{B}$ and $\boldsymbol{H}$ are parallel. However, if ε is not a scalar magnitude but a tensor matrix, as in the case of anisotropic materials, $\boldsymbol{E}$ is neither perpendicular to $\boldsymbol{k}$ nor parallel to $\boldsymbol{D}$ (see Eq. (2.17)). In such a way, $\boldsymbol{H}$ is normal to both $\boldsymbol{D}$, $\boldsymbol{E}$ and $\boldsymbol{k}$, and the latter three are coplanar. The Poynting vector $\boldsymbol{S} = \boldsymbol{E} \times \boldsymbol{H}$ is, in general, not transported in the direction of wave vector $\boldsymbol{k}$. Figure 2-1 shows the propagation of an electromagnetic wave inside this kind of optical media.

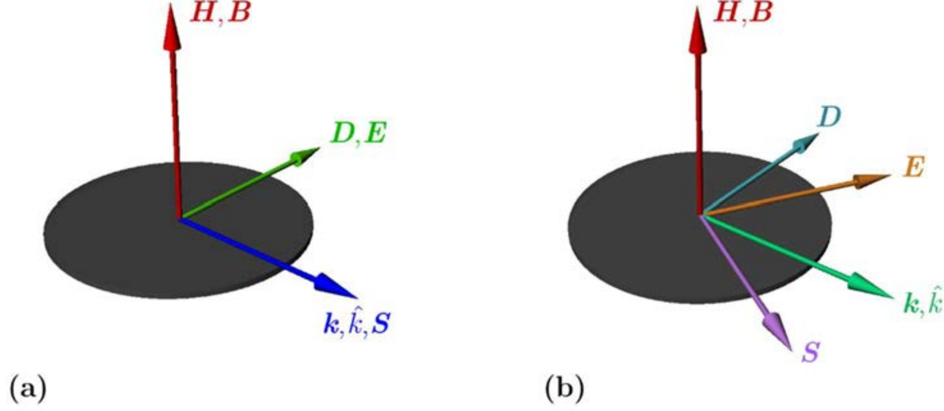

Figure 2-1. Fields of an electromagnetic wave propagating in (a) an isotropic medium, and (b) a uniaxial anisotropic medium.

By eliminating $\boldsymbol{H}$ from Eqs. (2.16) and (2.17), one obtains [99, 133, 134]

$$\boldsymbol{k} \times \left(\boldsymbol{k} \times \boldsymbol{E}\right) + \omega^2 \mu_0 \varepsilon \boldsymbol{E} = 0 \tag{2.20}$$

From the vector triple product identity [132], Eq. (2.20) can be rewritten as

$$\boldsymbol{k}\left(\boldsymbol{k} \cdot \boldsymbol{E}\right) - k^2 \cdot \boldsymbol{E} + \omega^2 \mu_0 \varepsilon \boldsymbol{E} = 0 \tag{2.21}$$

which is the wave equation for determining the permittivity tensor ε and the electric field $\boldsymbol{E}$ of a plane wave propagating in the wave vector direction $\hat{k}$.

2.1.3 Crystal Optics

The electric permittivity tensor can be written in matrix form referred to three arbitrary orthogonal axes (x', y', z') as

$$\varepsilon = \begin{pmatrix} \varepsilon_{x'x'} & \varepsilon_{x'y'} & \varepsilon_{x'z'} \\ \varepsilon_{y'x'} & \varepsilon_{y'y'} & \varepsilon_{y'z'} \\ \varepsilon_{z'x'} & \varepsilon_{z'y'} & \varepsilon_{z'z'} \end{pmatrix} \tag{2.22}$$

The value of the nine permittivity tensor components depends on the choice of the orthogonal axes relative to the material structure. Note that for a lossless and non-optically active medium, the electric permittivity tensor is symmetric [133, 134], $\varepsilon_{i,j} = \varepsilon_{j,i}$. This means that, in general, it has only six independent elements.

By choosing a convenient coordinate system (x, y, z) aligned to the crystal axes, the dielectric tensor can be written in its diagonal form [99, 133, 134]

$$\varepsilon = \begin{pmatrix} \varepsilon_x & 0 & 0 \\ 0 & \varepsilon_y & 0 \\ 0 & 0 & \varepsilon_z \end{pmatrix} = \varepsilon_0 \begin{pmatrix} n_x^2 & 0 & 0 \\ 0 & n_y^2 & 0 \\ 0 & 0 & n_z^2 \end{pmatrix} \quad (2.23)$$

where the directions x, y, z are called principal axes of the crystal, ε_x, ε_y, ε_z are the principal dielectric constants and n_x, n_y, n_z are the principal refractive indices.

In terms of values of the principal refractive indices, a crystal can be classified as follows [2, 133]:

- *Isotropic*: if $n_x = n_y = n_z$. This means that the principal dielectric constants are equal or, in other words, the speed of light is the same in all directions. In an isotropic medium the applied electric field $\boldsymbol{E}$ is parallel to its corresponding electric displacement vector $\boldsymbol{D}$ (as can be observed in Figure 2-1) because the dielectric tensor is reduced to a scalar magnitude (see Eq. (2.17)).

- *Anisotropic*: if the RI is different for at least one of the principal axes. The speed of light depends on the propagation direction into the material and $\boldsymbol{D}$ and $\boldsymbol{E}$ are no longer necessarily parallel (see Figure 2-1). Anisotropic materials can be divided into two groups: if two of the principal refractive indices are equal, the crystal is called *uniaxial anisotropic crystal* $\left(n_x = n_y \neq n_z\right)$ and if all of them are unequal, the material is called *biaxial anisotropic crystal* $\left(n_x \neq n_y \neq n_z\right)$. The existence of more than one RI makes that radiation propagating into an anisotropic crystal, with an arbitrary orientation with respect to the principal crystal axes x, y, z, is decomposed into two plane polarized waves that propagate with different velocities inside the crystal, except when propagating parallel to an optical axis direction.

The mathematical model described throughout this chapter allows the characterization of uniaxial and isotropic samples. In fact, a general model is following developed for uniaxial crystals, from which isotropic media are a particular case, when principal refractive indices are equal.

Introducing the diagonal dielectric tensor of a uniaxial crystal, i.e. $\varepsilon_x = \varepsilon_y = \varepsilon_o$ and $\varepsilon_z = \varepsilon_e$ in Eq. (2.23), into the wave equation for planar waves (Eq. (2.21)), three homogenous linear equations, which dependent on E_x, E_y and E_z, are obtained

$$\begin{pmatrix} \omega^2\mu_0\varepsilon_o - k_y^2 - k_z^2 & k_x k_y & k_x k_z \\ k_y k_x & \omega^2\mu_0\varepsilon_o - k_x^2 - k_z^2 & k_y k_z \\ k_z k_x & k_z k_y & \omega^2\mu_0\varepsilon_e - k_x^2 - k_y^2 \end{pmatrix} \begin{pmatrix} E_x \\ E_y \\ E_z \end{pmatrix} = \begin{pmatrix} 0 \\ 0 \\ 0 \end{pmatrix} \quad (2.24)$$

where ε_o and ε_e are the electric permittivity of the ordinary and extraordinary axis, respectively. For solutions to exist different than $|\boldsymbol{k}| = \omega = 0$, the determinant of the square matrix in Eq. (2.24) must be zero

$$\begin{vmatrix} \omega^2\mu_0\varepsilon_o - k_y^2 - k_z^2 & k_xk_y & k_xk_z \\ k_yk_x & \omega^2\mu_0\varepsilon_o - k_x^2 - k_z^2 & k_yk_z \\ k_zk_x & k_zk_y & \omega^2\mu_0\varepsilon_e - k_x^2 - k_y^2 \end{vmatrix} = 0 \tag{2.25}$$

This equation represents a three-dimensional surface in the $\boldsymbol{k}$-space, known as normal surface, and consists of two shells. These two shells in uniaxial anisotropic crystals touch at two points forming a straight line that passes through the origin of both figures. The direction of this line is called optical axis $\left(\hat{C}\right)$ and, as can be seen in Refs. [99, 133, 135], it coincides with the extraordinary principal axis, z-axis. Under this scenario, the principal refractive index in the optical axis direction is n_e and the RI of the plane perpendicular to the optical axis is n_o. If $n_e > n_o$ the crystal is said to be positive uniaxial anisotropic, and if $n_e < n_o$ negative uniaxial anisotropic.

Eq. (2.25) can be reduced by solving the determinant and by expressing the dielectric constants as a function of the refractive indices ($\varepsilon_o = \varepsilon_0 \cdot n_o^2$, $\varepsilon_e = \varepsilon_0 \cdot n_e^2$) [99, 133]

$$\left(\frac{k_x^2 + k_y^2}{n_e^2} + \frac{k_z^2}{n_o^2} - \frac{\omega^2}{c^2}\right)\left(\frac{\left|\boldsymbol{k}\right|^2}{n_o^2} - \frac{\omega^2}{c^2}\right) = 0 \tag{2.26}$$

In Eq. (2.26) the two shells are easily identified as a sphere (right term in left side) and an ellipsoid of revolution (left term in left side). Both surfaces give the relation between ω and $\boldsymbol{k}$. Moreover, there are two intersections between the direction of propagation and the normal surfaces, or, in other words, there exist two possible values of $\boldsymbol{k}$ that solve Eq. (2.26). These two points correspond to two different wave vectors $\boldsymbol{k}$ called the ordinary (o) and extraordinary (e) waves. The ordinary wave vector is related to the sphere surface. This means that it propagates with a constant velocity irrespective of its direction of propagation. On the other hand, the extraordinary wave vector is related to the ellipsoid of revolution surface, and thus, its velocity of propagation varies with the angle between the propagation direction and the optical axis. Thus, the extraordinary wave velocity depends on the direction of propagation [99]. The velocity of the extraordinary wave equals the velocity of the ordinary wave when propagating along the uniaxial anisotropic crystal optical axis direction [135].

Furthermore, Eq. (2.21) gives the components of the electric field vector as a function of the principal dielectric constants and the wave vector components (k_x, k_y, k_z) [2, 135]

$$E_i = \frac{k_i\left(\boldsymbol{k} \cdot \boldsymbol{E}\right)}{k^2 - \omega^2\mu_0\varepsilon_i} \tag{2.27}$$

with $i = x, y, z$. Multiplying both sides of Eq. (2.27) by k_i, adding the resulting three equations, dividing the obtained expression by the common factor $\boldsymbol{k} \cdot \boldsymbol{E}$, and using the relation in Eq. (2.11), the so-called Fresnel Equation is obtained [2, 133]

$$\frac{1}{n^2} = \frac{\hat{k}_x^{\,2}}{n^2 - n_o^2} + \frac{\hat{k}_y^{\,2}}{n^2 - n_o^2} + \frac{\hat{k}_z^{\,2}}{n^2 - n_e^2} \tag{2.28}$$

where n is the RI to be determined associated with the propagation unitary vector $\hat{k}$ [135]. The Fresnel Equation is quadratic in n, which means that two values of refractive indices are given by a wave propagating in an anisotropic medium. The two values of $\pm n$ corresponding to any value of n^2 are counted as one, since the negative value belongs to the opposite direction of propagation $-\hat{k}$.

In brief, in any given direction inside a uniaxial anisotropic crystal, there are generally two independent wave vector solutions, o and e, propagating with different velocities (see Eq. (2.26)). Both, the ordinary and extraordinary waves, present mutually orthogonal polarization states and also present different directions of energy that depend on the particular propagation direction [135]. It is important to note that the refractive index of the ordinary wave is n_o, while the RI of the extraordinary wave is the effective index n rather than n_e. However, in some particular situations it is limited to the extraordinary index of refraction n_e [2, 99, 134].

2.1.4 Polarization

The main idea of this chapter is to study the changes of the electric field in the interface formed between an isotropic medium and a uniaxial anisotropic medium. For the present discussion, the plane that contains the wave vector $\boldsymbol{k}$ and the unit vector pointing normal to the boundary is called the plane of incidence [2]. This plane presents some important properties that are explained throughout this section and in the next one. In the following, the mathematical description of the polarization for the isotropic and anisotropic cases is reviewed.

2.1.4.1 Polarization in isotropic media

In homogeneous isotropic media, the polarization of electromagnetic waves can be expressed as a combination of two orthonormal vectors, one of them is a unit vector $(\hat{s})$ perpendicular to the plane of incidence and the other is a unit vector $(\hat{p})$ parallel to the plane of incidence [103, 106]. From Eq. (2.10), the polarization of an electromagnetic wave inside an isotropic medium can be expressed considering the $(\hat{s},\ \hat{p})$ orthonormal basis as

$$\boldsymbol{E} = \left(A_s\hat{s} + A_p\hat{p}\right)\exp\left[i\left(\omega t - \boldsymbol{k}\cdot\boldsymbol{r}\right)\right] \tag{2.29}$$

where A_s is the amplitude of the electric field perpendicular to the plane of incidence and A_p is the amplitude that lies in the plane of incidence. Note that $\hat{u}_1$ in Eq. (2.10) can be written as $\hat{u}_1 = \left(\cos\phi\right)\hat{p} + \left(\sin\phi\right)\hat{s}$, where ϕ is the angle between the plane of incidence and the unitary vector $\hat{u}_1$.

Bearing in mind the orthogonality of the wave vector $\boldsymbol{k}$ and $\boldsymbol{E}$, in isotropic media, the parallel polarization vector is [103, 136]

$$\hat{p} = \frac{\boldsymbol{k}\times\hat{s}}{\left|\boldsymbol{k}\right|} \tag{2.30}$$

2.1.4.2 Polarization in uniaxial anisotropic media

To ease the mathematical treatment of polarization in the case of uniaxial anisotropic crystals, it is described by a basis formed by two different orthonormal vectors. As distinct from section 2.1.4.1, where the chosen basis is parallel and orthogonal to the plane of incidence, the new unitary vectors are function of the ordinary and extraordinary wave propagations. One parallel to the ordinary wave polarization vector, $\hat{o}$, and another parallel to the extraordinary wave polarization vector, $\hat{e}$. Both depend on the position of the optical axis $\hat{C}$ and their corresponding wave vectors.

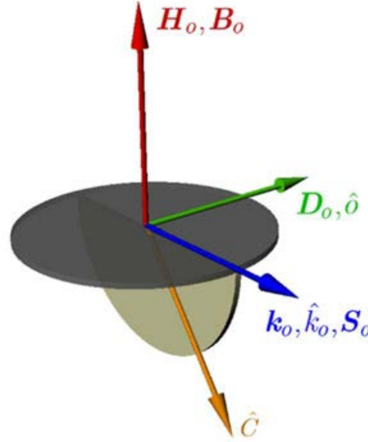

Figure 2-2. Fields of an ordinary electromagnetic wave propagating inside a uniaxial anisotropic crystal.

Let us begin for the ordinary wave description. As has been explained in section 2.1.3, the ordinary wave vector is related to a sphere shell (Eq. (2.26)), always presenting a constant phase velocity regardless of the direction of propagation [107, 133]. In this case, the unit vector in the direction of the displacement vector, $\hat{D}_o$, and the electric field vector direction, $\hat{o}$, share the same direction, and are always perpendicular to both $\hat{C}$ and the ordinary propagation vector $\hat{k}_o$ (see Figure 2-2). Mathematically $\hat{D}_o$ can be expressed as

$$\hat{D}_o = \frac{\hat{k}_o \times \hat{C}}{\left|\hat{k}_o \times \hat{C}\right|} \tag{2.31}$$

As $\hat{o}$ is parallel to $\hat{D}_o$ and as the optical axis is the extraordinary principal axis for uniaxial anisotropic crystals, *z*-axis according to the basis chosen in Eq. (2.25), i.e., $\hat{C} = \begin{pmatrix} 0, & 0, & 1 \end{pmatrix}$, the ordinary electric field vector direction is [99, 103]

$$\hat{o} = \hat{D}_o = \frac{1}{\left|\hat{k}_o \times \hat{C}\right|} \begin{pmatrix} \left|\hat{k}_{o,y}\right|, & -\left|\hat{k}_{o,x}\right|, & 0 \end{pmatrix}^T \tag{2.32}$$

where the superscript T means the transpose of the row vector. The ordinary wave is linearly polarized, and it is perpendicular to the plane formed by the ordinary wave vector and the optical axis direction $\hat{C}$. From the Pointing vector equation (Eq. (2.8)), it can be seen that $\boldsymbol{S}$ for the ordinary wave is parallel to $\hat{k}_o$ (see Figure 2-2).

For the extraordinary wave, the unit vector in the direction of the displacement vector, $\hat{D}_e$, is perpendicular to the extraordinary wave vector $\boldsymbol{k}_e$ and to $\hat{D}_o$ [99, 103]

$$\hat{D}_e = \frac{\hat{D}_o \times \boldsymbol{k}_e}{\left|\hat{D}_o \times \boldsymbol{k}_e\right|} \tag{2.33}$$

However, the electric field vector direction $\hat{e}$ is in general not parallel to $\hat{D}_e$, it lies in the plane formed by $\hat{D}_e$ and the propagation vector $\hat{k}_e$, with the condition $\hat{k}_e \cdot \hat{e} \neq 0$. In addition, the electric field vector of the ordinary and the extraordinary waves are not mutually orthogonal, because they correspond to the modes of two different directions of propagation. Particularly, $\hat{o} \cdot \hat{e}$ tends to zero as the anisotropy is reduced [106]. Expressing Eq. (2.27) as a function of the effective refractive index n and normalizing it, finally the extraordinary electric field unitary vector direction is found as [99, 103]

$$\hat{e} = \frac{\vec{e}}{\left|\vec{e}\right|} = \frac{1}{\left|\vec{e}\right|}\left(\frac{\left|\hat{k}_{e,x}\right|}{n^2 - n_o^2}, \frac{\left|\hat{k}_{e,y}\right|}{n^2 - n_o^2}, \frac{\left|\hat{k}_{e,z}\right|}{n^2 - n_e^2}\right)^T \tag{2.34}$$

The angle between $\hat{k}_e$ and the Pointing vector $\boldsymbol{S}$ for the extraordinary wave is equal to the angle between $\hat{D}_e$ and $\hat{e}$ (see Figure 2-3).

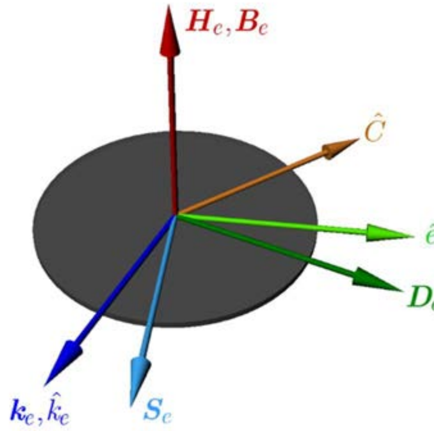

Figure 2-3. Fields of an extraordinary electromagnetic wave propagating inside a uniaxial anisotropic crystal.

Therefore, the structure of a uniaxial anisotropic crystal permits two monochromatic plane waves with two different linear polarizations and two different velocities to propagate in any given direction [2].

The representation of the ordinary and extraordinary displacement vectors as a function of the optical axis $\hat{C}$ and the propagation directions $\hat{k}_o$ and $\hat{k}_e$ is shown in Figure 2-4.

2.1.5 Boundary conditions

The electromagnetic field has to obey the Maxwell equations at the interface between any two different materials. As a consequence, some components of the field vectors (**E**, **D**, **H** and **B**) at the materials interface have to accomplish some boundary conditions, even if ε and μ change abruptly [2].

Considering the interface between medium 1 and medium 2 (ε_1, ε_2), both of them being dielectric and in absence of surface currents and charges, the boundary conditions for $\boldsymbol{D}$ and $\boldsymbol{B}$ are obtained from the Gauss divergence theorem [2, 99, 132]

$$B_1^{\perp} = B_2^{\perp}, \qquad \mathrm{D}_1^{\perp} = D_2^{\perp} \tag{2.35}$$

which means that the normal components of the electric displacement and the magnetic induction vectors to the interface are continuous.

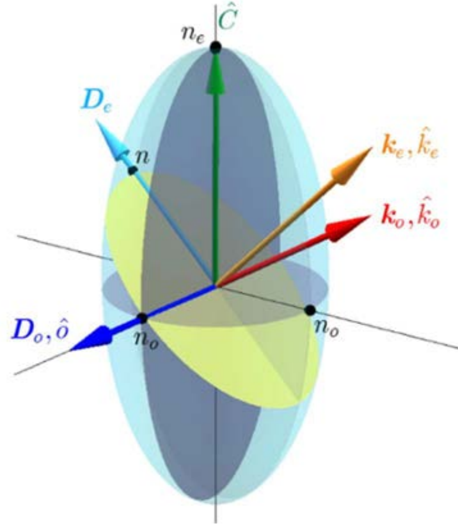

Figure 2-4. Index ellipsoid for a uniaxial anisotropic crystal. The directions of the ordinary and extraordinary displacement vectors are function of their respective wave vectors. The yellow plane is normal to the extraordinary wave vector and contains the ordinary and extraordinary wave vectors.

From Stokes theorem, the boundary conditions for the fields vectors $\boldsymbol{E}$ and $\boldsymbol{H}$ are obtained [2, 99, 132]

$$E_1^{\parallel} = E_2^{\parallel}, \qquad \mathrm{H}_1^{\parallel} = H_2^{\parallel} \tag{2.36}$$

The tangential components of the electric and magnetic fields are continuous across the interface when the surface charge density and surface current density are zero.

In the case of travelling waves at the boundary, the above-stated boundary conditions must also be accomplished. Let us consider the electric and magnetic waves approach to planar waves, where they share the generic structure (Eqs. (2.10) and (2.15)). By using this wave form, taking into account that a wave is partially reflected and partially transmitted at the interface, and by imposing that the fields in medium 1 and those in medium 2 must satisfy Eqs. (2.35) and (2.36), the following relation is obtained for all points lying on the interface [132]

$$\begin{aligned}(\quad)\exp\left[i\left(\omega_{1a}\cdot t-\boldsymbol{k}_{1a}\cdot\boldsymbol{r}\right)\right]+(\quad)\exp\left[i\left(\omega_{1b}\cdot t-\boldsymbol{k}_{1b}\cdot\boldsymbol{r}\right)\right]=\\=(\quad)\exp\left[i\left(\omega_{2c}\cdot t-\boldsymbol{k}_{2c}\cdot\boldsymbol{r}\right)\right]+(\quad)\exp\left[i\left(\omega_{2d}\cdot t-\boldsymbol{k}_{2d}\cdot\boldsymbol{r}\right)\right]\end{aligned} \tag{2.37}$$

where the subscripts $1a$ and $1b$ are those corresponding to the incident and reflected waves propagating in medium 1, and where $2c$ and $2d$ correspond to the ordinary and

extraordinary waves propagating in medium 2. The parenthesis ( ) in Eq. (2.37) state for the particular vector amplitudes, related to the normal ($\perp$) or tangential ($||$) components, according to the case.

In addition, the condition in Eq. (2.37) must be fulfilled independently of the spatial position at the boundary and for all times. This can only be satisfied if all the phase factors in Eq. (2.37) are equal, and thus, all the involved electromagnetic waves must have the same frequency ($\omega_{1a} = \omega_{1b} = \omega_{2c} = \omega_{2d}$) [135]. Under this scenario, the following relation is verified [132, 134, 135]

$$\boldsymbol{k}_{1a} \cdot \boldsymbol{r}\Big|_{\text{interface}} = \boldsymbol{k}_{1b} \cdot \boldsymbol{r}\Big|_{\text{interface}} = \boldsymbol{k}_{2c} \cdot \boldsymbol{r}\Big|_{\text{interface}} = \boldsymbol{k}_{2d} \cdot \boldsymbol{r}\Big|_{\text{interface}} \tag{2.38}$$

Moreover, as at the position vector $\boldsymbol{r}$ is always contained into the interface, the perpendicular component always satisfies $r^{\perp} = 0$, and thus,

$$k_{1a}^{||} = k_{1b}^{||} = k_{2c}^{||} = k_{2d}^{||} \tag{2.39}$$

According to Eq. (2.39), the tangential components along the boundary of the different wave vectors are identical regardless of the mediums materials at the interface, and the wave vectors on both sides of the interface form a plane, known as plane of incidence, which also contains the unitary vector normal to the interface [132, 135].

2.2 Reflection and refraction of electromagnetic radiation at a crystal surface

2.2.1 Wave vectors of the incident, reflected and transmitted beams

Let us consider a plane electromagnetic wave propagating through the interface formed by an isotropic medium and a uniaxial anisotropic crystal with an optical axis $\hat{C}$ arbitrary oriented. The refractive index of the isotropic medium is n_i, while the refractive indices of the ordinary and extraordinary axis of the uniaxial anisotropic crystal are n_o and n_e, respectively. The direction of the optic axis is given by two angles in spherical coordinates [107, 136]: the angle from the optical axis to the $(x,\ y)$ plane, labeled as θ_c, and the angle between the x-direction and the projection of $\hat{C}$ axis on the $(x,\ y)$ plane, called ϕ_c (see Figure 2-5).

The optical axis can be mathematically described by

$$\hat{C} = \cos\phi_c \cos\theta_c \hat{x} + \sin\phi_c \cos\theta_c \hat{y} + \sin\theta_c \hat{z} \tag{2.40}$$

The anisotropic medium is placed in such a way that the $(x,\ y)$ plane coincides with the interface, where the uniaxial anisotropic crystal is on the upper half-space ($z > 0$). Let us suppose an incident wave propagating in the positive direction of the z axis at the $(y,\ z)$ plane (blue arrows in Figure 2-6 and Figure 2-7). At the boundary, one part of the incident wave is reflected (reflected wave; violet arrows in Figure 2-6 and Figure 2-7) and the other part is transmitted (refracted waves; red and green arrows in Figure 2-6 and Figure 2-7)

as a combination of an ordinary wave and an extraordinary wave [103, 106]. As was discussed in section 2.1.5, reflected and refracted waves are contained on the same plane than the incident wave, the so-called plane of incidence. The above-stated scheme of propagation is sketched in Figure 2-6. Note that $\boldsymbol{k}_i$ and $\boldsymbol{k}_r$ are the wave vectors of the incident and the reflected waves, respectively, in the isotropic medium while the wave vectors of the ordinary and extraordinary transmitted waves in the anisotropic medium are $\boldsymbol{k}_{t,o}$ and $\boldsymbol{k}_{t,e}$.

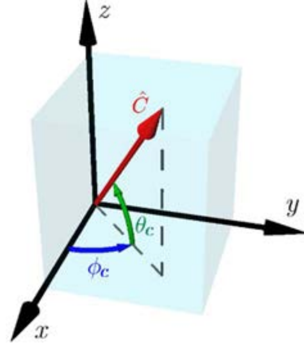

Figure 2-5. Optical axis orientation $\hat{C}$ (red arrow) described by the angle between the optical axis and $(x,\ y)$ plane, θ_c, (green arrow) and the angle between the projection of the optical axis on the $(x,\ y)$ plane and the x-direction, ϕ_c, (blue arrow).

From Eqs. (2.12) and (2.14), the modulus of the incident wave vector is written as

$$k_i = \left|\boldsymbol{k}_i\right| = \frac{\omega}{c} n_i \tag{2.41}$$

As has been seen in Eq. (2.39), the tangential components of the four wave vectors (incident, reflected, ordinary and extraordinary waves) along the boundary are equal. Let us call β the constant tangential component of all the wave vectors, according to Eq. (2.39) and Figure 2-6, we obtain [99, 103, 106]

$$\beta = \left|\boldsymbol{k}_i\right| \sin\theta_i = \left|\boldsymbol{k}_r\right| \sin\theta_r = \left|\boldsymbol{k}_{t,o}\right| \sin\theta_{t,o} = \left|\boldsymbol{k}_{t,e}\right| \sin\theta_{t,e} \tag{2.42}$$

where θ_i is the angle of incidence, θ_r is the angle of reflection and $\theta_{t,o}$ and $\theta_{t,e}$ are the ordinary and extraordinary refracted angles, respectively, all of them measured with respect to the normal, $\hat{z}$ axis.

The boundary conditions (see section 2.1.5) require that all the wave vectors lie in the same plane, called the plane of incidence [134]. Being consistent with the coordinates system chosen in Figure 2-6 and Figure 2-7, the wave vectors can be written as [99, 103, 106]

$$\boldsymbol{k}_i = \beta\hat{y} + k_{i,z}\hat{z} \tag{2.43}$$

$$\boldsymbol{k}_r = \beta\hat{y} - k_{r,z}\hat{z} \tag{2.44}$$

$$\boldsymbol{k}_{t,o} = \beta\hat{y} + k_{o,z}\hat{z} \tag{2.45}$$

$$\boldsymbol{k}_{t,e} = \beta\hat{y} + k_{e,z}\hat{z} \tag{2.46}$$

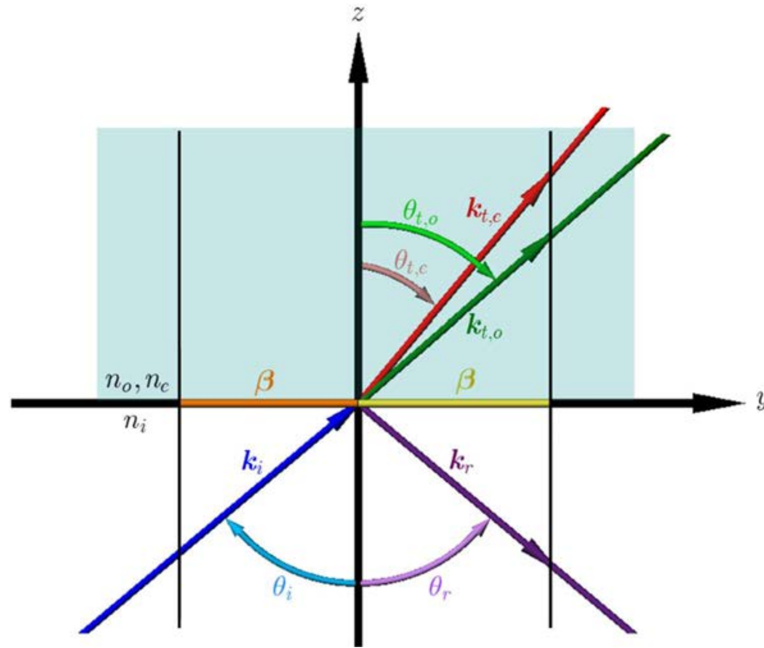

Figure 2-6. Reflection (violet arrow) and refraction (red and green arrows) of an incident wave vector (blue arrow) at a boundary between an isotropic (n_i) and an anisotropic medium (n_o and n_e). θ_i, θ_r, $\theta_{t,o}$ and $\theta_{t,e}$ are the angles of the different wave vectors, all of them measured with respect to the normal, and β is the constant tangential component of all the wave vectors.

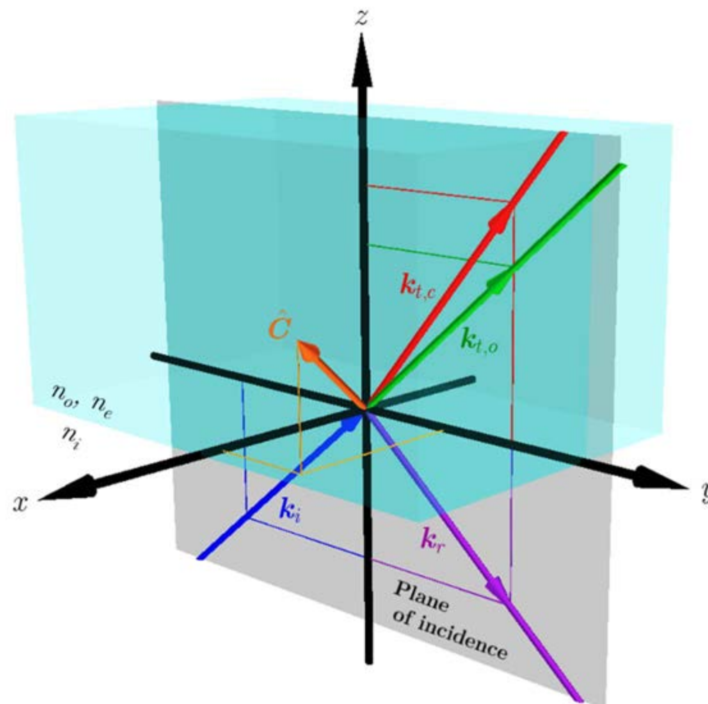

Figure 2-7. The wave vectors of the incident (blue arrow), reflected (violet arrow) and refracted (green and red arrows) waves at the interface between an isotropic and a uniaxial anisotropic media, all of them lie in the (y, z) plane or plane of incidence (grey plane). The optical axis $\hat{C}$ (orange arrow) is arbitrary oriented.

where $k_{i,z}$, $k_{r,z}$, $k_{o,z}$ and $k_{e,z}$ are normal to interface and their explicit forms are given by

$$k_{i,z} = \left|\boldsymbol{k}_i\right| \cos\theta_i; \quad k_{r,z} = \left|\boldsymbol{k}_r\right| \cos\theta_r; \quad k_{o,z} = \left|\boldsymbol{k}_{t,o}\right| \cos\theta_{t,o}; \quad k_{e,z} = \left|\boldsymbol{k}_{t,e}\right| \cos\theta_{t,e} \tag{2.47}$$

According to Eqs. (2.41) and (2.42), the tangential and normal amplitudes of the incident wave vector (Eq. (2.43)), as a function of the incident angle and the refractive index of the isotropic medium, are [103, 106]

$$\beta = k_i \sin\theta_i = \frac{\omega}{c} n_i \sin\theta_i \tag{2.48}$$

$$k_{i,z} = k_i \cos\theta_i = \frac{\omega}{c} n_i \cos\theta_i \tag{2.49}$$

In the case of the reflected wave, when the incident medium is isotropic, the law of reflection [132, 134] has to be followed. This law imposes that the incident and reflected wave vectors present the same angles ($\theta_i = \theta_r$). Hence, their normal components are equal in magnitude but opposite in sign, i.e. $k_{i,z} = k_{r,z}$, and Eq. (2.44) can be rewritten as

$$\boldsymbol{k}_r = \beta\hat{y} - k_{i,z}\hat{z} \tag{2.50}$$

On the other hand, the components of the ordinary and extraordinary refracted waves in z-direction ($k_{o,z}$ and $k_{e,z}$, respectively) depend on the directions of the vectors $\boldsymbol{k}_{t,o}$ and $\boldsymbol{k}_{t,e}$ with respect to the optical axis $\hat{C}$. To obtain them, the following method is applied. As was explained in section 2.1.3, the optical axis direction $\hat{C}$ is parallel to the extraordinary principal axis for uniaxial anisotropic crystals. Thus, let us consider a new coordinate system (X, Y, Z) aligned to the crystal axes, where the directions X, Y and Z are the principal axes of the crystal (see Figure 2-8). In such a new basis, the optical axis direction can be expressed as

$$\left(\hat{C}\right)_{ellip} = \hat{Z} \tag{2.51}$$

where the subscript *ellip* indicates that $\hat{C}$ is expressed in the coordinate system(X, Y, Z). This new coordinate system is going to be called the dielectric ellipsoid frame of reference [103].

The components of a vector in the (x, y, z) coordinate system (or incidence reference frame), $V_{x,y,z}$, can be related to those (X, Y, Z) in the dielectric ellipsoid frame, V_{ellip}, by a rotation matrix $\boldsymbol{M}_{rot}$

$$V_{ellip} = \boldsymbol{M}_{rot} \cdot V_{x,y,z} \tag{2.52}$$

with

$$\boldsymbol{M}_{rot} = \begin{pmatrix} -\cos\phi_c \sin\theta_c & -\sin\phi_c \sin\theta_c & \cos\theta_c \\ \sin\phi_c & -\cos\phi_c & 0 \\ \cos\phi_c \cos\theta_c & \sin\phi_c \cos\theta_c & \sin\theta_c \end{pmatrix} \tag{2.53}$$

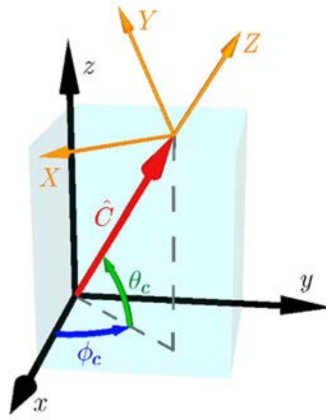

Figure 2-8. Representation of the direction of the optical axis $\hat{C}$ (red arrow) in the incidence reference frame, $(x,\ y,\ z)$ basis, (black arrows) and in the dielectric ellipsoid frame, $(X,\ Y,\ Z)$ basis, (orange arrows).

where the angles θ_c and ϕ_c specify the orientation of the optics axis in the $(x,\ y,\ z)$ coordinate system (see Figure 2-8). M can be calculated by using the Euler Angles [137], or by properly multiplying by two consecutive rotation matrices for the angles θ_c and ϕ_c.

To simplify the calculus of $k_{o,z}$ and $k_{e,z}$ in the incidence reference frame, first they are calculated in the $(X,\ Y,\ Z)$ coordinate system. By using Eqs. (2.45) and (2.46), in Eq. (2.52), the ordinary and extraordinary wave vectors in the dielectric ellipsoid system are found [103]

$$\left(\boldsymbol{k}_{t,o}\right)_{ellip} = \boldsymbol{M}_{rot} \cdot \boldsymbol{k}_{t,o} = \begin{pmatrix} -\sin\phi_c \sin\theta_c \beta + \cos\theta_c k_{o,z} \\ -\cos\phi_c \beta \\ \sin\phi_c \cos\theta_c \beta + \sin\theta_c k_{o,z} \end{pmatrix} \tag{2.54}$$

and

$$\left(\boldsymbol{k}_{t,e}\right)_{ellip} = \boldsymbol{M}_{rot} \cdot \boldsymbol{k}_{t,e} = \begin{pmatrix} -\sin\phi_c \sin\theta_c \beta + \cos\theta_c k_{e,z} \\ -\cos\phi_c \beta \\ \sin\phi_c \cos\theta_c \beta + \sin\theta_c k_{e,z} \end{pmatrix} \tag{2.55}$$

The norms of both vectors are

$$\left|\left(\boldsymbol{k}_{t,o}\right)_{ellip}\right| = \sqrt{\beta^2 + k_{o,z}^2}, \qquad \left|\left(\boldsymbol{k}_{t,e}\right)_{ellip}\right| = \sqrt{\beta^2 + k_{e,z}^2} \tag{2.56}$$

From Eq. (2.26), the normal surfaces (a sphere and an ellipsoid of revolution, respectively) for the ordinary and extraordinary wave vectors in the coordinate system aligned to the crystal axes, i.e., in the dielectric ellipsoid system, V_{ellip} can be written as [107]

$$\frac{\left|\left(\boldsymbol{k}_{t,o}\right)_{ellip}\right|^2}{n_o^2} = \frac{\omega^2}{c^2} \tag{2.57}$$

and

$$\frac{k_{e,X}^2 + k_{e,Y}^2}{n_e^2} + \frac{k_{e,Z}^2}{n_o^2} = \frac{\omega^2}{c^2} \tag{2.58}$$

where $k_{e,X}$, $k_{e,Y}$ and $k_{e,Z}$ are the components of the extraordinary wave vector in the ellipsoid coordinate system. Substituting the norm of the ordinary wave in $(X,\ Y,\ Z)$ basis (Eq. (2.56)) in Eq. (2.57), the z component of the ordinary wave in the incident coordinate system is obtained [99, 103, 138]

$$k_{o,z} = \pm\sqrt{\left(\frac{n_o\omega}{c}\right)^2 - \beta^2} \tag{2.59}$$

The positive and negative signs of $k_{o,z}$ represent the two possible ordinary waves propagating inside the uniaxial anisotropic crystal, the forward and the backward waves.

By replacing the expression for the extraordinary wave vector components, provided in Eq. (2.55), into the ellipsoid of revolution equation (Eq. (2.58)), we obtain

$$\frac{\left(-\sin\phi_c\sin\theta_c\beta + \cos\theta_c k_{e,z}\right)^2 + \left(-\cos\phi_c\beta\right)^2}{n_e^2} + \frac{\left(\sin\phi_c\cos\theta_c\beta + \sin\theta_c k_{e,z}\right)^2}{n_o^2} = \frac{\omega^2}{c^2} \tag{2.60}$$

Developing the squared terms in Eq. (2.60) and after some rearrangements, a quadratic equation as a function of $k_{e,z}$ is obtained. From that quadratic expression, the solutions for the z component of the extraordinary wave vector are readily obtained as [103, 107]

$$k_{e,z} = \frac{-b \pm \sqrt{b^2 - 4ad}}{2a} \tag{2.61}$$

with

$$a = n_o^2\cos^2\theta_c + n_e^2\sin^2\theta_c$$

$$b = 2\left(n_e^2 - n_o^2\right)\sin\phi_c\sin\theta_c\cos\theta_c\beta \tag{2.62}$$

$$d = n_o^2\left(\cos\phi_c\beta\right)^2 + \left(n_e^2\cos^2\theta_c + n_o^2\sin^2\theta_c\right)\left(\sin\phi_c\beta\right)^2 - \frac{n_e^2 n_o^2\omega^2}{c^2}$$

Again, the positive and negative signs for $k_{e,z}$ correspond to the z component of the forward and the backward extraordinary waves propagating inside the uniaxial anisotropic crystal.

Finally, the ordinary and extraordinary refracted angles, $\theta_{t,o}$ and $\theta_{t,e}$ respectively, can be obtained from geometrical relations (see Figure 2-6) [99]

$$\theta_{t,o} = \arctan\left(\beta / k_{o,z}\right) \tag{2.63}$$

and

$$\theta_{t,e} = \arctan\left(\beta \big/ k_{e,z} \right) \tag{2.64}$$

where β is given by Eq. (2.48) and $k_{o,z}$ and $k_{e,z}$ by Eqs. (2.59) and (2.61), respectively.

The ordinary wave vector is constant for all directions of propagation. This means that the RI in which the ordinary wave propagates always corresponds to the ordinary index of refraction of the uniaxial anisotropic crystal. It can be described by considering the Snell's law [99, 132]

$$n_o = \frac{n_i \sin\theta_i}{\sin\theta_{t,o}} \tag{2.65}$$

By contrast, the value of RI experienced by the extraordinary wave depends on the direction of propagation, and it is called effective refractive index, n. By introducing the expression for the propagation unitary vector in spherical coordinates into Eq. (2.28) and rearranging, the following relation for the effective refractive index is obtained [139]

$$\frac{1}{n^2} = \frac{1}{n^2\left(\theta_{t,e}\right)} = \frac{\cos^2\alpha}{n_o^2} + \frac{\sin^2\alpha}{n_e^2} \tag{2.66}$$

where α is the angle between the direction of propagation and the optical axis. Note that n varies between n_o for $\alpha = 0$ and n_e for $\alpha = \pi/2$.

Finally, the Snell's law from an isotropic material to an anisotropic material, for the extraordinary refracted wave is written as

$$n_i \sin\theta_i = n\left(\alpha\right)\sin\theta_{t,e} \tag{2.67}$$

2.2.2 Polarizations states

In the following, we define the vector-basis chosen to describe the polarization of each one of the travelling waves in Figure 2-6 (incident, reflected and refracted waves). These three polarization-bases are selected to ease the polarization description of the waves. However, they must also be described form a common basis. Therefore, the transformations between these selected bases and the (x, y, z) coordinate system are also described hereafter.

For the incident beam, we use the orthonormal basis $\left(\hat{s},\ \hat{p}\right)$, where $\hat{s}$ and $\hat{p}$ are two unitary vectors perpendicular and parallel to the plane of incidence, respectively (see section 2.1.4). We set the (y, z) plane as the incidence plane (see Figure 2-9), therefore, the unitary vector perpendicular to the plane of incidence is parallel to the $\hat{x}$ direction [103, 106]

$$\hat{s} = \hat{x} \tag{2.68}$$

In turn, unit vector $\hat{p}$ is parallel to the plane of incidence and it can be obtained by substituting both $\hat{s}$ and the incident wave vector $\boldsymbol{k}_i$ relations (Eq. (2.68) and Eq. (2.43), respectively) into the Eq. (2.30)

$$\hat{p} = \frac{\boldsymbol{k}_i \times \hat{s}}{\left|\boldsymbol{k}_i\right|} = \frac{k_{i,z}\hat{y} - \beta\hat{z}}{k_i} \tag{2.69}$$

The polarization of the reflected electric field is described in its corresponding orthonormal basis $(\hat{s}_r,\ \hat{p}_r)$. As the reflected wave vector lies in the plane of incidence, $\hat{s}_r = \hat{s}$ [103, 106]. On the other hand, the unit vector $\hat{p}_r$ is perpendicular to the reflected wave vector $\boldsymbol{k}_r$ (see Figure 2-9). Thus, by replacing $\hat{s}_r = \hat{s} = \hat{x}$ and Eq. (2.44) into Eq. (2.30), one obtains

$$\hat{p}_r = \frac{\boldsymbol{k}_r \times \hat{s}_r}{\left|\boldsymbol{k}_r\right|} = \frac{-\left(k_{i,z}\hat{y} + \beta\hat{z}\right)}{k_i} \tag{2.70}$$

where we used $|\boldsymbol{k}_r| = k_r = k_i$.

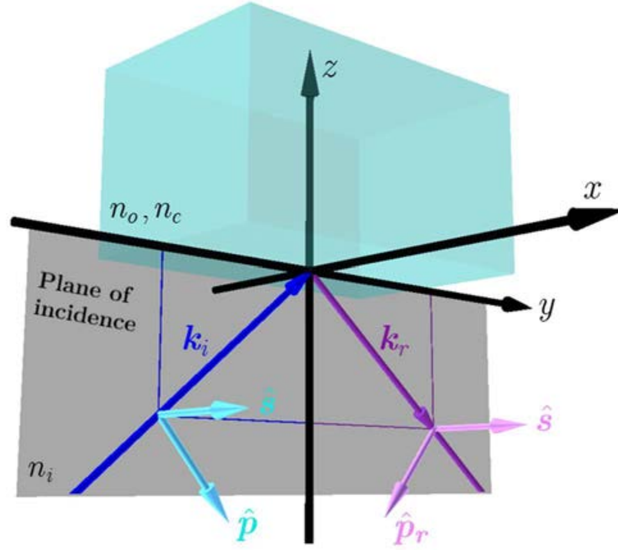

Figure 2-9. Perpendicular and parallel to the plane of incidence polarizations for the incident $\boldsymbol{k}_i$ (blue arrow) and reflected, $\boldsymbol{k}_r$ (violet arrow) waves. $\hat{p}$ and $\hat{p}_r$ are contained in the plane of incidence while $\hat{s}$ is normal to it.

Finally, the polarizations for the refracted electric waves are represented using the unit basis $(\hat{o},\ \hat{e})$, where $\hat{o}$ represents a unit vector parallel to the electric field vector of the ordinary wave and $\hat{e}$ is a unit vector parallel to the electric field of the extraordinary wave, both defined in section 2.1.4. The unit vectors $\hat{o}$ and $\hat{e}$ should be calculated inside the uniaxial anisotropic crystal. This means that a procedure similar to the calculation of $k_{o,z}$ and $k_{e,z}$ has to be followed. Both unitary vectors are function of the direction of propagation of the ordinary wave $\hat{k}_{t,o}$ and extraordinary wave $\hat{k}_{t,e}$. Thus, according to Eq. (2.54) and its norm in Eq. (2.56), the propagation direction unitary vector in the ellipsoid coordinate system for the ordinary wave can be written as [103]

$$\left(\hat{k}_{t,o}\right)_{ellip} = \frac{\left(\boldsymbol{k}_{t,o}\right)_{ellip}}{\left|\left(\boldsymbol{k}_{t,o}\right)_{ellip}\right|} = \frac{1}{\sqrt{\beta^2 + k_{o,z}^2}} \begin{pmatrix} -\sin\phi_c \sin\theta_c \beta + \cos\theta_c k_{o,z} \\ -\cos\phi_c \beta \\ \sin\phi_c \cos\theta_c \beta + \sin\theta_c k_{o,z} \end{pmatrix} \tag{2.71}$$

Analogously, considering Eq. (2.55) and Eq. (2.56), the propagation unitary vector for the extraordinary wave in the ellipsoid coordinate system is

$$\left(\hat{k}_{t,e}\right)_{ellip} = \frac{\left(\boldsymbol{k}_{t,e}\right)_{ellip}}{\left|\left(\boldsymbol{k}_{t,e}\right)_{ellip}\right|} = \frac{1}{\sqrt{\beta^2 + k_{e,z}^2}} \begin{pmatrix} -\sin\phi_c \sin\theta_c \beta + \cos\theta_c k_{e,z} \\ -\cos\phi_c \beta \\ \sin\phi_c \cos\theta_c \beta + \sin\theta_c k_{e,z} \end{pmatrix} \tag{2.72}$$

Taking into account the electric field vector direction of the ordinary wave in the principle axis basis given in Eq. (2.32) [103]

$$\left(\hat{o}\right)_{ellip} = N_o \left(-\cos\phi_c \beta, \quad \sin\phi_c \sin\theta_c \beta - \cos\theta_c k_{o,z}, \quad 0\right)^T \tag{2.73}$$

being N_o a normalizing constant that make $\hat{o}\cdot\hat{o} = 1$. Therefore, using the Euler rotation matrix, Eq. (2.53), $\hat{o}$ in the (x, y, z) frame of reference can be calculated

$$\hat{o} = M^{-1}\cdot\left(\hat{o}\right)_{ellip} = \begin{pmatrix} -\cos\phi_c \sin\theta_c & \sin\phi_c & \cos\phi_c \cos\theta_c \\ -\sin\phi_c \sin\theta_c & -\cos\phi_c & \sin\phi_c \cos\theta_c \\ \cos\theta_c & 0 & \sin\theta_c \end{pmatrix} \cdot \left(\hat{o}\right)_{ellip} \tag{2.74}$$

In turn, by replacing Eq. (2.72) in Eq. (2.34), the extraordinary electric field vector direction in the principle axis basis can be written as [103]

$$\left(\hat{e}\right)_{ellip} = N_e \left(\frac{-\sin\phi_c \sin\theta_c \beta + \cos\theta_c k_{e,z}}{n^2 - n_o^2}, \quad \frac{-\cos\phi_c \beta}{n^2 - n_o^2}, \quad \frac{\sin\phi_c \cos\theta_c \beta + \sin\theta_c k_{e,z}}{n^2 - n_e^2}\right)^T \tag{2.75}$$

where N_e is a normalizing constant of the extraordinary electric field direction and n is the effective refractive index. In the (x, y, z) coordinate system, $\hat{e}$ is given by

$$\hat{e} = M^{-1}\cdot\left(\hat{e}\right)_{ellip} = \begin{pmatrix} -\cos\phi_c \sin\theta_c & \sin\phi_c & \cos\phi_c \cos\theta_c \\ -\sin\phi_c \sin\theta_c & -\cos\phi_c & \sin\phi_c \cos\theta_c \\ \cos\theta_c & 0 & \sin\theta_c \end{pmatrix} \cdot \left(\hat{e}\right)_{ellip} \tag{2.76}$$

Remember that, as has been explained in section 2.1.4, $\hat{o}$ and $\hat{e}$ are, in general, not perpendicular because they correspond to normal modes of two different directions of propagation $\hat{k}_{t,o}$ and $\hat{k}_{t,e}$ [99].

2.2.3 Fresnel coefficients

The electric field expressions for the incident, reflected and refracted waves can be re-expressed with respect to the polarization unitary bases defined in section 2.2.2 [103, 106]

Incident: $$\boldsymbol{E}_i = \left(A_s\hat{s} + A_p\hat{p}\right)\exp\left[i\left(\omega t - \boldsymbol{k}_i\cdot\boldsymbol{r}\right)\right] \tag{2.77}$$

Reflected: $$\boldsymbol{E}_r = \left(B_s\hat{s} + B_p\hat{p}_r\right)\exp\left[i\left(\omega t - \boldsymbol{k}_r\cdot\boldsymbol{r}\right)\right] \tag{2.78}$$

Transmitted: $$\boldsymbol{E}_t = \left(G_o\hat{o}\exp\left[-i\boldsymbol{k}_{t,o}\cdot\boldsymbol{r}\right] + G_e\hat{e}\exp\left[-i\boldsymbol{k}_{t,e}\cdot\boldsymbol{r}\right]\right)\exp\left(i\omega t\right) \tag{2.79}$$

where A_s, A_p, B_s, B_p, G_o and G_e are complex amplitudes.

From the relation shown in Eq. (2.16), the magnetic fields of the incident, reflected and refracted waves can be written in terms of the wave vectors and the electric fields [103, 106]

Incident: $$\boldsymbol{H}_i = \frac{\boldsymbol{k}_i \times \boldsymbol{E}_i}{\omega\mu_0} = \frac{1}{\omega\mu_0}\left(\boldsymbol{k}_i \times \left(A_s\hat{s} + A_p\hat{p}\right)\exp\left[i\left(\omega t - \boldsymbol{k}_i\cdot\boldsymbol{r}\right)\right]\right) \tag{2.80}$$

Reflected: $$\boldsymbol{H}_r = \frac{\boldsymbol{k}_r \times \boldsymbol{E}_r}{\omega\mu_0} = \frac{1}{\omega\mu_0}\left(\boldsymbol{k}_r \times \left(B_s\hat{s}_r + B_p\hat{p}_r\right)\exp\left[i\left(\omega t - \boldsymbol{k}_r\cdot\boldsymbol{r}\right)\right]\right) \tag{2.81}$$

Transmitted: $$\boldsymbol{H}_t = \frac{\boldsymbol{k}_t \times \boldsymbol{E}_t}{\omega\mu_0} = \frac{1}{\omega\mu_0}\left(\boldsymbol{H}_{t,o} + \boldsymbol{H}_{t,e}\right)\exp\left(i\omega t\right) \tag{2.82}$$

with

$$\boldsymbol{H}_{t,o} = G_o\left(\boldsymbol{k}_{t,o} \times \hat{o}\right)\exp\left[-i\ \boldsymbol{k}_{t,o}\cdot\boldsymbol{r}\right] \tag{2.83}$$

$$\boldsymbol{H}_{t,e} = G_e\left(\boldsymbol{k}_{t,e} \times \hat{e}\right)\exp\left[-i\ \boldsymbol{k}_{t,e}\cdot\boldsymbol{r}\right] \tag{2.84}$$

Considering the boundary conditions of the electric and magnetic fields at the interface of dielectric surfaces (Eq. (2.36)), the tangential components of $\boldsymbol{E}$ and $\boldsymbol{H}$ must be continuous along the boundary ($z = 0$) [99, 140]. According to the electric waves form given in Eqs. (2.77), (2.78) and (2.79), the $\hat{x}$ and $\hat{y}$ tangential directions fulfil, respectively,

$$A_s + B_s = G_o\hat{s}\cdot\hat{o} + G_e\hat{s}\cdot\hat{e} \tag{2.85}$$

$$A_p\hat{y}\cdot\hat{p} + B_p\hat{y}\cdot\hat{p}_r = G_o\hat{y}\cdot\hat{o} + G_e\hat{y}\cdot\hat{e} \tag{2.86}$$

Analogously, by considering the relations given in (2.80), (2.81) and (2.82), the tangential components of $\boldsymbol{H}$ fulfil

$$A_p\hat{x}\cdot\left(\boldsymbol{k}_i \times \hat{p}\right) + B_p\hat{x}\cdot\left(\boldsymbol{k}_r \times \hat{p}_r\right) = \hat{x}\cdot\boldsymbol{H}_{t,o} + \hat{x}\cdot\boldsymbol{H}_{t,e} \tag{2.87}$$

$$A_s k_{i,z} - B_s k_{i,z} = \hat{y}\cdot\boldsymbol{H}_{t,o} + \hat{y}\cdot\boldsymbol{H}_{t,e} \tag{2.88}$$

Calculating the scalar and cross products and using Eqs. (2.45), (2.46) and (2.49), the four equations obtained from the boundary conditions result finally in

$$A_s + B_s = G_o o_{t,x} + G_e e_{t,x} \tag{2.89}$$

$$\left(A_p - B_p\right)\frac{k_{i,z}}{k_i} = G_o o_{t,y} + G_e e_{t,y} \tag{2.90}$$

$$-\left(A_p k_i + B_p k_i\right) = \left(\beta o_{t,z} - k_{o,z}o_{t,y}\right)G_o + \left(\beta e_{t,z} - k_{e,z}e_{t,y}\right)G_e \tag{2.91}$$

$$A_s k_{i,z} - B_s k_{i,z} = \left(k_{o,z}o_{t,x}\right)G_o + \left(k_{e,z}e_{t,x}\right)G_e \tag{2.92}$$

where the projection of the ordinary vector $\hat{o}$ onto x, y, z axes are called $o_{t,x} = \hat{x}\cdot\hat{o}$, $o_{t,y} = \hat{y}\cdot\hat{o}$ and $o_{t,z} = \hat{z}\cdot\hat{o}$, and the projection of the unit extraordinary axis $\hat{e}$ onto x, y, z axes are called $e_{t,x} = \hat{x}\cdot\hat{e}$, $e_{t,y} = \hat{y}\cdot\hat{e}$ and $e_{t,z} = \hat{z}\cdot\hat{e}$.

From the above-stated equations, Eqs. (2.89) - (2.92), we can calculate the Fresnel coefficients for the reflected and the transmitted waves, i.e., the relation between the amplitudes B_s, B_p, G_o and G_e and the incident field amplitudes, A_s and A_p. Let us begin with the transmitive case. By isolating B_s and B_p amplitudes from Eqs. (2.89) and (2.90), respectively, one obtains

$$B_s = G_o o_{t,x} + G_e e_{t,x} - A_s \tag{2.93}$$

$$B_p = A_p - \frac{k_i}{k_{i,z}}\left(G_o o_{t,y} + G_e e_{t,y}\right) \tag{2.94}$$

Substituting Eqs. (2.94) and (2.93) into Eqs. (2.91) and (2.92) respectively, B_s and B_p terms are eliminated, this leading to [99]

$$2A_s k_{i,z} = AG_o + BG_e \tag{2.95}$$

$$2A_p k_{i,z} = CG_o + DG_e \tag{2.96}$$

where A, B, C and D are constants given by

$$A = \left(k_{o,z} + k_{i,z}\right) o_{t,x} \tag{2.97}$$

$$B = \left(k_{e,z} + k_{i,z}\right) e_{t,x} \tag{2.98}$$

$$C = \left(k_{i,z} \frac{k_{o,z} o_{t,y} - \beta o_{t,z}}{k_i} + k_i o_{t,y}\right) \tag{2.99}$$

$$D = \left(k_{i,z} \frac{k_{e,z} e_{t,y} - \beta e_{t,z}}{k_i} + k_i e_{t,y}\right) \tag{2.100}$$

Equations (2.95) and (2.96) can be represented in matrix form as follows

$$\begin{pmatrix} 2A_s k_{i,z} \\ 2A_p k_{i,z} \end{pmatrix} = \begin{pmatrix} A & B \\ C & D \end{pmatrix} \begin{pmatrix} G_o \\ G_e \end{pmatrix} \tag{2.101}$$

The amplitudes of the transmitted electric field, G_o and G_e, can be obtained by isolating them from Eq. (2.101) [84, 107]

$$\begin{pmatrix} G_o \\ G_e \end{pmatrix} = \begin{pmatrix} t_{s,o} & t_{p,o} \\ t_{s,e} & t_{p,e} \end{pmatrix} \begin{pmatrix} A_s \\ A_p \end{pmatrix} \tag{2.102}$$

where the parameters $t_{s,o}$, $t_{p,o}$, $t_{s,e}$ and $t_{p,e}$, are the Fresnel transmission coefficients for uniaxial anisotropic crystals and are given by [99]

$$t_{s,o} = \frac{2k_{i,z} D}{AD - BC} \tag{2.103}$$

$$t_{p,o} = \frac{-2k_{i,z} B}{AD - BC} \tag{2.104}$$

$$t_{s,e} = \frac{-2k_{i,z}C}{AD - BC} \tag{2.105}$$

$$t_{p,e} = \frac{2k_{i,z}A}{AD - BC} \tag{2.106}$$

The subscripts for the incident amplitudes in Eq. (2.102), A_s and A_p, refer to the case of an incident wave $\hat{s}$-polarized or $\hat{p}$-polarized, while the subscripts for the transmitted waves, G_o and G_e, refer to the ordinary (o) and extraordinary (e) waves, respectively.

Next, we also consider the reflective case. By conducting an analogous mathematical procedure than that described for the transmissive case, the Fresnel reflection coefficients of a uniaxial anisotropic crystal arbitrarily oriented can be also obtained. By removing G_o and G_e amplitudes from Eqs. (2.89) - (2.92), the amplitudes of the reflected electric field, perpendicular and parallel to the incident plane (B_s and B_p, respectively), can be written as [99]

$$B_s = \left(2k_{i,z}\frac{o_{t,x}D - e_{t,x}C}{AD - BC} - 1\right)A_s + \left(2k_{i,z}\frac{e_{t,x}A - o_{t,x}B}{AD - BC}\right)A_p \tag{2.107}$$

$$B_p = \left(2k_i\frac{o_{t,y}D - e_{t,y}C}{AD - BC}\right)A_s + \left(2k_i\frac{e_{t,y}A - o_{t,y}B}{AD - BC} - 1\right)A_p \tag{2.108}$$

Rewriting Eqs. (2.107) and (2.108) in 2×2 matrix form, the amplitudes for the reflected wave are given by [84]

$$\begin{pmatrix} B_s \\ B_p \end{pmatrix} = \begin{pmatrix} r_{s,s} & r_{p,s} \\ r_{s,p} & r_{p,p} \end{pmatrix}\begin{pmatrix} A_s \\ A_p \end{pmatrix} \tag{2.109}$$

where $r_{s,s}$, $r_{p,s}$, $r_{s,p}$ and $r_{p,p}$ are the Fresnel reflection coefficients, whose explicit forms are given by

$$r_{s,s} = \frac{\left(2k_{i,z}o_{t,x} - A\right)D - \left(2k_{i,z}e_{t,x} - B\right)C}{AD - BC} \tag{2.110}$$

$$r_{p,s} = \frac{2k_{i,z}e_{t,x}A - 2k_{i,z}o_{t,x}B}{AD - BC} \tag{2.111}$$

$$r_{s,p} = \frac{2k_i o_{t,y}D - 2k_i e_{t,y}C}{AD - BC} \tag{2.112}$$

$$r_{p,p} = \frac{\left(2k_i e_{t,y} - D\right)A - \left(2k_i o_{t,y} - C\right)B}{AD - BC} \tag{2.113}$$

Note that in the double-subscript notation used in Eqs. (2.110) - (2.113), the first subscript is related to the polarization of the incident wave, whereas the second subscript refers to the reflected wave polarization. For example, the Fresnel coefficient $r_{p,s}$ gives the reflected electric field amplitude perpendicular to the plane of incidence ($\hat{s}$), when the incident electric field is parallel to the plane of incidence ($\hat{p}$). In this sense, $r_{s,s}$ and $r_{p,p}$ are direct reflection coefficients, whereas $r_{p,s}$ and $r_{s,p}$ are cross-reflection coefficients [99].

2.3 Approximations and considerations

The model presented in section 2.2 can be simplified in some cases. When the birefringence is small, i.e., $\left|n_e - n_o\right| \ll 1$, $n^2 - n_o^2 \approx 0$ and $n^2 - n_e^2 \approx 0$, an approximated expression for the electric field direction $\hat{e}$, different than that in Eq. (2.34), can be used to ease the calculations. In particular, the ellipsoid of revolution normal surface for the extraordinary wave vector, Eq. (2.58), can be approximated as [106]

$$\frac{\omega^2}{c^2} = \frac{k_{e,X}^2 + k_{e,Y}^2}{n_e^2} + \frac{k_{e,Z}^2}{n_o^2} \simeq \frac{\left|\left(\boldsymbol{k}_{t,e}\right)_{ellip}\right|^2}{n_o^2} \tag{2.114}$$

and, from Eq. (2.57),

$$\frac{\left|\left(\boldsymbol{k}_{t,e}\right)_{ellip}\right|^2}{n_o^2} \simeq \frac{\omega^2}{c^2} = \frac{\left|\left(\boldsymbol{k}_{t,o}\right)_{ellip}\right|^2}{n_o^2} \tag{2.115}$$

Accordingly, the wave vectors $\boldsymbol{k}_{t,e}$ and $\boldsymbol{k}_{t,o}$ are approximately equal, as are the refraction angles $\theta_{t,o}$ and $\theta_{t,e}$. Under this scenario, $\hat{e}$ can be considered parallel to the displacement vector, $\hat{D}_e$, and perpendicular to the ordinary electric field vector $\hat{o}$ and to the wave vectors $\boldsymbol{k}_{t,o}$ and $\boldsymbol{k}_{t,e}$. Thus, under this approximation, the unitary vector $\hat{e}$ can be written as [107]

$$\hat{e} \approx \frac{\boldsymbol{k}_{t,o} \times \hat{o}}{\left|\boldsymbol{k}_{t,o} \times \hat{o}\right|} \tag{2.116}$$

2.4 Wave propagation inside the uniaxial anisotropic crystals and the emerging waves

As stated in the introduction, the main goal of this thesis is to apply a polarimetric microscope working in reflection to measure the refractive index of non-planar dielectric materials. Therefore, the calculation of the amplitudes of the electromagnetic waves transmitted through the sample is not necessary for our purposes. However, the mathematical formulation provided in section 2.2 is general, and the amplitudes for the waves refracted into the sample for a given incident wave are already calculated (G_o and G_e, ordinary and extraordinary amplitudes, respectively). Note that these G_o and G_e amplitudes constitute the first step to study the wave propagation along the material. Although transmissive calculations are not going to be used in forthcoming sections, they can be of interest for the study of certain samples, as they can be used as complementary measurements to solve the problem of measuring the RI. For this reason, the propagation of light inside uniaxial anisotropic crystals is presented in this sub-section, but the corresponding calculations are not provided with the detail given in section 2.2.

Let us suppose that the uniaxial anisotropic medium studied is finite with a thickness d, and that light strikes from and exits to the same isotropic medium, i.e. the indices of refraction for the input and output mediums are equal, n_i (see Figure 2-10).

At the second surface of the sample ($z = d$), the ordinary and extraordinary waves, that are propagating inside the uniaxial anisotropic crystal, are reflected and transmitted (see Figure 2-10) [103, 107]. Before studying the reflected and emerged waves from the second boundary of the uniaxial anisotropic crystal, we have to consider that the ordinary and extraordinary waves propagating inside a birefringent medium introduce a certain retardation to their electric field vectors, which depends on the path traversed into the medium. At the second interface, after the propagation inside the uniaxial anisotropic crystal, the amplitudes of the transmitted electric fields, G'_o and G'_e, are given by [136, 141]

$$\begin{pmatrix} G'_o \\ G'_e \end{pmatrix} = \begin{pmatrix} G_o\left(z = d\right) \\ G_e\left(z = d\right) \end{pmatrix} = \begin{pmatrix} \exp\left(-ik_{o,z}d_o\right) & 0 \\ 0 & \exp\left(-ik_{e,z}d_e\right) \end{pmatrix} \begin{pmatrix} t_{s,o} & t_{p,o} \\ t_{s,e} & t_{p,e} \end{pmatrix} \begin{pmatrix} A_s \\ A_p \end{pmatrix} \tag{2.117}$$

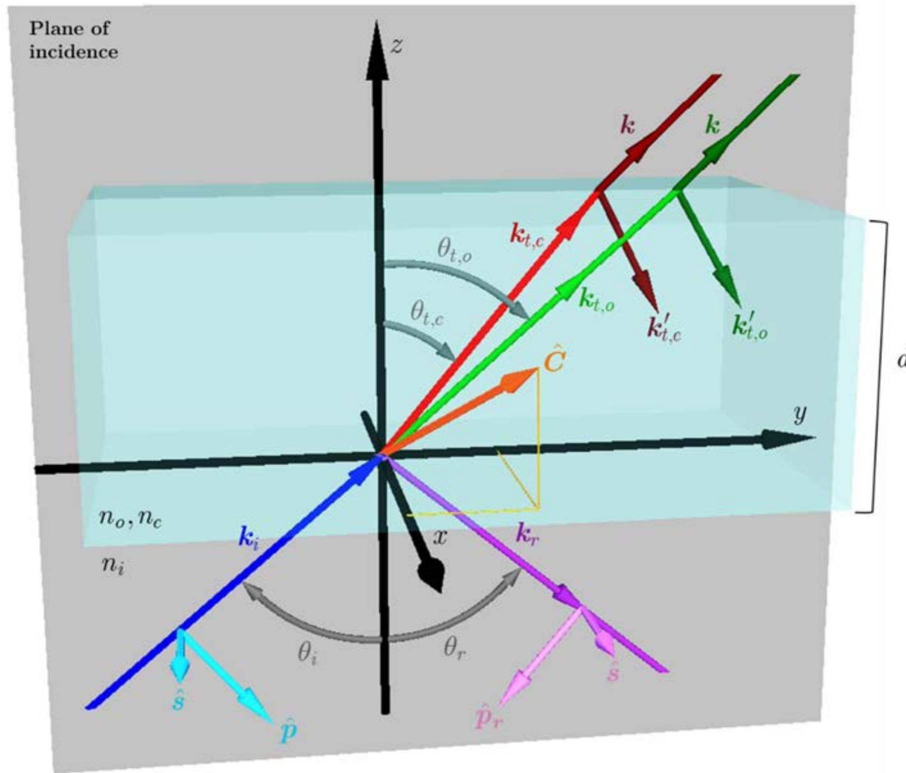

Figure 2-10. Reflection and refraction of light incident upon a uniaxial anisotropic crystal with arbitrary oriented optical axis $\hat{C}$ (orange arrow) within an isotropic medium. The propagation directions of the incident (dark blue arrow), reflected (violet arrow), forward-propagating ordinary and extraordinary (red and light green arrows), and backward-propagating ordinary and extraordinary (brown and dark green arrows) waves are shown. The plane of incidence coincides with the (y, z) plane. ($\hat{s}$, $\hat{p}$) and ($\hat{s}$, $\hat{p}_r$) are the polarizations for the incident and reflected waves respectively, and θ_i, θ_r, $\theta_{t,o}$ and $\theta_{t,e}$ (grey arrows) are the angles of the different wave vectors with respect to the normal.

being $\exp(-i\,k_{o,z}\,d_o)$ and $\exp(-i\,k_{e,z}\,d_e)$ the retardance of the ordinary and extraordinary waves, respectively [134]. Both retardances depend on the path lengths of the ordinary ray, $d_o = d/\cos(\theta_{t,o})$, and the extraordinary ray, $d_e = d/\cos(\theta_{t,e})$.

Finally, the electric wave amplitudes at the output of the anisotropic medium can be described with respect to the $(\hat{s},\ \hat{p})$ basis as a function of the ordinary and the extraordinary amplitudes of the transmitted electric fields. In particular, according to Eq. (2.102), one obtains [106, 107]

$$\begin{pmatrix} A_s' \\ A_p' \end{pmatrix} = \begin{pmatrix} t_{o,s} & t_{e,s} \\ t_{o,p} & t_{e,p} \end{pmatrix} \begin{pmatrix} G_o' \\ G_e' \end{pmatrix} \tag{2.118}$$

or, in other words,

$$\begin{pmatrix} A_s' \\ A_p' \end{pmatrix} = \begin{pmatrix} t_{o,s} & t_{e,s} \\ t_{o,p} & t_{e,p} \end{pmatrix} \begin{pmatrix} \exp\left(-ik_{o,z}d_o\right) & 0 \\ 0 & \exp\left(-ik_{e,z}d_e\right) \end{pmatrix} \begin{pmatrix} t_{s,o} & t_{p,o} \\ t_{s,e} & t_{p,e} \end{pmatrix} \begin{pmatrix} A_s \\ A_p \end{pmatrix} \tag{2.119}$$

where A'_s and A'_p are the $\hat{s}$-polarized and $\hat{p}$-polarized amplitudes of the emerging electric field and $t_{o,s}$, $t_{o,p}$, $t_{e,s}$ and $t_{e,p}$ are the Fresnel transmission coefficients at the second interface. Equation (2.119) relates the emerging electric field in terms of the amplitudes of the incident wave.

The explicit form for the coefficients $t_{o,s}$, $t_{o,p}$, $t_{e,s}$ and $t_{e,p}$ can be found in the specialized literature, as for example Refs. [103, 106, 107, 134, 136, 142].

2.5 Jones and Mueller Matrix formalisms

The electric field of any polarized wave can be expressed as a two-element vector using the Jones formalism. The two elements of a Jones vector are two orthogonal polarizations of the wave. Considering the $(\hat{s},\ \hat{p})$ basis chosen in section 2.1.4, the Jones vector of the incident wave, $\boldsymbol{J}_i$, can be expressed as [111]

$$\boldsymbol{J}_i = \begin{pmatrix} E_p \\ E_s \end{pmatrix} = \begin{pmatrix} A_p e^{i\phi_p} \\ A_s e^{i\phi_s} \end{pmatrix} \tag{2.120}$$

where E_p and E_s are the components of the incident electric field parallel and perpendicular to the plane of incidence, respectively. Both are function of their corresponding real amplitudes, $(A_s,\ A_p)$ and phases, $(\phi_p,\ \phi_s)$. The interaction between the incident wave and the uniaxial anisotropic medium transforms Eq. (2.120) into another Jones vector, $\boldsymbol{J}_{out}$. This can be calculated by using the Jones matrix formulism [85, 111]

$$\boldsymbol{J}_{out} = \begin{pmatrix} E_p^{out} \\ E_s^{out} \end{pmatrix} = \begin{pmatrix} J_{pp} & J_{sp} \\ J_{ps} & J_{ss} \end{pmatrix} \begin{pmatrix} A_p e^{i\phi_p} \\ A_s e^{i\phi_s} \end{pmatrix} \tag{2.121}$$

where E_p^{out} and E_s^{out} are the electric fields of the output waves, parallel and perpendicular to the plane of incidence, respectively, and the complex elements J_{pp}, J_{sp}, J_{ps} and J_{ss} are the four elements of the Jones Matrix, which describe the polarimetric properties of the sample. Note that, as has been commented in section 2.2.3, the first subscript of the Jones Matrix elements is referred to the polarization of the incident wave, whereas the second subscript is related to the reflected wave polarization. As the aim of this thesis is to develop a microscope working in reflection, the complex components of the output Jones vector, E_p^{out} and E_s^{out}, can be calculated from the reflected polarization wave equations obtained in section 2.2 [106, 136, 143], through the Jones matrix for the reflective interaction

$$\begin{pmatrix} E_p^{out} \\ E_s^{out} \end{pmatrix} = \begin{pmatrix} J_{pp} & J_{sp} \\ J_{ps} & J_{ss} \end{pmatrix} \begin{pmatrix} A_p e^{i\phi_p} \\ A_s e^{i\phi_s} \end{pmatrix} = \boldsymbol{R} \begin{pmatrix} A_p e^{i\phi_p} \\ A_s e^{i\phi_s} \end{pmatrix} \tag{2.122}$$

with [108, 143, 144]

$$\boldsymbol{R} = \begin{pmatrix} r_{p,p} & r_{s,p} \\ r_{p,s} & r_{s,s} \end{pmatrix} \tag{2.123}$$

The diagonal elements of the matrix $\boldsymbol{R}$ describe the Fresnel reflection coefficients for $\hat{p}$ and $\hat{s}$ polarizations with respect to the incidence plane. The off-diagonal elements of the matrix describe the polarization conversion between $\hat{p}$ and $\hat{s}$ polarizations that occurs when the sample is anisotropic.

One of the main goals of this thesis is to construct a physical model, based on experimental measurements, allowing us to characterize the optical properties of the studied samples. To this aim, we need to experimentally measure the polarimetric properties of the sample. This is done, according to the Mueller-Stokes formalism, by using an imaging Mueller matrix polarimeter integrated into a conoscopic microscope, which will be explained in detail in a further chapter. From the theoretical Jones matrix of the sample, the equivalent Mueller matrix can be calculated and compared with the experimental Mueller matrix of the sample. Therefore, the optical characteristics of the sample, as the refractive index, can be obtained by properly fitting the basic parameters of the model with the experimental data. Moreover, although the light employed for illumination and the samples studied during this work can be considered as fully polarized, experimental factors can introduce certain depolarization content, that is also taken into account by using the Mueller-Stokes formalism, and that can be studied and/or filtered from data. Consequently, we need to use the relation between Jones matrix and the fully polarized content of Mueller matrix. In particular, corresponding theoretical Mueller matrix, $\boldsymbol{M}$, is obtained from Jones matrix as [85, 111]

$$\boldsymbol{M} = \boldsymbol{A} \left\langle \boldsymbol{R} \otimes \boldsymbol{R}^* \right\rangle \boldsymbol{A}^{-1} \tag{2.124}$$

where $\otimes$ represents the Kronecker product, the asterisk represents the complex conjugate of the reflection Jones matrix $\boldsymbol{R}$ and the matrix $\boldsymbol{A}$ is given by [85, 111]

$$\boldsymbol{A} = \begin{pmatrix} 1 & 0 & 0 & 1 \\ 1 & 0 & 0 & -1 \\ 0 & 1 & 1 & 0 \\ 0 & i & -i & 0 \end{pmatrix} \tag{2.125}$$

Chapter 3 Mueller conoscopy

This chapter aims to describe the changes in electromagnetic fields produced when a highly convergent light beam is reflected by a sample. This kind of beams, obtained when light passes through a high numerical aperture objective (HNAO), consists of a set of angles of incidence (azimuthal and polar angles) that are interesting to characterize samples in reflection due to the large data redundancy they provide. By using the Mueller-Stokes formalism, the optical parameters of isotropic and uniaxial anisotropic samples can be obtained from the angle-resolved Mueller matrix image. Each pixel of the measured Mueller matrix image is associated to a particular pair of angles (azimuthal and polar angles), and thus, to a polarization change.

The chapter has the following structure. First, we introduce the theoretical background of reflective conoscopy in section 3.1. Then, section 3.2 generalizes the Jones and Mueller matrices obtained in Chapter 2 in order to express them as a function of azimuthal and polar angles of incidence. The polarimetric measurement matrix principle used to acquire the Mueller matrix image, and the errors introduced by the polarimetric system, are also explained in this section. Next, we simulate Mueller matrix images of several samples to discuss the viability of the proposed conoscopic Mueller microscope (section 3.3) and its polarimetric sensitivity (section 3.4). The last part of this chapter is divided in two sections. First of all, section 3.5 describes the method developed to obtain the refractive indices of materials comparing experimental and theoretical Mueller matrix images and then, section 3.6 studies the validity of this method by using synthetic Mueller matrix images, previously simulated.

3.1 Theoretical background of reflection conoscopy

3.1.1 General considerations on reflective Mueller matrices

As has been mentioned throughout the previous chapters, the main objective of this thesis is to measure the refractive index of non-planar dielectric materials by using a

polarimetric microscope working in reflection. The mathematical formalism has been explained in Chapter 2, where the Mueller matrix of uniaxial anisotropic materials, with an arbitrary orientation of the optical axis $\hat{C}$, has been obtained in reflection.

From the mathematical formalism presented in the previous chapter, we realized that the Fresnel reflection coefficients and the Mueller matrix of a uniaxial anisotropic medium are function of:

- The wavelength of the incident light (λ_i), since the modulus of the incident wave vector is $k_i = 2\pi/\lambda_i$.
- The angle of incidence (θ_i).
- The refractive index of the isotropic incident medium (n_i) and the studied media (n for isotropic materials or n_o and n_e for uniaxial anisotropic crystals).
- If the sample is uniaxial anisotropic, the orientation of the optical axis, $\hat{C}\left(\phi_c,\theta_c\right)$.

Therefore, considering that the incident medium is air ($n_i = 1$), for a particular wavelength and a certain angle of incidence, we can synthetize Mueller matrices for different RIs. Accordingly, by comparing the experimental Mueller matrix measured in the laboratory with the predicted one, calculated from the mathematical formalism given in Chapter 2, the refractive indices of the sample as well as the orientation of its optical axis can be obtained.

To evaluate how well the predicted Mueller matrix matches the experimental matrix, the statistical function *MSE* (Mean Squared Error) is used. In particular, to quantify how close the predicted refractive indices and the optical axis orientation $\hat{C}\left(\phi_c,\theta_c\right)$ are from the actual experimental parameters, the following equation is used [115, 145]

$$MSE = \frac{1}{16}\sum_{j,k=0}^{4}\left(\frac{M_{j,k}^{\text{exp}}}{M_{0,0}^{\text{exp}}} - \frac{M_{j,k}^{\text{pred}}}{M_{0,0}^{\text{pred}}}\right)^2 \tag{3.1}$$

where $M_{j,k}^{\text{exp}}$ is the element (j, k) of the experimental Mueller matrix and $M_{j,k}^{\text{pred}}$ is the same element but for the predicted Mueller matrix. The proper orientation of $\hat{C}\left(\phi_c,\theta_c\right)$ and the corresponding RIs of the sample are those that minimize the statistical function *MSE*. In order to do so, it is necessary to use an iterative optimization algorithm that look for the unknown parameters that minimize the *MSE* between both simulated and experimental Mueller matrices. Thereby, the refractive indices of the studied samples as well as the orientation of their optical axes can be obtained by using this minimization procedure.

We want to emphasize that for a uniaxial anisotropic crystal, just a single 4×4 Mueller matrix, this being function of θ_i, may not provide enough information to obtain the four desired parameters (n_e, n_o, ϕ_c, θ_c), due to mathematical correlations. However, we know that RI is an intrinsic parameter of all samples and it is independent of the angle of incidence related to the input $\boldsymbol{k}_i$. In other words, the value of the obtained theoretical and experimental Mueller matrices varies with θ_i, while the refractive indices of the studied material remain constant. Thus, an optical set-up allowing us to measure the Mueller

matrix for different angles of incidence, leads to the same value for the refractive indices for all the tested θ_i. As a consequence, system data redundancy can be easily increased just by measuring the same sample with different angles of incidence.

In the literature, one can find different set-ups that are used to measure the Mueller matrix in reflection as a function of a range of input incident angles θ_i. Some representative examples are several types of microscopes integrated in mechanical arms [146, 147], objective lenses [148, 149], among others [115].

In our case, to avoid mechanical errors associated to the positioning of mechanical arms, which set the different incident angles, we propose an alternative reflective instrumentation. The idea is to design a conoscopic polarimetric microscope working in reflection.

3.1.2 Conoscopic illumination

Orthoscopy and conoscopy are the two most important techniques in light polarization microscopy. The resulting parameters obtained after the optical analysis depend on the light propagation inside the microscope and how the light beam is reflected or transmitted by the crystallographic sample.

In an orthoscopic configuration, the sample is illuminated by collimated (or slightly convergent) rays due to a low aperture objective lens (Figure 3-1 (a)). The light transmitted or reflected by the surface of the sample travels in the same direction or nearly so, in such a way that the crystal is imaged on a camera sensor, usually giving a magnified image. All the directions that light takes after the transmission or reflection on the sample are essentially integrated at each spatial point. The surface sample image, observed by an orthoscope, allows one to view the striations, variations of optical activity, etc. [25, 119, 123].

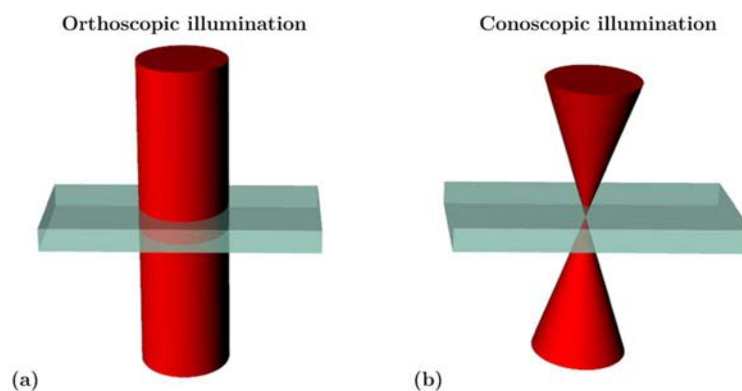

Figure 3-1. Comparison of the ray paths for (a) orthoscopic illumination, and (b) conoscopic illumination in transmission.

On the other hand, in a conoscopic configuration, the sample is illuminated by a highly convergent cone of light (Figure 3-1 (b)) where all the incident rays of the cone travel along different directions (different $\boldsymbol{k}_i$). A conoscope analyzes a single point in the sample,

and each spatial position on the detector is related to a different incident wave vector illuminating the sample. To highly focus the incident beam and to obtain a wide range of incident angles on the sample, a short focal length positive lens is commonly used [25, 123].

In this thesis, the optical element chosen to focus the input light beam onto the sample is a high numerical aperture objective (HNAO). The two main reasons are:

- Any collimated light beam is highly focused after passing through this kind of microscope objectives (conoscopic illumination).
- According to the Debye approximation [117, 118], the wavefront in the focal region of any high numerical aperture objective may be considered as a superposition of plane waves whose propagation vector must fall inside the cone of light formed by drawing straight lines from the focal point to the edge of the aperture (see Figure 3-1 (b)).

Therefore, a geometrical optics approximation can be used to describe the angular spectrum of the incident, reflected and transmitted fields. The cone of light generated by the high numerical aperture objective can be treated as an infinite number of incident wave vectors, each one of them having a different angle of incidence θ_i. The mathematical formalism explained in the previous chapter, which supposes incident, reflected and refracted plane waves, only remains valid to describe the set of incident rays with different orientations generated by any HNAO.

The incident focused beam makes possible to cover a wide range of $\boldsymbol{k}_i$-vectors at the same time, without any mechanical movement. Each incident wave vector is defined by two angles:

- θ_i is the polar angle, called angle of incidence in Chapter 2. It varies from the normal to a maximum angle that is defined by the numerical aperture (NA) of the lens used to generate the highly convergent cone of light (see Figure 3-2 (a)).
- ε is the azimuthal angle, this being the angle between the incident plane (set by the incident ray direction and the normal to the surface) and the x-axis. It varies from 0° to 360° (see Figure 3-2 (a)).

A two-dimensional representation of the two angles can be seen in Figure 3-2 (b) where we plotted a violet spot highlighting the spatial position corresponding to a particular pair of angular values for the incident angle ($\theta_i \sim 0.6 \cdot \theta_{i,\max}$) and the azimuthal angle ($\varepsilon = 70°$). Marked by two red circles, two different polar angles are represented (θ_i and the maximum angle of incidence, $\theta_{i,\max}$). By contrast, the blue lines point out ten azimuthal angles, ε, (0°, 45°, 70°, 90°, 135°, 180°, 225°, 250°, 270°, 315°). Any point at the back focal plane of the microscope objective as well as any incident beam ($\boldsymbol{k}_i$), can be expressed by a combination of these two angles.

Once the light cone is reflected by the sample surface, there are two possibilities to collect the reflected wave vectors. One possible configuration is to use a second microscope objective (see Refs. [115, 116]), while another conoscopic configuration is to use the same

microscope objective to collect the various reflected rays (see Refs. [118, 148]). In both situations, the incident wave vectors are reflected back and go to a different position (θ_i, ε) in the back focal plane of the collection microscope objective. For instance, see transmitted-reflected green spot in Figure 3-2 (b) corresponding to the incident violet spot. As a result, the obtained image on a detector placed after the collection objective, maps the wave vector distribution of light reflected by the sample, i.e., the two-dimensional conoscopic pattern obtained on the detector gives an angle-resolved image of light reflected by the sample surface. Hence, each pixel of the camera is related to a different reflected wave vector ($\boldsymbol{k}_r$ (θ_i, ε)). Note that the pixel size of camera introduces a certain limit in the resolution of the method, as a certain range of $\boldsymbol{k}$ are averaged at each pixel.

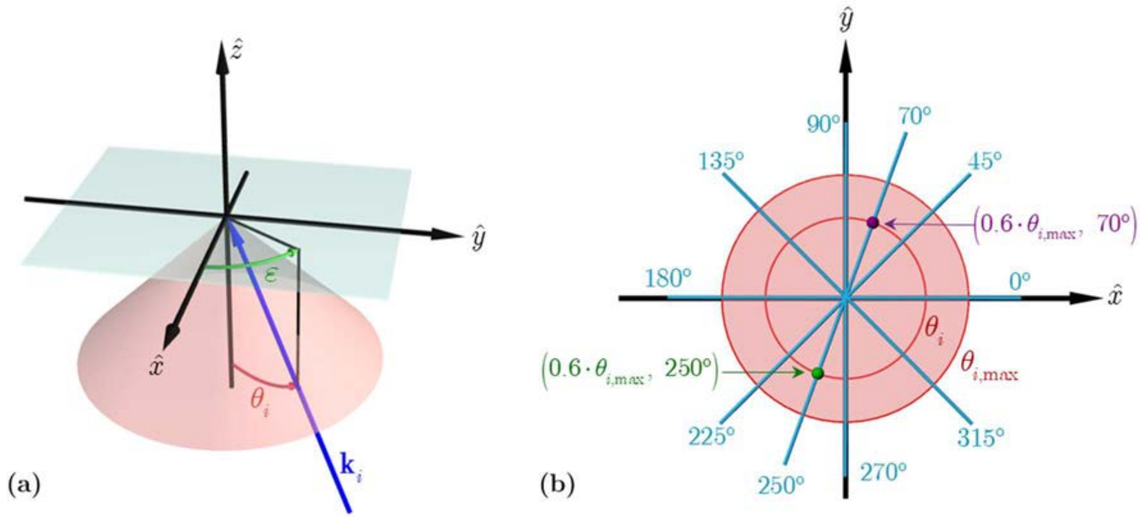

Figure 3-2. (a) Three-dimensional representation of the polar and azimuthal angles of an incident wave vector $\boldsymbol{k}_i$. (b) Polar and azimuthal angles corresponding to each point over the back focal plane of the microscope objective. The maximum angle of incident is $\theta_{i,\max}$. The violet spot highlights the point representing the angle of incidence $\theta_i \sim 0.6 \cdot \theta_{i,\max}$ and the azimuthal angle $\varepsilon = 70°$. In turn, the green spot ($\theta_r \sim 0.6 \cdot \theta_{i,\max}$, $\varepsilon = 250°$) represents the position of the reflected wave corresponding to the incident beam marked by the violet spot.

As in more detail in a further section, by properly modulating the polarization of the input focused beam and measuring the spatially varying polarization properties of the light reflected/transmitted by a sample, at the back focal plane of the high *NA* objective, the Mueller matrix image of the sample can be measured. This experimental Mueller matrix image has the characteristic that each pixel represents the Mueller matrix of a particular incident wave vector (θ_i and ε), which in general will be different (i.e., the Mueller matrix image consists of an array of single Mueller matrices, each one due to a different orientation of the incident beam).

Conoscopy can be a valuable tool for characterization of isotropic and anisotropic samples. In our case, in order to eliminate any mechanical arm, light is focused and collected by the same microscope objective, in a reflective configuration. The proposed

optical configuration of a conoscopic microscope is able to measure the angle-resolved Mueller matrix in reflection at numerous incident angles simultaneously, obtaining data redundancy without any mechanical motion of the set-up.

3.1.3 Focusing light with a High Numerical Aperture Objective

Let us assume an aberration-free objective designed for infinite conjugate ratio with rotational symmetry about its axis. The orientation of this microscope objective is such that its optical axis is perpendicular to the sample surface. Considering that the high numerical aperture objective has to obey the Abbe's sine condition [150], a spherical wavefront is produced after the incident light beam passes through it. A diagram of the focalization of a high *NA* objective can be seen in Figure 3-3. Consequently, the positions of the different incident plane waves on the entrance pupil of the HNAO and the polar, θ_i, and the azimuthal, ε, angles are related by [118, 151, 152]

$$\boldsymbol{r} = f \sin\theta_i \cdot \left(\cos\varepsilon,\ \ \sin\varepsilon\right) \tag{3.2}$$

where $\boldsymbol{r}$ is the distance of an incident ray upon the objective aperture to the aperture center and f is the focal length of the objective.

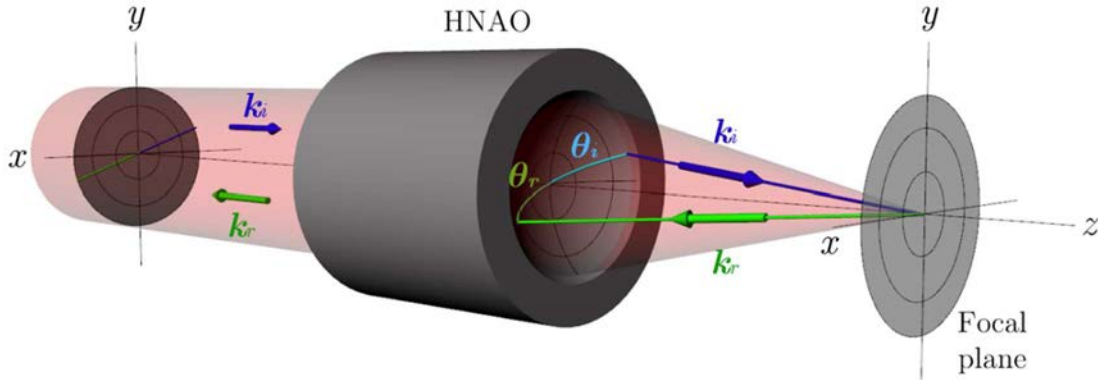

Figure 3-3. Diagram showing a ray focused by a high numerical aperture objective (HNAO) into a sample. The incident wave vector $\boldsymbol{k}_i$ (blue arrow) passes through the microscope objective and is reflected by the sample placed at the focal plane. $\boldsymbol{k}_r$ is the reflected wave vector (green arrow). Both wave vectors are contained on the same plane of incidence. θ_i and θ_r are the incident and reflected polar angles, respectively.

Under this scenario, θ_i can be redefined as the angle between any converging ray in the image space and the optical axis of the microscope objective at the focal point. As the microscope objective is circularly symmetric about its axis, its pupil radius is defined by

$$r_{\max} = f \sin\theta_{i,\max} \tag{3.3}$$

where $\theta_{i,\max}$ is the maximum angle of incidence on the sample surface we can reach. This angle is obtained from the value of the numerical aperture (*NA*) of the objective lens [1, 119, 153]

$$\theta_{i,\max} = \arcsin\left(\frac{NA}{n_i}\right) \tag{3.4}$$

where n_i is the refractive index of the medium between the objective front lens and the sample and NA determines the resolving power of the objective.

On the other hand, Abbe's sine condition requires that all the reflected rays within the reflected cone pass through the microscope objective at the same height $|\boldsymbol{r}|$ at which they entered to the system [150], i.e., the microscope objective is designed in such a way that if the microscope is illuminated with a collimated beam, and the sample surface is placed normal to the HNAO optical axis and at its focal plane, the reflected beam will be collimated once again after passing back through the same objective. Taking into account this affirmation, any incident ray and its corresponding reflection will present the same polar angle ($\theta_r = \theta_i$) but opposite azimuthal angles ($\varepsilon_r = \varepsilon_i + 180°$). The reflected ray passes again through the objective at a new distance $\boldsymbol{r}$ that can be calculated using again Eq. (3.2). As the reflected beam comes from the focal point of the system, it exits the microscope aperture parallel to the optical axis of the system with a constant height $|\boldsymbol{r}|$, and the existing beam is collimated. The combination of the reflected plane waves forms a two-dimensional conoscopic pattern at the back focal plane of the HNAO. This angularly resolved pattern represents the image of the sample surface in the Fourier domain and it can be recorded if the back focal plane is imaged on a detector [121, 124, 125, 148]. On the other hand, the image of the sample surface being conoscopically illuminated will be formed at the infinity, where in each point of the image, all the wave vectors defined by the aperture are averaged.

A particular point in Cartesian coordinates (x, y) on the entrance pupil of the high numerical aperture objective is related to a wave vector illuminating the sample at an incident angle θ_i and an azimuthal angle ε. As a conoscope maps the wave vector distribution that appears in the back focal plane of the HNAO (in the θ_i and ε polar system) and images it on a CCD camera (expressed in Cartesian coordinates), the correspondence between both coordinate systems is required to relate each pixel on the detector with the orientation of the reflected wave vector at that position. The relation between both systems is given by [105, 154]

$$\left(\theta_i,\ \varepsilon\right) = \left(\arctan\left[\frac{\tan\theta_{i,\max}\cdot\sqrt{x^2+y^2}}{r_{\max}}\right],\ \arctan\left(\frac{y}{x}\right)\right) \tag{3.5}$$

where $r = \sqrt{x^2 + y^2}$ is the modulus of the height in the back focal plane, $r = |\boldsymbol{r}|$. Consequently, considering that the image on the CCD camera is the rescaled image of the back focal plane, any pixel of the camera can be related to the orientation of the reflected wave vectors (θ_i, ε).

Moreover, one notes that having a sufficiently high numerical aperture objective implies a large number of different incident angles and a small focal length. Therefore, the input beam will be focused sharply on a tiny spot. If the focused beam is adjusted to illuminate a very small area, the effects of spatial nonuniformities in the sample will be minimized. In

fact, non-planar surfaces can be approximated to planar surfaces when the focal spot size is tiny compared to the sample surface curvature or nonuniformities. Finally, we want to note that if a light beam is tightly focused, the HNAO introduces changes in the local polarization of the incident and reflected beams. In fact, there exists a correspondence between the beam polarization at the laboratory system (Cartesian coordinate) with those of the multiple wave planes with $\boldsymbol{k}_i$ directions at the back focal plane, (θ_i, ε) polar system. As the refractive indices will be obtained from the Mueller matrix images of the sample, these polarization correspondences have to be considered and studied in more detail.

3.2 Conoscopic Mueller microscope

By keeping in mind that the aim of this thesis is to measure the Mueller matrix of any uniaxial anisotropic or isotropic sample, we propose to transform the standard conoscopic microscope into a polarimeter. Figure 3-4 shows a first scheme of a conoscopic microscope able to measure an angle-resolved Mueller matrix. Based on the set-up proposed by [125, 148], a Polarization State Generator (PSG) and a Polarization State Analyzer (PSA) are introduced. The PSG and the PSA systems will be explained in detail in further sections, but they are able to set the polarization of the input beam and to analyze the polarization of the reflected beam, respectively. Through them, the Mueller matrix corresponding to a wide range of different incident plane waves can be measured, where the high numerical aperture objective plays the dual role of focusing the incident beam over the sample surface and collimating the reflected one.

As stated before, the HNAO set an array of incident beams, each one characterized by their (θ_i, ε) angles and related to a particular pixel at the detector plane. Once the cone of light illuminates the sample, it modifies the polarization of different input beams in different ways due to the Fresnel coefficients. Therefore, each particular incident beam leads to a particular Mueller matrix of the sample, associated to a particular pixel position. The polarization resolved pattern on the detector can be analyzed to infer the array of Mueller matrices that characterize the sample for different angles of incidence. From now on, the whole set of Mueller matrices is referred to as a Mueller matrix image or angle-resolved Mueller matrix to differentiate it from a single Mueller matrix.

The values of the refractive indices and the orientation of the optical axis can be obtained from the Mueller matrix images by using the mathematical formalism studied in Chapter 2. In this sense, data redundancy is spatially obtained from intensity images on a pixelated detector. As a consequence, the quantity of redundancy data is only limited by the detector pixel size and the number of pixels, without requiring an increase of the measuring time (i.e., redundancy data is instantaneously obtained).

The conoscopic Mueller microscope architecture can be divided in three different blocks, according to their specific role (see Figure 3-4):

- Illumination block (red arrows in Figure 3-4): is the responsible to collimate the input light and set the input polarization through the polarization state generator (PSG) system. It sets the light that illuminates the entrance pupil of the high numerical aperture objective.

- High numerical aperture regime (green arrows in Figure 3-4): is the responsible to focus the input beam onto the sample and to collect the reflected light. The angular spectrum of plane waves illuminating the sample interacts with the sample and produces a new angular spectrum of reflected plane waves in the back focal plane of the HNAO.

- Detection block (blue arrows in Figure 3-4): is responsible to image the back focal plane of the microscope objective on the pixelated detector. The state of polarization (SoP) of the reflected beam is spatially analyzed (pixel-to-pixel) with the polarization state analyzer (PSA) system.

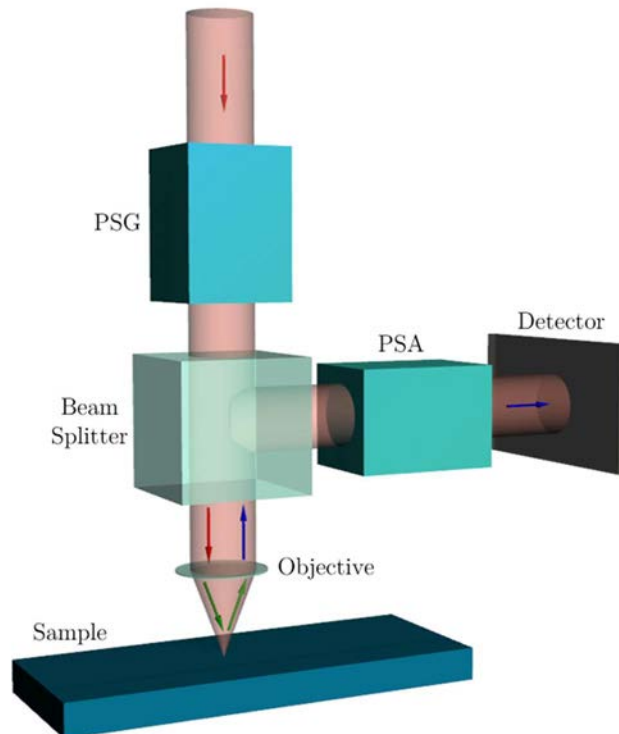

Figure 3-4. Scheme of the conoscopic Mueller matrix microscope. Input light traverses a non-polarizing beam-splitter and is focused onto the sample through the objective, which also redirects the reflected waves to the detector. The Polarization State Generator (PSG) and the Polarization State Analyzer (PSA) control the polarization of input and reflected lights, respectively, to measure the angle-resolved Mueller matrix image of the sample. The scheme can be divided in three blocks: illumination block (red arrows), high numerical aperture regime (green arrows) and detection block (blue arrows).

3.2.1 Polarization transformations at high numerical aperture systems

Let us assume that the polarization of the light beam after the PSG is fully polarized and spatially homogeneous, such as linear, elliptical, or circular polarizations. This polarization can be decomposed into its two orthogonally polarized components and can be described by its polarization ellipse. When any polarized beam is focalized by a high numerical aperture objective, variations of the electromagnetic field components may be spatially introduced with respect to a reference system, this significantly modifying the local incident polarizations [119, 153]. Under this scenario, polarization effects cannot be neglected and must be considered.

In order to understand these polarization transformations through focalization, Figure 3-5 (a) shows an example of a linear polarized light beam focused by a HNAO. After the high numerical aperture objective, the input beam is bent in different directions (all those set by the cone of light). Four different polarization transformations (related to four different incident directions on the sample) are highlighted in Figure 3-5 (a), they being pointed out by the four (red, green, violet and orange) arrows. We have set an incident polarization, before the high numerical aperture objective, as lineal, homogeneous and parallel to the $\hat{y}$-axis (see blue arrow in Figure 3-5 (a)).

Four particular polarization changes are shown in Figure 3-5 (a). After the high numerical aperture objective, the input beam is bent in different directions (all those setting the cone of light) with different polarizations. The plane waves at the top and the bottom of the microscope objective (red and orange arrows, respectively) are tilted in such a way that both can be decomposed as a combination of $\hat{y}$- and $\hat{z}$-axis. On the other hand, the plane waves that pass through the objective lens at its intersection with the (x, z) plane, remain parallel to the $\hat{y}$-axis (violet and green arrows). Any other incident wave in the cone surface present a polarization with some contribution to all three axes $\left(\hat{x}, \hat{y}, \hat{z}\right)$. From this scheme, we clearly observe how the different plane waves impinging the sample do not share the same polarization. For instance, by noticing that the incident plane at the light cone regime rotates with the azimuthal angle ε, we see how whereas red and orange arrows are linearly polarized parallel to the plane of incidence, the violet and green arrows are linearly polarized perpendicular to the plane of incidence, this fact having an impact in the local Fresnel coefficients.

Figure 3-5 (b) shows another example where a right-handed circularly polarized light beam generated by the PSG is bent by the high *NA* objective. In this case, the polarization of the illumination beam before the microscope objective can be expressed as a combination of two equal amplitudes, parallel to the $\hat{x}$- and $\hat{y}$- axes (blue arrows). The $\hat{x}$-components of the electric field in the intersection between the objective lens and the (x, z) plane are tilted in such a way that they can be decomposed as a combination of $\hat{x}$- and $\hat{z}$-axes (see violet and green arrows), while the $\hat{y}$-components remain parallel to the $\hat{y}$-axis. By contrast, $\hat{x}$-component of the homogeneous circular polarized beam at the top and the bottom of the collimated beam before the HNAO are not tilted when the planar waves pass

through the microscope objective (red and orange arrows, respectively). These different scenarios introduce significant differences in local polarizations.

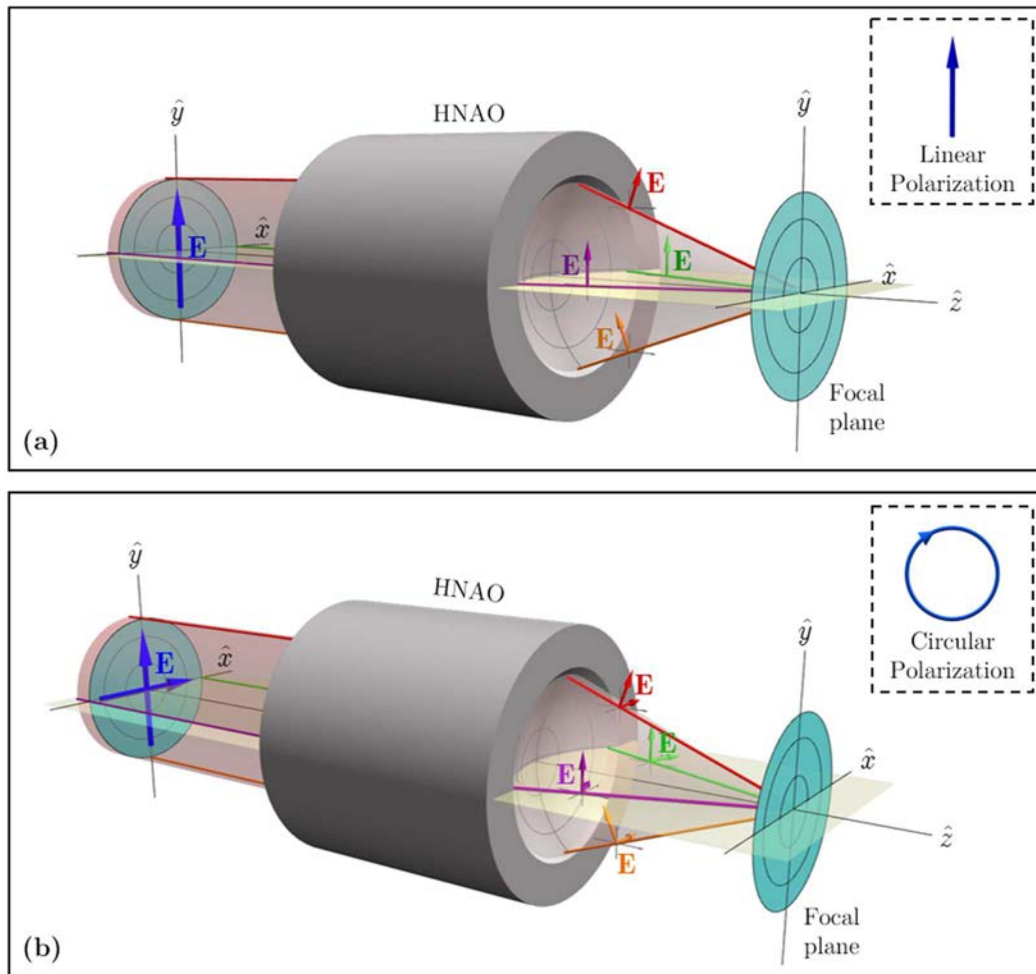

Figure 3-5. Schematic diagram illustrating focusing effect and polarization dependence of: (a) linearly polarized light beam parallel to $\hat{y}$ -axis; and (b) circular polarized beam focused by high numerical aperture objective microscope (HNAO). The electric fields are bent after passing through the microscope objective. The polarization of each planar incident wave after focalization is a function of its polar and azimuthal angles. Different positions in the back focal plane of the HNAO present different polarization transformations (see red, green, orange and violet arrows).

From these two examples, it is easy to conclude that the polarization transformation introduced by the high numerical aperture objective depends on the polarization of the homogeneous input illumination beam as well as on the spatial coordinates of the illumination plane waves on the entrance pupil of the HNAO.

On the other hand, the polarization of the reflected plane waves is once again transformed when the light beam passes back through the high numerical aperture objective, in an equivalent but inverse transformation. For this reason, the theoretical Mueller matrix obtained in Chapter 2 has to be recalculated by considering the local polarization transformations suffered by the incident and reflected beams.

3.2.2 Calculation of Mueller matrices after the high *NA* objective

Let us start by generalizing the mathematical formalism described along the Chapter 2 for different azimuthal angles of incidence, ε. In Chapter 2, the theoretical Mueller matrix of a uniaxial anisotropic sample in reflection as well as the corresponding Fresnel coefficients were expressed as a function of the incident angle θ_i but for a particular position of the plane of incidence. In particular, the incident, reflected and refracted waves were considered to be lying in the $(y,\ z)$ plane (see Figure 2-6 and Figure 2-7), while their respective polarizations were expressed by the orthonormal basis $\left(\hat{s},\ \hat{p}\right)$, where the unitary vectors $\hat{s}$ and $\hat{p}$ were perpendicular and parallel to the plane of incidence, respectively (see Figure 2-9). Therefore, $\hat{s}$ was parallel to $\hat{x}$-axis while $\hat{p}$ was expressed as a combination of $\hat{y}$- and $\hat{z}$-axes. Such mathematical model considers any polar angle of incidence θ_i (between 0° to the maximum incident angle, $\theta_{i,\max}$) to calculate the Fresnel reflection coefficients. Different θ_i implied a reorientation of the incident, reflected and refracted wave vectors as well as the direction of $\hat{p}$, while $\hat{s}$ direction always remained constant. Nevertheless, the azimuthal (ε) rotation of the wave vectors might initially seem that was not considered.

As has been above-discussed, the set-up proposed in this chapter includes a high numerical aperture objective that introduces an infinity number of incident wave vectors, depending not only on the polar angle θ_i, but also on the azimuthal angle ε. While it may appear that the formalism of the previous chapter is incomplete, in fact, the azimuthal rotation is considered. That is because a rotation of the plane of incidence with respect to the sample is equivalent to a rotation of the sample to the contrary sense, with respect to the plane of incidence.

If the sample being analyzed is a uniaxial anisotropic crystal, this is equivalent to a rotation of the optical axis. Thus, the mathematical model proposed in Chapter 2 can be readapted by substituting the angle of the optical axis ϕ_c (see Figure 2-5 or Eq. (2.40)), for an azimuthal angle (ϕ) that describes the different positions of the optical axis as function of the azimuthal angle of incidence ε. In this sense, ϕ and ϕ_c are related by

$$\phi = \phi_c - \varepsilon \tag{3.6}$$

where the azimuthal angle ε varies from 0° to 360°.

On the other hand, in the case of isotropic samples, the Fresnel coefficient values remain constant whichever is the azimuthal rotation. The form for the reflected and refracted waves is independent of the azimuthal orientation of the medium. Consequently, for the same angle of incidence θ_i, the Mueller matrix of an isotropic specimen is constant regardless of the angle ε. Some examples may be observed in the next sections, where several simulations of Mueller matrix images are represented in the high numerical aperture regime.

3.2.3 Mueller matrices in the laboratory system

Let us call (X_{ill}, Y_{ill}, Z_{ill}) and (X_{det}, Y_{det}, Z_{det}) the coordinate systems of the illumination (*ill*) and detection (det) systems, respectively. The former refers to the collimated beam incident to the microscope objective, and the latter to the collimated beam propagating backwards (see incident red line and reflected blue line, respectively, in Figure 3-4). In both areas the coordinate systems are fixed, and they are defined by the direction of propagation of the illumination and detection wave vectors, $\hat{k}_{ill}$ and $\hat{k}_{det}$, respectively. The measured experimental Mueller matrix on the CCD camera is expressed in the detection coordinate system, where the detection wave vectors are parallel to the $\hat{Z}_{det}$-axis, while their polarizations can be described as a combination of the orthonormal vectors $\hat{X}_{det}$ and $\hat{Y}_{det}$. In turn, the illumination wave vector $\hat{k}_{ill}$ propagates in the direction of the $\hat{Z}_{ill}$-axis and in the positive sense. Therefore, $\hat{k}_{ill}$ shares the same direction than $\hat{Z}_{det}$-axis, but propagates in the opposite sense (i.e., $\hat{k}_{ill} = -\hat{k}_{det}$ and $\hat{Z}_{ill} = -\hat{Z}_{det}$). Accordingly, the polarization of the illumination beam, generated by the PSG, is described by a combination of $\hat{X}_{ill}$ and $\hat{Y}_{ill}$ vectors. Figure 3-6 shows both coordinate systems as well as the directions of the illumination and detection wave vectors (orange and violet arrows, respectively).

On the other hand, the polarizations of the incident and reflected waves in the high numerical aperture objective regime (into the light cone) are expressed in the orthonormal $(\hat{s},\ \hat{p})$ basis. The particularity of this basis is that it depends on the orientation of the incident wave vector (i.e., of the plane of incidence). Therefore, the angular coordinates describing a wave direction into the cone (i.e., the particular values for the incident wave azimuthal rotation, ε, and the tilt due to the angle of incidence, θ_i) define a specific spatial orientation of the $(\hat{s},\ \hat{p})$ basis with regard to the laboratory basis. Three different incident wave vector $\hat{k}_i$ and their respective $(\hat{s},\ \hat{p})$ basis are shown in Figure 3-6 (red, blue and green arrows). One can see the variation of $\hat{s}$ and $\hat{p}$ directions when the plane of incidence is rotated 90°.

The ultimate purpose of this thesis is to measure the refractive indices and the optical axis orientation of dielectric samples, which is achieved by comparing their experimental and the theoretical Mueller matrix images. To that end, both angle-resolved Mueller matrices have to be obtained in the same coordinate system.

In the following, the theoretical Mueller matrix image obtained from the mathematical formulism described in Chapter 2 is recalculated according to the HNAO scenario, in which the polarizations of the incident and reflected plane waves are described in the $(\hat{s},\ \hat{p})$ basis. However, by using our polarimetric microscope scheme, the experimental Mueller matrix image of any uniaxial anisotropic or isotropic sample is measured in the detection basis. Consequently, the theoretical and experimental Mueller matrix images are expressed in different coordinate systems, and the corresponding transformation must also be considered.

Going back to the previous chapter, the Jones matrix $\boldsymbol{R}$ (see Eq. (2.123)) was calculated for a set of plane waves incident at the sample from the high numerical aperture objective in the $(\hat{s},\ \hat{p})$ basis. As the vector normal to the sample surface is parallel to the optical

axis of the microscope objective, the rotation angle that transforms the $(\hat{s},\ \hat{p})$ basis into the Cartesian coordinate system of the illumination region, is the azimuthal angle ε. According to [115, 155], a rotation of an angle ε in the Jones matrix formalism is expressed by the following matrix

$$\boldsymbol{Rot}(\varepsilon) = \begin{pmatrix} \cos\varepsilon & -\sin\varepsilon \\ \sin\varepsilon & \cos\varepsilon \end{pmatrix} \tag{3.7}$$

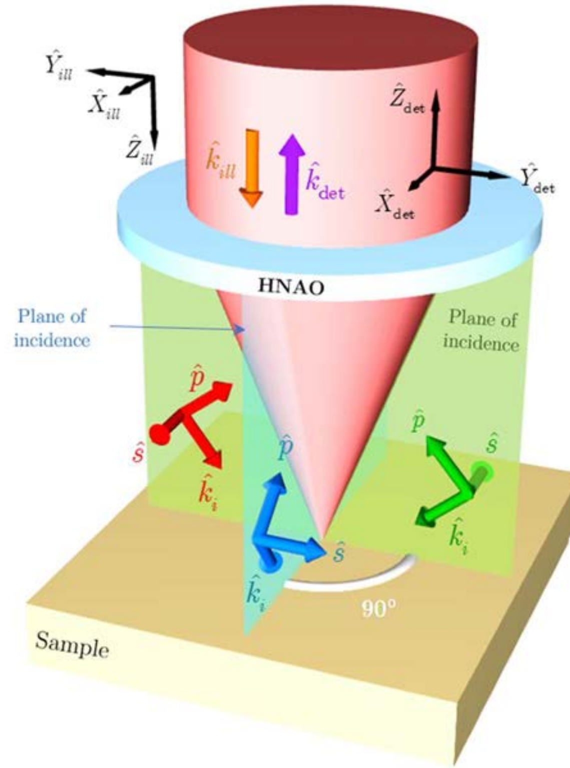

Figure 3-6. Diagram to define the coordinate systems used at the illumination (X_{ill}, Y_{ill}, Z_{ill}), detection (X_{det}, Y_{det}, Z_{det}) and focalization $(\hat{s},\ \hat{p})$ regions. In the illumination (*ill*) and detection (det) regions, the direction of propagation of wave vectors, $\hat{k}_{ill}$ (orange arrow) and $\hat{k}_{det}$ (violet arrow), coincides with $\hat{Z}_{ill}$ and $\hat{Z}_{det}$ directions, respectively. Their respective (*ill*) and (det) coordinate systems are fixed in the space with respect the laboratory system. By contrast, the $(\hat{s},\ \hat{p})$ basis, used to describe the polarization of focalized waves, is variable and depends on the incident wave vector direction $\hat{k}_i$ (red, blue and green arrows).

This rotation must be applied to each point at the back focal plane of the microscope objective to pass from the $(\hat{s},\ \hat{p})$ basis to the (X_{ill}, Y_{ill}, Z_{ill}) coordinate system. Mathematically this is expressed as

$$\boldsymbol{R}_{ill} = Rot(\varepsilon) \cdot \begin{pmatrix} r_{p,p} & r_{s,p} \\ r_{p,s} & r_{s,s} \end{pmatrix} \cdot Rot(-\varepsilon) \tag{3.8}$$

Before calculating the Mueller matrix image of the sample, another change in the coordinate system has to be considered. As shown in Figure 3-6, the directions of propagation of the illumination and the detection wave vectors are opposite. This implies

that $Z_{ill} = -Z_{\mathrm{det}}$ and $Y_{ill} = -Y_{\mathrm{det}}$. As the experimental Mueller matrix image is measured in the detection region, the reflection Jones matrices must be rotated from the illumination coordinate system to the (X_{det}, Y_{det}, Z_{det}) system. The reflection Jones matrix in the detection region, $\boldsymbol{R}_{\mathrm{det}}$, is given by

$$\boldsymbol{R}_{\mathrm{det}} = \begin{pmatrix} 1 & 0 \\ 0 & -1 \end{pmatrix} \boldsymbol{R}_{ill} \tag{3.9}$$

Once the reflection Jones matrix is calculated in the proper coordinate system, substituting $\boldsymbol{R}_{\mathrm{det}}$ into Eq. (2.124), the theoretical angle-resolved Mueller matrix in the fixed (X_{det}, Y_{det}, Z_{det}) coordinate systems is obtained.

3.2.4 Polarimetric measurement matrix principle

As previously stated, the goal of the proposed conoscopic Mueller microscope is to measure Mueller matrix images in reflection with a high number of different polar and azimuthal angles. To measure the Mueller matrix of samples, the proposed conoscopic microscope includes a Mueller polarimeter composed of a PSG, which controls the polarization of the illumination beam, a PSA, which analyzes the light reflected by the sample after the high numerical aperture objective, and a pixelated detector which acquires the intensity pattern exiting from the polarization analyzer (see Figure 3-4). Under this scenario, each input polarization selected with the PSG and polarization analyzer set with the PSA yield to a particular intensity image at the detector. As is known, 4×4 Mueller matrices relate the input and output polarizations (defined by its corresponding Stokes vectors, $\boldsymbol{S}$), describing the linear polarization-matter interactions through the relation ($\boldsymbol{S}_{out} = \boldsymbol{M}_{\mathrm{sample}} \cdot \boldsymbol{S}_{in}$). Therefore, to solve this linear system and completely obtain the Mueller matrix image of the sample, we need to record at least 16 independent intensity patterns. The procedure followed to obtain the Mueller matrix image and the errors introduced by the system are explained in this section.

Let us start describing the measurement matrix method. A Mueller matrix can be understood as the transfer function of a polarimetric system, giving the relationship between the states of polarization (SoPs) of the illumination and exiting beams. For our particular case, the existing beam is the reflected beam in the detection region. Considering that the number of pixels of the detector is $N_i \times N_j$, each pixel of the camera can be expressed as (i, j) where $1 \le i \le N_i$ and $1 \le j \le N_j$. As explained above, the intensity pattern acquired by the detector varies according to the angles (θ_i, ε). Therefore, the intensity of each pixel, $I_{i,j}$, for a fixed PSG and PSA configurations can be written as [111, 112]

$$I_{i,j} = \boldsymbol{a} \cdot \boldsymbol{M}_{i,j} \cdot \boldsymbol{S}_{in} = \begin{pmatrix} A_0 & A_1 & A_2 & A_3 \end{pmatrix} \cdot \begin{pmatrix} m_{00} & m_{01} & m_{02} & m_{03} \\ m_{10} & m_{11} & m_{12} & m_{13} \\ m_{20} & m_{21} & m_{22} & m_{23} \\ m_{30} & m_{31} & m_{32} & m_{33} \end{pmatrix}_{i,j} \cdot \begin{pmatrix} S_0 \\ S_1 \\ S_2 \\ S_3 \end{pmatrix} \tag{3.10}$$

where $\boldsymbol{S}_{in}$ is the Stokes vector that characterizes the SoP generated by the PSG, $\boldsymbol{M}_{i,j}$ is the single Mueller matrix at the pixel (i, j) of the image, i.e., the Mueller matrix corresponding to an specific combination of the incident and azimuthal angles (θ_i, ε), and the analyzer vector $\boldsymbol{a}$, commonly called polarization analyzer (PA), is the first row of the PSA matrix [111, 112]. When the input polarization equals the polarization set by the analyzer vector $\boldsymbol{a}$, the maximal intensity is recorded at the detector.

As stated above, to fully characterize each 4×4 Mueller matrix, we should measure at least 16 values of $I_{i,j}$, combining different configurations of the PSG and PSA that should be linearly independent. However, the Mueller matrices can be extracted for more than 16 measurements of $I_{i,j}$, in order to reduce noise from redundancy data.

Let us suppose that we are making a set of measurements, combining different configurations of the PSG and PSA, with m and q being the number of polarization generators and polarization analyzers, respectively. The matrix of the measured intensities for the (i, j) pixel can be written in matrix form as,

$$\begin{pmatrix} I_{1,1} & I_{1,2} & \cdots & I_{1,m} \\ I_{2,1} & I_{2,2} & \cdots & I_{2,m} \\ \vdots & \vdots & \ddots & \vdots \\ I_{q,1} & I_{q,2} & \cdots & I_{q,m} \end{pmatrix}_{i,j} = \begin{pmatrix} A_{1,0} & A_{1,1} & A_{1,2} & A_{1,3} \\ A_{2,0} & A_{2,1} & A_{2,2} & A_{2,3} \\ \vdots & \vdots & \vdots & \vdots \\ A_{q,0} & A_{q,1} & A_{q,2} & A_{q,3} \end{pmatrix} \cdot \boldsymbol{M}_{i,j} \cdot \begin{pmatrix} S_{0,1} & S_{0,2} & \cdots & S_{0,m} \\ S_{1,1} & S_{1,2} & \cdots & S_{1,m} \\ S_{2,1} & S_{2,2} & \cdots & S_{2,m} \\ S_{3,1} & S_{3,2} & \cdots & S_{3,m} \end{pmatrix} \tag{3.11}$$

Eq. (3.11) can be rewritten as

$$\boldsymbol{B}_{i,j} = \boldsymbol{A} \cdot \boldsymbol{M}_{i,j} \cdot \boldsymbol{S}\,. \tag{3.12}$$

where $\boldsymbol{B}_{i,j}$ is the $q \times m$ matrix of the measured intensities. The columns in the $\boldsymbol{S}$ matrix correspond to the Stokes vectors generated by the PSG, and reciprocally, $\boldsymbol{A}$ is a matrix whose rows contain the different polarization analyzers used by the PSA. The ranks for matrices $\boldsymbol{S}$ and $\boldsymbol{A}$ have to be 4 and their values are known after a complete calibration of the PSG and the PSA systems. Once $\boldsymbol{A}$ and $\boldsymbol{S}$ matrices are known, single Mueller matrices at every pixel (i, j) can be obtained, i.e., the angle-resolved Mueller image is retrieved.

To achieve the value of the Mueller matrix, the polarimetric measurement matrix $\boldsymbol{W}$ is used. This matrix is obtained by computing the Kronecker product of $\boldsymbol{S}$ and $\boldsymbol{A}$ [112]

$$\boldsymbol{W} = \left(\boldsymbol{A} \otimes \boldsymbol{S}\right) \tag{3.13}$$

and it is independent on the sample Mueller matrix. As $\boldsymbol{W}$ is defined by the optical elements comprising the Mueller polarimeter, it is determined during the polarimetric calibration of the set-up.

Let us compact a single Mueller matrix of a particular pixel $\boldsymbol{M}_{i,j}$ into a 16×1 Mueller column vector, $\vec{\boldsymbol{M}}_{i,j} = \begin{pmatrix} m_{00} & m_{01} & m_{02} & m_{03} & m_{10} & \ldots & m_{33} \end{pmatrix}^T$, and the respective matrix of experimental intensities ($\boldsymbol{B}_{i,j}$) into a $(m \cdot q) \times 1$ intensity column vector, $\vec{\boldsymbol{B}}_{i,j} = \begin{pmatrix} I_{1,1} & I_{1,2} & \ldots & I_{1,m} & I_{2,1} & \ldots & I_{q,m} \end{pmatrix}^T$, both in lexicographic order, where the superscript T denotes the transpose of a vector. The measured intensity vector $\vec{\boldsymbol{B}}_{i,j}$ is

related to the sample Mueller vector $\vec{\boldsymbol{M}}_{i,j}$ through the $(m \cdot q) \times 16$ polarimetric measurement matrix $\boldsymbol{W}$ [112]

$$\vec{\boldsymbol{B}}_{i,j} = \boldsymbol{W} \cdot \vec{\boldsymbol{M}}_{i,j} \tag{3.14}$$

At this point, we would like to stress that the calculus of $\vec{\boldsymbol{M}}_{i,j}$ depends both on: (1) the number of polarization generators (m) and analyzers (q) used to measure $\vec{\boldsymbol{B}}_{i,j}$; and (2) the matrix $\boldsymbol{W}$ inversion.

For $m = q = 4$, the matrices $\boldsymbol{S}$ and $\boldsymbol{A}$ are square matrices and therefore, $\boldsymbol{W}$ is also a square matrix. If $\boldsymbol{W}$ is a non-singular matrix, its inverse $\boldsymbol{W}^{-1}$ will exist and can be calculated [111]. The complete Mueller vector is then obtained as

$$\vec{\boldsymbol{M}}_{i,j} = \boldsymbol{W}^{-1} \cdot \vec{\boldsymbol{B}}_{i,j} \tag{3.15}$$

If m, $q > 4$, the matrices for $\boldsymbol{S}$ and $\boldsymbol{A}$ are rectangular, so it is also the case for the matrix $\boldsymbol{W}$ (see Eq. (3.13)). In addition, the system presents more equations than unknowns, so it is overdetermined. References [112, 156] show how the optimal (least-squares) polarimetric data reduction equation for calculating the Mueller vector of the sample at each pixel uses the pseudoinverse $\boldsymbol{W}_P^{-1}$ of the polarimetric measurement matrix

$$\vec{\boldsymbol{M}}_{i,j} = \boldsymbol{W}_P^{-1} \cdot \vec{\boldsymbol{B}}_{i,j} = \left(\boldsymbol{W}^T \boldsymbol{W}\right)^{-1} \boldsymbol{W}^T \cdot \vec{\boldsymbol{B}}_{i,j} \tag{3.16}$$

It can be seen from Eqs. (3.15) and (3.16) that the Mueller matrix at each pixel can be obtained just by selecting one of the infinite PSG-PSA configuration combinations able to build-up a non-singular matrix $\boldsymbol{W}$ and measuring its respective intensity vector $\vec{\boldsymbol{B}}_{i,j}$.

In terms of error amplification, not all the possible solutions for $\boldsymbol{W}$ are equally suitable for measuring the Mueller matrix images. If we consider experimental non-correlated noise in the intensity measures, the inverse or pseudoinverse matrix of $\boldsymbol{W}$ may amplify errors at the $\vec{\boldsymbol{B}}_{i,j}$ matrix (noise) to the calculus of the Mueller matrix. In order to minimize error amplification from $\vec{\boldsymbol{B}}_{i,j}$ to $\vec{\boldsymbol{M}}_{i,j}$, the matrix $\boldsymbol{W}$ should be as far as possible from singular matrices. The most common mathematical criterion used for the optimization of any Mueller polarimeter is the so-called condition number of $\boldsymbol{W}$, $CN(\boldsymbol{W})$, which is defined as the ratio of the smallest over the largest singular values (different from zero) of $\boldsymbol{W}$ [157, 158]. The range of the condition number is from 1, corresponding to a unitary matrix, which does not amplify the error, to infinity, corresponding to a singular matrix. In the case of polarimetric systems, the minimum condition number is equal to $\sqrt{3}$ [158]. As $\boldsymbol{W}$ is calculated by the Kronecker product of $\boldsymbol{S}$ and $\boldsymbol{A}$ matrices, its condition number is calculated as [156]

$$CN\left(\boldsymbol{W}\right) = CN\left(\boldsymbol{S}\right) \cdot CN\left(\boldsymbol{A}\right) \tag{3.17}$$

Thereby, the criterion for the optimization of any Mueller polarimeter is to optimize the condition numbers of $\boldsymbol{S}$ and $\boldsymbol{A}$. In experimental implementations, these polarimetric matrices are limited according to the specific PSG and PSA configurations. Consequently, the optimum condition number of the polarimeter strongly depends on the type of optical

elements used to build the PSG and the PSA systems [129]. References [128, 156, 158] analyzed the matrices $\boldsymbol{S}$ and $\boldsymbol{A}$ and determined optimum PSG-PSA configurations. These are obtained when the SoPs of the polarization generator and analyzer matrices are equally spaced throughout the Poincaré sphere. In addition, to mitigate the calibration errors and/or imperfectness of the used optical components, authors in Ref. [159] suggested that the numbers of illumination (m) and analysis (q) states should be larger than 4. The increment of the number of generators and analyzers does not affect the value of the CN but reduces the variances associated to the Mueller coefficients measurement.

To optimize our PSG and PSA systems, in terms of noise amplification, we focus on optimizing the $\boldsymbol{S}$ and $\boldsymbol{A}$ matrices. In this sense, we have used an optimization function that calculates the minimum CN and its corresponding polarization generator and analyzer matrices. Furthermore, in order to reduce measuring time, the number of chosen polarization generators and analyzers is $m = q = 6$. In Figure 3-7, we show a set of obtained theoretical polarization states for generation (blue points) that result in a minimization of the condition number. The calculated best-fit CN of the polarimetric measurement matrices describing this PSG system is $\sqrt{3}$, which corresponds to the minimum possible value for polarimetric systems. The same polarization basis is also valid for analyzers, to set the PSA configuration. We can observe that the blue points are drawing a regular octahedron, in agreement with results described in Ref. [128], where it is shown how polarization states at the Poincaré Sphere surface that are placed at the vertex of Solid Platonics lead to optimum configurations.

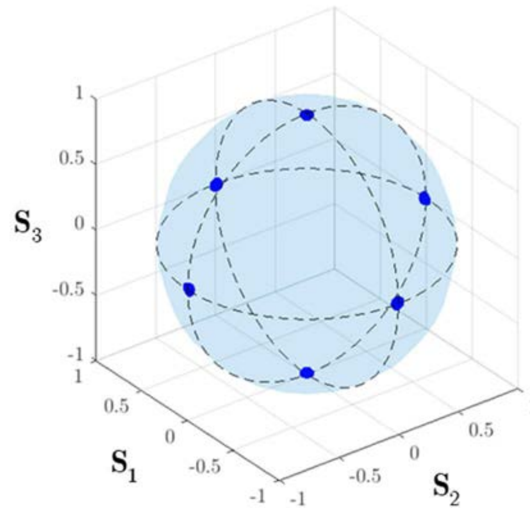

Figure 3-7. Theoretical set of polarization states (blue points) for the optimized polarization state generator and analyzer.

Nevertheless, errors due to non-ideal optical elements used in the real experimental set-up and the possibility that the SoPs of the PSG and PSA systems change with time (variations with temperature, pressure, etc.), result in deviations from the theoretical states of polarization given in Figure 3-7. In order to minimize this source of errors, the conoscopic Mueller microscope is calibrated frequently and the real measured polarization generators and analyzers are used to calculate the polarimetric measurement matrix $\boldsymbol{W}$.

3.3 Simulated conoscopic Mueller matrix images

According to the theoretical methodology above-described for the calculus of angle-resolved Mueller matrices, throughout this section some simulations are shown to study isotropic and uniaxial anisotropic samples. The different examples selected in this section attempt to verify that our mathematical formalism gives expected results.

The images shown throughout this chapter are achieved from simulations run on MATLAB software and they are two-dimensional representations of the back focal plane of the microscope objective. We selected to represent these two-dimensional images in a Polar representation (i.e., the $N_i \times N_j$ *pixels* of a Mueller coefficient are represented into the area of a circle of radius $f \cdot \sin \theta_{i,\max}$, according to their corresponding coordinates θ_i and ε). We chose this format to the sake of comparison with experimental measurements. In fact, as will be seen in further sections, the experimental Mueller matrix images of the sample are constructed from a set of intensity patterns registered by the camera. Due to the circular aperture of the microscope and the Gaussian profile of the used light source, the sixteen components of the experimental Mueller matrix images present circular symmetry. In this way, by setting the Polar representation for the simulated Mueller matrix images, they present the same form than the experimental ones.

Certain initial parameters were introduced to obtain the resulting images: the number of pixels (1000×1000), the maximum incident angle $\theta_{i,\max} = 90^{\circ}$ and the chosen wavelength $\lambda = 635\ nm$. The theoretical angle-resolved Mueller matrices were normalized and calculated in the high numerical aperture objective regime and the detection coordinate system, to see the visual differences between them.

First, a graphical representation of the incident angles is shown in Figure 3-8. From Figure 3-8 (a), one can see that the center of the image coincides with the angle $\theta_i = 0^{\circ}$ and, going radially out from the center pixel, the incident angle increases to the maximum angle, in this case 90°, at the edge of the pupil. Figure 3-8 (b) shows the azimuthal angle ε, that starts at 0° and varies around the pupil to 360°.

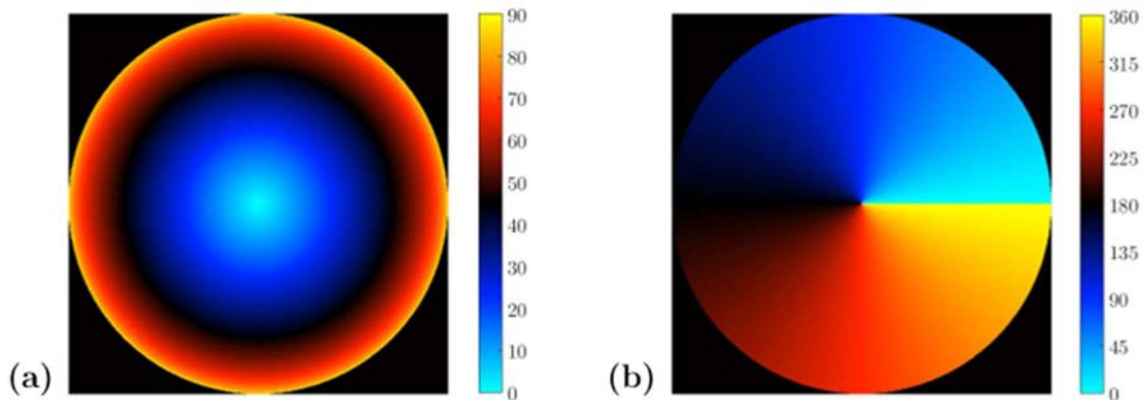

Figure 3-8. Representation of (a) the polar angle θ_i with maximum incidence angle of 90° and, (b) the azimuthal angle ε.

3.3.1 Simulated Mueller matrix images of isotropic samples

The Mueller matrix image of an isotropic sample obtained by using the reflection Mueller microscope presented throughout this chapter can be calculated by using the polar and azimuthal angles showed in Figure 3-8. Let us assume a refractive index of $n = 1.5$ and a maximum angle of incidence of 90°. Considering all these parameters, a simulation program allows us to obtain the angle-resolved Mueller matrix of this hypothetical material. Figure 3-9 shows the resulting image in the fixed detection coordinate system $(X_{\text{det}},\ Y_{\text{det}},\ Z_{\text{det}})$, while Figure 3-10 shows the analogous image obtained in the $\left(\hat{s},\ \hat{p}\right)$ basis.

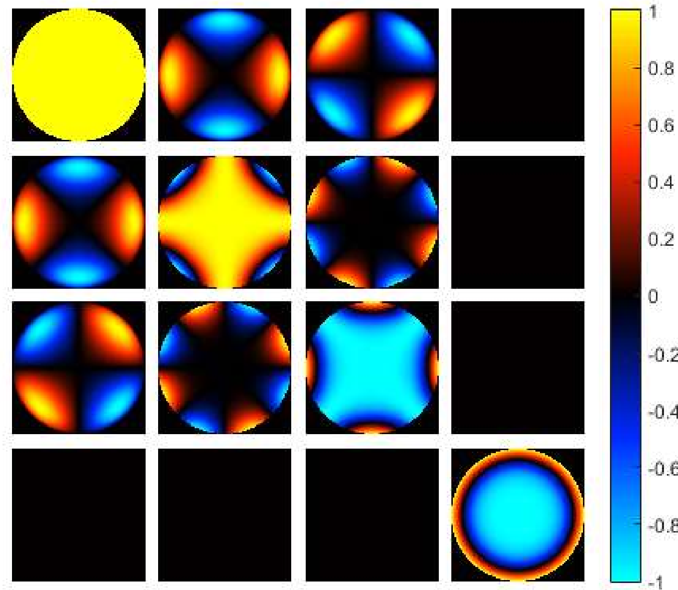

Figure 3-9. Simulation of a Mueller matrix of an isotropic sample with refractive index $n = 1.5$. The normalized angle-resolved Mueller matrix is expressed in the detection coordinate system and the maximum angle of incidence is 90°.

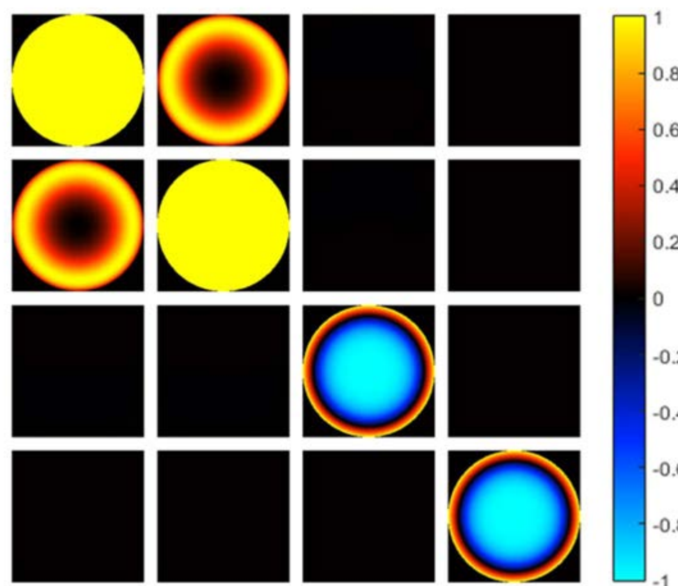

Figure 3-10. Normalized angle-resolved Mueller matrix of an isotropic sample in the orthonormal basis $\left(\hat{s}, \hat{p}\right)$. The refractive index of the sample is $n = 1.5$.

It is important to note that the angle-resolved Mueller matrices of Figure 3-9 does not only show one Mueller matrix, but 1000×1000 Mueller matrices (i.e., the number of pixels selected, they being related to the number of simulated input rays —angles— illuminating the sample). An individual 4×4 Mueller matrix (related to a particular input ray direction described by its specific angles θ_i and ε) is represented by a single pixel that shares the same location (θ_i, ε) in each one of the sixteen Mueller matrix coefficient images. For the sake of example, the M_{11} coefficient in Figure 3-9 is isolated in Figure 3-11, where one can see highlighted a set of azimuthal (Figure 3-11 (a)) and polar (Figure 3-11 (b)) angles overlapped upon the M_{11} image.

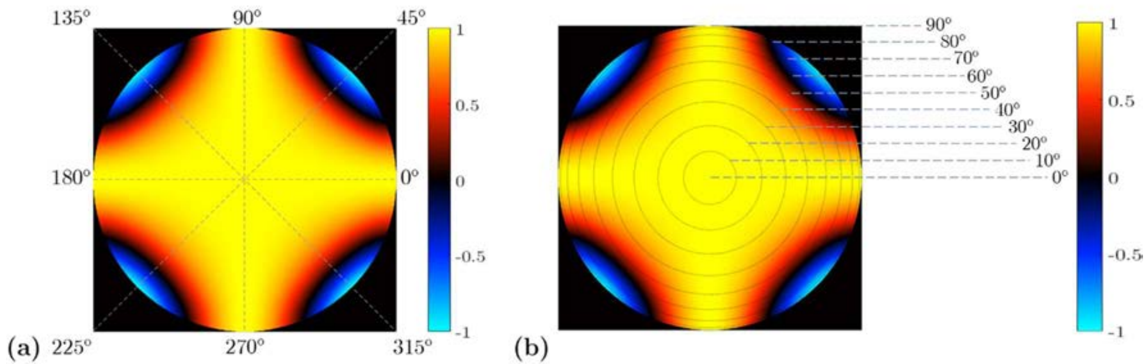

Figure 3-11. Description of the variation on the M_{11} element of the Mueller matrix image of (a) the azimuthal angle ε and, (b) the polar angle θ_i. A combination of both angles indicates the position of a single Mueller matrix.

As was described in Figure 3-6, the orthonormal $(\hat{s},\ \hat{p})$ basis spatially varies with respect to the laboratory coordinate system, for each particular incident angle. These spatial transformations make that the different elements of the Mueller matrix present cylindrical symmetry in this basis, and the dependence with the azimuthal angle ε is lost (see Figure 3-10). Notice that to obtain the refractive index comparing the elements of a theoretical and an experimental angle-resolved Mueller matrix by using data redundancy, the wide range of changes in each element of the Mueller matrix image showed in Figure 3-9 will be more interesting and will provide more information in this respect than the changes observed in Figure 3-10.

Figure 3-12 shows the variation of $(\hat{s},\ \hat{p})$ basis for different azimuthal angles, while the Cartesian $(\hat{x},\ \hat{y})$ coordinate system is fixed. The rotation of the polarization basis is responsible for rotational symmetry shown in Figure 3-10.

Considering the polarimetric measurement method explained in section 3.2.4, the experimental Mueller matrix image can be calculated from the thirty-six intensity images produced by the combination of SoPs of the PSG and the PAs of the PSA shown in Figure 3-7, when the sample is placed at the focal plane of the HNAO. In Figure 3-13, we show the simulated intensity images, corresponding to the different combinations of PSG-PSA configurations, recorded by a camera placed after the PSA, for the proposed isotropic material ($n = 1.5$). Columns are corresponding to different SoPs of the homogeneous input beam generated by the PSG. Furthermore, rows are corresponding to the projections of

the reflected beams onto the polarization analyzers of the PSA. The resulting intensity images show the dependence on the input polarizations and the angles (θ_i, ε), as well as the particular properties of the chosen isotropic sample. By using the Eq. (3.16), the thirty-six projection images shown in Figure 3-13 (that can be recorded by a camera placed after the PSA) are then reduced to sixteen Mueller matrix elements shown in Figure 3-9.

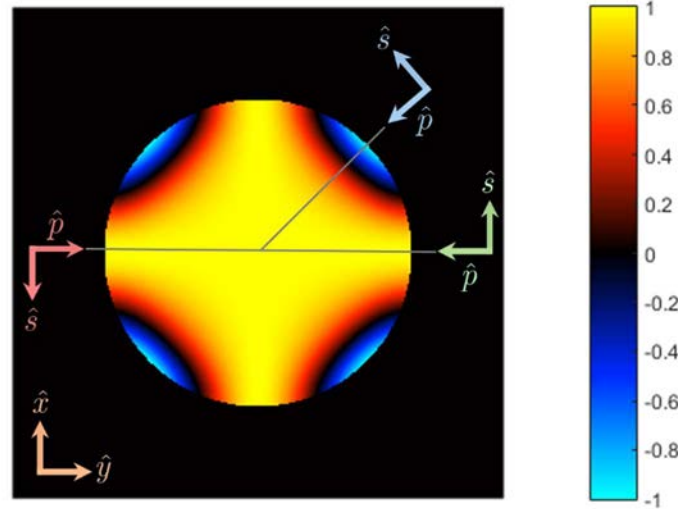

Figure 3-12. $\left(\hat{s},\ \hat{p}\right)$ coordinate system rotation for different azimuthal axis ε (green, blue and pink arrows) on the M_{11} element of the Mueller matrix image. Orange arrows show the fixed Cartesian coordinate system $\left(\hat{x},\ \hat{y}\right)$.

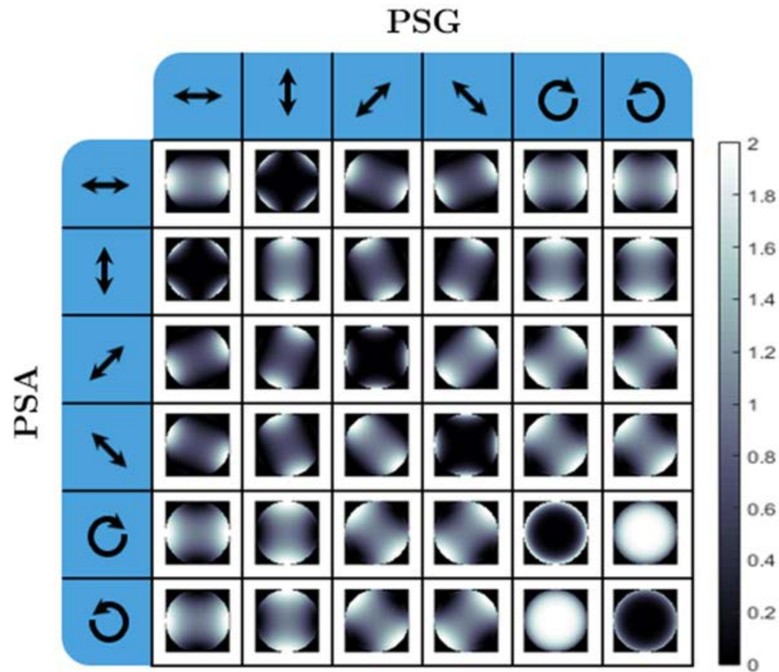

Figure 3-13. Intensity images corresponding to the thirty-six polarization projections of an isotropic sample with refractive index $n = 1.5$, $\lambda = 635\ nm$ and a maximum angle of incidence of 90°. Columns are corresponding to different SoPs generated by the polarization state generator (PSG) and rows are corresponding to the projections of the reflected beams onto the polarization state analyzer (PSA).

3.3.2 Simulated Mueller matrix images of anisotropic samples

Some simulated Mueller matrix images of a uniaxial anisotropic sample are shown in Figure 3-14 for four different orientations of the material optical axis (θ_c, ϕ_c) (see Figure 2-5). The chosen uniaxial anisotropic crystal is calcite, whose ordinary and extraordinary refractive indices for the chosen wavelength ($\lambda = 635\ nm$) are $n_o = 1.6556$ and $n_e = 1.4849$, respectively [160]. There are significant differences between the four Mueller images in Figure 3-14 (a) – (d), where the strong influence of the optical axis orientation in the angle-resolved Mueller matrix image is observed, specially in coefficients M_{01} and M_{10}.

In addition, Figure 3-14 (d) shows that when the optical axis angle θ_c is 90°, the Mueller matrix image is similar to that shown in Figure 3-9. In fact, the two image patterns are exactly the same (anisotropic and isotropic cases) when the RI of the isotropic sample is equal to the ordinary index n_o of the anisotropic sample. In other words, the uniaxial anisotropic crystal acts as an isotropic material for $\theta_c = 90°$.

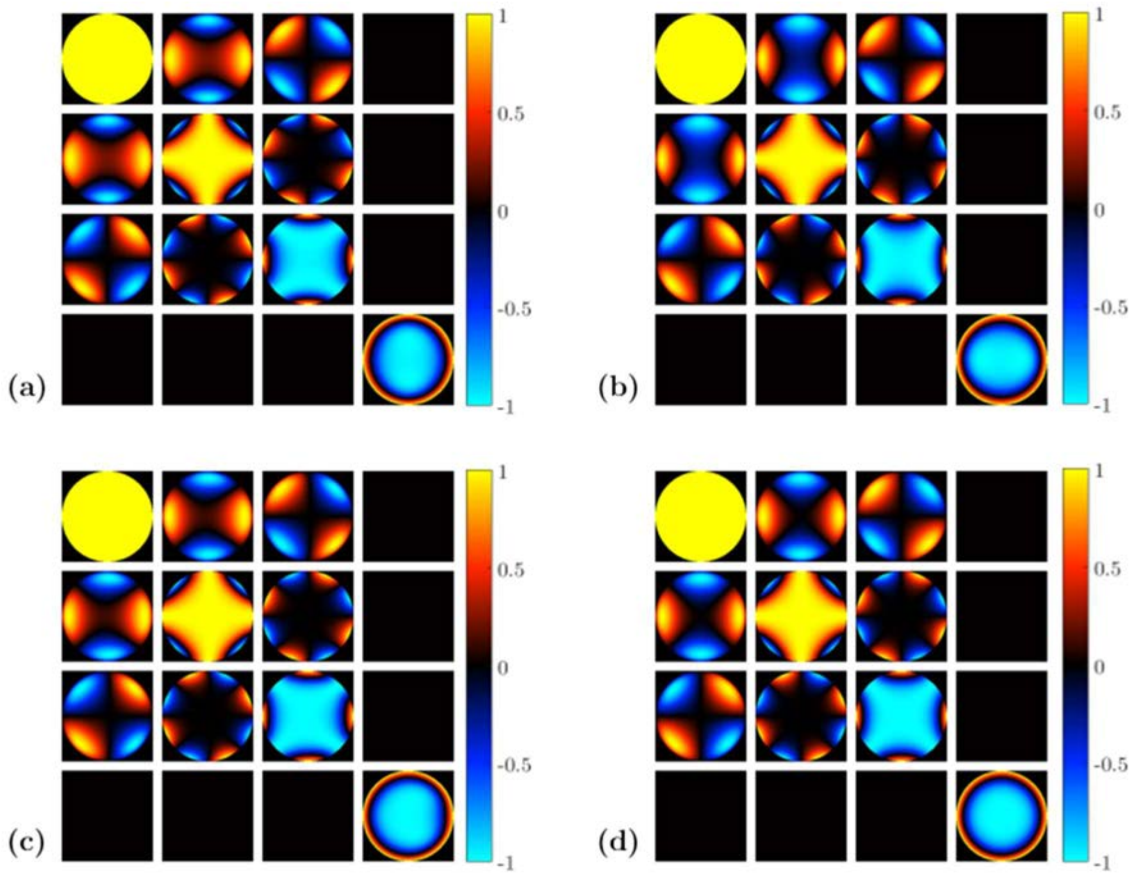

Figure 3-14. Simulated angle-resolved Mueller images of the calcite ($n_e = 1.4849$ and $n_o = 1.6556$) for four different orientations of the optical axis (θ_c, ϕ_c) (a) (0°, 0°), (b) (0°, 90°), (c) (45°, 25°); and (d) (90°, 0°).

Finally, the Mueller matrix images for the calcite, this time in the $(\hat{s},\ \hat{p})$ basis, are shown in Figure 3-15. Again, the simulations are repeated for different orientations of the uniaxial anisotropic crystal (Figure 3-15 (a)-(d)). As expected, a clear difference between Mueller matrix images represented at the detector basis (Figure 3-14) and at the $(\hat{s},\ \hat{p})$

basis (Figure 3-15) is observable. Regarding to the $(\hat{s},\ \hat{p})$ basis, a break of revolution symmetry is seen at some coefficients, at Figure 3-15 (a)-(c), being related to the optical axis orientation. By contrast, for $\theta_c = 90°$ (Figure 3-15 (d)), there is no variation with the azimuthal angle ε. This last result is in agreement with the fact that a uniaxial anisotropic material acts as an isotropic material for $\theta_c = 90°$.

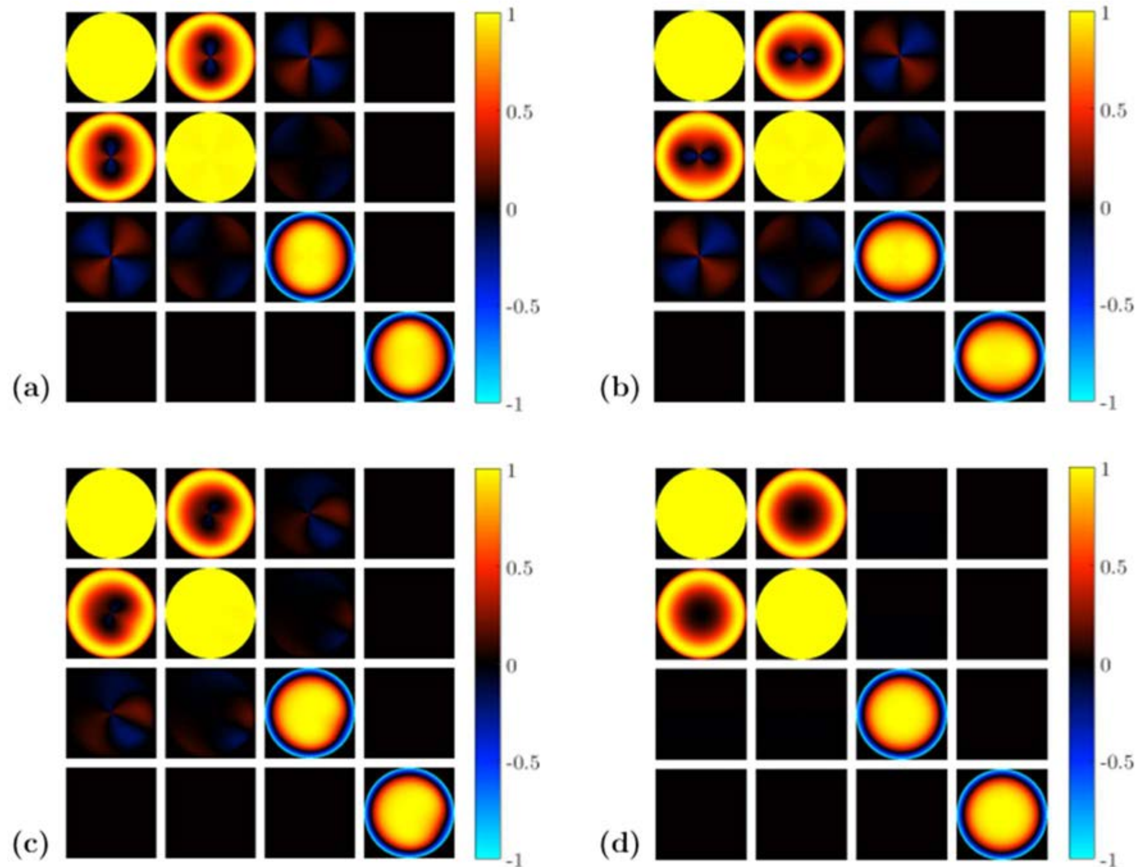

Figure 3-15. Angle-resolved Mueller matrices for the calcite in the orthonormal $(\hat{s},\ \hat{p})$ axis for the angles of the optical axis (θ_c, ϕ_c) equal to (a) (0°, 0°), (b) (0°, 90°), (c) (45°, 25°); and (d) (90°, 0°). The birefringence breaks the rotational symmetries for angles θ_c different than 90°.

3.4 Polarimetric sensitivity

To estimate the influence of some physical parameters in the polarimetric sensitivity of the designed conoscopic Mueller microscope, some parameters of interest are studied in this sub-section. For example, we analyzed the dependence of the angle-resolved Mueller matrices on the selected range of angles of incidence (i.e., on the selected maximum incident angle) or on the refractive indices.

3.4.1 Maximum angle of incidence

By analyzing the simulations shown in Figure 3-9 and Figure 3-14, we see how the Mueller matrix coefficients maintain quite constant values for small angles of incidence, θ_i, whereas larger polarimetric variations are observed as we increase the incident angle (i.e., larger polarimetric variations are observed at the edges of the images). In order to study the importance of the maximum angle of incidence, four simulations of Mueller matrix images for the isotropic material presented in section 3.3.1, i.e., $n = 1.5$, are shown in Figure 3-16. We have simulated an isotropic material to only analyze the effect of the incident angle, and to avoid other physical parameters also introducing spatial variations of the Mueller coefficients, such as the position of the optical axis or the birefringence. The chosen maximum angles of incidence are $\theta_{i,\max} = 30^{\circ}$, 50°, 70°, 90°.

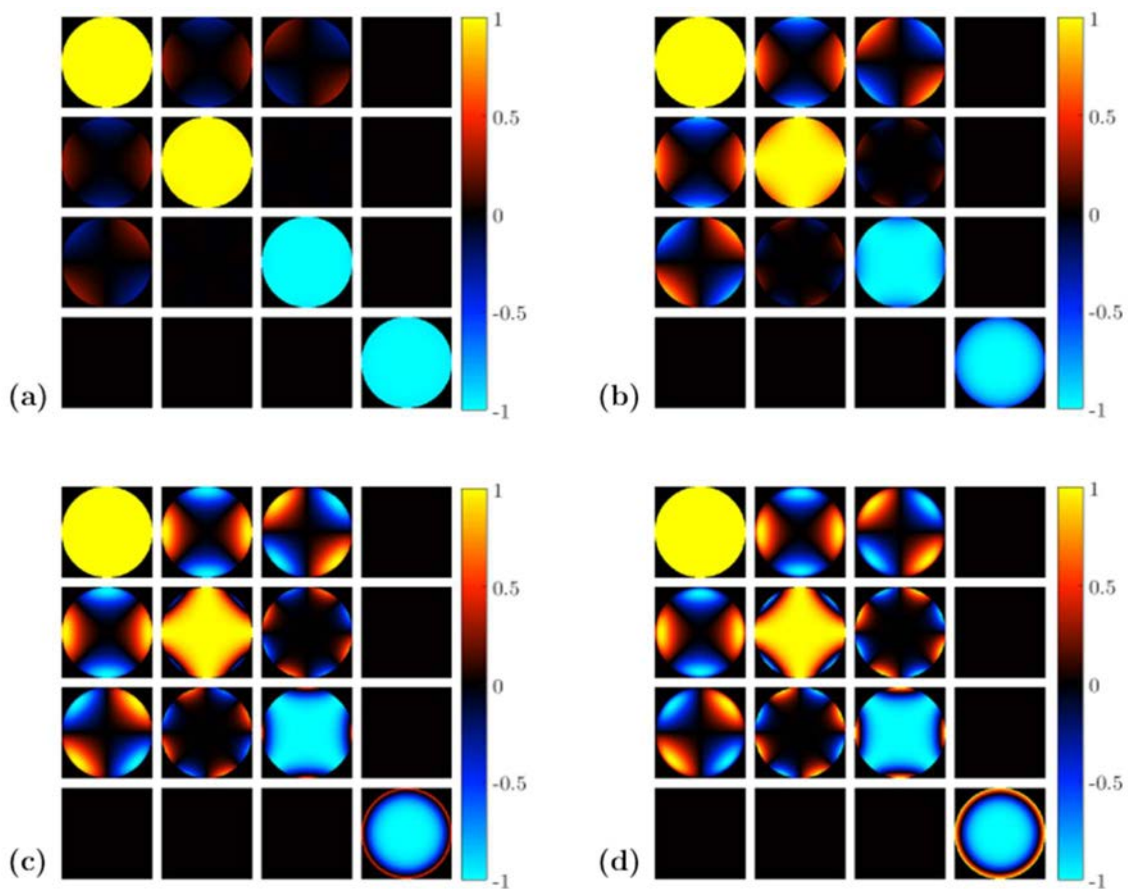

Figure 3-16. Four simulated Mueller matrix images for an isotropic sample with a refractive index of $n = 1.5$, when the maximum angle of incidence is: (a) $\theta_{i,\max} = 30^{\circ}$, (b) $\theta_{i,\max} = 50^{\circ}$, (c) $\theta_{i,\max} = 70^{\circ}$; and (d) $\theta_{i,\max} = 90^{\circ}$. The normalized Mueller matrix images are expressed in the detection coordinate system.

From Figure 3-16 (a), where $\theta_{i,\max} = 30^{\circ}$, i.e., the used microscope objective would be a low numerical aperture system, one can observe that the diagonal components of the Mueller matrix image are practically constant. The only coefficients showing spatial polarimetric variations are the coefficients $M_{0,1}$, $M_{0,2}$, $M_{1,0}$ and $M_{2,0}$, showing small polarimetric variations which are especially located at the edges of the images. All the

other elements are approximately zero. As shown in Figure 3-16 (b)-(d), to obtain larger polarimetric sensitivity in the system, i.e., to obtain larger variations of the Mueller matrices coefficients, it is interesting to work with microscope objectives that have larger numerical apertures. Indeed, higher NA values allow larger $\theta_{i,\max}$. The wider the incidence and reflected angles, the larger the polarization changes between pixels are observed, as polarimetric differences between $\hat{s}$ and $\hat{p}$ Fresnel coefficients are maximized for larger incident angles (the maximum polarimetric sensitivity is usually obtained close to the Brewster angle). This fact is qualitatively seen in Figure 3-16. As a result, higher numerical apertures are recommended to increase the polarimetric sensitivity of the polarimeter, fact that will be crucial to obtain the parameters of interest from theoretical-experimental fitting procedures.

The dependence of the polarimetric response across the pupil of the Mueller matrix images with the angle of incidence was also quantitatively studied from cross-sections set along those Mueller coefficients images showing larger variations. To this end, cross-sections along three directions were taken to compare the variations between some Mueller matrix elements observed in Figure 3-16. The three cross-sections pass through the center of the images. One of them is taken parallel to the $\hat{x}$-axis, another to the $\hat{y}$-axis (see Figure 3-12), and the last one is parallel to the diagonal (from the top-left to the bottom-right corners) of each element of Mueller matrix images. The obtained results for the $\hat{y}$, $\hat{x}$, and diagonal cross-sections are provided in Figure 3-17 (a)-(c), respectively. In each case, the coefficients cross-sections were obtained for different $\theta_{i,\max}$, being represented as different colors in Figure 3-17.

By analyzing the resulting plots, one can observe that the greater the maximum angle of incidence, the larger variations observed for the Mueller matrices values in the cross-sections. The cross-section values for an incident angle of $\theta_{i,\max} = 30^{\circ}$ (blue lines) are practically constant, while for greater maximum angles of incidence ($\theta_{i,\max} = 50^{\circ}$ (red lines), $\theta_{i,\max} = 70^{\circ}$ (yellow lines) and $\theta_{i,\max} = 90^{\circ}$ (violet lines)), the variations of the cross-sections significantly increase. In addition, for $\theta_{i,\max} > 50^{\circ}$, one can clearly see that the Mueller matrix coefficients sharply variate as we are getting close to the Brewster angle of the material.

The conclusions reached here for the isotropic samples case, are general and can be extended to uniaxial anisotropic crystals. Consequently, characterization of uniaxial anisotropic or isotropic samples by using a conoscopic Mueller microscope requires high numerical aperture objectives that increase the polarimetric sensitivity of the system.

3.4.2 Refractive indices

The second parameter to be analyzed is the refractive index. In this subsection, we study the dependence of the Mueller matrix images coefficients with variations on the RI. To this end, Mueller matrix images of some samples are simulated.

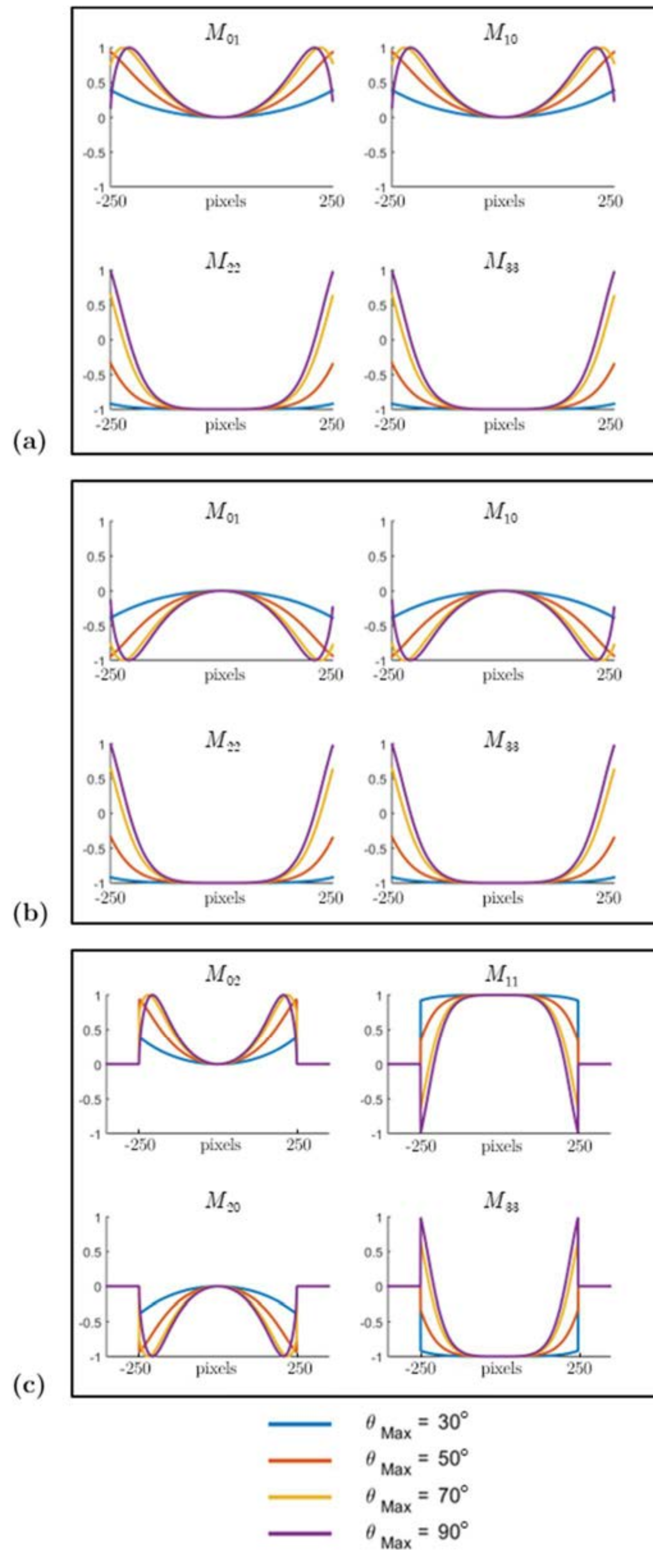

Figure 3-17. Intensity pixels-cross-sections obtained from some of the Mueller matrix coefficient images shown in Figure 3-16. The cross-sections are: (a) parallel to the $\hat{y}$ -axis, (b) parallel to the $\hat{x}$ -axis; and (c) in the diagonal direction (decreasing sense). All the three cross-sections pass through the center (pixel (0,0)) in the Mueller matrix images. The maximum angles of incidence are $\theta_{i,\max} = 30^{\circ}$ (blue line), $\theta_{i,\max} = 50^{\circ}$ (red line), $\theta_{i,\max} = 70^{\circ}$ (yellow line); and $\theta_{i,\max} = 90^{\circ}$ (violet line).

3.4.2.2 Isotropic samples

Let us start by analyzing four isotropic samples with different refractive indices. In order to make the simulations more realistic, we chose four materials that exist in nature. Figure 3-18 shows the Mueller matrix images of distilled water ($n = 1.331$), halite ($n = 1.5415$), cubic zirconia ($n = 2.1514$) and diamond ($n = 2.4104$) for a wavelength $\lambda = 635\ nm$ and a maximum incident angle $\theta_{i,\max} = 90^{\circ}$ [160, 161]. The four materials were chosen because their refractive indices allow us to test a wide range of RI values, and thus, it is fairly easy to qualitatively exemplify significant differences between their Mueller matrix images. Visual differences are observed in Figure 3-18 (a)-(d), as for instance in coefficients M_{11} and M_{22}.

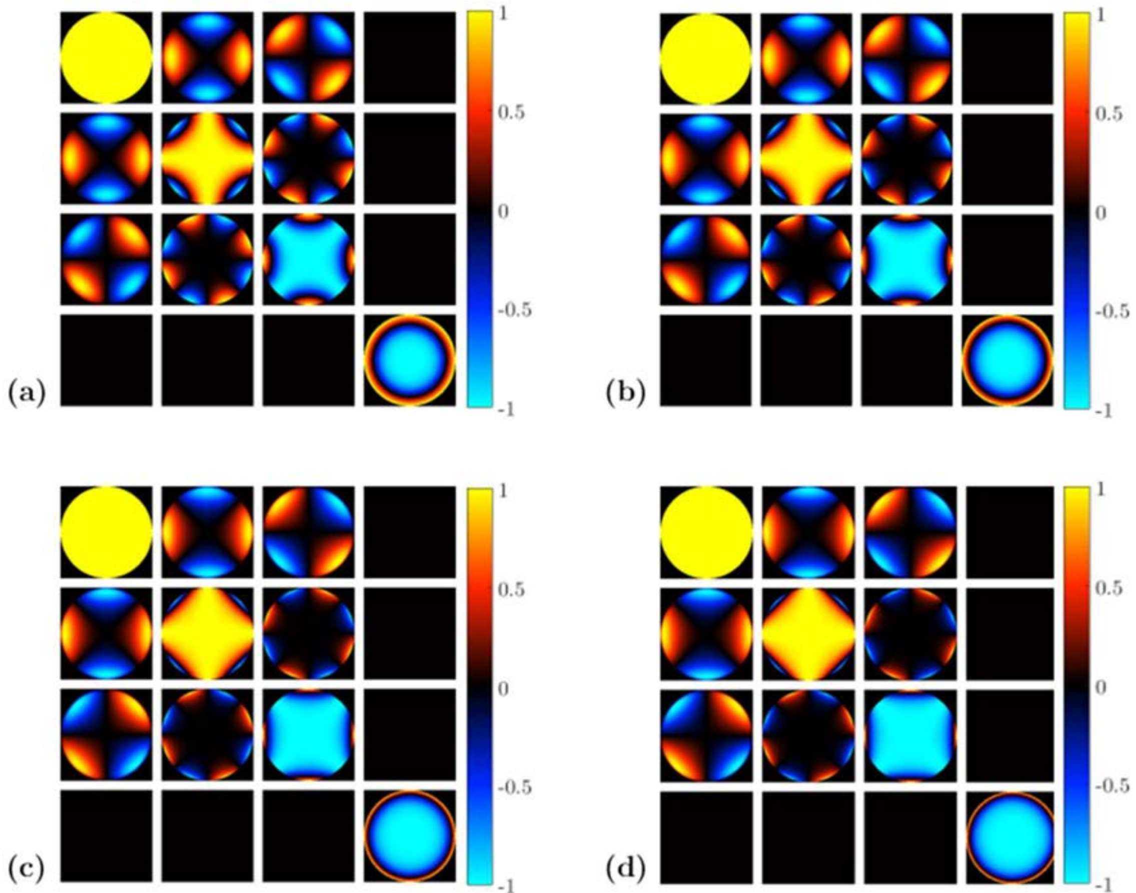

Figure 3-18. Mueller matrix images for different isotropic materials: (a) distilled water ($n = 1.331$), (b) halite ($n = 1.5415$), (c) cubic zirconia ($n = 2.1514$); and (d) diamond ($n = 2.4104$) for a maximum angle of incidence $\theta_{i,\max} = 90^{\circ}$.

Once again, to obtain the same information form a quantitative point of view, three intensity cross-sections, parallel to the $\hat{x}$ -axis, to the $\hat{y}$ -axis (both directions are represented in Figure 3-12) and to the diagonal direction, all of them passing through the center of the images, were obtained for the same four Mueller matrix elements previously selected in the isotropic case (see Figure 3-18). The resulting cross-sections for the different materials (different colors) are overlapped and shown in Figure 3-19, for the $\hat{y}$, $\hat{x}$ and diagonal cases (Figure 3-19 (a) - (c), respectively). In all the cases, the incident angle was

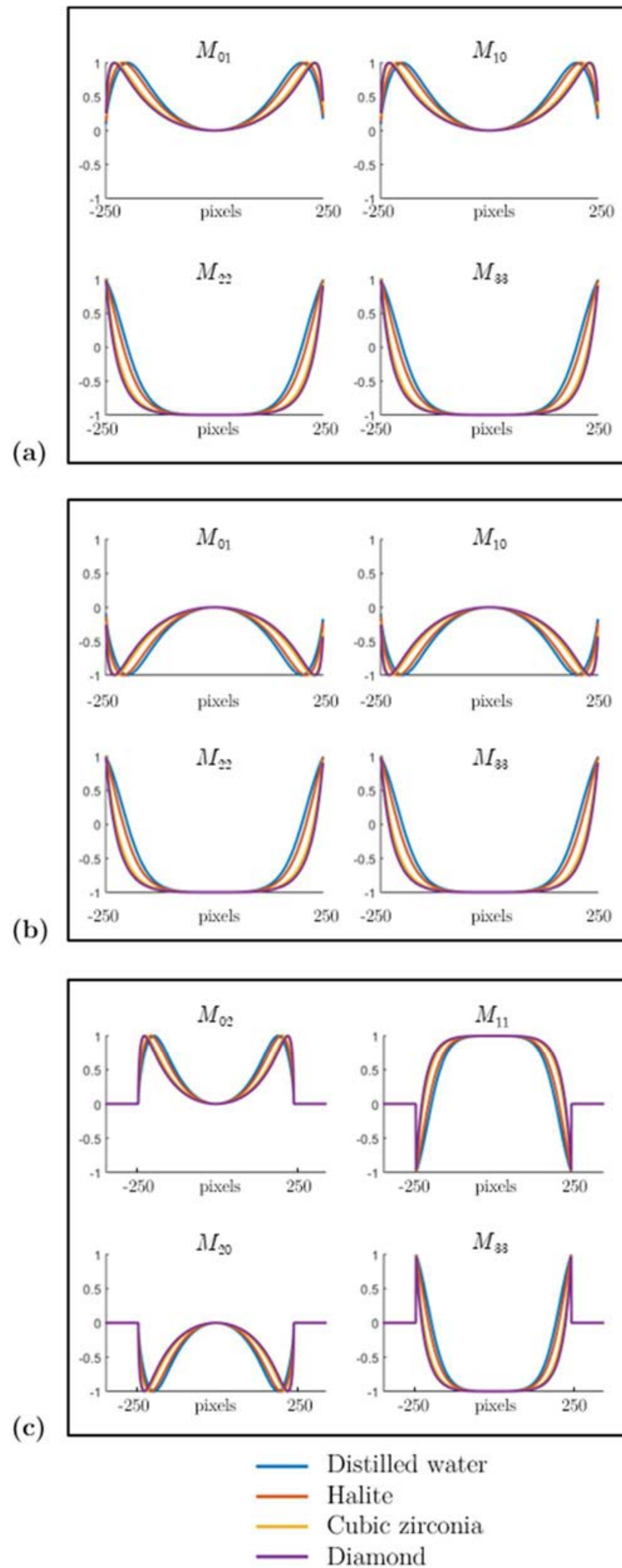

Figure 3-19. Cross-sections of four elements of the Mueller matrix images shown in Figure 3-18. The cross-sections are: (a) parallel to the $\hat{y}$-axis, (b) parallel to the $\hat{x}$-axis; and (c) in the diagonal (from the top-left to the bottom-right corners). All the selected cross-sections pass through the center of the Mueller matrix images. The simulated samples are distilled water ($n = 1.331$), halite ($n = 1.5415$), cubic zirconia ($n = 2.1514$) ; and diamond ($n = 2.4104$).

fixed to a value of $\theta_{i,\max} = 90^o$. The dependence of the Mueller matrix images polarimetric response with the refractive indices is verified and clearly observed.

From the cross-sections shown in Figure 3-19, we see significant variations between the different color curves, describing the performance of different materials. These variations indicate that the system provides enough polarimetric sensitivity to differentiate between different RIs. In the same way, in section 3.4.1, we observed that the larger polarimetricsensitivity occurred for higher incident angles. This fact states that the regions of greater interest for measuring the sample optical characteristics are those where the angles of incidence are higher. For the purpose of measuring the refractive indices of isotropic samples, microscope objectives with high NA are needed. In a further section 3.6, the accuracy of the method to measure the characteristic parameters of samples is described.

3.4.2.3 Uniaxial anisotropic crystals

Let us study the influence of the ordinary and extraordinary refractive indices in the response of the Mueller matrix coefficient images. In this case, four uniaxial anisotropic crystals oriented at $(\theta_c, \phi_c) = (0^o, 0^o)$ have been simulated. The chosen samples are quartz ($n_o = 1.544$, $n_e = 1.553$), tourmaline ($n_o = 1.669$, $n_e = 1.638$), calcite or “Iceland Spar” ($n_o = 1.658$, $n_e = 1.486$) and rutile ($n_o = 2.616$, $n_e = 2.903$) for a wavelength $\lambda = 590\ nm$ and a maximum angle of incidence $\theta_{i,\max} = 90^o$ [160–162]. Their respective Mueller matrix images are shown in Figure 3-20, revealing qualitative differences between them. The polarimetric differences between the chosen birefringent materials (different colors) in four different Mueller coefficients are quantitatively compared in the cross-sections shown in Figure 3-21 (a) - (c) ($\hat{y}$, $\hat{x}$ and diagonal directions respectively).

We observe how different coefficients provide different polarimetric sensitivity at different incident angle regions. In the $\hat{x}$- and $\hat{y}$-axes cross-sections at the M_{01} and M_{10} coefficients, one can see that for small angles of incidence, the Mueller matrices values of these two coefficients are not nulls and show differences between different materials (this giving certain polarimetric sensitivity to the refractive index). This polarimetric response for small angles of incidence is contrary to the observations realized in the isotropic case (see Figure 3-19). Therefore, unlike isotropic materials, birefringent materials have some impact in the linear diattenuation and polarizance of the system (see M_{01} and M_{10} coefficients in Figure 3-21) for small incident angles, and this information can be valuable to retrieve the orientation and the RIs of anisotropic samples.

In addition, one can see that a conoscopic Mueller microscope can be used, not only to measure a uniaxial anisotropic crystal having high birefringence, but also small differences between n_e and n_e. An example can be seen in Figure 3-21 (b) where the cross-sections of quartz and tourmaline, both uniaxial anisotropic crystals, are totally different and clearly appreciated, even when the difference between their birefringence is around 0.02, $\left|n_e - n_o\right|^{\text{quartz}} < 0.01$ and $\left|n_e - n_o\right|^{\text{tourmaline}} \simeq 0.03$.

Although the birefringence of a crystal, unlike the isotropic case, is sensitive to small angles of incidence, certain polarimetric sensitivity is also present at high angles of incidence. Therefore, a wide angular spectrum is recommended to characterize anisotropic materials.

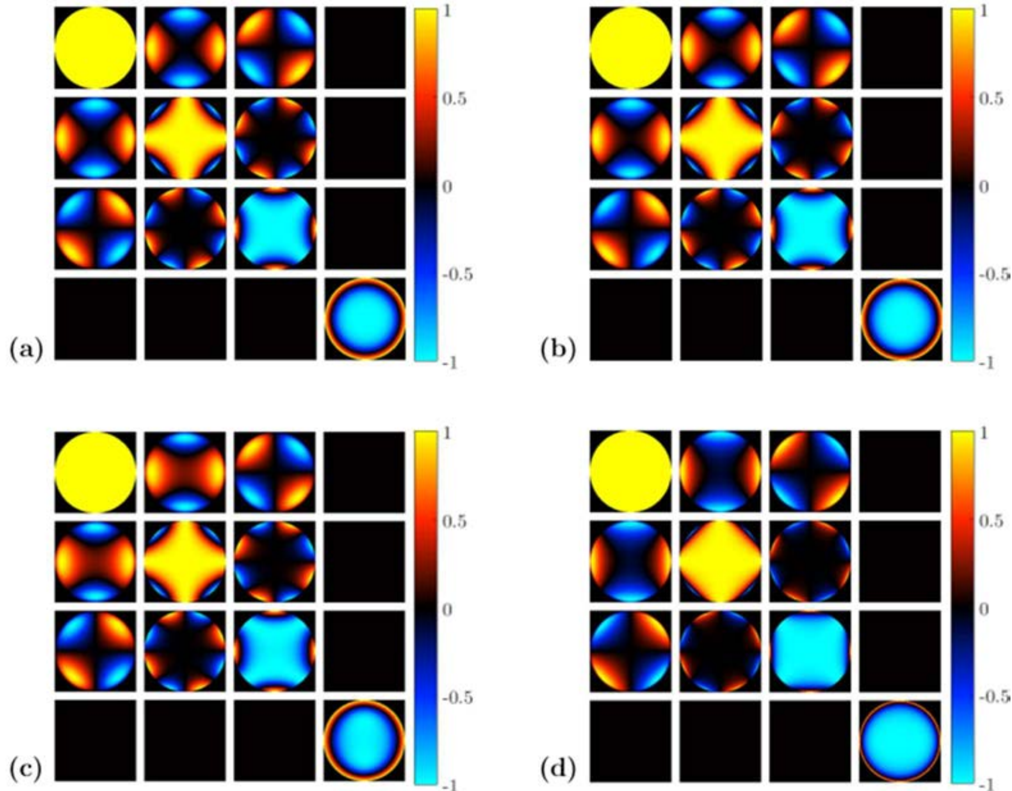

Figure 3-20. Mueller matrix images for different anisotropic materials: (a) quartz (n_o = 1.544, n_e = 1.553), (b) tourmaline (n_o = 1.669, n_e = 1.638), (c) calcite (n_o = 1.658, n_e = 1.486) ; and (d) rutile (n_o = 2.616, n_e = 2.903) for a wavelength $\lambda = 590$ nm and a maximum angle of incidence $\theta_{i,\max} = 90^o$. The optical axis orientations are $(\theta_c, \phi_c) = (0^o, 0^o)$ in all cases.

3.5 Constrained variational analysis method to obtain the optical parameters

So far, we clearly demonstrated that a conoscopic Mueller microscope, equipped with a high numerical aperture objective, can be used to measure the characteristic angle-resolved Mueller matrix of any isotropic and uniaxial anisotropic samples. We corroborated through some MATLAB simulations that various refractive indices and orientations of different samples generate different Mueller matrix images, this allowing us to discriminate between different materials. At this stage, an analysis method has to be developed in order to obtain the desired parameters comparing experimental and theoretical Mueller matrix images. In this case, we have used a constrained nonlinear optimization algorithm implemented in MATLAB.

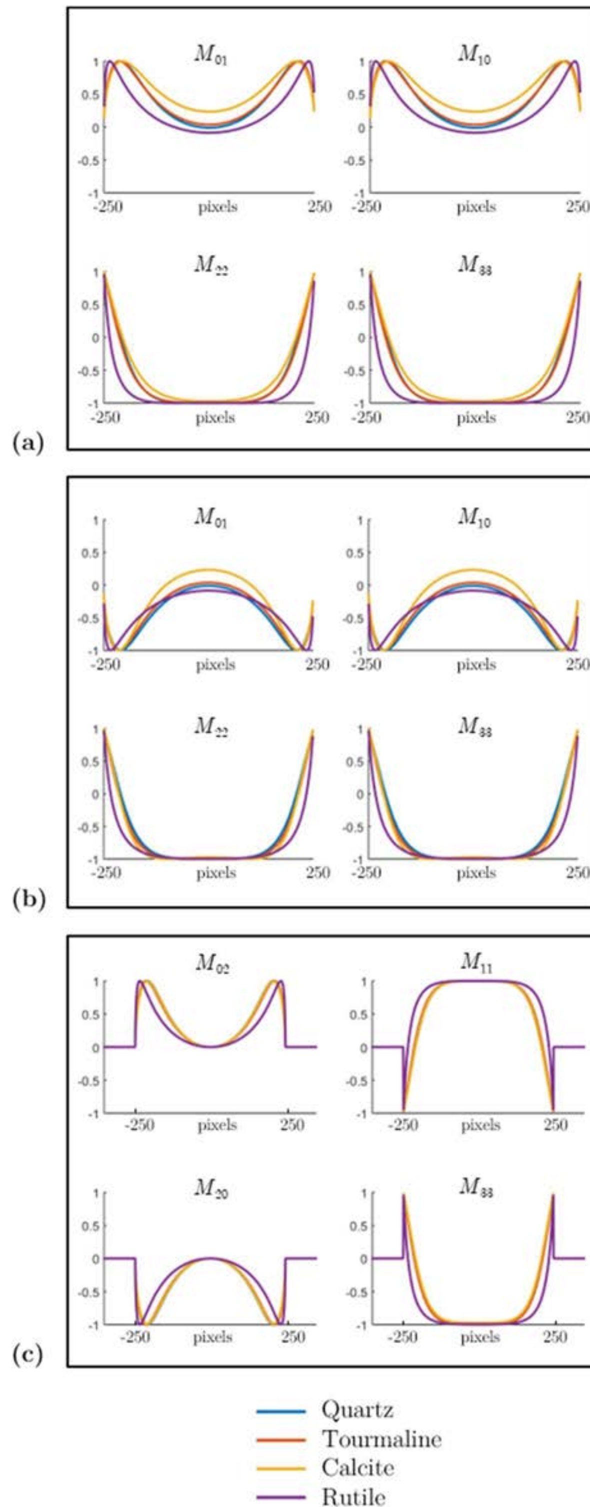

Figure 3-21. Horizontal, vertical and diagonal cross-sections of four different elements in the Mueller matrix images shown in Figure 3-20, for different anisotropic materials: quartz (blue lines), tourmaline (red lines), calcite (yellow lines) and rutile (violet lines). In all the cases, the optical axis orientation is set to $(\theta_c, \phi_c) = (0^{\circ}, 0^{\circ})$ and the maximum incident angle is fixed to $\theta_{i,\max} = 90^{\circ}$. The cross-sections are passing through the center of each element of the Mueller matrix images and they are: (a) parallel to the $\hat{y}$ -axis, (b) parallel to the $\hat{x}$ - axis; and (c) in the diagonal direction.

The following steps describe the process for determining the refractive indices of samples, and the orientation of their optical axis:

1) To measure the experimental angular-resolved Mueller matrix of the sample by using the conoscopic Mueller microscope with a HNAO.

2) To estimate the model physical parameters (refractive index/indices and optical axis orientation) from previous knowledge of the sample, to simulate an initial theoretical Mueller matrix image in reflection, and to set of lower and upper bounds on the unknown variables.

3) To calculate the Mean Squared Error (*MSE*) between predicted and experimental Mueller matrix images. In Eq. (3.1) the Mean Squared Error is given for an angle of incidence. The *MSE* for the whole image is given by

$$MSE = \frac{1}{16N}\sum_{i}^{N}\sum_{j,k=0}^{4}\left(\frac{M_{j,k}^{\exp,i}}{M_{0,0}^{\exp,i}} - \frac{M_{j,k}^{\mathrm{pred},i}}{M_{0,0}^{\mathrm{pred},i}}\right)^2 \tag{3.18}$$

where N is the number of pixels and i is the evaluated pixel of the experimental and predicted single Mueller matrices. The actual refractive indices and the orientation of the optical axis values are those providing the *MSE* value as small as possible. Note that the large redundancy data given by N, helps the *MSE* based calculations to fall at the correct sample parameters.

4) To use a constrained nonlinear optimization algorithm that attempts to find a local minimum of the *MSE* function by comparing the experimental angle-resolved Mueller matrix with different predicted images. The value of the characteristic parameters of the simulated sample is subjected to the upper and lower constraints described in the step 2).

5) To set an iterate process to determinate the desired parameters of the sample using the new simulated Mueller matrix as the next input to the optimization routine to be compared to the experimental Mueller matrix image. When the step size factor of the iteration is smaller than a value we decided, the optical parameters of the sample are found.

While the refractive indices and the orientations of $\hat{C}$ are the desired parameters, and therefore, the goal of this thesis, other experimental constraints need to be considered in this optimization process. If the camera is not centered and/or the sample is slightly out of focus, the resulting Mueller matrix image obtained in the laboratory will suffer some variations from the theoretical expected ones (i.e., the image would no longer be centered, and thus, the angles of incidence and the azimuthal angles will be modified). In addition, the maximum angle of incidence varies as a function of the entrance pupil size illuminated by the incident beam. For these reasons, the value of the maximum angle of incidence $\theta_{i,\max}$, a certain shift in the center of the image (x_0, y_0) and an initial azimuthal rotation offset (ε_0) have to be introduced as variables in the optimization process.

Figure 3-22 (a) shows and example of the Mueller matrix image of an isotropic sample that is shifted and rotated. The simulated sample parameters are the same shown in Figure 3-9 (n = 1.5, $\theta_{i,\max} = 90^{\circ}$, λ = 635 *nm*), but now we introduce an initial center shift (x_0, y_0) = (20, -20) *pixels* and azimuthal rotation ($\varepsilon_0 = 15^{\circ}$). The resulting Mueller coefficients images in Figure 3-22 (a) are thus, shifted and rotated with respect to images in Figure 3-9. For instance, it is easily seen that the incident angle $\theta_{i,\max} = 0^{\circ}$ is no longer at the center of the images but shifted, and the axis $\varepsilon = 0^{\circ}$ is not parallel to the $\hat{x}$-axis but rotated (see the new angular representations given in (Figure 3-22 (b) and (c)), to be compared with Figure 3-8).

The optimization algorithm was implemented in MATLAB considering all the parameters that can affect the resulting Mueller matrix images, (x_0, y_0), ε_0, $\theta_{i,\max}$, θ_c, ϕ_c, n_e and n_o.

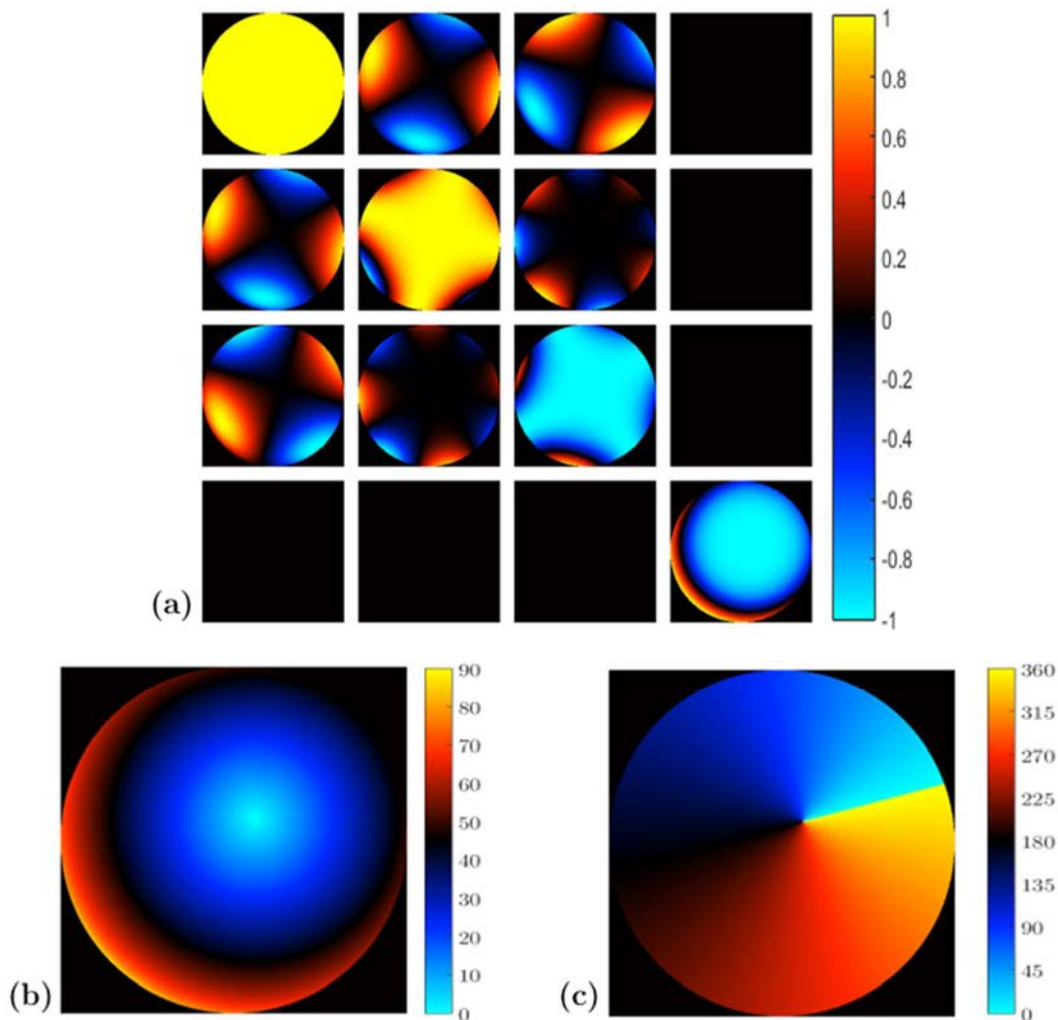

Figure 3-22. (a) Simulation of the Mueller matrix image of an isotropic sample (n = 1.5) when the observation plane is shifted (x_0, y_0) = (20, -20) *pixels* and rotated $\varepsilon_0 = 15^{\circ}$. Representation of (b) the off-centered angle of incidence or polar angle and, (c) the off-centered azimuthal angle rotated 15°.

3.6 Accuracy of the optimization program

Before calculating the refractive indices and the orientation of the optical axis from an experimental Mueller matrix image, the iterative algorithm has been validated by calculating the optical parameters of some artificial angle-resolved Mueller matrices we generated with our developed software. These images are the best approach to test our optimization program, as they simulate experimental images measured in the laboratory.

In order to study a realistic situation, we have simulated Mueller matrix images of real materials. In this subsection, just two examples are shown, BK7 optical glass as isotropic material (n = 1.5150) for λ = 635 *nm* [160] and calcite as uniaxial anisotropic crystal (n_o = 1.658, n_e = 1.486) for λ = 590 *nm*. In addition, other parameters have been considered such as: air (n_i = 1) was selected as the medium between the sample under study and the objective front lens, the chosen *NA* of the microscope objective was 0.90 (giving a maximum angle of incidence of $\theta_{i,\max} \sim 64^{o}$), the number of pixels of the images were N = (500×500) *pixels* and the simulated images were shifted (x_0, y_0) = (5, 3) *pixels* and rotated $\varepsilon_0 = 5°$.

Constrains (upper and lower value limits) and initial parameters used to generate an initial Mueller matrix, from which starting the searching routine (see step 2 in section 3.5), are given in the Table 3-1. The set of lower and upper bounds on the unknown variables was selected to be large to demonstrate that a completely unknown experimental sample could still be measured by using this method. The large amount of data of a Mueller matrix image reduces the correlation between the variables.

Parameters	**Initial parameters**	**Constrained parameters**
x_0	0	$-100 \rightarrow 100$
y_0	0	$-100 \rightarrow 100$
ε_0	0°	$-15° \rightarrow 15°$
$\theta_{i,\max}$	50°	$30° \rightarrow 70°$
n_o	1.6	$1.3 \rightarrow 3$
n_e	1.6	$1.3 \rightarrow 3$
θ_c	10°	$0° \rightarrow 90°$
ϕ_c	10°	$0° \rightarrow 90°$

Table 3-1. Initial parameters and set of lower and upper constrains used in the iterative routine for the calculus of the best-fit optical parameters.

The difference between the theoretical values and the best-fit results for BK7 optical glass (isotropic sample) and for calcite (anisotropic sample) are very small. In the same way, the resulting *MSE* obtained with the iterative routine for both simulated materials is

also small ($MSE \sim 7.5 \cdot 10^{-7}$). Therefore, the optimization program is able to find good best fit parameters.

In addition, the Squared Absolute Error (SAE), i.e., the square of the difference between the simulated (from best-fit values) and synthetized parameters can be used to analyze the accuracy of the iterative program. The refractive indices SAE ($(n_{\text{fit}} - n_{\text{theo}})^2$) of the BK7 optical glass is very small ($1 \cdot 10^{-16}$), where n_{theo} is the RI used to simulate the Mueller matrix image and n_{fit} is the obtained best-fit refractive index. Thus, we have obtained an excellent agreement between the synthetized BK7 optical glass and the physical parameters provided by the searching algorithm. In Figure 3-23 (a) and (b), we can observe the simulated Mueller matrix image and the squared absolute error image between the synthetized and the best-fit Mueller matrix images, respectively. In this sense, the SAE between pixels of the simulated and best-fit images (Figure 3-23 (b)) is smaller than $1 \cdot 10^{-15}$, showing that the optimization program can find the desired values with high accuracy. We can remark that the optimization output gives equal ordinary and extraordinary refractive indices for BK7 glass, which means that the iterative program can differentiate between isotropic and uniaxial anisotropic samples even if we do not consider this constrain. The optimization routine also provides the position of the non-existent optical axis for isotropic materials which have not physical sense and can be neglected.

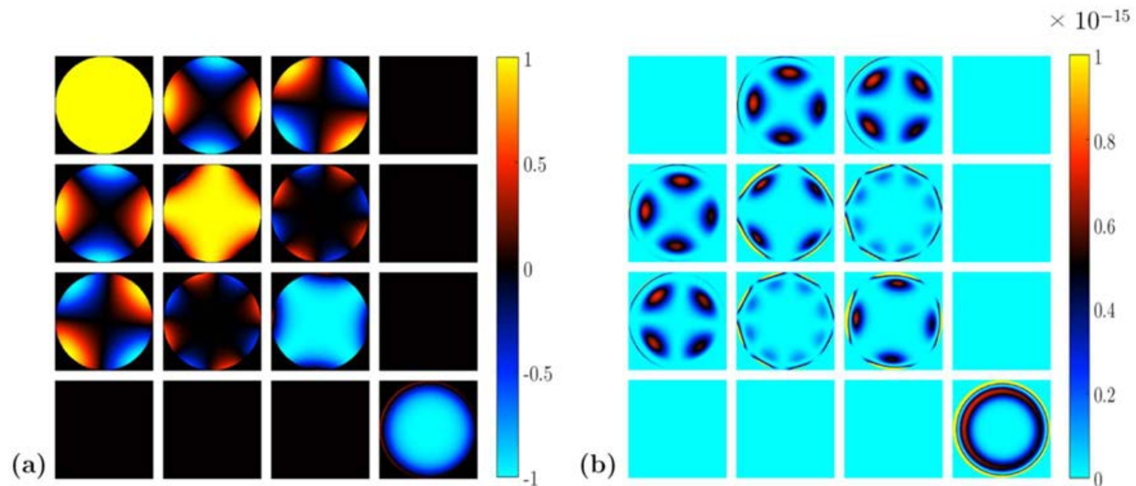

Figure 3-23. (a) Simulated Mueller matrix image of BK7 glass (isotropic material, with $n = 1.5150$ and $\lambda = 635$ nm) and, (b) Squared absolute error image between the synthetized and the best-fit Mueller matrix images.

On the other hand, we also tested the uniaxial anisotropic case. To this aim, we chose calcite as example of a common birefringent material, and the method also provided excellent results. In fact, the errors between the synthetized calcite parameters and the obtained best-fit ones are very small. In particular, the SAE error for the ordinary and extraordinary axes is smaller than $2.5 \cdot 10^{-11}$ and $1.6 \cdot 10^{-11}$, respectively. In the case of the optical axis orientation, the SAE error is smaller than $3.5 \cdot 10^{-10}$ for both angles, ϕ_c and θ_c. Figure 3-24 (a) shows the synthetized Mueller matrix, while in Figure 3-24 (b), we can observe the SAE between simulated and best-fit Mueller matrices. As in the isotropic example, the SAE value between respective pixels is smaller than $1 \cdot 10^{14}$, showing that the

optimization program can find the RIs and the position of the optical axis with high accuracy.

Although the eight unknown model parameters ((x_0, y_0), ε_0, $\theta_{i,\max}$, θ_c, ϕ_c, n_e and n_o) in the optimization process give the values with a very small error for the synthetized materials, any reduction in the number of parameters to be considered in the model and/or upper and lower constraints closer to the real ones (from previous knowledge of the sample), lead to major computational savings and should result in more accurate values for the refractive indices and optical axis orientations.

Once it has been corroborated that the optimization program can measure an isotropic and a uniaxial anisotropic sample, the accuracy of the method is studied.

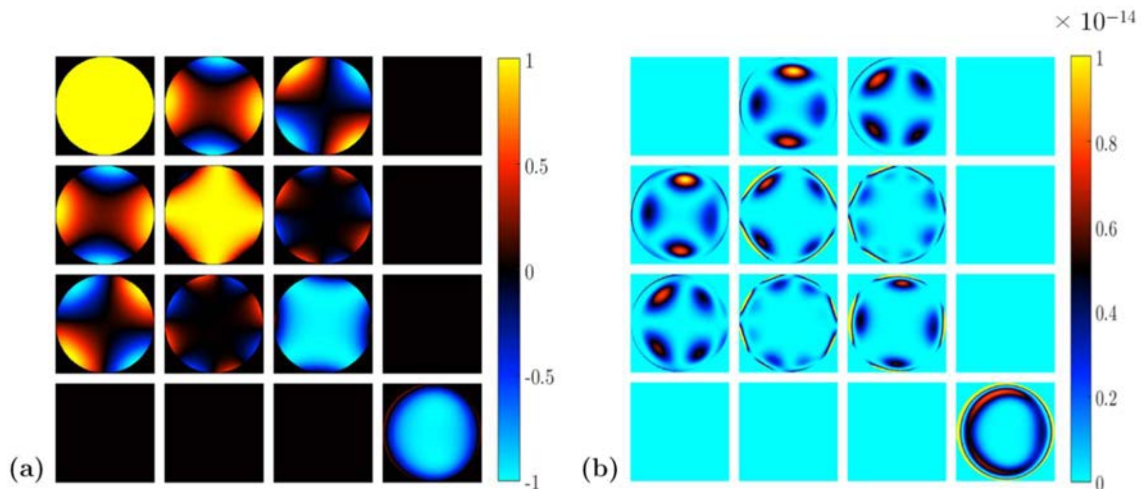

Figure 3-24. (a) Simulated Mueller matrix image of calcite (uniaxial anisotropic crystal, with $n_o = 1.658$, $n_e = 1.486$) and $\lambda = 590\ nm$). (b) Squared absolute error image between the synthetized and the best-fit Mueller matrix images.

3.6.1 Accuracy as a function of the maximum angle of incidence

First, we have studied the influence of the maximum angle of incidence on the determination of refractive indices and crystal orientation. In particular, we have tested the accuracy of the method by synthetizing different materials sharing the same parameters with the exception of the maximum angle of incidence. Note that this accuracy is studied under the presence of artificial rotations and shifts, to simulate experimental misalignments.

Following the previous subsection, we have decided to use the same isotropic and uniaxial anisotropic samples (under the same (x_0, y_0, ε_0) conditions). In this sense, to analyze the accuracy of the optimization routine as a function of $\theta_{i,\max}$, a sampling of eleven Mueller matrix images with a maximum angle of incidence between 40° and 90°, were synthetized. Then, their parameters were found by using the iterative optimization program described in section 3.5. For each incident angle selected, the iterative routine calculates 10 times the optical parameters of the corresponding synthetized angle-resolved

Mueller matrix by slightly changing the starting parameters. This allows us to study the influence of the starting parameters in the best-fit results by calculating the corresponding standard deviations. A flow chart showing the followed steps can be seen in Figure 3-25.

Isotropic samples

Let us consider BK7 glass ($n = 1.5150$ for $\lambda = 635\ nm$ [160]) as isotropic material under study. We have decided to use this isotropic glass because its refractive index is close to the RI of a typical optical material used in laboratories.

By using the optimization program and following the process explained in the flow chart in Figure 3-25, the minimum *MSE* is calculated between the artificial-experimental ($\mathbf{M}_{\text{artificial-exp}}$) and the best-estimated ($\mathbf{M}_{\text{best-estimated}}$) Mueller matrix images, for the eleven maximum angles of incidence evaluated.

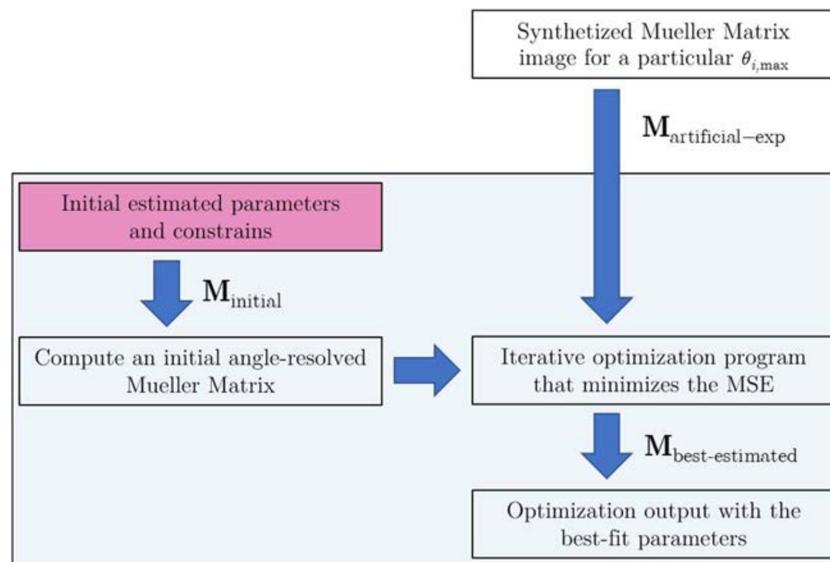

Figure 3-25. Flow chart showing the steps followed by the searching routine. For each one of the eleven synthetized Mueller matrix images (related to different incident angles), the initial parameters (pink box) are modified 10 times, calculating, each time, the best-fit parameters (blue box) and the associated error bars (standard deviations).

The obtained values are shown in Figure 3-26 (a). On the other hand, the absolute errors between the RIs set for the artificial sample and the calculated best-fit refractive indices, n_{theo} and n_{fit} , are represented in Figure 3-26 (b) as a function of $\theta_{i,\max}$. As we can clearly appreciate, *MSE* and the RI absolute errors $|n_{\text{theo}} - n_{\text{fit}}|$ decrease by increasing the maximum angle of incidence. In addition, by variating the initial estimated parameters and constrains, the obtained best-fit parameters change, as observed from the associated error bars. However, the error introduced by the chosen initial parameters and constrains is clearly minimized for higher $\theta_{i,\max}$ (error bars significantly decrease with incident angle), so the method is more robust when we consider larger incident angles. To better visualize that the decreasing tendency of the error bars values still occurs for high incident angles,

an inset image in Figure 3-26 (b) provides a zoomed image of the 60º - 95º incident angle range. Therefore, from Figure 3-26 we can conclude that when we are trying to characterize the RI of isotropic samples, the iterative program is more accurate for higher angles of incidence, this being in agreement with the analysis provided in section 3.4.1. Therefore, the interest of working with high numerical apertures is confirmed.

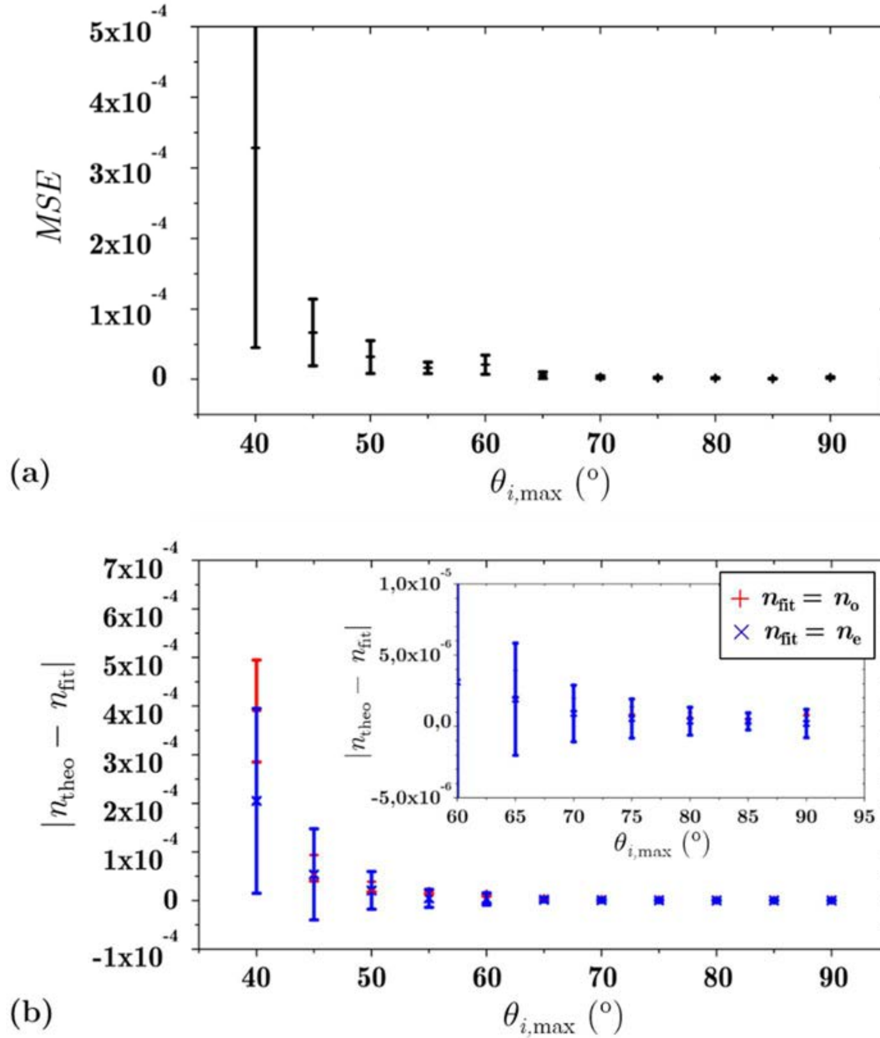

Figure 3-26. Obtained best-fit parameters for BK7 glass (n_{theo} = 1.5150 for $\lambda = 635$ *nm*). As a function of the maximum angle of incidence ($\theta_{i,\max}$): (a) Mean Squared Error (*MSE*) (black plus signs); and (b) Refractive index absolute error ($|n_{\text{theo}} - n_{\text{fit}}|$) for $n_{\text{fit}} = n_{\text{o}}$ (blue plus signs) and $n_{\text{fit}} = n_{\text{e}}$ (red crosses). The inset shows $|n_{\text{theo}} - n_{\text{fit}}|$ for high $\theta_{i,\max}$.

Uniaxial anisotropic crystals

We repeat the study conducted for isotropic samples but now we consider a uniaxial anisotropic sample (calcite) oriented at a particular position. First, the Mueller matrix images of calcite ($n_o = 1.6556$ and $n_e = 1.4849$ for $\lambda = 590$ *nm* [160] with its optical axis oriented at $(\theta_c, \phi_c) = (21°, 5°)$) are simulated for the same eleven maximum angles of incidence used in the isotropic sample case (from 40° to 90°). Then, the optimization

program is used to calculate the optical parameters of the sample. Once again, the robustness of the method to variations of the initial parameters and constrains is studied by analyzing 10 times the same Mueller matrix image (for a particular maximum angle of incidence), each time by starting from different initial parameters, and calculating the standard deviations of the corresponding best-fit data.

The obtained results are presented in Figure 3-27. Figure 3-27 (a) shows the Mean Squared Error (*MSE*) as a function of the maximum angle of incidence, $\theta_{i,\max}$, while Figure 3-27 (b) provides the absolute error between theoretical (artificial-experimental sample) and best-fit refractive indices, n_{theo} and n_{fit} respectively, for the ordinary (n_o) and extraordinary (n_e) RIs as a function of $\theta_{i,\max}$. As it can be observed, both *MSE* and $|n_{\text{theo}} - n_{\text{fit}}|$ values decrease by increasing the maximum angle of incidence, in agreement with the tendency observed for the isotropic case. Furthermore, it seems that the optimization program is slightly more accurate finding the ordinary RI than the extraordinary RI. It is important to remark that the error introduced by the initial estimated parameters and constrains also decreases with the incident angle, as shown by associated error bars. The error bars decreasing tendency is still observable for high incident angles (see inset image in Figure 3-27 (b)). Thus, when dealing with anisotropic samples, the iterative program is also more accurate by setting higher angles of incidence.

3.6.2 Accuracy as a function of the refractive indices

We analyze the influence of the refractive indices over the calculated best-fit parameters for isotropic and uniaxial anisotropic materials. In this sense, we have synthetized a set of Mueller matrix images with different refractive indices, fixing the maximum angle of incidence. As was conducted in the previous section, each generated Mueller matrix image (related to a different RI) was calculated several times by changing the initial estimated parameters and the associated error bars were also calculated. Under this scenario, the influence of the chosen initial values in the accuracy of the method is studied.

To study the performance of the optimization program reproducing a scenario as close as possible to the real experimental conditions, we fixed the maximum angle of incidence of the synthetized images to $\theta_{i,\max} = 63^{\circ}$ (this value coincides to that generated by a real HNAO with $NA = 0.9$ ($\theta_{i,\max} \sim 63^{\circ}$)). Note that from data in Figure 3-26 and Figure 3-27, we observed that the absolute error between the theoretical and the best-fit RI ($|n_{\text{theo}} - n_{\text{fit}}|$) is negligible for $\theta_{i,\max} > 60^{\circ}$.

Isotropic crystals

To study the accuracy of the optimization program for different refractive indices, twelve different angle-resolved Mueller matrices (with RI from 1.4 to 2.5) were synthetized and the corresponding best-fit values were obtained by using the optimization routine. The iterative routine is repeated 10 times for each one of the twelve simulated Mueller matrix images (related to different RIs), by changing the initial constrains and values. The

corresponding standard deviations (error bars) are also calculated. Note that the process is similar to the followed in the previous subsection, section 3.6.1. The obtained *MSE* and refractive index absolute error results are shown in Figure 3-28.

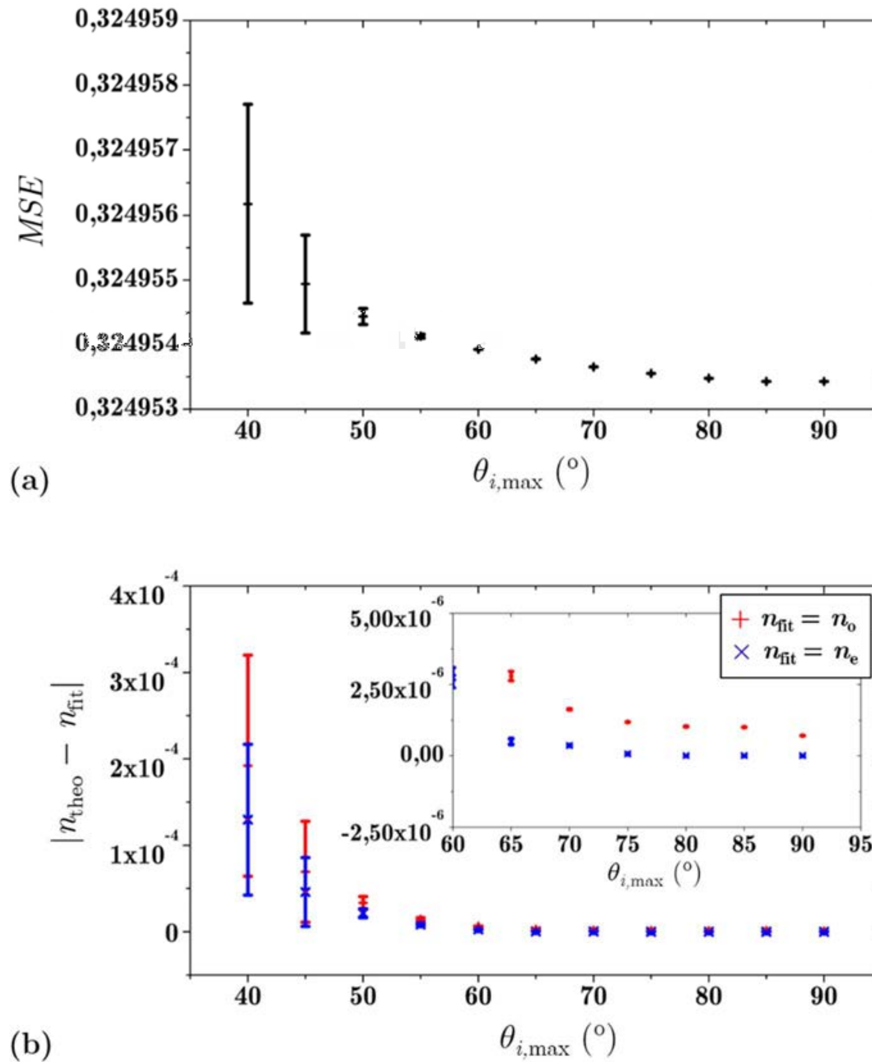

Figure 3-27. Obtained best-fit parameters for calcite (n_o = 1.6556 and n_e = 1.4849 for $\lambda = 590$ nm) as a function of the maximum angle of incidence ($\theta_{i,\max}$): (a) Mean Squared Error (*MSE*) (black plus signs) ; and (b) refractive index absolute error ($|n_{\text{theo}} - n_{\text{fit}}|$) for n_{o} (blue plus signs) and n_{e} (red crosses). The inset image shows $|n_{\text{theo}} - n_{\text{fit}}|$ for high $\theta_{i,\max}$.

From Figure 3-28 (a) it is clear that the optimization program is more accurate for high RIs, where the obtained Mean Squared Error is smaller. In addition, the associated error bars are also significantly smaller for larger incident angles. On the other hand, Figure 3-28 (b) shows the same tendency, where the error bars associated to the absolute ordinary and extraordinary refractive indices errors tend to decrease for high RIs. Note that absolute errors, $|n_{\text{theo}} - n_{\text{fit}}|$, for the ordinary and extraordinary refractive indices, provide the same values, as we are simulating isotropic materials. What is more, they are always smaller than $2 \cdot 10^{-7}$, highlighting the accuracy of the method.

Uniaxial anisotropic crystals

The same study is repeated for the anisotropic case. Again, we fixed the maximum angle of incidence to $\theta_{i,\max} = 63°$. To study the influence of the anisotropy in the optimization routine, twelve different Mueller matrix images are synthetized for a constant value of the ordinary refractive index $n_o = 1.658$ but different extraordinary RIs, n_e, from 1.4 to 2.5. As a particular case, the isotropic case is also studied ($n_e = n_o = 1.658$) to compare the

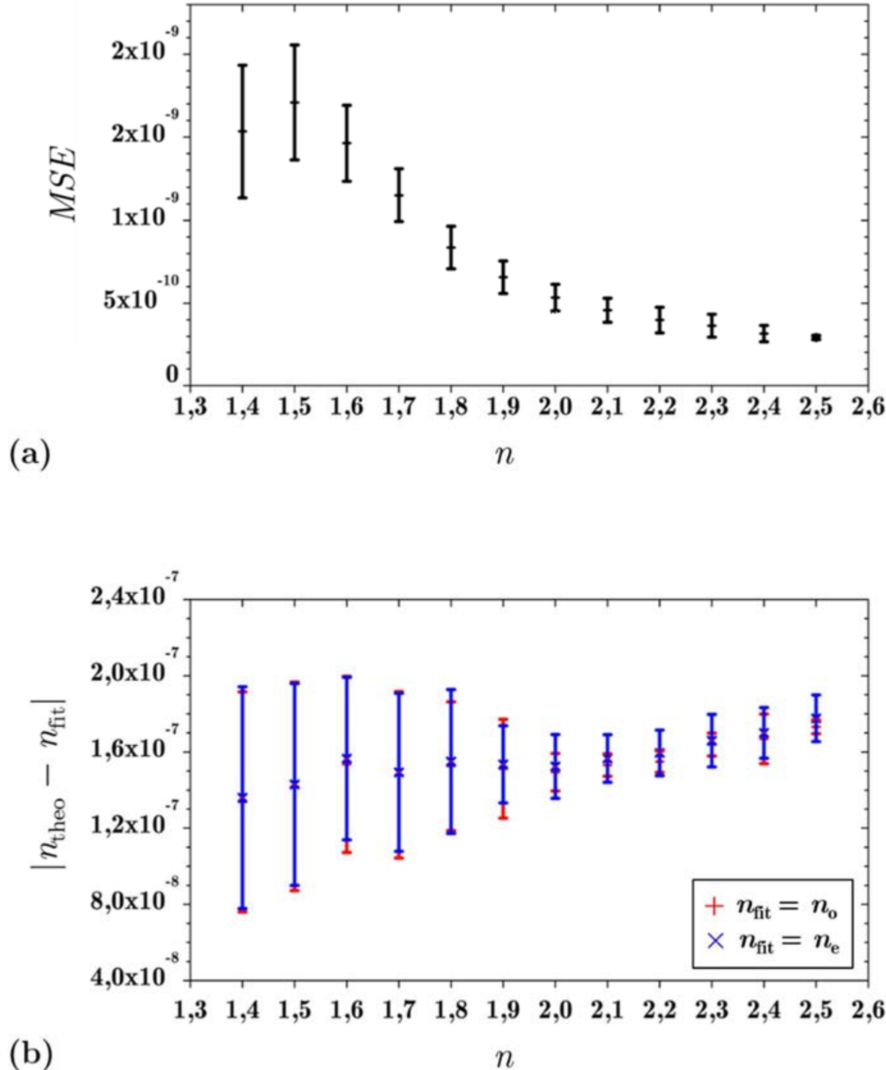

Figure 3-28. Best-fit parameters for different isotropic samples and for a fixed maximum angle of incidence $\theta_{i,\max} = 63°$. Data is shown as a function of the theoretical refractive index (n): (a) Mean Squared Error (*MSE*) (black crosses) ; and (b) refractive index absolute error ($|n_{\text{theo}} - n_{\text{fit}}|$) for n_o (blue plus signs) and n_e (red crosses). Note that n_o and n_e provide the same mean values, as we are simulating isotropic materials

accuracy of the optimization program without birefringence. Once again, the quantitative study is based on the *MSE* and $|n_{\text{theo}} - n_{\text{fit}}|$ figures of merit, which are respectively represented in Figure 3-29 (a) and (b) versus the theoretical birefringence $\Delta n = (n_o - n_e)$. Obtained data show how the optimization program is more accurate for isotropic samples,

in which the $|n_{\text{theo}} - n_{\text{fit}}|$ value presents a minimum, or for anisotropic samples with small birefringences, $|\Delta n| < 0.2$. This situation can be related with the fact that the mathematical model is simplified for isotropic samples, and a lower number of parameters is involved in the searching process. However, we want to emphasize that in all the cases, absolute errors in Figure 3-29 (b) are always smaller than $5 \cdot 10^{-6}$, providing the accuracy of the method to determine the optical parameters of anisotropic materials.

Finally, the optimization routine is also analyzed for a constant global birefringence ($\Delta n = 0.173$) but different ordinary and extraordinary refractive indices. This allows us to

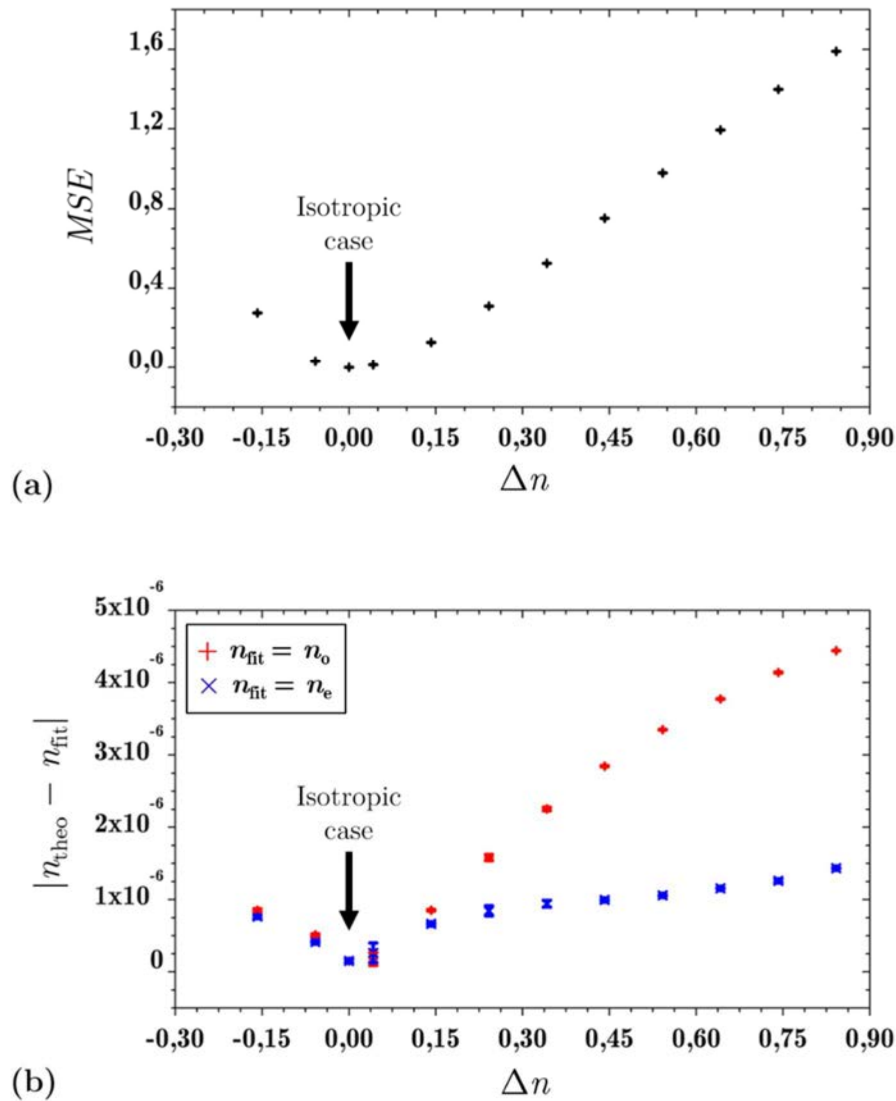

Figure 3-29. Best-fit parameters obtained with the optimization program for different theoretical birefringences (Δn) and a fixed maximum angle of incidence $\theta_{i,\max} = 63°$. Data is given as a function of the theoretical Δn: (a) Mean Squared Error (*MSE*) (black crosses); (b) refractive index absolute error ($|n_{\text{theo}} - n_{\text{fit}}|$) for n_o (blue plus signs) and n_e (red crosses).

study the accuracy of the method for constant birefringences but into different RIs ranges. The same procedure explained in previous studies is here applied, i.e., the best-fit

parameters are found for twelve different synthetized Mueller matrix images, and the obtained *MSE* and $|n_{\text{theo}} - n_{\text{fit}}|$ values are represented in Figure 3-30 (a) and (b) versus the chosen theoretical n_e, which samples into a range (from 1.4 to 2.3). We appreciate how the *MSE* and the extraordinary RI absolute error decrease when the extraordinary refractive index increases, so the extraordinary index measure is more accurate for high RI ranges, where small RI variations are more significant in terms of polarimetric response. By turn, the ordinary RI absolute error for the ordinary index slightly increases, because it suffers from some correlation with other model parameters. Importantly, absolute errors in Figure 3-30 (b) are always smaller than $2 \cdot 10^{-6}$, confirming the accuracy of the method to determine the optical parameters of anisotropic materials.

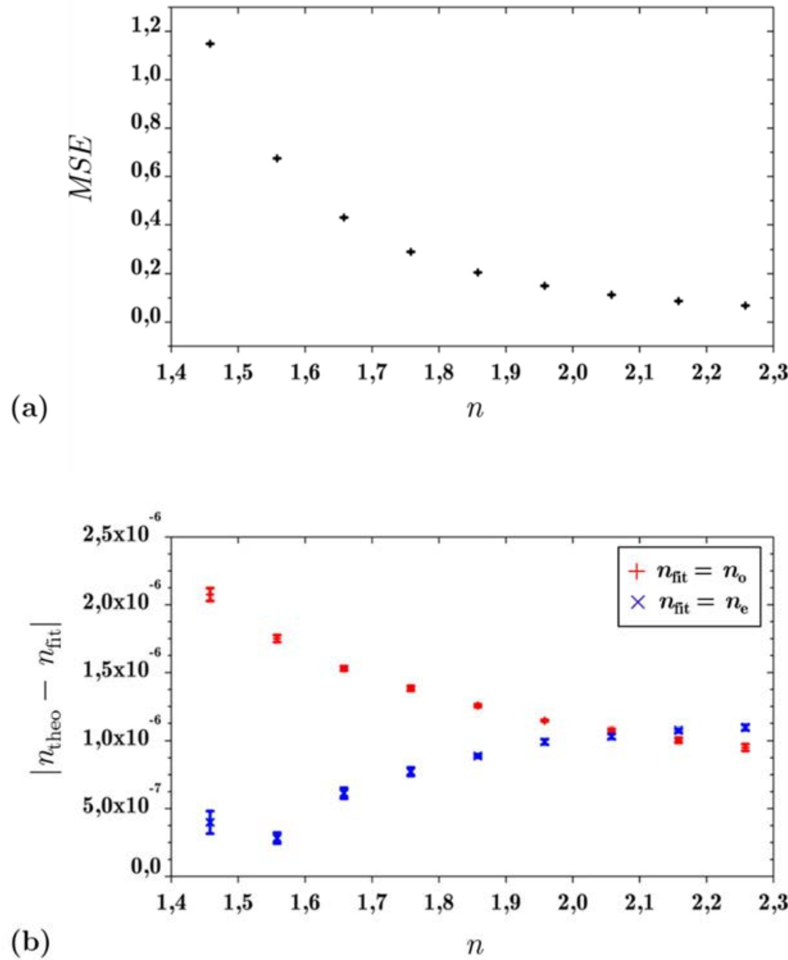

Figure 3-30. Best-fit parameters obtained with the optimization program for a constant birefringence $\Delta n = 0.173$ and a maximum incident angle of 63°. Data is given as a function of the theoretical n_e: (a) Mean Squared Error (*MSE*) (black crosses); and (b) refractive index absolute error ($|n_{\text{theo}} - n_{\text{fit}}|$) for n_o (blue plus signs) and n_e (red crosses).

From the obtained results we can conclude that the optimization routine is more accurate for isotropic materials than for anisotropic materials. The main reason is that anisotropic samples introduce extra optical parameters in the searching process, as the angular position of the optical axis $\hat{C}\left(\phi_c,\ \theta_c\right)$ or the extraordinary refractive index value.

However, for a maximum angle of incidence of $\theta_{i,\max} = 63°$, the refractive index absolute error ($|n_{\text{theo}} - n_{\text{fit}}|$) is smaller than $5 \cdot 10^{-6}$, both on isotropic and uniaxial anisotropic materials, providing the suitability of the method to be tested in both cases.

3.6.3 Influence of noise

Experimental Mueller images are always affected, to a certain extent, by non-desired noise added to their constituent intensity images, recorded by the Mueller polarimeter. Therefore, in this section the influence of noise is also studied to verify the accuracy of the optimization program in a more realistic situation. Note that the Mueller matrix images may not be ideal due to slightly variations of the generated states of polarizations and of the polarization analyzers, intensity changes with time of the beam produced by the light source, electronic noise introduced by the camera, etc. To analyze the optimization routine, several Mueller matrix images were generated by adding different levels of random noise to the intensities used to calculate the synthetized Mueller matrix image of BK7 glass shown in Figure 3-23 (a). In particular, the noise effect is simulated in the following way. The pixels of the ideal thirty-six intensity images are corrupted by adding computer-generated random numbers to each point of the image (from 1.5% to 25%). After that, the noise synthetized Mueller matrix image of BK7 glass is calculated (section 3.2.4). To study the effect introduced by the magnitude of the random noise, different random noises levels were selected to be added to the intensity images of BK7 glass. Two examples, where the effects of varying the level of random noise are quite evident, can be seen in Figure 3-31. For the sake of clarity, the applied procedure is sketched in the flow chart shown in Figure 3-32. By applying this procedure, a set of synthetized angle-resolved Mueller matrices were obtained for each chosen level of random noise.

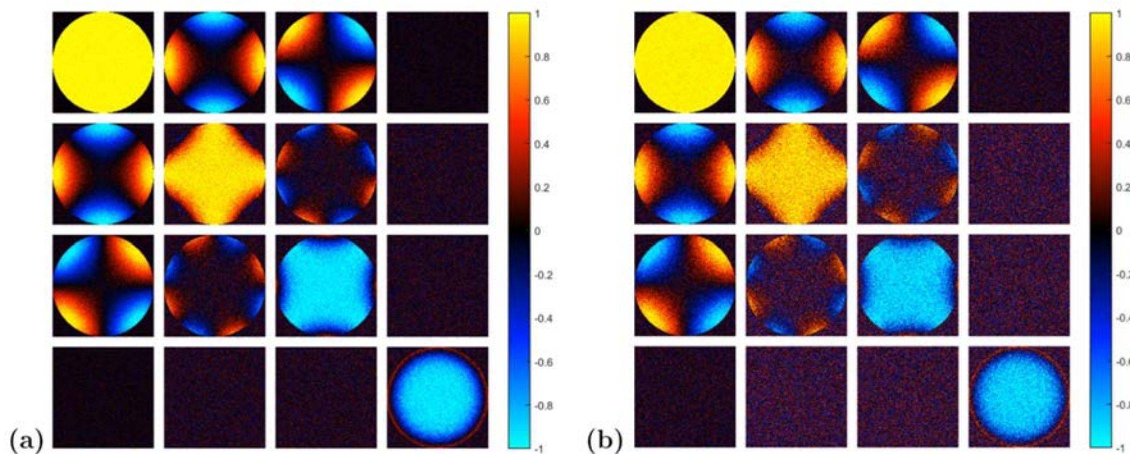

Figure 3-31. Two different levels of random noise added to the synthetized Mueller matrix images for BK7 ($n = 1.515$ and $\theta_{i,\max} = 63°$). (a) ~13% of random noise and, (b) ~25% of random noise. The original angle-resolved Mueller matrix can be observed in Figure 3-23 (a).

The optimization program was applied for the noisy angle-resolved Mueller matrices, and for each noise level selected, the best-fit parameters were calculated 10 times; these

different calculations were related to different initial estimations and constrains). From these calculations, a set of best-fit parameters were obtained for each level of random noise, and the corresponding standard deviations (error bars) were also calculated. Figure 3-33 shows the obtained *MSE* values (Figure 3-33 (a)) and the RI absolute errors (Figure 3-33 (b)) for different noise levels. In both cases, when the noise level increases, the accuracy of the routine decreases, as stated by the magnitude of the associated error bars. Consequently, and as logical, it is confirmed that noise added to the Mueller matrix images has an important effect on the accuracy of the obtained best-fit parameters. Nonetheless, even for significant levels of noise added to the Mueller images, the associated absolute errors remain lower than $2 \cdot 10^{-3}$, which still constitutes a remarkable result. Despite this, to accurately characterize the refractive index of samples, it is highly recommended to minimize noise added to the angle-resolved Mueller matrices as much as possible.

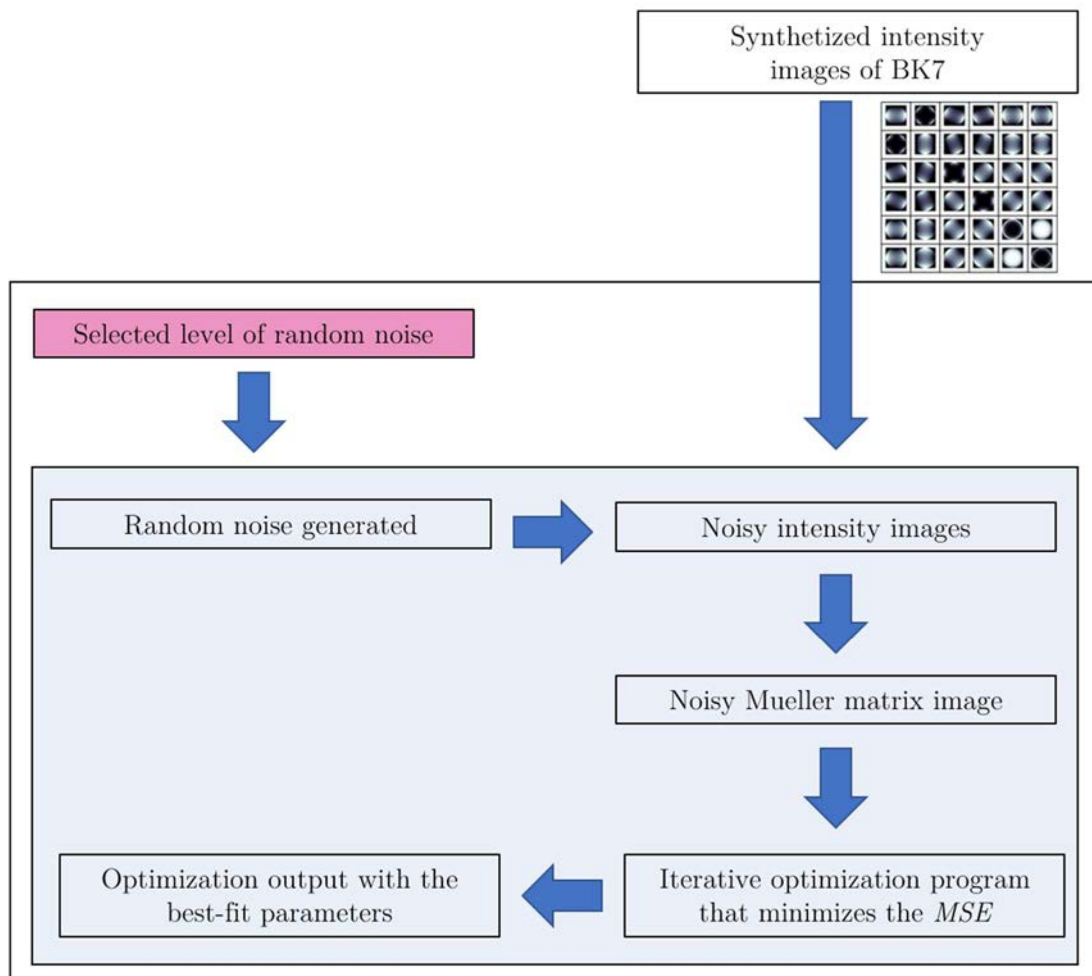

Figure 3-32. Flow chart explaining the random noise added to the synthetized Mueller matrix image of BK7 glass. For a selected level of random noise (pink box), several noisy angle-resolved Mueller matrices are generated to be compared with the theoretical BK7 glass Mueller matrix image. Then, best-fit parameters are found (blue box).

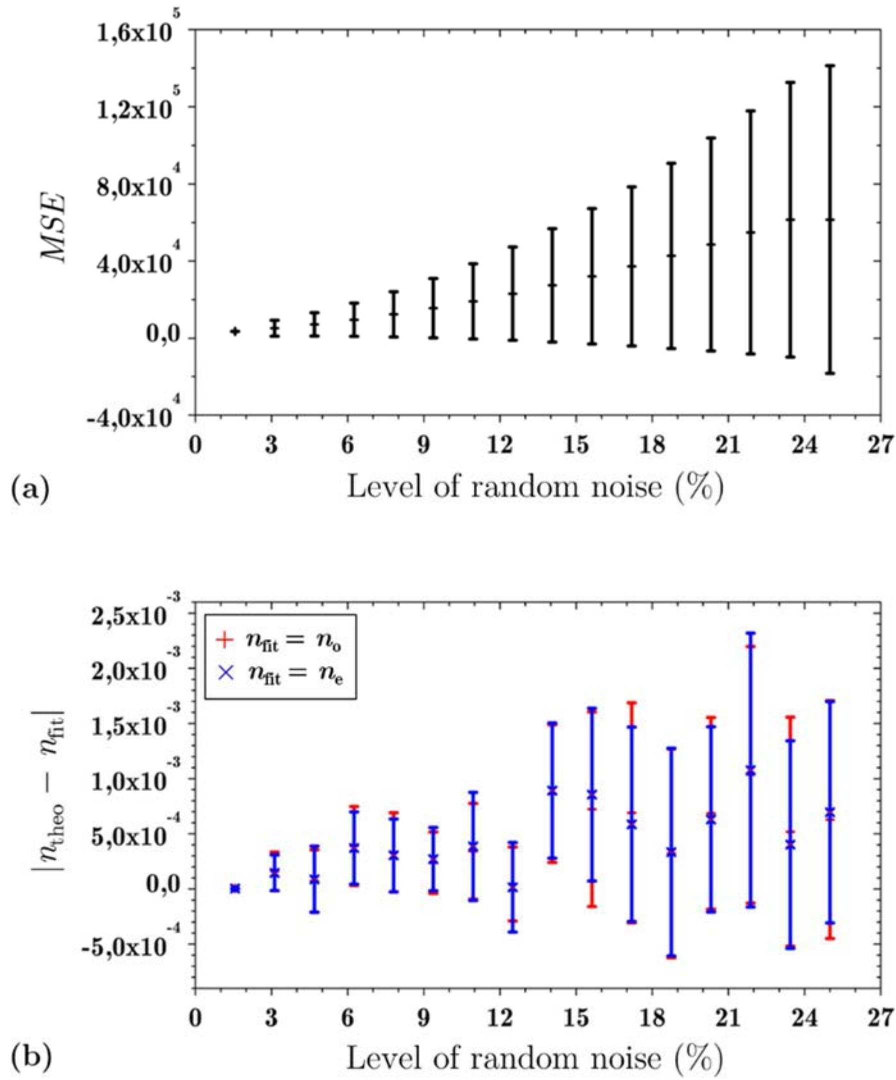

Figure 3-33. Best-fit results obtained with the optimization program for different Mueller matrix images. (a) Mean Squared Error (*MSE*) as a function of the level of random noise and, (b) $|n_{theo} - n_{fit}|$ as a function of the random noise.

Chapter 4 Experimental implementation and calibration of the set-up

In order to measure the angle-resolved Mueller matrix of isotropic samples and uniaxial anisotropic crystals in reflection, a conoscopic Mueller microscope working in reflection was built. This chapter aims at describing the implementation and calibration of the set-up developed in the laboratory during this thesis.

Different Mueller microscopes configurations were built during this period. From this knowledge, we learnt how to improve the set-up as well as the alignment protocol. From this collection of optical arrangements, the most optimal optical architecture is presented in this chapter. Such selected instrumentation was used to measure the experimental Mueller matrix images presented in Chapter 5.

4.1 Experimental configuration of the microscope

The architecture of the conoscopic Mueller microscope working in reflection is presented in this section. The designed microscope is able to measure the change of the polarization upon interacting with an isotropic or uniaxial anisotropic sample.

Let us explain the light path through the conoscopic Mueller microscope, built in our laboratory, before we discuss the alignment of the microscope. From the light source to the detector, its optical components are described and analyzed. Our set-up comprises four different parts. Figure 4-1 shows the scheme of the set-up and the direction of the propagation of the light beam in each part (see the different colored arrows). Three of these parts have already been introduced in the previous chapter (section 3.2)

- **Illumination Arm** generates a collimated input light beam that is polarized (see red curly-bracket in Figure 4-1 (b)). It consists of an optical fiber fed by a laser diode, a collimator and a polarization state generator. The PSG consists of a linear polarizer (LP) followed by two thermally stabilized Liquid Crystal Displays (LCDs).

- **High Numerical Aperture Objective Focusing System** focuses polarized input beam on the sample, collects the reflected beam and collimates and steers it to the backwards direction (see green curly-bracket in Figure 4-1 (b)). It consists of an achromatic non-polarizing beam-splitter cube (NP-BS) and a high numerical aperture objective (HNAO).

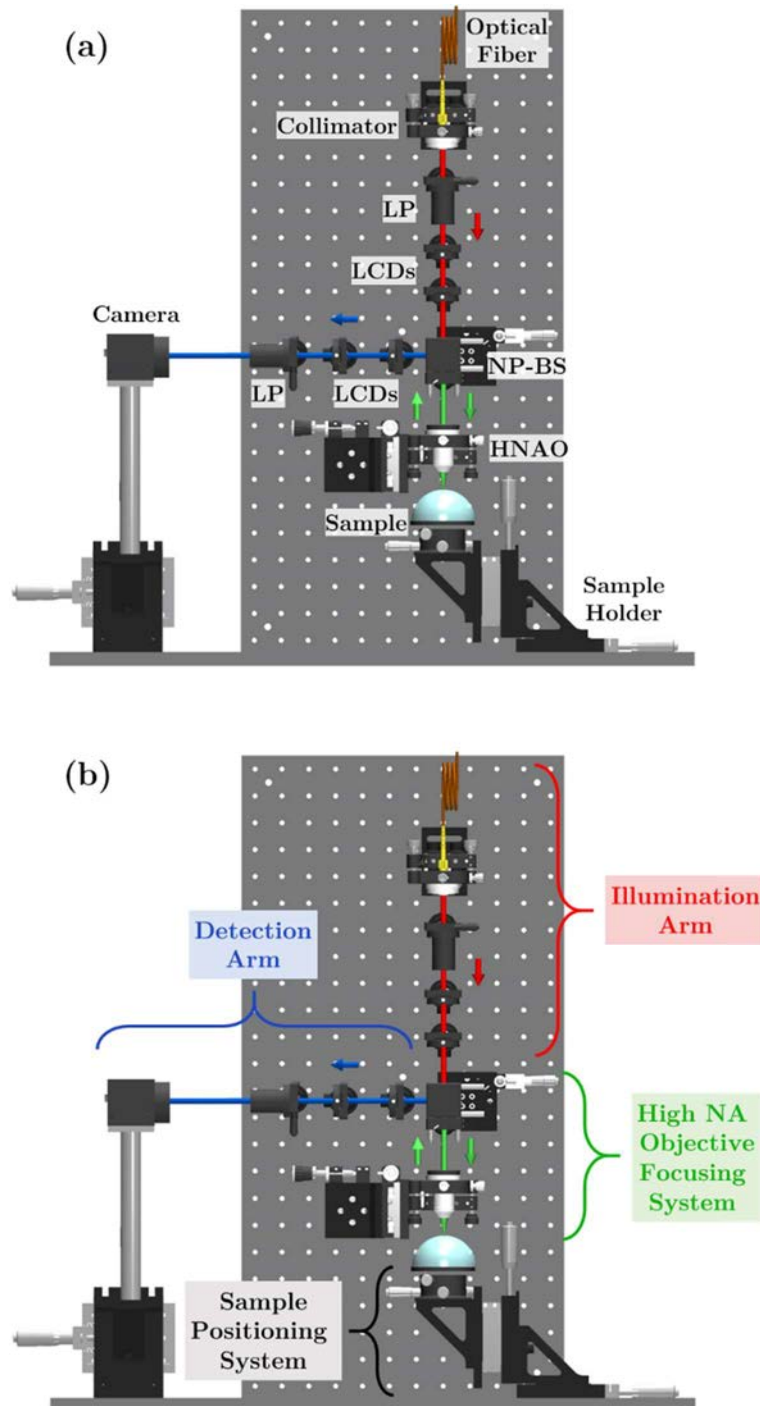

Figure 4-1. Scheme of the conoscopic Mueller microscope: (a) a label for each of the principal optical elements forming the microscope is presented; and (b) the same sketch is shown but now, the four main parts of the microscope are indicated. Red, green and blue arrows indicate the direction of propagation of the light beam.

- **Sample Positioning System** allows us both to place the sample at the high *NA* objective focal plane and to accurately align the sample surface perpendicularly to the optical axis of the HNAO (see black curly-bracket in Figure 4-1 (b)). The system consists of a sample holder presenting different translation and rotation platforms of high precision.

- **Detection Arm** images the back focal plane of the HNAO on a CMOS camera. The polarization pattern exiting from the high *NA* objective focusing system is analyzed by using a polarization state analyzer (see blue curly-bracket in Figure 4-1 (b)). Note that the intensity image after the PSA contains spatial information of the polarization changes on the input beam produced by the sample, and thus of the sample optical constants. This system consists of two temperature-controlled LCDs, a linear polarizer and a CMOS camera.

A good alignment is essential to obtain an appropriate image quality. To facilitate the alignment process of the conoscopic Mueller microscope, all the optical elements (with exception of the CMOS camera and the sample holder) are placed on a common optical breadboard. This optical breadboard is vertically placed in the laboratory and thus, the sample holder is set in the horizontal plane, this allows us to avoid gravity effects on samples. The solid optical breadboard enables to align the set-up in an easier way and fix it in the proper position when the set-up is well aligned. In Figure 4-1, the optical components on the breadboard can be seen. In addition, the conoscopic Mueller microscope is mounted on an optical isolation table to prevent from mechanical vibrations caused from external environment.

Every component of these four parts is explained with more detail in the next sub-sections.

4.1.1 PSG and PSA design

To measure the Mueller matrix of an isotropic or uniaxial anisotropic sample, a polarization state generator (PSG) as well as a polarization state analyzer (PSA) are needed. The PSG generates the polarization state of the illumination beam, while the PSA analyzes the polarization state after its interaction with the sample. In literature, one can find a large number of configurations able to measure Mueller matrices as rotating retardation plates [163–166], liquid crystal variable retarders [130, 159, 167], photoelastic modulators [168, 169], rotating compensators [170, 171], etc.

In our case, to eliminate the influence of alignment and positioning errors related to mechanical movements of the measuring arms, we are interested in using static configurations for the PSG and PSA systems. Optical elements as liquid crystal displays (LCDs) are interesting because they can be modeled as variable linear retarders. What is more, they introduce variable retardance depending on the voltage addressed and the orientation of their fast axes, without requiring any mechanical movement. The LCDs proposed to design the PSG and the PSA are composed of transparent liquid crystal

molecules that have an ordered orientation. With no voltage applied, the molecules lie parallel to the windows and the introduced retardation is maximal. When a voltage is applied, they tend to reorient parallel to the electric field propagation direction. In addition, the effective retardance depends on the particular spatial tilt of the liquid crystal molecules, which in turn depends on the addressed voltage (i.e., we can change the effective birefringence of the material with the applied voltage). The more the molecules tilt, the smaller the retardation. In the limit case, when the molecules are parallel to the electric field propagation direction, the LC material acts as an isotropic sample. In this way, the retardance of LCD can be controlled by changing the applied voltage.

The four-selected liquid crystal displays used as full-wave variable retarders are mono-pixel parallel aligned nematic liquid crystal cells (*Thorlabs, LCC1223T-A*). The retardation of the LCDs, produced by the molecules orientation, strongly depends on the operating wavelength, drive voltage and temperature. In our case, a diode laser is used as a monochromatic light source with a wavelength of 635 *nm*, and thus, the retardance calibration is only required for this particular wavelength.

The specifications of the used LCDs (*Thorlabs, LCC1223T-A*) show the dependence on the temperature of the devices. As temperature increases, the retardation decreases with it (see Figure 4-2). Considering that the ambient laboratory temperature may variate more than 20 °C between summer and winter and few degrees within a day, a temperature sensing and control option is added to our LCDs for accurate controlling of the operating temperature. The temperature of our retarders can be controlled to ± 0.1 °C using the recommended temperature controller (*Thorlabs, TC200*). Temperature stabilization provides constant retardance even if ambient temperature changes and also allows for faster switching times [172].

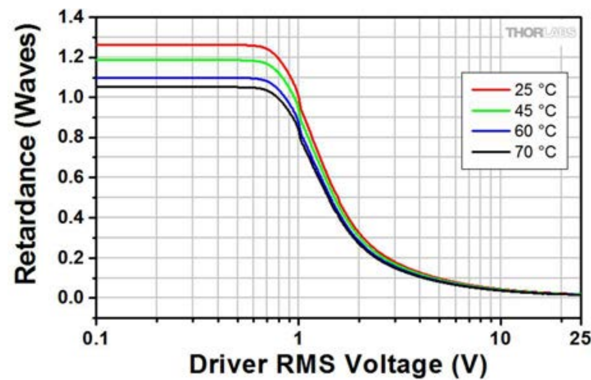

Figure 4-2. Retardance versus driver RMS voltage for a single (*Thorlabs, LCC1223T-A*) LCD, for a wavelength of 635 *nm* (*Thorlabs, Inc.*) [172].

The configuration proposed to generate any fully polarized state of polarization (PSG system) is a linear polarizer (LP) followed by the two nematic liquid crystals. Similarly, the polarization state analyzer consists of the two nematic LCDs followed by a linear polarizer [130, 159]. The schemes of the PSG and PSA systems are presented in Figure 4-3.

When the temperature of the LCDs is stabilized, the PSG and the PSA can be fully characterized by eight parameters: the angles between the linear polarizer axis (fixed at 0° of the laboratory vertical) and the fast axes of the LCDs (ψ_1, ψ_2, ψ_3, ψ_4) and their retardances (δ_1, δ_2, δ_3, δ_4).

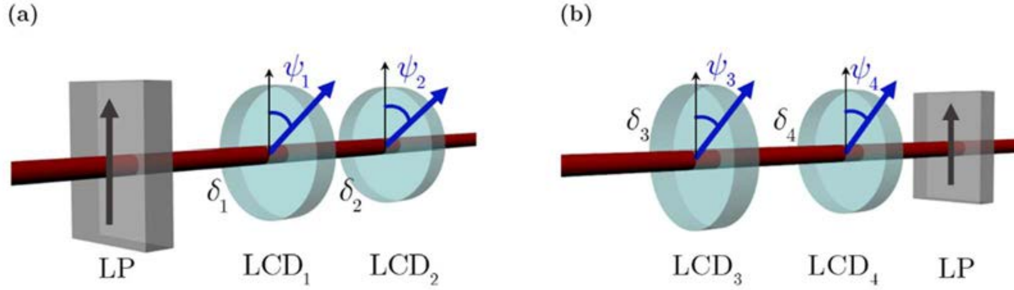

Figure 4-3. Scheme of the (a) PSG; and (b) PSA. Both are a combination of a linear polarizer (LP) and two liquid crystal displays (LCD_1 and LCD_2). Black arrows show the direction of the linear polarizer axes and blue arrows the fast axis direction of the LCDs. The retardance is given by δ_1, δ_2, δ_3 and δ_4, and the angle between the linear polarizer axes and the fast axes of the LCDs are ψ_1, ψ_2, ψ_3 and ψ_4.

For the PSG scheme above-described, it has been demonstrated that angles between the linear polarizer axis and the fast axes of the LCDs with values of $\psi_1 = 45^o$ and $\psi_2 = 0^o$ are optimal in terms of polarization generation, as this configuration allows generating any fully polarized state of polarization [159]. Analogously, angles of $\psi_3 = 0^o$ and $\psi_4 = 45^o$ set for the PSA system, allows measuring any state of polarization.

Under the above-stated configuration, the incident Stokes vector generated by using the PSG, $\boldsymbol{S}_{in}$, has the following expression

$$\boldsymbol{S}_{in} = \boldsymbol{M}_{LR}\left(\delta_2,\ 0^o\right) \cdot \boldsymbol{M}_{LR}\left(\delta_1,\ 45^o\right) \cdot \boldsymbol{S}_{LP}\left(0^o\right) \tag{4.1}$$

where $\boldsymbol{S}_{LP}(0°)$ is the Stokes vector of a linear polarizer oriented at 0° [111] and $\boldsymbol{M}_{LR}(\delta, \psi)$ is the Mueller matrix of a linear retarder with a fast axis orientated at an angle ψ and a retardance of δ [111, 112]

$$\boldsymbol{M}_{LR}\left(\delta,\psi\right) = \begin{pmatrix} 1 & 0 & 0 & 0 \\ 0 & \cos^2 2\psi + \cos\delta \sin^2 2\psi & \left(1-\cos\delta\right)\sin 2\psi \cos 2\psi & \sin\delta \sin 2\psi \\ 0 & \left(1-\cos\delta\right)\sin 2\psi \cos 2\psi & \sin^2 2\psi + \cos\delta \cos^2 2\psi & \sin\delta \cos 2\psi \\ 0 & \sin\delta \sin 2\psi & -\sin\delta \cos 2\psi & \cos\delta \end{pmatrix} \tag{4.2}$$

By replacing the expression for the Mueller matrix of a linear retarder, provided in Eq. (4.2), into Eq. (4.1), the parameters of the Stokes vector generated by using the PSG are obtained

$$\boldsymbol{S}_{in} = \begin{pmatrix} 1 \\ \cos\delta_1 \\ -\sin\delta_1 \sin\delta_2 \\ \sin\delta_1 \cos\delta_2 \end{pmatrix} \tag{4.3}$$

Note that the generated Stokes vectors are function of the PSG liquid crystal retardances δ_1 and δ_2. Eq. (4.3) is analogous to spherical coordinates with radius 1, where δ_1 and δ_2 are the polar and azimuthal angles, respectively. By taking into account the SoPs representation upon the Poincaré sphere [111], Eq. (4.3) shows how any fully polarized state of polarization (points upon the Poincaré sphere surface) can be generated by properly choosing the pair of retardances δ_1 and δ_2.

On the other hand, the intensity measured on the detector (CMOS camera in Figure 4-1) corresponds to the projection of the Stokes vector, after the light beam interacts with the sample, onto the polarization analyzer (PA) set by the PSA. The mathematical relation for the polarization analyzer corresponds to the first row of the Mueller matrix that characterizes the whole PSA

$$\boldsymbol{M}_{PSA} = \boldsymbol{M}_{LP}\left(0^{\circ}\right) \cdot \boldsymbol{M}_{LR}\left(\delta_4,\ 45^{\circ}\right) \cdot \boldsymbol{M}_{LR}\left(\delta_3,\ 0^{\circ}\right) \tag{4.4}$$

where $\boldsymbol{M}_{LP}(0°)$ is the Mueller matrix of a linear polarizer placed at 0° [111].

Therefore, from Eq. (4.4) we find that the polarization analyzers provided by our system can be written as

$$\boldsymbol{A} = \frac{1}{2}\begin{pmatrix} 1 & \cos\delta_4 & \sin\delta_4 \sin\delta_3 & -\sin\delta_4 \cos\delta_3 \end{pmatrix} \tag{4.5}$$

It can be observed that the measured intensities are function of the PSA liquid crystal retardances δ_3 and δ_4, and so, on the applied voltages. Therefore, according to Eqs. (4.3) and (4.5) the PSG and PSA polarizations are fully characterized by the corresponding LC panels retardances.

The retardances δ of each LC panel in the PSG and PSA are controlled by the voltage applied to them. In our case, these voltages are computer controlled in order to automatize the data acquisition process. Before measuring the Mueller matrix image, the PSG and PSA are experimentally calibrated to accurately relate the applied voltages with the retardances of each LC panel (and thus, with the generated polarizations). In addition, the LC panels are mounted on rotating holders, allowing us to control the orientation of their fast axes during the calibration process. The characterization process is explained in detail in the forthcoming calibration section 4.3.2.

4.1.2 Illuminating arm

Figure 4-4 shows the illumination arm scheme. As a light source we use a diode-laser working at 635 *nm* and connected to a single-mode fiber (*Thorlabs, P1-630A-FC-1*). The edge of the fiber is coupled to a zoom fiber collimator (*Thorlabs, ZC618FC-A*) that provides

a variable focal length between 6 *mm* and 18 *mm*, while maintaining the collimation of the beam. As a result, the size of the beam can be changed without altering the collimation. In addition, the existing beam has a nearly Gaussian intensity profile. This system is mounted on a 6-freedom degrees holder (*Thorlabs, K6XS*), including shifts and rotations. In particular, it allows us to shift, tip and tilt the zoom fiber collimator in the $\hat{x}$- and $\hat{y}$-axis directions.

Afterwards, a prism-based linear polarizer (*Thorlabs, GTH10M-A*) and two LCDs (*Thorlabs, LCC1223T-A*) are placed to form the PSG that permits to generate any fully polarized SoP.

In this situation, a collimated beam with customized polarization, labelled as illumination beam, is achieved. Note that thanks to the holders and mounts, the input beam can be steered to the proper propagation direction with high precision.

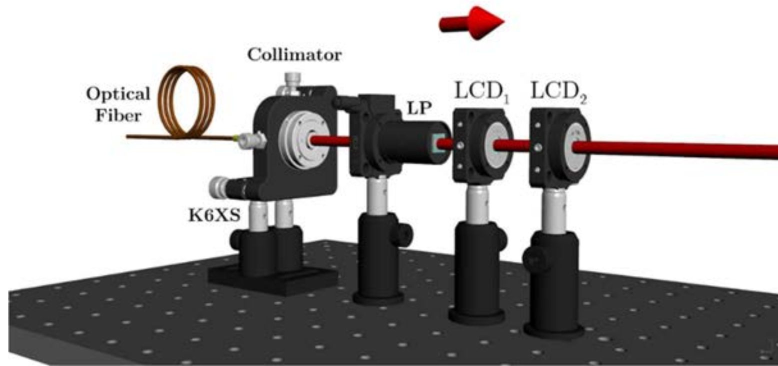

Figure 4-4. Layout of the illumination arm. The red arrow indicates the direction of propagation of the illumination beam. Light is steered to a collimator via an optical fiber. The K6XS mount allows for the adjustment of the collimated beam direction of propagation. The linear polarizer (LP) and the two liquid crystal displays (LCD_1 and LCD_2) form the PSG that generate any desired fully polarized state of polarization.

4.1.3 High *NA* Objective Focusing Systems (HNAOFS)

The illumination beam, after passing through the non-polarizing beam-splitter cube (see Figure 4-1), is focused onto the sample by the high numerical aperture objective. Table 4-1 gives the specifications of the chosen HNAO (*Nikon, CFI LU Plan Fluor EPI P 100x*) (see Figure 4-5). It is a planar objective, i.e., it corrects field curvature aberrations bringing to focus the off-axis image in a flat image plane. In addition, it is infinity corrected and ideal for polarizing applications. Moreover, it has a long working distance (1 *mm*), i.e., long distance between the front lens element of the microscope objective and the closest surface of the sample. The chosen HNAO is aberration corrected and the medium that should be present between the front lens of the microscope objective and the object being examined is air ($n_i = 1$). The angular range provided by the used HNAO, calculated from Eq. (3.4), is of $\theta_{i,\max} = 64.16^{\circ}$.

Under this scenario, a widespread range of incident plane waves, each one with its characteristic angle of incidence, is focused and afterwards back propagated after being reflected on the sample surface. As was analyzed in the previous chapters, the HNAO makes possible to measure Mueller matrices over polar angles, θ_i, varying from 0° to $\theta_{i,\max}$ and over all azimuthal angles ε (0, 360°) without the requirement of mechanical movements (see Figure 3-2), as it is the case of other existing reflective conoscopic microscopes based on mechanical arms [115, 116]. The use of a high numerical aperture provides large sample redundancy data (all the pairs (θ_i, ε) inspected) and allows performing fast and accurate measurements. Figure 4-6 shows a detailed scheme of the HNAO focusing system.

HNAO Specifications: ***CFI LU Plan Fluor EPI P 100x*** ***Nikon***	
Magnification	**100x**
Numerical Aperture	**0.9**
Working Distance	**1 *mm***
Polarizing	**Ideal**
Immersion	**Air**

Table 4-1. Technical specifications of the high numerical aperture objective chosen to focus the incident beam and to collect the reflected beam.

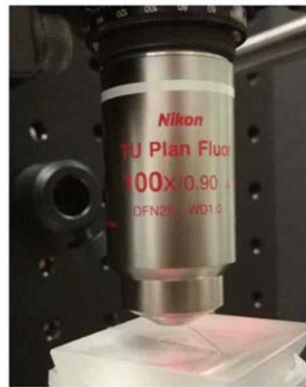

Figure 4-5. Photo of the HNAO: CFI LU Plan Fluor EPI P 100x Nikon.

As we are dealing with a microscope with a very high *NA*, any small misalignment results in a distortion of the Mueller matrix image. To minimize the misalignments, the microscope objective is placed in a holder with the same 6-freedom degrees than the used for the laser (*Thorlabs, K6XS*), but now, including an extra x-y translation platform with longer shifting distances. This new holder is included to ensure the proper alignment of the objective.

The HNAO also collects the light reflected by the sample. As the microscope objective is infinity corrected and the sample is placed at focal plane of the microscope, the resulting reflected beam is collimated and propagates backwards (see blue arrow in Figure 4-6). Note that this reflected beam must be steered to the CMOS camera. This is made by using a

non-polarizing beam-splitter cube (*Thorlabs, CM1-BS013*) with operating wavelength range from 400 *nm* to 700 *nm*.

The dielectric beam-splitter consists of two prisms and a coating that is applied to the hypotenuse of one of the prisms that make up the cube (see Figure 4-7 (a)). This cube provides a 50:50 splitting ratio that is nearly independent of the polarization of the incident light. As we are going to measure the polarization changes produced by the sample, a non-polarizing beam-splitter is needed. The low polarization dependence of the metallic-dielectric coating allows the transmission and reflection for $\hat{s}$ and $\hat{p}$ polarizations to be within 10% or 15% of each other (see Figure 4-7 (b)). The used NP-BS is specifically designed for applications in which polarization effects must be minimized. In addition, the beam-splitter cube has an antireflection coating deposited on each face to minimize unwanted reflections.

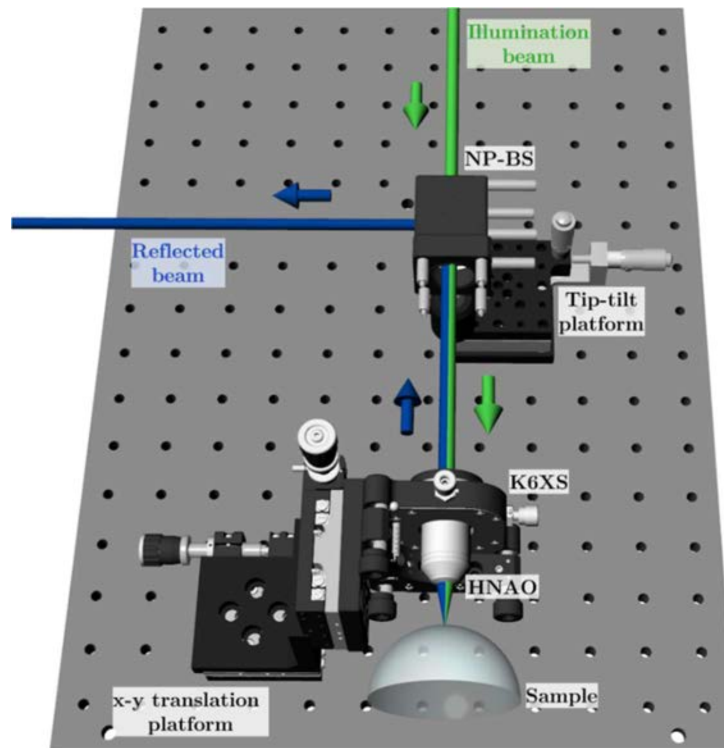

Figure 4-6. Scheme of the high numerical aperture objective focusing system. Green arrows indicate the direction of propagation of the incident waves, while blue arrows indicate the direction of propagation of the reflected waves.

To accurately align the NP-BS, it is placed on a pitch and yaw tilt platform with micrometric precision (*Thorlabs, PY003/M*).

In order to locate the focusing spot just on the sample surface, a high accuracy translation stage is needed to drive the sample in the $\hat{z}$-direction. To this aim, the motorized linear movement stage (*Thorlabs, MTS25/M-Z8*) is used. Its minimum step of 0.05 μm allows focusing the light beam on the sample surface with precision. In addition, two motorized goniometers (*Attocube, ECGt5050* and *ECGp5050*) are placed on the tip-tilt stage to accurately rotate the sample, within a small angular range, about a fixed point in the space. The rotation of the sample permits to place a region of the curved sample

surface normal to the optical axis of the HNAO, in order to reflect back the incident beam without deviations.

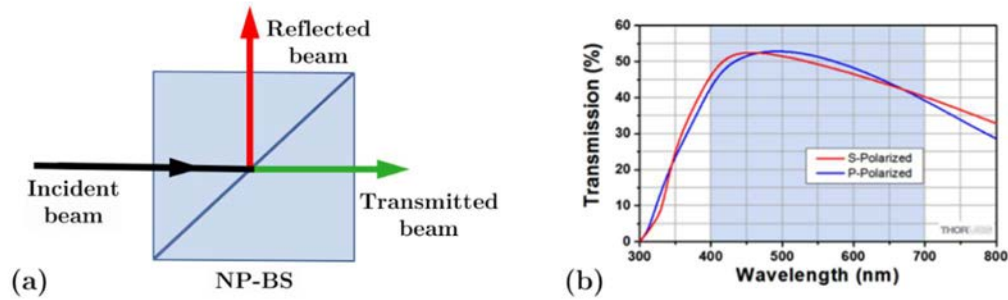

Figure 4-7. (a) Scheme of a non-polarizing beam-splitter cube (NP-BS cube), (b) Transmission curves versus wavelength for the used 50:50 non-polarizing beam-splitter. Red and blue lines indicate $\hat{s}$ and $\hat{p}$ polarization transmission curves (*Thorlabs, Inc.*) [172].

The sample positioning system is placed on the main horizontal optical table and not connected with the vertical breadboard to avoid possible vibrations of the conoscopic Mueller microscope due to positioning movements. A scheme of the sample positioning system is shown in Figure 4-8.

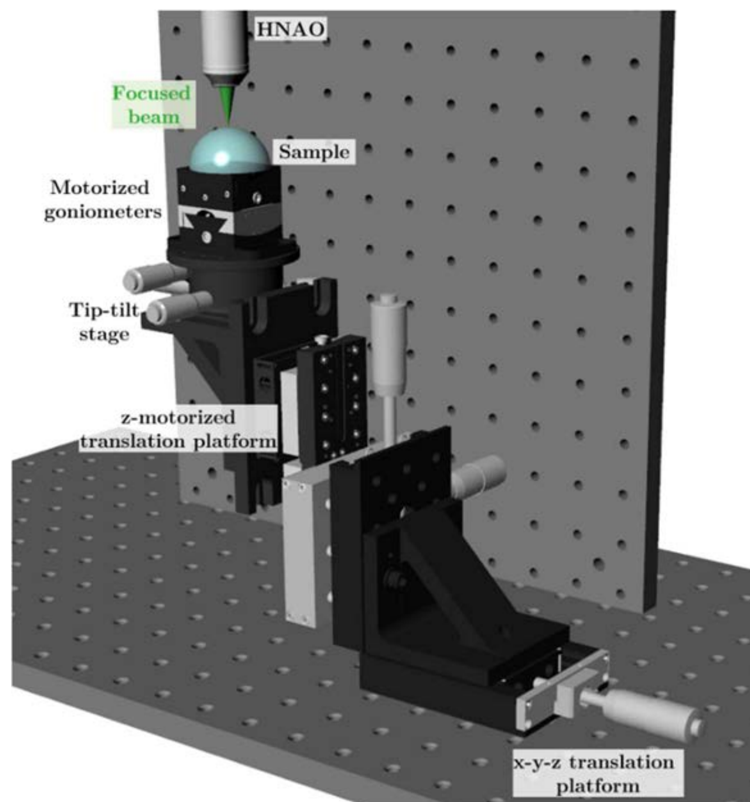

Figure 4-8. Scheme of the sample positioning system. The sample has to be placed at the focal plane of the high numerical aperture objective (HNAO) and the reflected beam has to be parallel to the incident beam. Thus, a x-y-z linear stage and a tip-tilt stage allow us to pre-align the sample. Then, motorized goniometers and a z-motorized translation platform are used to move the sample with high accuracy.

4.1.4 Detection Arm

Finally, the detection arm is described. Its schematic representation can be seen in Figure 4-9. The light reflected by the NP-BS passes through the PSA that analyzes the polarization of the reflected beam. The technical specifications of the linear polarizer and both LCDs in the PSA are equivalent to the previously described PSG elements in the illumination arm, (*Thorlabs, GTH10M-A*) and (*Thorlabs, LCC1223T-A*).

The camera used to measure the different intensity patterns is a sCMOS camera (*PCO, pco.edge 4.2 USB*) that has 16-bits of dynamic range, a high-resolution of 2048×2048 *pixels* and a pixel size of 6.5 μm × 6.5 μm. The sensor format diagonal is 18.8 *mm*. Note that a high-resolution camera is important to acquire the intensity patterns. The larger the number of pixels in the camera and the smaller the size they have, the larger the number of reflected angles that can be studied, i.e., higher resolution lead to larger measuring precision (see Eq. (3.5)). In this sense, a high dynamic range is also important to have a greater range of measured intensities.

The camera was also selected considering the possibility to measure low reflectivity samples. In fact, this sCMOS sensor produces low-noise images in low light conditions and it has a homogeneous pixel response to light and high quantum efficiency.

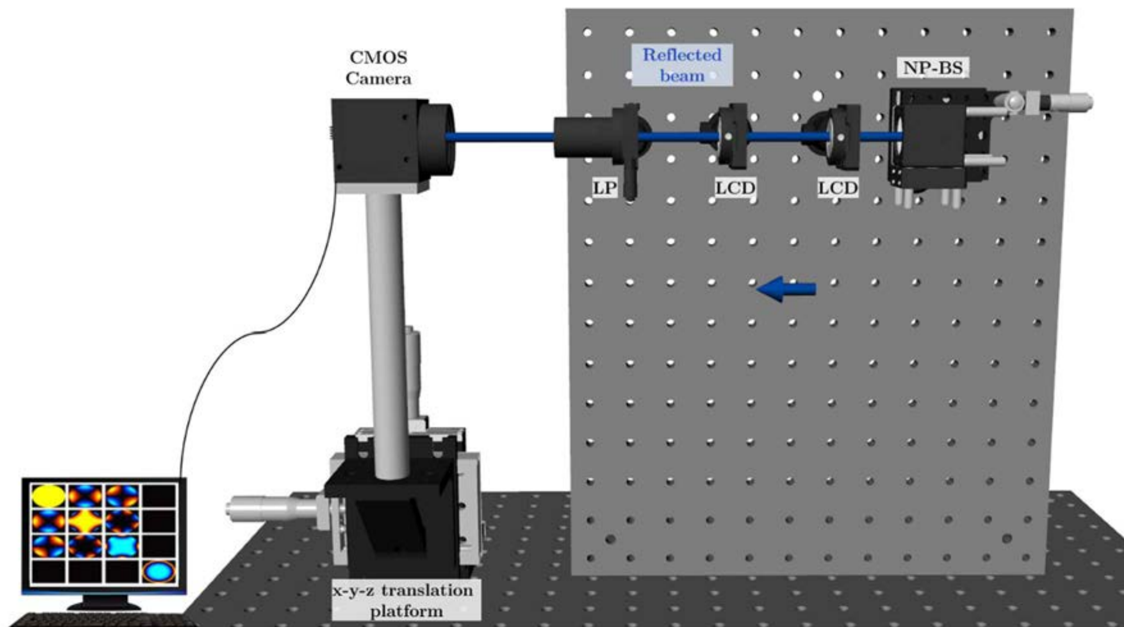

Figure 4-9. Schematic representation of the detection arm. The light beam reflected by the non-polarizing beam-splitter (NP-BS) is analyzed by the PSA, formed by two liquid crystal displays (LCDs) and a linear polarizer (LP). The CMOS camera acquires the different intensity patterns, from which the Mueller matrix image of the sample is calculated. The blue arrow represents the direction of propagation of the collimated reflected light beam.

The CMOS camera is placed in an x-y-z translation platform (see Figure 4-9), used to center the recorded intensity images.

Some references, as [173], analyze some imaging configurations for Fourier microscopy. Initially, we consider that the reflected beam is well-collimated. Thus, to avoid more complications during the alignment process, the intensity image of the back focal plane is not magnified at the CMOS camera plane. However, for some studies of the angle-resolved Mueller matrix, a lens system is placed between the PSA and the CMOS camera to magnify the back focal plane of the microscope objective onto the camera.

The opto-electronical components of the detection arm, as well as all the other electronic elements in the conoscopic Mueller microscope, are controlled by a customized Labview program developed by our group, which is able to:

- Acquire intensity images from the PCO camera.
- Change the voltages of the four LCDs, allowing us to generate and measure different SoPs and PAs.
- Move the goniometers and the motorized linear stage along the $\hat{z}$-axis to align the sample and to focus the incident beam on the sample surface.
- Calculate the characteristic Mueller matrix image of isotropic and uniaxial anisotropic samples.

4.2 Alignment method

When dealing with experimental set-ups involving HNAO, all the misalignments present in the set-up are critically magnified. Under this scenario, to achieve a system alignment with high accuracy may result problematic and a proper alignment procedure is required. In this case, we need that the laser beam follows the path without deviating when it passes through the multiple optical elements. This situation may be critical if the final system is composed by many optical components in the set-up.

The most critical alignment in our system results in correcting angular displacements between the laser source and the high numerical aperture objective. To solve this issue, most of the optical components in the set-up can be shifted in different directions and/or rotated in different angles. Therefore, we can control and correct the position and the angle of the incident and reflected beams, eliminating any possible misalignment.

Throughout this section, the alignment method followed in the laboratory is explained.

4.2.1 Laser collimation and width measurement

For a proper illumination of the microscope objective, the input light beam has to exhibit a Gaussian profile, as well as a beam radius slightly smaller than the objective aperture one. If these two conditions are not accomplished, some non-desired effects may degrade the proper operationally of the set-up. For instance, if the beam profile is larger

than the objective aperture, diffraction patterns may appear at the reflected beam after the back focal plane of the HNAO, modifying the pure sample polarimetric information. On the other hand, if the input beam is smaller than the objective aperture, the entire aperture of the objective cannot be illuminated, and the maximum angle of incidence will be reduced regardless of the *NA* of the microscope objective (in such scenario, the data redundancy provided by the system is not fully exploited). In addition, if the incident beam is shifted or exhibits a non-Gaussian profile, some of the angular trajectories provided by the HNAO will be limited when focusing the input beam over the sample under study. The collimation and the width measurement of the light beam are explained in this section.

As stated before, our light source is a laser diode coupled to a short piece of a single mode fiber optic in order to steer the input light to the set-up. The output of the optical fiber is highly divergent, and as a consequence, a fiber collimator is necessary to transform it into a collimated beam. This is achieved by using a zoom fiber collimator that provides a variable focal length between 6 *mm* and 18 *mm*. This kind of collimator is chosen because it does not introduce spherical aberration and the beam diameter can be customized. Figure 4-10 shows a graphical representation of the beam diameter at $\lambda = 633$ *nm* (close to the 635 *nm* wavelength we use in experiments) for some collimator focal lengths given by *Thorlabs, Inc* [172]. A position $f = 18$ *mm* shows a beam diameter more or less constant and smaller than 4 *mm*.

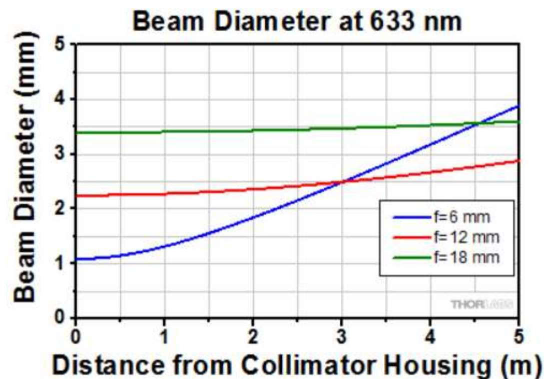

Figure 4-10. Theoretical beam diameter as a function of the collimator housing distance for a 633 *nm* illumination. The parameter *f* is the focal length of the collimator (*Thorlabs, Inc.*) [172].

The estimated laser beam diameter is smaller than the microscope aperture (5 *mm*). We can adjust the longitudinal distance between the collimator lens and the tip of the fiber optic by rotating the outer barrel of the collimator.

To analyze if the laser beam is collimated, we have studied the transversal beam size in different axial planes, by measuring the spot diffused on a screen in two different ways. This was performed out of the set-up in order to measure the size of the spot in a large range of measuring distances.

First, we have adjusted the beam diameter by rotating the outer barrel of the collimator in order to obtain a collimated beam of 4 *mm*. As our laboratory is approximatively 10 *m*

long, the beam size was compared in different axial planes within this full distance. When the beam diameter remained constant in a distance larger than 8 *m*, we considered that the laser beam was collimated in a first approximation.

To obtain larger collimation accuracy for the illumination beam, a second approach was conducted. In particular, the “knife-edge” method [174–176] is considered to quantitatively characterize the intensity distribution of our input light beam. The main idea of this metrology technique consists on measuring, with a photodetector, the gradual intensity variation of diverse uneclipsed beam portions. To obtain the different intensities, we have used a sharp knife-edge that partially covers the input beam in a given axial plane. Under this configuration, we block different areas of the input beam, by conducting different transversal displacements of the knife, and the corresponding intensity is recorded at the photodetector for each applied displacement of the knife. From this collection of intensities related to different displacements of the knife-edge, we are able to reconstruct the intensity profile of the collimated input beam. The design of the experimental knife-edge configuration is shown in Figure 4-11. Analyzing the obtained data, the diameter of the collimated beam can be obtained.

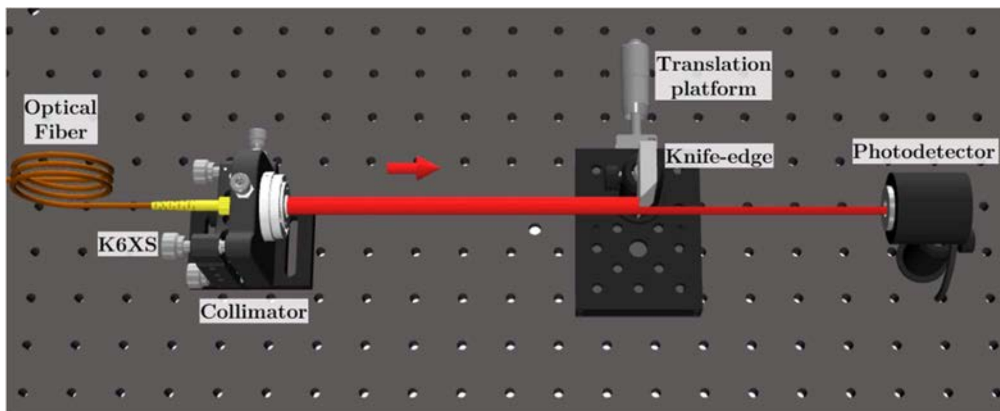

Figure 4-11. Design of the knife-edge set-up used for the measurement of laser beam radius. The collimated light beam is initially blocked by the knife-edge. Then, the translation platform can be adjusted in appropriate transversal increments and the transmitted power is obtained by the photodetector.

To implement the above-described optical scheme, we placed the knife-edge onto a micrometer-driven translation platform (see Figure 4-11), and we shifted the platform, in equal steps, from an initial position (completely blocked beam) until a final position (the whole laser beam was illuminating the photodetector). By doing so, the input beam profile was spatially scanned for different transversal positions of the knife-edge, and from the corresponding intensity measurements recorded at the photodetector, the transmitted power as a function of the knife-edge shift was obtained. The method was repeated to measure the beam diameter in two positions, near the fiber collimator (4 *cm*) and far away from it (2 *m*). From this data, the Gaussian profiles as well as the beam radius of the beam were studied.

According to Reference [174–176], when scanning a Gaussian beam as that of the laser, the transmitted power data as a function of the knife-edge displacement leads to a characteristic S-shaped curve, going from a null power (when the beam is completely blocked) to a maximum power $P_{\max}$ (when all light is collected by the photometer). In our case, we have obtained the corresponding experimental data, at two different axial positions of the beam (the knife-edge plane was placed at 4 cm and at 200 cm far away from the source). Corresponding results are shown in Figure 4-12 (a) and (b), respectively. A total of 82 different transmitted powers ($P(x)$) were measured in each case, for the 82 different x-displacements of the knife-edge. Each position step was of 100 μm long. As above-stated, the first x position corresponds to a knife-edge position where the laser beam was completely blocked, whereas the final x position was chosen when the power was constant and equal to $P_{\max}$.

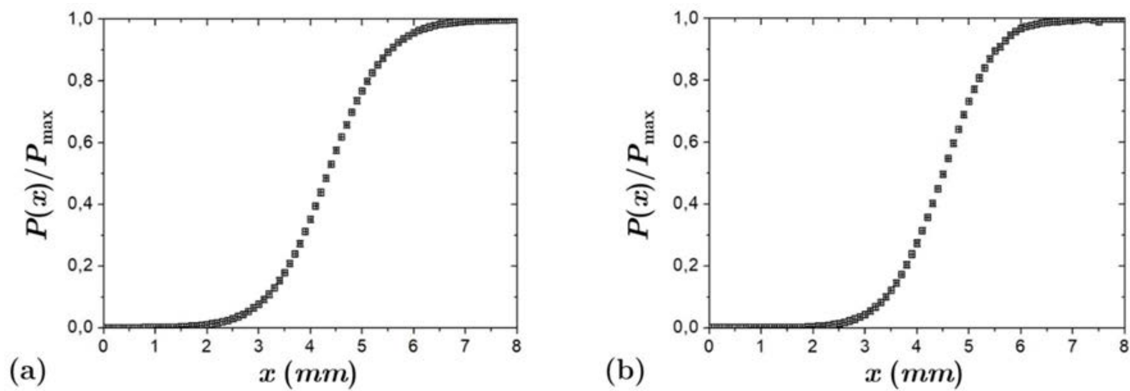

Figure 4-12. Plots of normalized optical power ($P(x)/P_{\max}$) versus knife-edge x-displacement, measured at (a) 4 cm; and (b) 2 m distances from the source.

In Ref. [175], the third degree approximation for the beam radius is obtained from power versus position curves. By using this approach and data in Figure 4-12, we calculated the experimental radius of the used laser beam, r_0. Note that the laser profile can be represented by a Gaussian function when representing the beam irradiance as a function of the beam spatial position in the direction of the radius. Therefore, different irradiance values are related to different Gaussian widths, and thus, to different radius values. In our case, we set as a beam radius that corresponding to an irradiance with a value of $I_{\max}/e$ ($I_{\max}$ is the maximum irradiance of the beam, found at its center of symmetry and e is the Euler's number). Under this scenario, the obtained radius values for the two evaluated axial positions are given in Table 4-2.

Position	r_0
(4 ± 1) cm	(1.75 ± 0.12) mm
(200 ± 1) cm	(1.69 ± 0.10) mm

Table 4-2. Calculated radius for two positions of the knife-edge.

From the results shown in Table 4-2, we see how the illumination beam is slightly convergent. The corresponding error in the laser beam radius is smaller than 7%. The

decrease of the beam radius is very small, so we consider the input beam as a good approximation of a collimated beam. Moreover, the diameter of the illumination beam is slightly smaller than the HNAO aperture (HNAO aperture = 5 *mm*).

In addition, from the obtained results, we simulated the corresponding irradiance pattern (I) of the Gaussian beam at these two positions (4 *cm* and 200 *cm*), following the expression given in Ref. [175]

$$I\left(x\right) = I_{\max} \exp\left[-2\frac{\left(x - x_0\right)^2}{r_0}\right] \tag{4.6}$$

where $I_{\max}$ is the maximum intensity of the beam at its center and x_0 is the coordinate of the center. Obtained results for the 4 *cm* and 200 *cm* distances are plotted in Figure 4-13 as blue and red lines, respectively. The green dashed line represents the value where the maximum intensity ($I_{\max}$) decreases to 1/e times its maximum value. Therefore, half of the distance between the points where the $I_{\max}$/e dashed line cuts the Gaussian profile corresponds to the radius r_0. Last but not least, we can see how for irradiances smaller than $I_{\max}$/e, the illumination beam radii are larger than r_0. Although the intensities at these irradiance ranges are very small, these Gaussian profiles can still produce diffraction effects in the experimental Mueller matrix image due to the interaction with the optical apertures in the set-up.

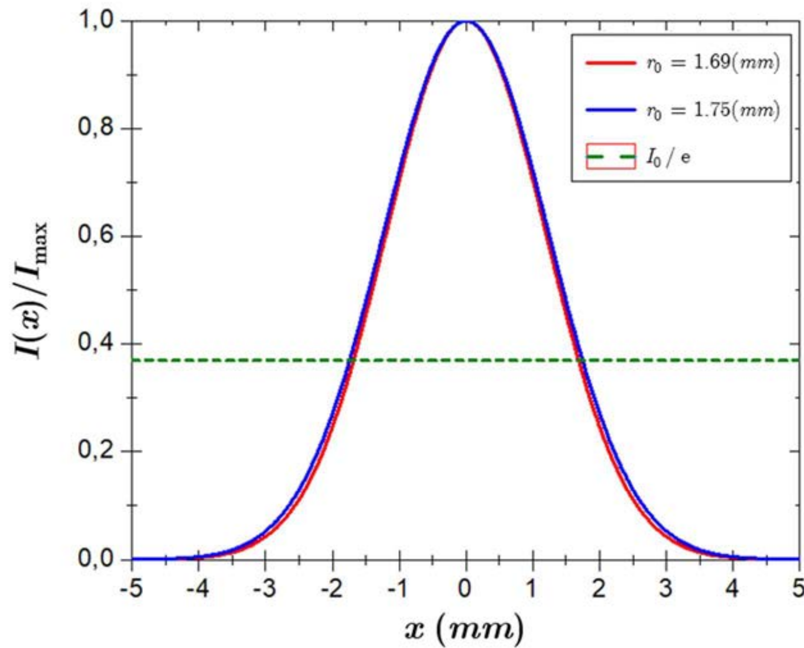

Figure 4-13. Gaussian profile for our input laser beam obtained at (a) 4 *cm* (blue line); and (b) 200 *cm* (red line). The dashed line (green colour) represents the value where the maximum intensity ($I_{\max}$) decreases to $1/e$ times its maximum value. The horizontal distance between the two values where the green dashed line cuts the Gaussian profiles is $2 \cdot r_0$.

4.2.2 Proper Alignment of the Microscope

Once the input beam was collimated to certain extent, we have built the conoscopic Mueller microscope considering the alignments concerns. The two main types of misalignments that can occur in our set-up are the parallel and the angular misalignments of the optical elements. The former occurs when there is an offset between the optical axis of the different optical elements and the direction of propagation of the laser beam. In turn, the latter occurs when there is an angular deviation between the optical axis elements and the laser beam direction. For the sake of clarity, these two situations are sketched in Figure 4-14. These two types of misalignments can exist in either the vertical or horizontal directions as well as in any combination of them. The effects of the misalignments between elements on the angle-resolved Mueller matrix are important because they reduce the image quality by introducing aberrations into the system.

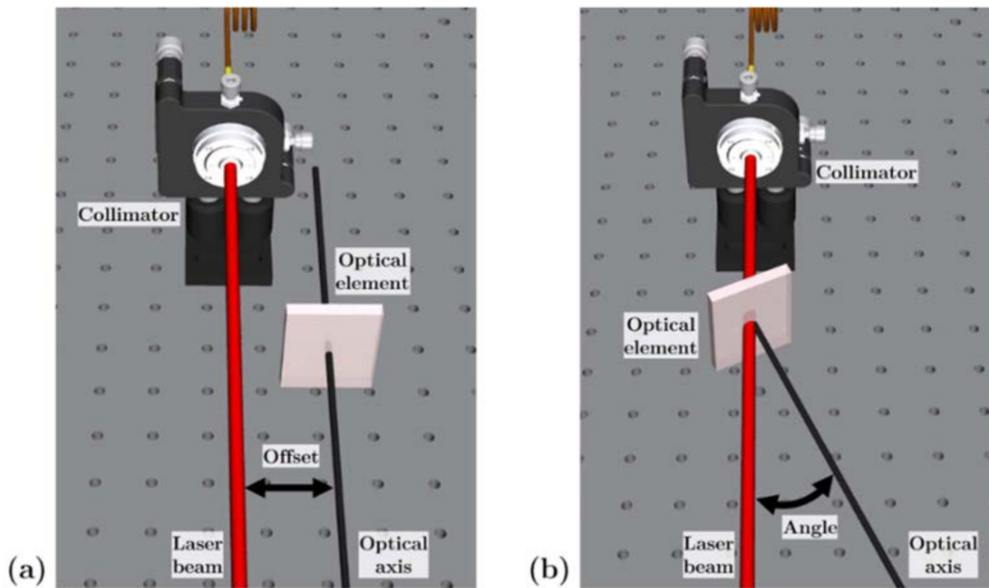

Figure 4-14. (a) Parallel; and (b) angular misalignments of an optical element with respect to collimated laser beam.

To correct the deviation of the laser beam produced by each optical element that defines our set-up, we have introduced high-precision holders that provide different degrees of freedom, i.e., displacements along the Cartesian axis and rotations. These should allow us to accurately align the set-up, leading to a minimization of the misalignment errors.

In addition, to define the optical axis of our set-up, we used two irises, which can be considered as two punctual points placed at two different axial positions. For a proper alignment, any incident, transmitted or reflected beam must pass through these two small apertures, and thus, they become our references during the alignment process.

The most critical part in this procedure is the alignment of the HNAO that requires highly sensitive alignment. Let us start by explaining the steps followed to build the illumination and detection arms, as well as the sample positioning system of our conoscopic Mueller microscope.

The optical breadboard is fixed parallel to the optical isolation table and the zoom fiber collimator is placed on it. The optic fiber collimator is placed in a 6-axis kinematic optic mount (*Thorlabs, K6XS*) so that the illumination beam can be adjusted with high precision along 6 axes. As the propagation of the collimated laser beam marks the optical axis of the system, its direction of propagation is chosen parallel to the lines defined by the holes grid in the breadboard and to the optical table surface, facilitating the alignment process.

Next, the PSG, that controls and manipulates the polarization of the illumination beam, is placed near the light source. The misalignments introduced by the PSG may be corrected by displacing the linear polarizer. We assume that the LCDs forming the PSG and PSA are thin enough, so we can neglect the defocus and the shift of the beam when adding them in the light path.

Following, the non-polarizing beam-splitter is placed in a platform, which allows correcting the pitch and yaw tilt misalignments. After passing through the beam-splitter, the illumination beam is divided into one transmitted beam and one reflected beam. Then, two mirrors are located as far away as possible from the NP-BS (see M_1 and M_2 in Figure 4-15). As a consequence, the reflected and transmitted beams are reflected back, returning to the non-polarizing beam-splitter. In this sense, a Michelson interferometer is created. Taking into account the interference patterns produced according to the NP-BS positioning, its orientation is accurately corrected. The designed Michelson interferometer is shown in Figure 4-15.

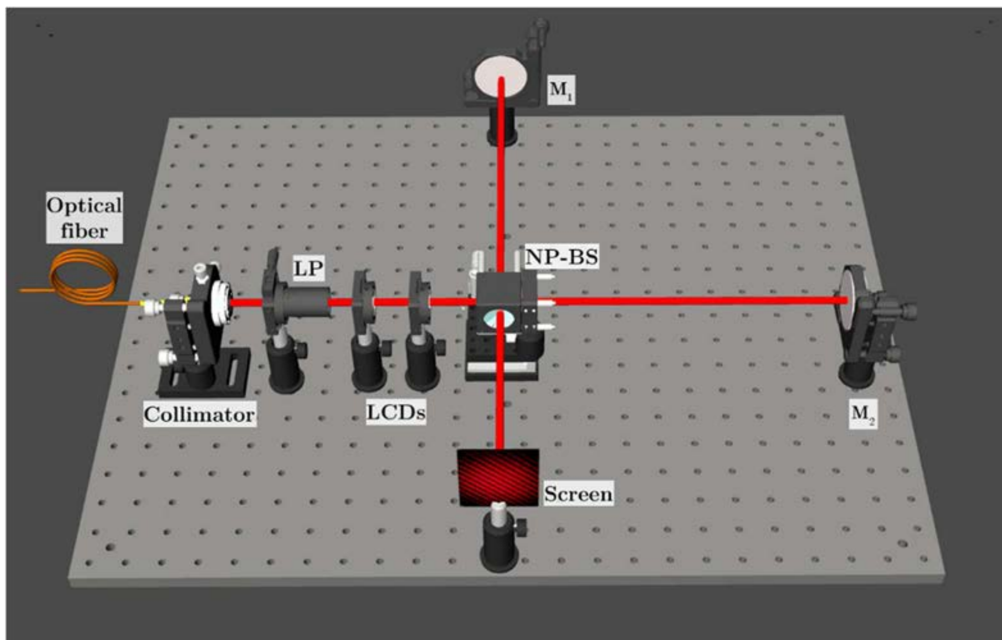

Figure 4-15. Michelson interferometer built to align the non-polarizing beam-splitter (NP-BS). The reflected and transmitted beams are reflected on the mirrors M_1 and M_2, respectively. Afterwards, they propagate back to the NP-BS and coherently recombine. The recombination of the two beams produces a pattern of interference, which can be observed by using a screen. The particular orientation and period of the interference fringes is related to misalignments on the NP-BS and is used to correct its positioning in the set-up.

Next, the optical breadboard is mounted vertically on a horizontal optical table using 90° breadboard angle brackets. This allows us to set the direction of the illumination and the NP-BS transmitted beams parallel to the laboratory vertical axis. The transport and re-collocation of the optical breadboard over the horizontal optical table can produce misalignments of the optical elements, mainly of the NP-BS, which is the element most sensitive to misalignments. By using the Michelson interferometer, all the possible misalignments produced during the relocation can be controlled and solved quickly.

Then, the PSA and the CMOS camera are placed in the set-up. This is done by specially controlling the beam deviation produced by the linear analyzer. Finally, the position of the camera has to be adjusted ensuring that detection beam is centered (see Figure 4-16). Note that for the alignment of the PSA and the CMOS camera, the laser light reflected from the M_1 mirror is used as reference as it was previously accurately aligned. In other words, M_1 sets the optical axis of the detection arm and thus, the position of M_1 is never changed to keep this reference.

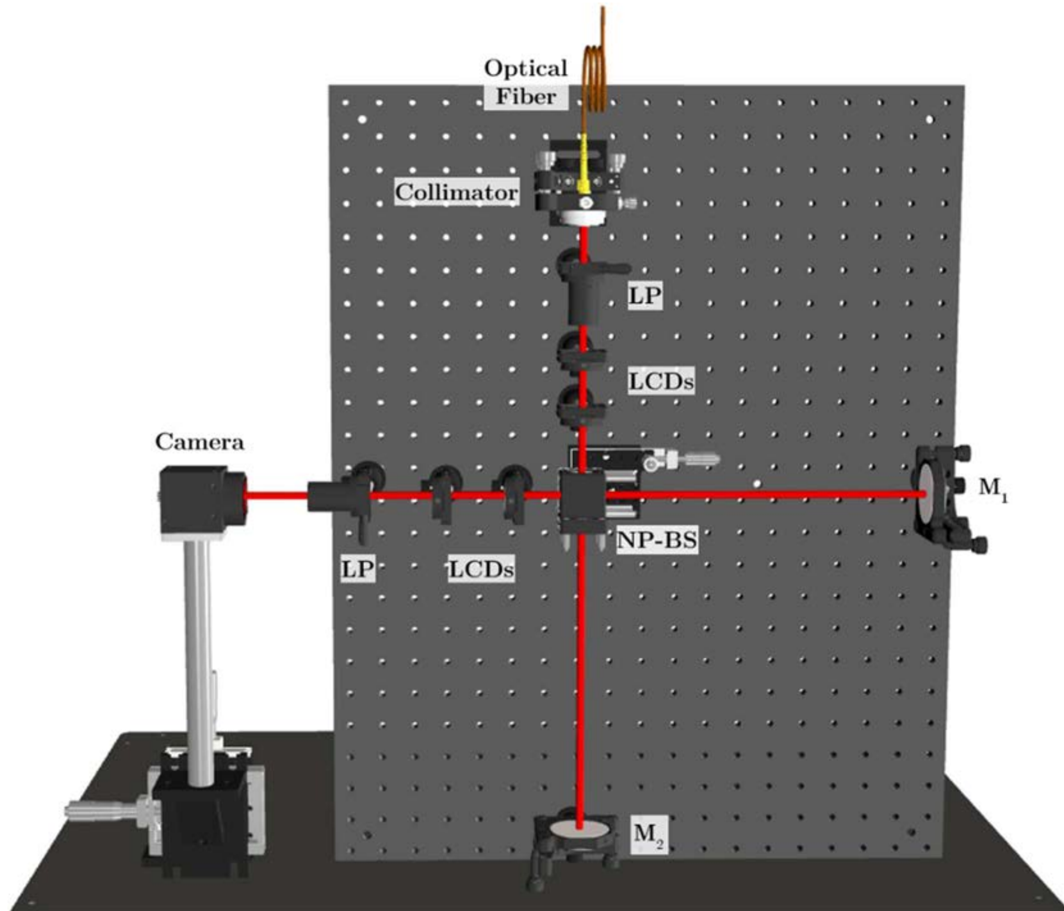

Figure 4-16. Set-up for the alignment of the Polarization State Analyzer and the CMOS camera.

At this point, the mirror reflecting light transmitted at the beam-splitter (M_2) is removed from the system to make room to the holder where the samples are placed. Finally, when a sample is inserted in the sample holder, and the transmitted beam is reflected back on the sample surface, the orientation of the sample has to be accurately

adjusted until the beam coming from the sample is as parallel as possible to the optical axis of the detection arm (light reflected on M_1).

We want to emphasize that the sample positioning system present in the sample holder is set in the laboratory horizontal optical table, separated from the vertical breadboard, so that any vibration caused by moving the sample do not affect the alignment of the microscope system, specially of the high numerical aperture objective.

4.2.3 High *NA* Microscope Objective aligning method

The alignment of a 100× microscope objective is very critical, and results in a very challenging process.

The method used to align the 100× microscope is following described. A high reflective plane mirror is placed at the sample plane on the sample positioning system (let us call it M_0). The NP-BS splits the collimated laser beam into two beams, as shown in Figure 4-16. The partially transmitted beam travels to the mirror M_0, placed at the sample plane, and the partially reflected one travels to mirror M_1. When the mirror M_0 is properly aligned, the reflected beams travel parallel to the detection arm axis.

As a first approximation, the HNAO-holder, where the 100× microscope will be placed, is afterwards set in the vertical breadboard and adjusted until the light beam passes just through its center. Then, the high numerical aperture objective is inserted in the HNAO-holder, which consists of a combination of two different holders. By properly adjusting these two holders, the alignment of the microscope can be corrected. In particular, one holder allows us to align the HNAO in *XY* position (*x*-*y* translation platform) and the other allow us to align the angle (tip and tilt optic mount). The mirror set in the sample positioner (M_0) is shifted in *z*-direction by using the motorized platform to focus the incident light beam on the mirror surface. The camera is used to analyze the conoscopic pattern produced by sample mirror. By properly selecting the polarization of the PSG and PSA systems, the intensity distribution obtained at the CMOS camera, corresponding to the sample M_0, shows a symmetric pattern, that can be used to facilitate the alignment process. In fact, HNAO misalignments result in visible asymmetric images in the CMOS camera. When the observed pattern in the camera is as symmetric as possible, and the reflected beam is collimated, we consider that the conoscopic Mueller microscope is built and well-aligned.

The actual implementation of the conoscopic Mueller microscope we have built in the laboratory is shown in Figure 4-17. The main components are labeled to show the optical elements.

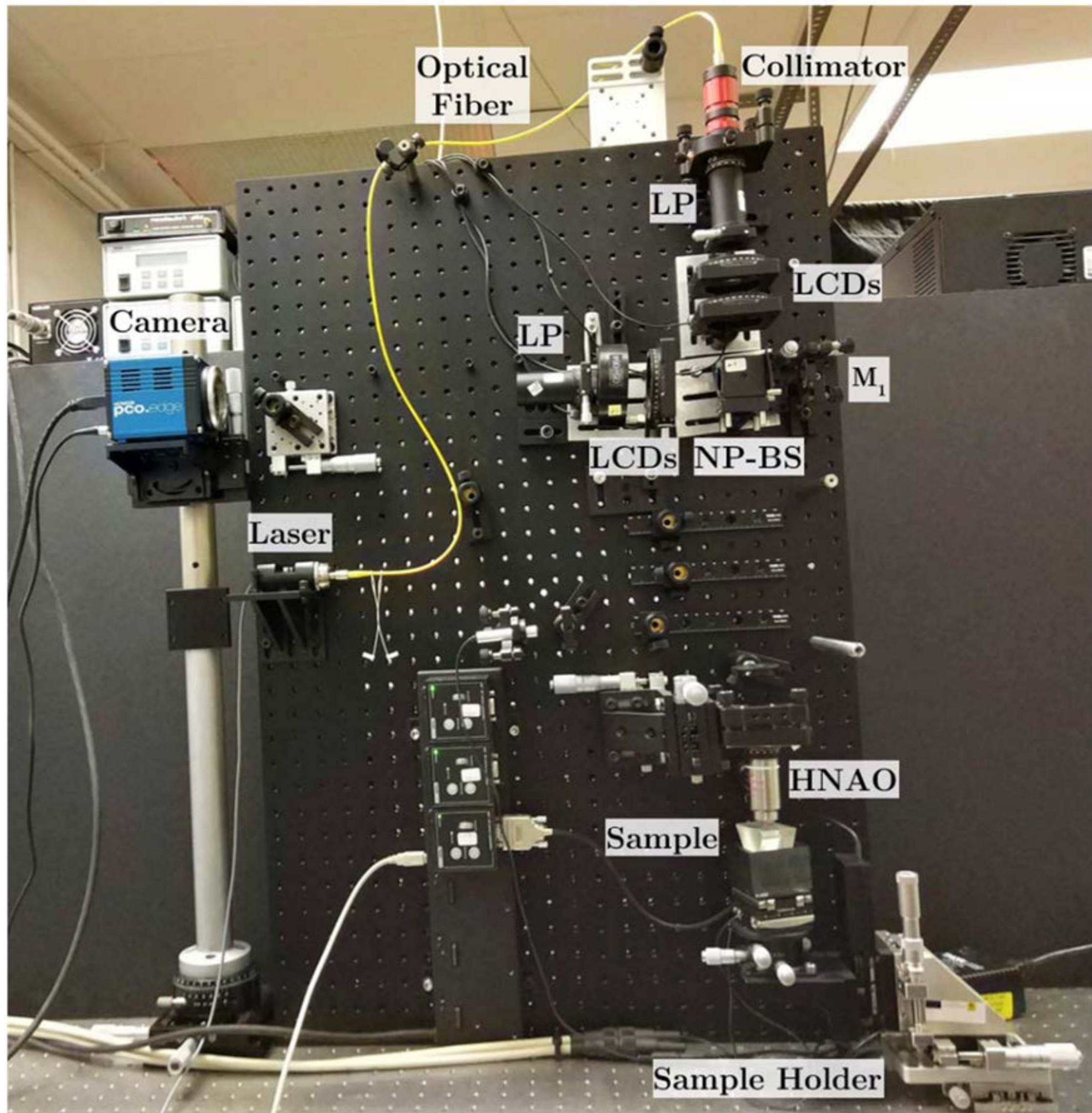

Figure 4-17. Actual implementation of the conoscopic Mueller microscope in our laboratory.

4.3 Calibration

Experimental implementations always introduce small differences with expected theoretical parameters. For instance, the polarization elements used to build our conoscopic Mueller microscope (LCD, polarizers, non-polarizing beam-splitter, etc.) always present certain limit in the angular positioning, and their polarimetric values (retardances, transmittances, etc.) are not ideal, or may slightly variate with time. For this reason, an accurate polarimetric calibration of the system is always required in experimental implementations. The calibration process is done in two parts. First, the different polarization elements are calibrated and then whole set-up is tested.

4.3.1 Beam-splitter calibration

Although the used NP-BS is specifically designed for applications in which polarization effects must be minimized, we have observed that the beam-splitter cube introduces a small retardance that has to be taken into account. Any small polarization effect can be critical because light passes twice in the NP-BS, once the input beam and once the reflected beam. As a consequence, the non-polarizing beam-splitter was characterized by measuring the Mueller matrix both in transmission and in reflection before being placed in the final set-up.

By using a Mueller matrix dual-rotating retarder polarimeter given in Refs. [163–166], the experimental Mueller matrices of the NP-BS for reflection and transmission were obtained. Figure 4-18 shows the schemes of two set-ups used to calibrate the NP-BS in transmission and in reflection. Ideally, the Mueller matrices of the NP-BS should be close to the identity matrix, but the measured matrices, given in Table 4-3 and Table 4-4, show some important differences. From the measured $\boldsymbol{M}_{\text{measured}}$ matrices, and by using the Lu-Chipman decomposition [111, 177], the Mueller matrices of the equivalent retarders and diattenuators were calculated (see $\boldsymbol{M}_{\text{diattenuator}}$ and $\boldsymbol{M}_{\text{retarder}}$ in Table 4-3 and Table 4-4).

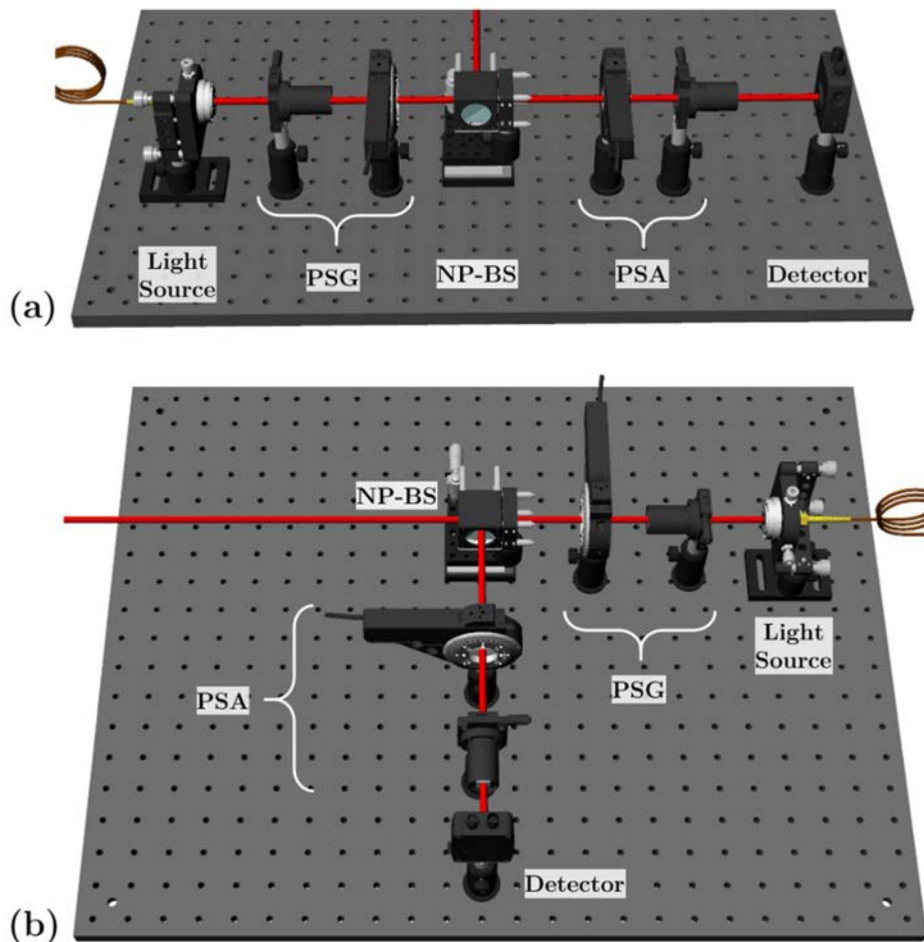

Figure 4-18. Schemes of the set-ups used for measuring the Mueller matrix of the non-polarizing beam-splitter (NP-BS): (a) in transmission; and (b) in reflection.

Normalized Mueller matrices of the NP-BS measured in reflection	
Measured Mueller Matrix	$\boldsymbol{M}_{\text{measured}} = \begin{pmatrix} 1.0000 & 0.0137 & 0.0018 & -0.0057 \\ -0.0122 & 0.9707 & -0.1488 & -0.0544 \\ -0.0093 & -0.1468 & -0.7254 & -0.6437 \\ 0.0116 & 0.0414 & 0.6609 & -0.7345 \end{pmatrix}$
Diattenuator Matrix	$\boldsymbol{M}_{\text{diattenuator}} = \begin{pmatrix} 1.000 & 0.014 & 0.002 & -0.006 \\ 0.014 & 1.000 & 0.000 & 0.000 \\ 0.002 & 0.000 & 1.000 & 0.000 \\ -0.006 & 0.000 & 0.000 & 1.000 \end{pmatrix}$
Retarder Matrix	$\boldsymbol{M}_{\text{retarder}} = \begin{pmatrix} 1 & 0 & 0 & 0 \\ 0 & 0.987 & -0.145 & -0.062 \\ 0 & -0.150 & -0.735 & -0.661 \\ 0 & 0.050 & 0.662 & -0.748 \end{pmatrix}$

Table 4-3. Normalized Mueller matrices of the non-polarizing beam-splitter measured in reflection. $\boldsymbol{M}_{\text{diattenuator}}$ and $\boldsymbol{M}_{\text{retarder}}$ are obtained from Lu-Chipman decomposition of the measured Mueller matrix ($\boldsymbol{M}_{\text{measured}}$).

The diattenuation $D(M)$ of a Mueller matrix is a measure of the variation of intensity transmittance with the incident SoPs and can be obtained from [111, 112]

$$D(M) = \frac{\sqrt{m_{01}^2 + m_{02}^2 + m_{03}^2}}{m_{00}} \tag{4.7}$$

The total retardance R can be found from [111]

$$R = \arccos\left(\frac{Tr\left(M_{\text{retarder}}\right)}{2}\right) - 1 \tag{4.8}$$

where Tr denotes the trace of the matrix $\boldsymbol{M}_{\text{retarder}}$.

The values of retardance and diattenuation introduced by the NP-BS to the light beam in transmission and reflection are obtained from Eqs. (4.7) and (4.8). In transmission, we obtain $R_T = 10.53°$ and $D_T = 0.018$, while in reflection $R_R = 138.39°$ and $D_R = 0.015$. From these results, we observe how the diattenuation values introduced by the NP-BS can be neglected, but non-negligible retardance transformations into the reflected and transmitted light beams are introduced by such device. Therefore, they have to be taken into account for the beam propagation modeling.

In addition, we have notice that the antireflective coating deposited on each face of the beam-splitter cube to minimize unwanted reflections is not perfect and dual images appear on the camera. The unwanted reflections are blocked using a diaphragm during the measuring process.

Normalized Mueller matrices of the NP-BS measured in transmission	
Measured	$\boldsymbol{M}_{\text{measured}} = \begin{pmatrix} 1 & 0{,}0030 & -0{,}0163 & 0{,}0064 \\ 0{,}0030 & 0{,}9716 & 0{,}0072 & 0{,}0148 \\ 0{,}0240 & 0{,}0033 & 0{,}9501 & 0{,}1758 \\ 0{,}0102 & -0{,}0125 & -0{,}1776 & 0{,}9530 \end{pmatrix}$
Diattenuator	$\boldsymbol{M}_{\text{diattenuator}} = \begin{pmatrix} 1.000 & 0.003 & -0.002 & 0.006 \\ 0.003 & 1.000 & 0.000 & 0.000 \\ -0.002 & 0.000 & 1.000 & 0.000 \\ 0.006 & 0.000 & 0.000 & 1.000 \end{pmatrix}$
Retarder	$\boldsymbol{M}_{\text{retarder}} = \begin{pmatrix} 1 & 0 & 0 & 0 \\ 0 & 1.000 & 0.001 & 0.013 \\ 0 & -0.003 & 0.983 & 0.182 \\ 0 & -0.013 & -0.182 & 0.983 \end{pmatrix}$

Table 4-4. Normalized Mueller matrices of the non-polarizing beam-splitter measured in transmission. $\boldsymbol{M}_{\text{diattenuator}}$ and $\boldsymbol{M}_{\text{retarder}}$ are obtained from Lu-Chipman decomposition of the $\boldsymbol{M}_{\text{measured}}$ Mueller matrix.

4.3.2 PSG and PSA calibration

In section 4.1.1, it was introduced that the PSG and the PSA consist of a linear polarizer and two thermally stabilized liquid crystal variable retarders. The proposed PSG and PSA are able to implement any polarization generator and analyzer by properly selecting the orientation of the fast axis of the LCDs, $\psi_1 = \psi_4 = 45^{\text{o}}$ and $\psi_2 = \psi_3 = 0^{\text{o}}$, and their pair of retardances, (δ_1, δ_2) and (δ_3, δ_4).

The LCDs supplier company provides the function that relates the retardance of the liquid crystal panel and the applied voltage for a set of wavelengths. Since the LCDs performance depends on the operating temperature and the particular used wavelength, in order to get better accuracy, the PSG and the PSA should be calibrated. In addition, the NP-BS introduce an extra retardance, both in reflection and in transmission (see Table 4-3 and Table 4-4), that has to be considered during the calibration process, because generated input polarizations and output analyzers are affected by this extra retardance. Therefore, to include the NP-BS effect and accurately calibrate the incident SoPs and the analyzers of the system, we have calibrated the PSG including the NP-BS in transmission, and the PSA with the beam-splitter in reflection.

The procedure followed to calibrate the PSG and PSA systems, including the effects introduced by the NP-BS element, are followed discussed.

a) PSG and NP-BS in transmission calibration

To accurately calibrate the generated SoPs, we have measured the polarization of the incident beam after the beam-splitter, this being the actual polarization incident to the HNAO. As the retardance introduced by the non-polarizing beam-splitter in transmission is constant, the states of polarization generated by the PSG + NP-BS system are only function of the pair of retardances (δ_1 and δ_2).

Therefore, different pair of voltages were applied to the LCDs and the generated SoPs were measured, after the light beam passes through the NP-BS, using a commercial polarimeter (*Thorlabs, PAX5710VIS-T*). The measurement process of the commercial polarimeter consists of a rotating quarter waveplate, a fixed polarizer and a photodiode, and it is able to analyze the state of polarization and the degree of polarization of an optical signal. The accuracy of the used polarimeter is of 0.2° for the azimuth angle, of 0.2° for the ellipticity angle, and of 0.005 for the normalized Stokes components (S_1, S_2, S_3).

Figure 4-19 shows the scheme of the PSG calibration. A look-up-table was created to contain the voltages applied to LCD_1 and LCD_2 and their respective generated SoPs. A total of 10,000 states of polarization were generated by using voltages steps of $0.02\,V$ and $0.05\,V$ for the LCD_1 and LCD_2, respectively. In that way, the created SoPs were uniformly distributed on the Poincaré sphere surface. The liquid crystals were thermally stabilized during the calibration process to 33°C.

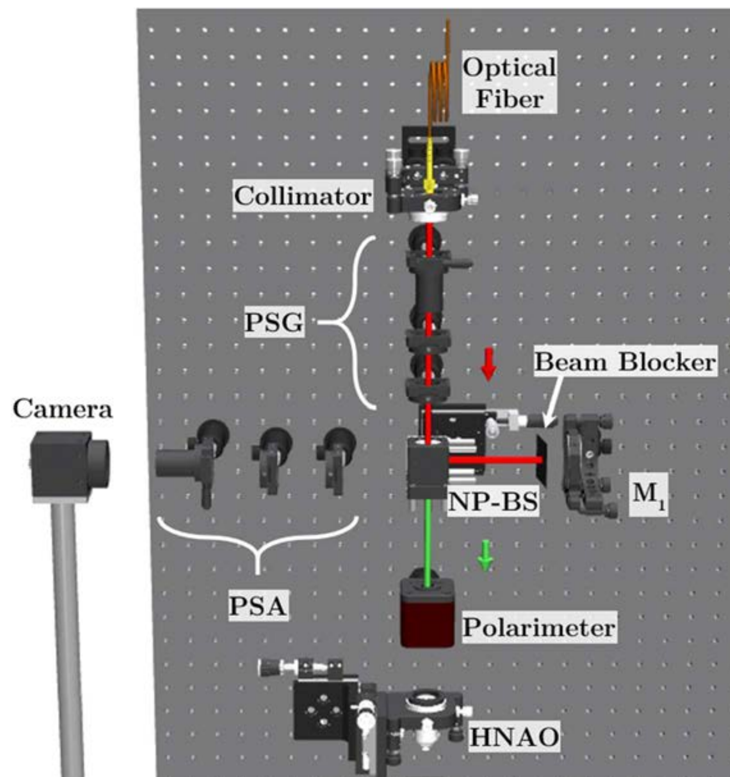

Figure 4-19. Calibration of the polarization state generator (PSG) and the non-polarizing beam-splitter (NP-BS) in transmission using a commercial polarimeter. The light beam reflected by the NP-BS is blocked by using a Beam Blocker.

In order to fully characterize the Mueller matrix of polarimetric samples, only a small set of polarizations, from the whole 10,000 generated SoPs, are needed. In fact, the minimum number of polarization states required to form a polarization generator basis is of 4 SoPs. To make the conoscopic Mueller microscope less sensitive to errors and noise but, at the same time, to have a small measuring and processing time, we use the basis of 6 generators explained in section 3.2.4.

By using the look-up-table relating the 10,000 experimental SoPs, we used a programming code able to find those SoPs closer to the six theoretical values we are interested in (see Figure 3-7), and the corresponding voltages required to generate them. The six obtained polarizations states are given in Table 4-5. Note that as the Stokes vector $\boldsymbol{S}$ is normalized, S_0 is equal to 1.

Polarizations	$\boldsymbol{S_1}$	$\boldsymbol{S_2}$	$\boldsymbol{S_3}$	$\boldsymbol{V_1}$	$\boldsymbol{V_2}$
Horizontal linear	0.999795	-0.01993	-0.00371	1.234	1.440
Vertical linear	-0.99998	0.005658	-0.00248	1.665	3.250
45° linear	-0.002470	0.999974	-0.00679	4.321	1.465
135° linear	0.001629	-0.99996	0.00873	2.382	3.650
Right circular	-0.01644	-0.01145	0.999799	2.822	2.030
Left circular	0.001387	0.018235	-0.99983	3.090	1.010

Table 4-5. Normalized states of polarization obtained after the calibration of the PSG and the beam-splitter in transmission. V_1 is the voltage applied to LCD_1 and V_2 is the voltage applied to LCD_2.

Although the LCDs are thermally stabilized and their axes as well as the polarizer axis are fixed, the PSG needs regular calibration to ensure that it is properly working and measuring accurately. In this sense, the calibration process is reduced to measure the SoPs generated by the six pairs of voltages given in Table 4-5. The polarization states obtained after every recalibration are always very close to the theoretical ones shown in Figure 3-7. This method allows us to frequently recalibrate the PSG system, having an accurate input SoPs basis and minimizing the calibration time. In addition, during each calibration, the six generated states of polarizations were measured ten times and their averages were used to compute the generator matrix $\boldsymbol{S}$ (see Eq. (3.12)).

b) PSA and NP-BS in reflection calibration

To calibrate the polarization state analyzer system, including the effect of the non-polarizing beam-splitter in reflection (i.e., the NP-BS + PSA system), we have used as polarized incident beams those calibrated in the previous section. As the Mueller polarimeter works in reflection, we have placed a mirror in the sample holder to reflect the polarized incident beam and steer it back to the NP-BS. The beams reflected by the mirror (backwards propagation) are those considered as the input beams to the NP-BS + PSA system. Note that the polarization of the beams illuminating the NP-BS + PSA system is

the one set by the PSG + NP-BS system (already calibrated), affected by the mirror reflection. Once the reflected beam passes through the PSA, a photodetector is used to analyze the intensity of the beam at the exit of the system. Figure 4-20 shows a scheme of the set-up used to calibrate the detection arm.

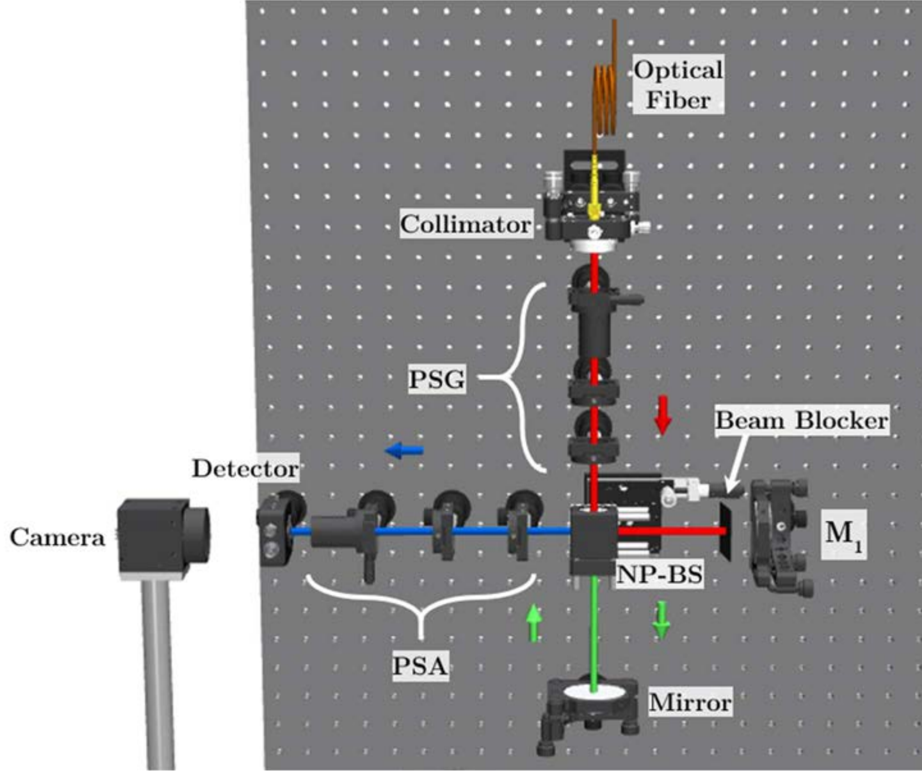

Figure 4-20. Calibration of the non-polarizing beam-splitter (NP-BS) + PSA system by using the PSG to generate the incident SoPs. The effect of a mirror used to reflect the incident beam must be considered. A photodetector is used to measure the beam intensities after the PSA. Red, green and blue arrows show the direction of propagation of light at different system sectors. A beam blocker removes the effect of light coming from the M_1 mirror.

The intensity of the beam measured by the detector is the projection of the polarization state reflected by the mirror over the unknown polarization analyzers (see Eq. (3.10)). To calibrate the analyzers, the six different SoPs obtained during the PSG calibration are used to illuminate the system. For a particular pair of voltages set to the LCDs of the PSA, six intensity measures are obtained corresponding to the six used input SoPs, leading to a system of independent linear equations similar to Eq. (3.12). In particular, the polarization analyzer $\boldsymbol{a}$, corresponding to a selected pair of voltages, is given by [178]

$$\boldsymbol{a} = \boldsymbol{B} \cdot \boldsymbol{S}_P^{-1} \tag{4.9}$$

where $\boldsymbol{B} = (I_1 \ldots I_6)$ is the 1×6 intensity vector and $\boldsymbol{S}_P^{-1}$ is the pseudoinverse matrix of the 4×6 incident Stokes matrix $\boldsymbol{S} = \boldsymbol{M}_{\text{mirror}} \cdot (\boldsymbol{S}_{in,1} \ldots \boldsymbol{S}_{in,6})$, where the six different $\boldsymbol{S}_{in,i}$ are arranged in column. As the direction of propagation of the incident beam is perpendicular to the plane mirror surface, the Mueller matrix of the mirror can be written as [111]

$$\boldsymbol{M}_{\text{mirror}} = \begin{pmatrix} 1 & 0 & 0 & 0 \\ 0 & 1 & 0 & 0 \\ 0 & 0 & -1 & 0 \\ 0 & 0 & 0 & -1 \end{pmatrix} \tag{4.10}$$

Equation (4.9) describes the basic prescription for the experimental measurement of a polarization analyzer $\boldsymbol{a}$. The same procedure is repeated for different pair of retardances, δ_3 and δ_4, of the liquid crystal panels of the PSA, this constituting the different analyzers a_i. This sequential method allowed us to calibrate 10,000 different analyzers. From this set of analyzers, 6 polarization analyzers were selected (the ones described in section 3.2.4) to form the analyzer matrix $\boldsymbol{A}$. Table 4-6 gives the normalized ($A_0 = 1$) experimentally measured analyzer vectors closer to the theoretical analyzers shown in Figure 3-7, and their corresponding pair of voltages.

Polarizations	$\boldsymbol{A}_1$	$\boldsymbol{A}_2$	$\boldsymbol{A}_3$	$\boldsymbol{V}_3$	$\boldsymbol{V}_4$
Horizontal linear	1.009	-0.077	0.055	5.30	1.61
Vertical linear	-0.991	-0.056	0.019	1.93	0.75
45° linear	0.007	0.989	0.083	1.54	1.50
135° linear	0.088	-1.014	0.117	2.74	1.52
Right circular	0.001	-0.005	1.022	2.63	2.15
Left circular	-0.012	0.007	-0.971	1.52	2.15

Table 4-6. Normalized polarization analyzers obtained after the calibration of the PSA, including the effects of the beam-splitter in reflection. V_3 is the voltage applied to LCD3 and V_4 is the voltage applied to LCD_4.

As in the PSG calibration case, the PSA is regularly recalibrated. Nevertheless, only the pair of voltages shown in Table 4-6 are applied to the LCDs during the recalibration. The analyzers are measured 10 times during each calibration and then are averaged to calculate the matrix $\boldsymbol{A}$, that is always close to the theoretical one.

c) PSG and PSA validation

The SoPs obtained after the calibration (PSG in Table 4-5 and PSA Table 4-6) are represented over the Poincaré sphere in Figure 4-21 (a) and (b), respectively. Although the matrices $\boldsymbol{S}$ and $\boldsymbol{A}$ are close to the optimized polarizations described in section 3.2.4, the calibrated SoPs (red spots over the Poincaré sphere) present small deviations from the theoretical values (blue spots over the Poincaré sphere), especially for the PSA case. However, the experimental Mueller polarimeter defined by the calibrated $\boldsymbol{S}$ and $\boldsymbol{A}$ matrices is still very well-conditioned, minimizing the noise amplification (the $CN(\text{PSG}) = 1.76$ and the $CN(\text{PSA}) = 1.78$; note that the theoretical minimum is $\sqrt{3} \sim 1.73$ (section 3.2.4)).

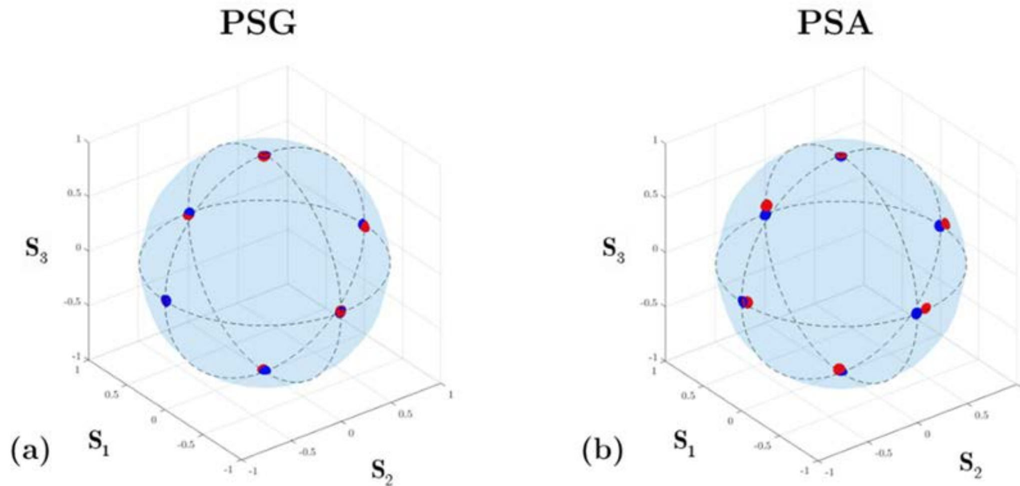

Figure 4-21. Representation of the six states of polarization chosen to form: (a) the matrix $\boldsymbol{S}$; and (b) the matrix $\boldsymbol{A}$. Red spots show the experimentally calibrated SoPs and blue spots show the theoretical expected SoPs.

4.3.3 CMOS camera calibration

Each pixel of the CMOS camera may have different dark noise properties at a particular temperature and exposure time. Taking into account that the goal of the conoscopic Mueller microscope is to measure isotropic samples and uniaxial anisotropic crystals in a reflective configuration, intensity values acquired by the CMOS camera may be very small (i.e., in some cases, the camera may work in low intensity conditions due to the reflective measure of dielectrics). For this reason, the camera was tested to determine the background noise effect on the error of the measure, trying to minimize it. Some references as [179] propose to calibrate the camera by acquiring a number of dark frames in total darkness and averaging them. In this sense, some measurements were taken to analyze the dark noise, varying the exposure time of the camera as well as the Frame Average (FA).

Let us start by analyzing dark images obtained for different number of averaged frames. Figure 4-22 shows four images for 1, 10, 30 and 100 averaged snapshots. We observe how the background image is more uniform when averaging larger number of images (100 averaged images). Similarly, intensity images can present errors in some pixels for low intensities. For this reason, each intensity image used for the SoPs calculations is obtained from the average of a number of snapshots. In particular, to minimize the measuring time, we decided to average 30 snapshots per measure.

Dark images were also obtained by varying the exposure time. Figure 4-23 shows four dark images for 30 averaged snapshots. Based on these results, a small exposure time (1 *ms* or lower) is desired to reduce dark noise produced by the camera. Note that some PSG-PSA configurations imply low intensity measures, thus, small exposure times are interesting for accurate Mueller matrix images, independently of the sample reflectivity.

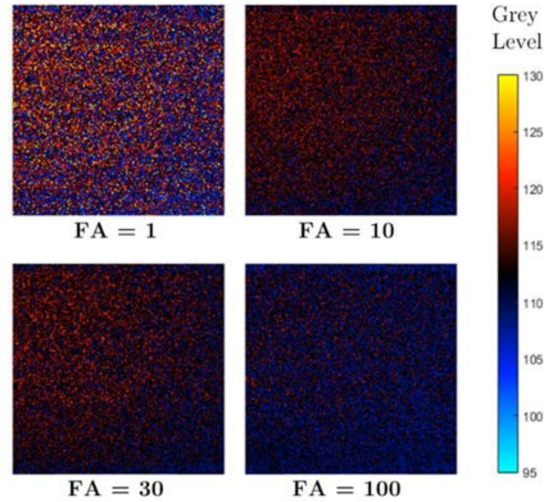

Figure 4-22. Background images obtained by averaging a different number of frames (FA): (a) 1, (b) 10, (c) 30; and (d) 100. The color bar shows the grey level value (maximum grey level of 65536 (16-bit)).

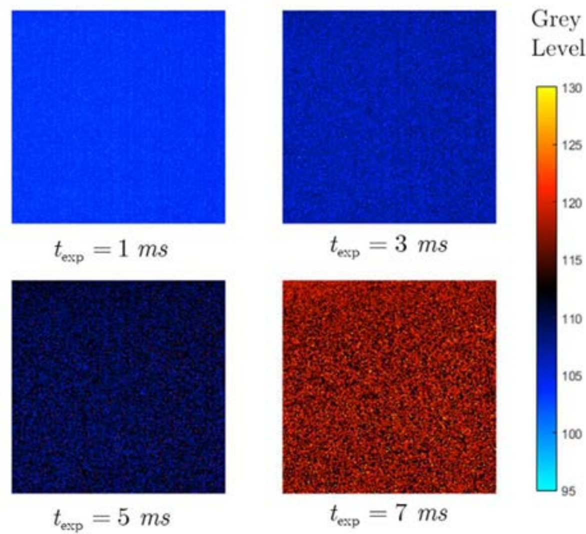

Figure 4-23. Dark images obtained with different exposure time for 30 averaged snapshots. The color bar shows the grey level value (maximum grey level of 65536 (16-bit)).

As dark noise is temperature dependent, the used camera is warmed up before being applied and dark images are taken each time the Mueller matrix image is measured. The obtained dark image is subtracted from the intensity images acquired by the camera, minimizing the background random noise.

Chapter 5 Results: Validation, applications and perspectives

In the previous chapters, the design and experimental implementation of a conoscopic Mueller microscope working in reflection that is able to measure the angular-resolved Mueller matrix image of dielectric isotropic and uniaxial anisotropic samples, as well as the mathematical model proposed to obtain the optical parameters of interest (refractive indices and, when it exists, the orientation of the optical axis) have been presented. The first part of this chapter analyzes the validity of the reflective Mueller polarimeter (section 5.1) and describes some filtering techniques posteriorly used to improve the measured Mueller matrix images (section 5.2). Then, in section 5.3, the high numerical aperture objective is calibrated and introduced in the set-up to convert the reflective polarimeter in a conoscopic Mueller microscope able to measure angle-resolved Mueller matrices. The aim of the current chapter is to show the measured data and the best-fit parameters for some materials. In this regard, different samples with diverse physical characteristics (isotropic, anisotropic, planar and curved surfaces) were measured to provide the potential of the method. Finally, some perspectives are discussed in section 5.4, which may enhance the performance of the method.

5.1 Experimental validation of the reflective Mueller polarimeter

Before measuring any isotropic or uniaxial anisotropic sample with our conoscopic Mueller microscope, the Mueller polarimeter built in the laboratory is tested to assess its accuracy and repeatability.

To validate the Mueller polarimeter some Mueller matrix images of well-known polarimetric samples are measured. The experimental Mueller matrix images are calculated by using Eq. (3.16), where the intensity vector $\vec{\boldsymbol{B}}_{i,j}$ for each sample is measured with the CMOS camera. The obtained images were analyzed and compared with the expected theoretical results. As the used test-samples are transmissive samples (as polarizers or

waveplates), but we measure in a reflective configuration, we have placed a plane mirror at the back of samples, to reflect light back and to steer it to the PSA arm. The instrumental configuration set to validate the samples is similar to that shown in Figure 4-20 (PSA calibration configuration). The test samples are placed between the NP-BS and the mirror in a double-pass configuration of the polarimeter. Note that light passes twice across the measured sample, propagating in opposite directions (forward and backward propagations). The equation that represents a general double-pass Mueller matrix image is

$$\boldsymbol{M}_{\mathrm{DP}} = \boldsymbol{M}^{-}{}_{\mathrm{sample}} \cdot \boldsymbol{M}_{\mathrm{mirror}} \cdot \boldsymbol{M}^{+}{}_{\mathrm{sample}} \tag{5.1}$$

where the "DP" subscript stands for *double-pass* configuration, $\boldsymbol{M}_{\mathrm{mirror}}$ (see Eq. (4.10)) represents the Mueller matrix of the used plane dielectric mirror placed normal to the incident beam and the plus and minus signs indicate the direction of light when passing through the sample. The plus sign corresponds to the forward direction, when light propagated towards the mirror, and the minus sign to the backward direction, when light had already been reflected and travels away from the mirror, towards the NP-BS.

Figure 5-1 shows the measured Mueller matrix image of the plane mirror used during the calibration process and a simulation of the expected Mueller matrix image, where an excellent agreement is observed.

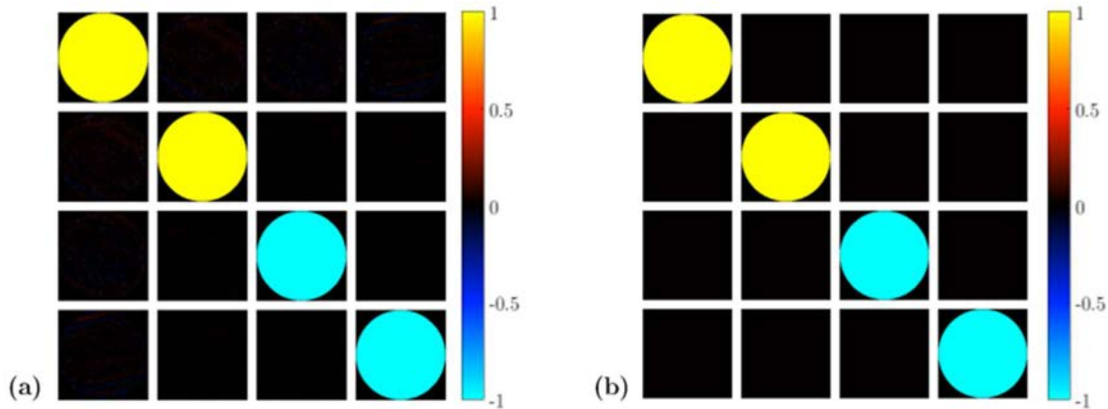

Figure 5-1. Mueller matrix image of a mirror obtained after the PSG and PSA calibration. (a) Real measure; and (b) simulation.

The polarimetric response across the pupil of the Mueller matrices can be quantitatively seen from cross-sections set along the Mueller coefficients images. To this end, cross-sections along two directions were taken to compare the variations between some Mueller matrix elements observed in Figure 5-1. The two cross-sections pass through the center of the images, one of them is parallel to the horizontal and another is parallel to the vertical. The obtained results are provided in Figure 5-2 (a) and (b), respectively. In each case, the coefficients cross-sections were obtained for the theoretical and the experimental Mueller matrix images, being represented as red and blue colors, respectively, in Figure 5-2. The error of the experimental image can be observed in some components, as M_{01}, M_{02}, M_{10} and M_{20}. The averaged Mean Absolute Error (MAE) of each pixel on the experimental normalized Mueller matrix image is 0.003 (this is a ~0.15% error taking into account the full M coefficient range $[-1, 1]$), that is calculated by using

$$MAE = \frac{\sum_{i=1}^{N}\sum_{j,k=0}^{4}\left|\frac{M_{j,k}^{\exp,i}}{M_{0,0}^{\exp,i}} - \frac{M_{j,k}^{\text{pred},i}}{M_{0,0}^{\text{pred},i}}\right|}{N} \tag{5.2}$$

where $M_{j,k}^{\exp}$ and $M_{j,k}^{\text{pred}}$ are the (j, k) elements of the experimental (exp) and predicted (pred) Mueller matrix, respectively, N is the number of pixels and i is the evaluated pixel of the experimental and predicted single Mueller matrices.

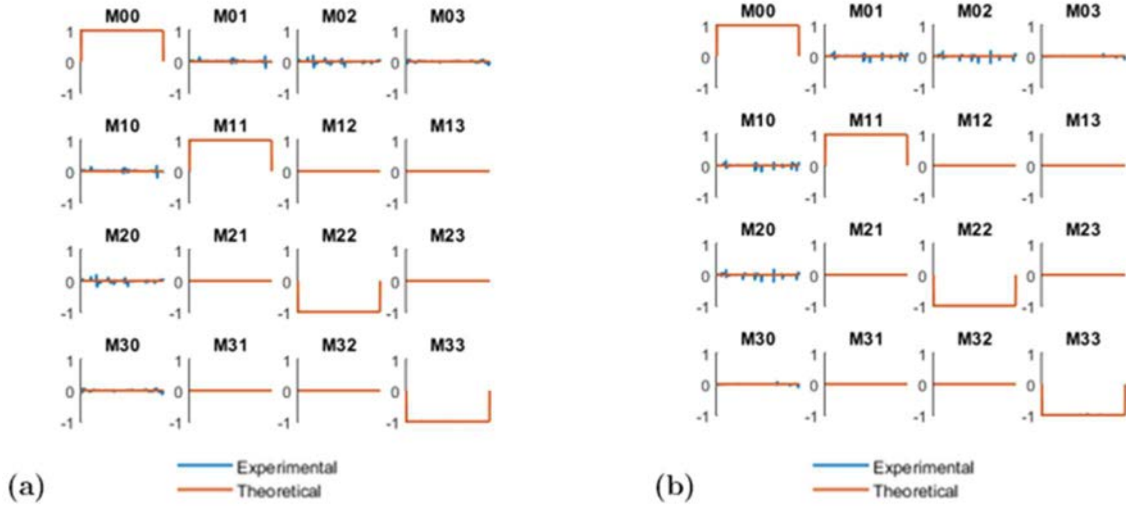

Figure 5-2. Intensity pixels-cross-sections obtained from the mirror Mueller matrix images shown in Figure 5-1. The taken cross-sections are: (a) horizontal; and (b) vertical, both passing through the center ((0,0) *pixels*) in the Mueller matrix images.

Furthermore, a polarizer and a quarter wave plate were used as polarimetric validation samples. As was explained, each validation sample was placed between the non-polarizing beam-splitter and the plane mirror used during the calibration process, in a *double-pass* configuration. The measured results have been compared with their respective simulations calculated by using Eq. (5.1). Figure 5-3 and Figure 5-4 show the experimental and simulated Mueller matrix images of the used polarizer and quarter wave plate, respectively, at different orientations angles of their axis, α. The Mueller matrix images were normalized, i.e. all the pixels of the different Mueller coefficients are divided by the M_{00} value for the corresponding pixel (note we were dealing with a Gaussian beam).

We calculated the remaining Mean Absolute Error on each normalized single matrix, i.e., the Mueller matrix of each pixel, and we found it smaller than 0.78% for the polarizer, and 0.39% for the quarter wave plate . Although the above-obtained errors show an optimal performance of the polarimeter implemented, the small errors observed in the experimental images can be related to small changes in polarimetric $\boldsymbol{S}$ and $\boldsymbol{A}$ matrices. However, we think that these errors are not only related to the polarimeter sensitivity, but mostly (in a higher error order) to the fact that the measured polarimetric elements are not ideal and they present an offset with respect to the theoretical characteristic parameters, for instance, in the orientation or the transmission-extinction coefficients for the measured polarizer,

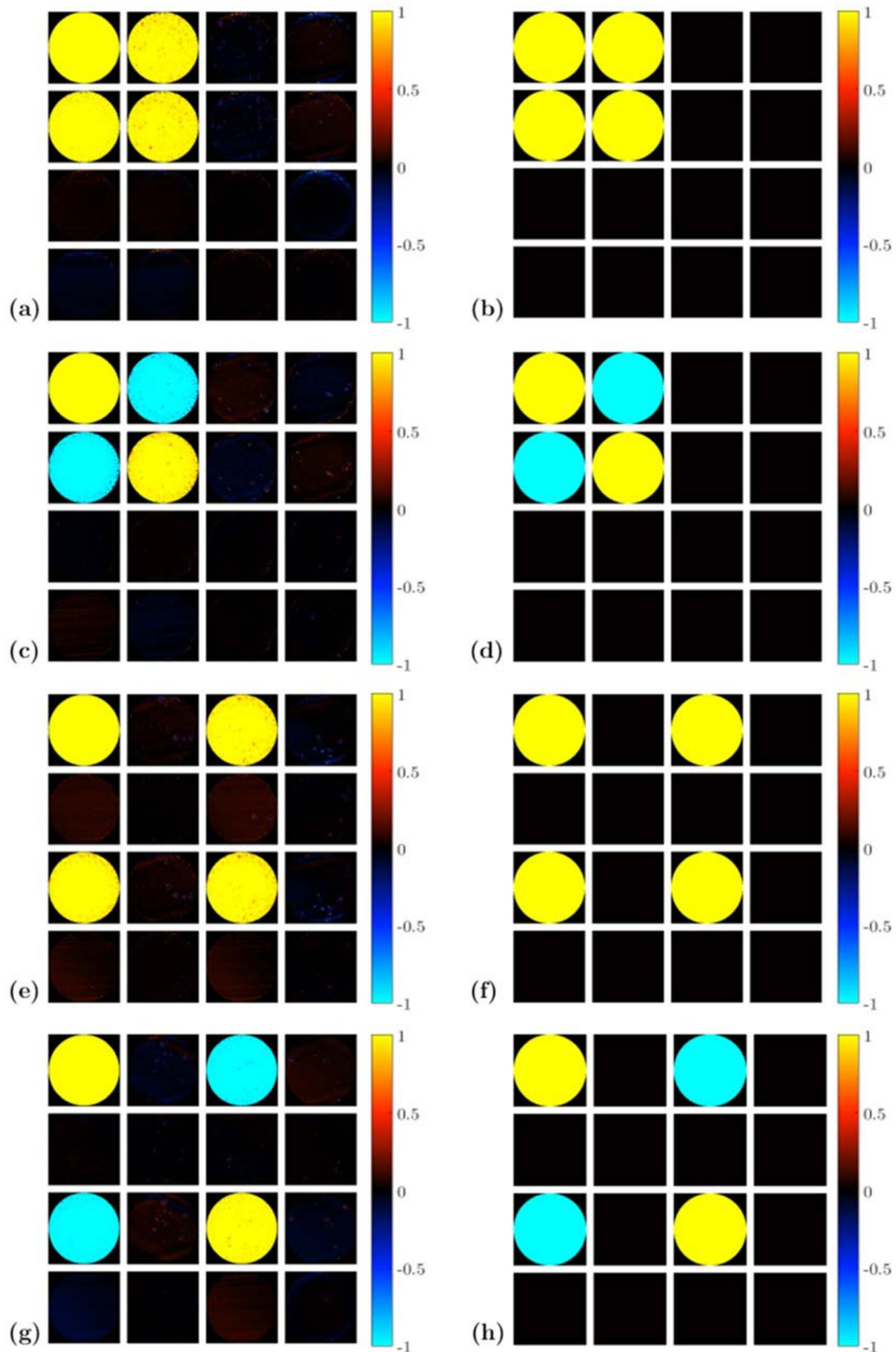

Figure 5-3. Mueller matrix images of a *double-pass* linear polarizer and a mirror for different orientation angles of the polarizer. The measured Mueller matrix images are shown in the first column while their respective simulations are in the second column. The orientation angles of the polarizer are (a) – (b) $\alpha = 0°$; (c) – (d) $\alpha = 90°$; (e) – (f) $\alpha = 45°$; and (g) – (h) $\alpha = 135°$.

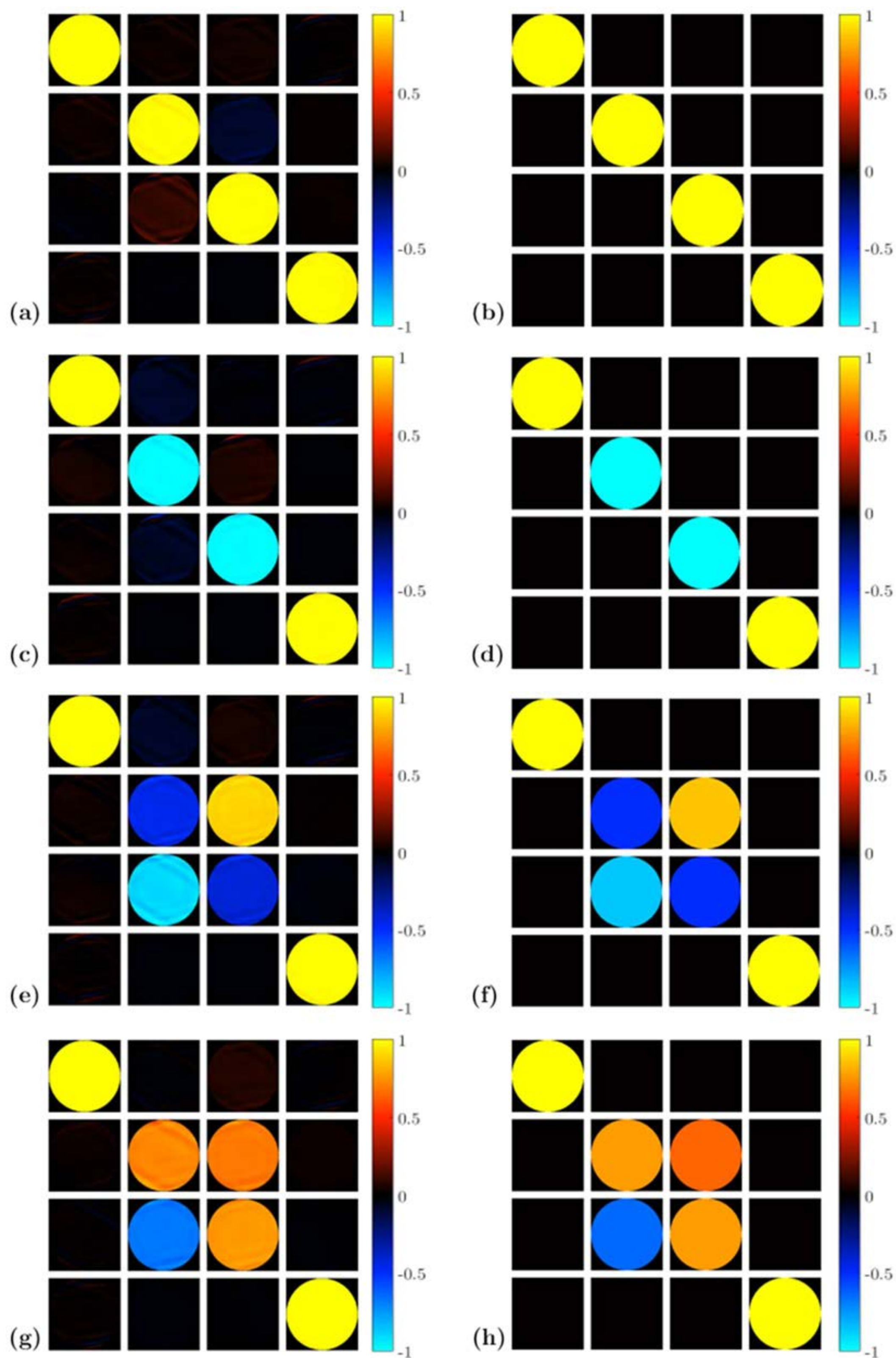

Figure 5-4. Mueller matrix images of a *double-pass* quarter wave plate (QWP) and a mirror for different orientations of the QWP fast axis. The measured Mueller matrices are in the first column while their respective simulations are in the second column. The orientation angles of the quarter wave plate fast axis are (a) – (b) $\alpha = 0°$; (c) – (d) $\alpha = 45°$; (e) – (f) $\alpha =$ -60°; and (g) – (h) $\alpha = 80°$.

and in the orientation or the retardance for the quarter wave plate. As an example, in Figure 5-4 (a) and (c), the experimental offset of the quarter wave plate can be appreciated by taking into account certain coefficients that show non-zero values, contrary to the simulated data (Figure 5-4 (b) and (d)).

In addition, some distortions in the images can also be observed in the experimental images. They are due to condensate droplets related to air that slips into the CMOS camera protector glass and condensate above certain CMOS camera temperature. What is more, they cannot be eliminated because it is an inaccessible part of the camera. The condensation appears when the camera is overheated, and the cooling fan is working. The temperature changes and the vibration produced during the cooling process changes the droplets positions and sizes. These changes imply that when single Mueller matrices are normalized some depolarization effects appear in the resulting images. We can appreciate the droplets-based depolarization effect in Figure 5-3; while in Figure 5-4, the camera was cooled and the condensation not yet occurred.

The depolarization produced by the undesired small droplets observed in Figure 5-3 and Figure 5-4 can be quantitatively seen from cross-sections set along the Mueller coefficients. To this end, cross-sections are taken parallel to the horizontal and passing through the center of the images. The obtained results are provided in Figure 5-5 and Figure 5-6. In each case, the coefficients cross-sections where obtained for the measured (or experimental) and the expected (or theoretical) results, being represented as different colors, blue and red, respectively. Small discrepancies are observed between theoretical and experimental data for some pixels as blue picks.

5.2 Improving experimental Mueller matrix images

The refractive indices and the orientation of the optical axis of the measured sample are determined by an optimization program, described in section 3.5, which compares a measured Mueller matrix image with multiple simulated Mueller matrix images. The optical parameters of the simulated Mueller matrix leading to the minimum Mean Squared Error (MSE) are those selected by the software as the correct solution.

During the measuring time some undesired effects can affect the measured angle-resolved Mueller matrices, making more difficult to obtain the actual parameters that characterize the samples. As stated before, in Figure 5-1 and Figure 5-3, we can observe undesired changes in the experimental Mueller matrix images produced by condensate droplets on the CMOS camera protector glass. In addition, other effects may come from scattered light due to defects and inhomogeneities of the analyzed samples, from undesired reflected light coming from planes different than the HNAO focal plane, from diffraction patterns due to the size of the relative HNAO aperture and beam sizes and from camera electronic noise, among others. All these error sources can introduce variations in the acquired intensity patterns used to calculate the experimental angle-resolved Mueller matrix image (see Eq. (3.16)).

Since the theoretical model used to simulate Mueller matrix images of isotropic or uniaxial anisotropic samples does not take into account the above-stated undesired effects, it is important to remove them as much as possible from the experimental Mueller images.

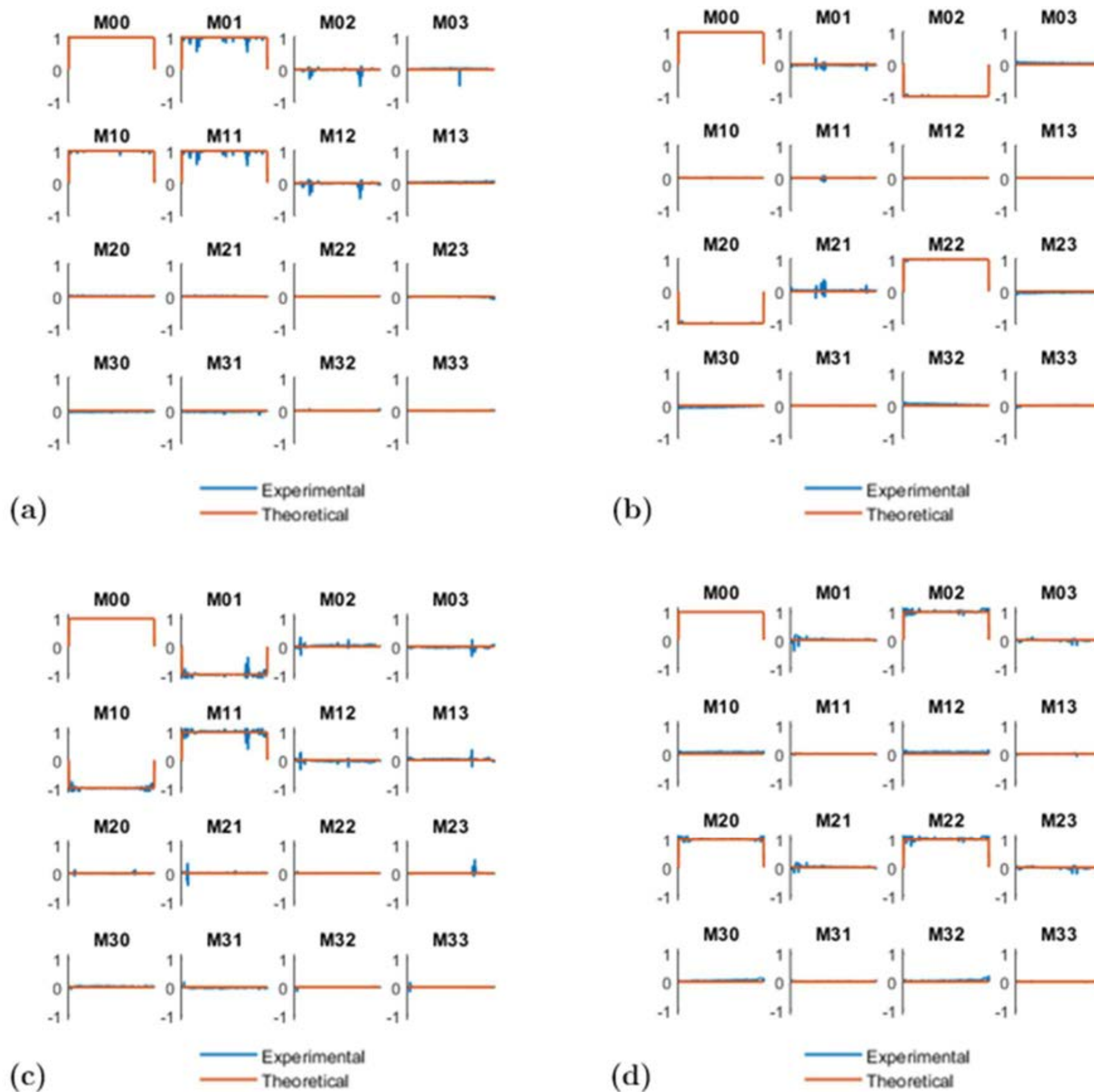

Figure 5-5. Cross-sections of the Mueller matrix images shown in Figure 5-3. The polarizer axis is at (a) $\alpha = 0°$; (b) $\alpha = 45°$; (c) $\alpha = 90°$; and (d) $\alpha = 135°$.

In the literature, there are several contributions of various authors who have dealt with these undesired effects and they provide several ways to improve the resulting elements of Mueller matrices. The following sections offer an overview of the Mueller matrix image processing that were carried out to improve the experimental results before the optimization program was used.

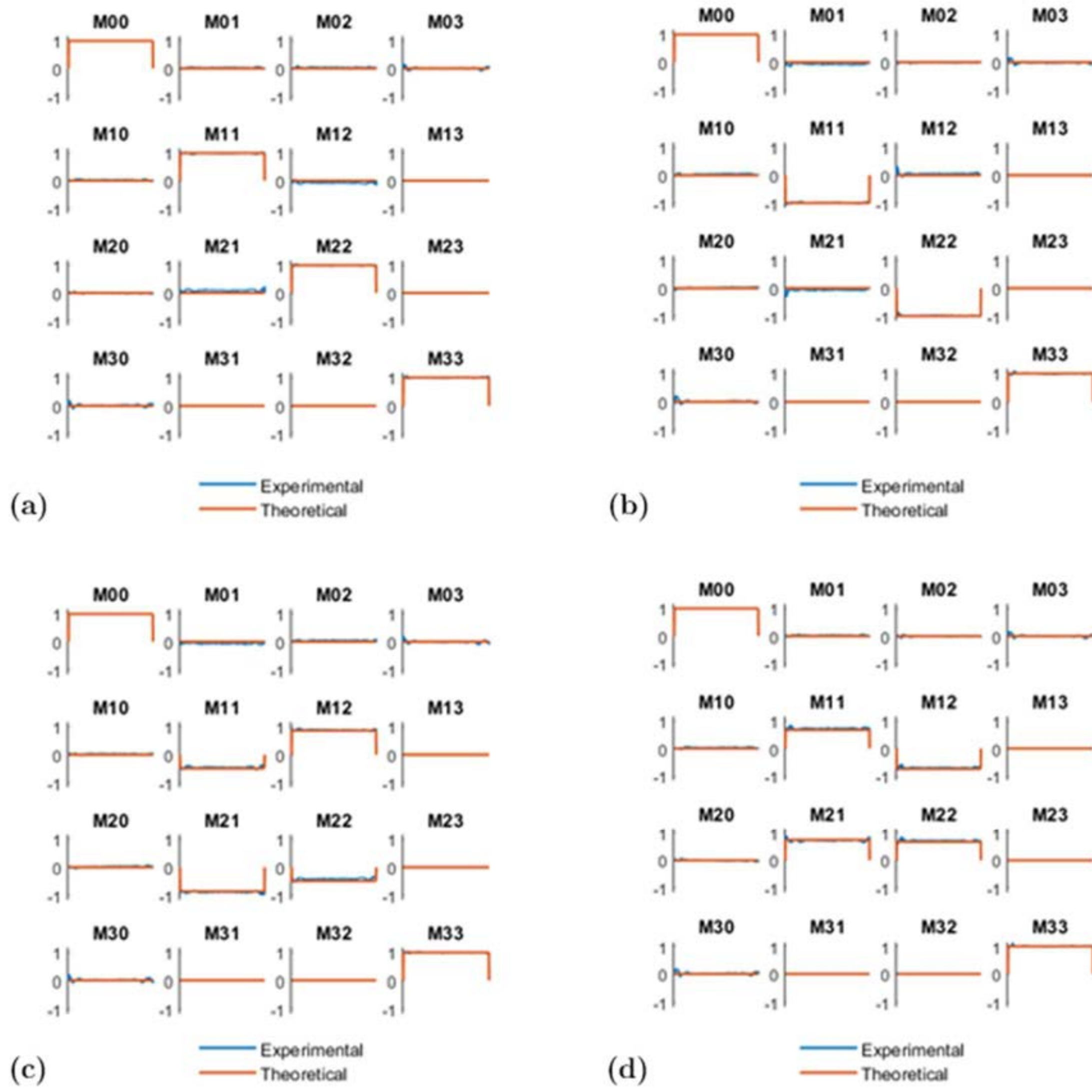

Figure 5-6. Cross-sections of the Mueller matrix images shown in Figure 5-4. The quarter wave plate fast axis is placed at (a) $\alpha = 0°$; (b) $\alpha = 45°$; (c) $\alpha = -60°$; and (d) $\alpha = 80°$.

5.2.1 Covariance filtering

The coherency matrix or Hermitian matrix $\boldsymbol{H}$ can be calculated as a unitary transformation of Mueller matrices. The coherency matrix associated to a physically realizable Mueller matrix has to be necessarily positive semidefinite or, in other words, its four eigenvalues (λ_i) have to be non-negative [180–183]. Given an experimental Mueller matrix, it is possible to build its respective 4×4 Hermitian matrix by using the following relation [182]

$$
\boldsymbol{H}=\frac{1}{4}\begin{pmatrix} m_{00}+m_{01}+m_{10}+m_{11} & m_{02}+m_{12}+i\left(m_{03}+m_{13}\right) & m_{20}+m_{21}-i\left(m_{30}+m_{31}\right) & m_{22}+m_{33}+i\left(m_{23}-m_{32}\right) \\ m_{02}+m_{12}-i\left(m_{03}+m_{13}\right) & m_{00}-m_{01}+m_{10}-m_{11} & m_{22}-m_{33}-i\left(m_{23}+m_{32}\right) & m_{20}-m_{21}-i\left(m_{30}-m_{31}\right) \\ m_{20}+m_{21}+i\left(m_{30}+m_{31}\right) & m_{22}-m_{33}+i\left(m_{23}+m_{32}\right) & m_{00}+m_{01}-m_{10}-m_{11} & m_{02}-m_{12}+i\left(m_{03}-m_{13}\right) \\ m_{22}+m_{33}-i\left(m_{23}-m_{32}\right) & m_{20}-m_{21}+i\left(m_{30}-m_{31}\right) & m_{02}-m_{12}-i\left(m_{03}-m_{13}\right) & m_{00}-m_{01}-m_{10}+m_{11} \end{pmatrix}
$$

(5.3)

where $m_{i,j}$ (i, j = 0, 1, 2, 3) are the sixteen elements of the Mueller matrix images. Note that the coherency matrix can be represented as $\boldsymbol{H} = \boldsymbol{V} \cdot \boldsymbol{D} \cdot \boldsymbol{V}^*$ where $\boldsymbol{V}$ and $\boldsymbol{V}^*$ are orthogonal matrices and $\boldsymbol{D}$ is a diagonal matrix. The matrix $\boldsymbol{V}$ contains the eigenvectors of matrix $\boldsymbol{H}$ arranged by columns, and $\boldsymbol{V}^*$ is its conjugate transpose. In turn, $\boldsymbol{D}$ represents the diagonal matrix composed of the four non-negative eigenvalues of $\boldsymbol{H}$ ordered so that $0 \le \lambda_3 \le \lambda_2 \le \lambda_1 \le \lambda_0$.

The undesired effects produced during the measure time introduce variations in the recorded intensity patterns used to calculate the Mueller matrix images, and consequently in corresponding λ_i. In other words, certain non-physically realizable content is present in the measured Mueller matrices, which translates as negative values for some of the eigenvalues λ_i. References [183–185] propose to filter the coherency matrix setting all negative eigenvalues to zero. The main reason is that as negative eigenvalues are unphysical, by removing $\lambda_i < 0$ we are filtering experimental noise. The filtered coherency matrix $\boldsymbol{H}'$ is built from the resultant covariance-filtered eigenvalues. Once the filtered coherency matrix $\boldsymbol{H}'$ is calculated, its nearest physically realizable Mueller matrix image $\boldsymbol{M}'$ is calculated by [182]

$$
\boldsymbol{M}'=\frac{1}{4}\begin{pmatrix} h_{00}+h_{11}+h_{22}+h_{33} & h_{00}-h_{11}+h_{22}-h_{33} & h_{01}+h_{10}+h_{23}+h_{32} & -i\left(h_{01}-h_{10}\right)-i\left(h_{23}-h_{32}\right) \\ h_{00}+h_{11}-h_{22}-h_{33} & h_{00}-h_{11}-h_{22}+h_{33} & h_{01}+h_{10}-h_{23}-h_{32} & -i\left(h_{01}-h_{10}\right)+i\left(h_{23}-h_{32}\right) \\ h_{02}+h_{20}+h_{13}+h_{31} & h_{02}+h_{20}-h_{13}-h_{31} & h_{03}+h_{30}+h_{12}+h_{21} & -i\left(h_{03}-h_{30}\right)+i\left(h_{12}-h_{21}\right) \\ i\left(h_{02}-h_{20}\right)+i\left(h_{13}-h_{31}\right) & i\left(h_{02}-h_{20}\right)-i\left(h_{13}-h_{31}\right) & i\left(h_{03}-h_{30}\right)+i\left(h_{12}-h_{21}\right) & h_{03}+h_{30}-h_{12}-h_{21} \end{pmatrix}
$$

(5.4)

where $h_{i,j}$ (i, j = 0, 1, 2, 3) are the sixteen elements of the filtered coherency matrix $\boldsymbol{H}'$. This new filtered Mueller matrix satisfies the conditions for realizability and it is a good estimation for the experimental Mueller matrix.

In this way, we propose to filter each pixel of the Mueller matrix image, measured with our conoscopic Mueller microscope, by using the covariance method to obtain a physically realizable $\boldsymbol{M}'$ image.

5.2.2 Depolarization filtering

On the other hand, experimental Mueller matrix image may present depolarization contributions. Although depolarizers represent physical realizable situations, depolarization contributions do not describe our actual situation as we are measuring non-depolarizing samples. The depolarization content present in experimental Mueller matrices can be originated from multiple reflections, scattering processes or due to spatial or temporal

integration over each pixel with varying polarimetric response. As the theoretical formalism presented in Chapter 2 and Chapter 3 considers fully polarized Mueller matrix images, the developed optimization program that compares simulated and experimental patterns will only be efficiently used to characterize samples if the depolarization of experimental data is removed.

As was shown in section 4.3.1, Lu-Chipman presented an algorithm to decompose a Mueller matrix into three component pure Mueller matrices representing depolarization, pure retardance, and pure diattenuation [177]

$$\boldsymbol{M}' = \boldsymbol{M}_{\text{Depolarizer}} \cdot \boldsymbol{M}_{\text{Retarder}} \cdot \boldsymbol{M}_{\text{Diattenuator}} \tag{5.5}$$

Thus, by calculating Lu-Chipman decomposition, the Mueller matrix images obtained from Eq. (5.4) can be filtered again, eliminating undesired depolarization effects. A remultiplication of the retardance and diattenuation matrices, by removing the depolarization content (i.e., $\boldsymbol{M}_{\text{Depolarizer}}$ is considered as the identity matrix in the remultiplication), results in a non-depolarizing Mueller matrix, ready for the calculus of the refractive index.

The obtained filtered Mueller matrix image (after covariance and depolarization filtered) is used to calculate the characteristic optical parameters of the sample.

5.3 Measured Mueller matrix images of samples

After the calibration and validation processes of the Mueller polarimeter, the HNAO is placed and aligned to convert the set-up into the conoscopic Mueller microscope. As was explained in section 3.2, the polarization transformation introduced by the high numerical aperture objective depends on the polarization of the homogeneous input beam as well as on the spatial coordinates of the illumination plane waves on the back focal plane of the HNAO. To measure the angle-resolved Mueller matrices, the six selected SoPs (see Table 4-5) are generated by the PSG and, after the interaction of the polarized light beam with the sample, the output beam is projected onto the six PAs (given in Table 4-6) by using the PSA. The resulting thirty-six intensity images are recorded using the CMOS camera and processed to obtain the characteristic Mueller matrix images of the sample. In Figure 3-13, we can observe an example of the thirty-six intensity distributions, for $n = 1.5$, $\lambda = 635$ nm and a maximum angle of incidence of 90º, used to calculate the simulated Mueller matrix image shown in Figure 3-9.

5.3.1 High *NA* Objective calibration

Although the chosen high numerical aperture objective is specific for polarization applications, we have to polarimetrically calibrate it before measuring any angle-resolved Mueller matrix, to analyze any polarimetric effect it can introduce that can affect our measure; as diattenuation, retardance or depolarization.

Reference [121] presents a method to calibrate the HNAO by using a high quality spherical mirror. According to the Debye approximation, we consider the wavefront in the focal region of the high numerical aperture objective as a superposition of plane waves. When the center of the spherical mirror is superimposed with the focal point of the HNAO, each light ray $\boldsymbol{k}_i$ is reflected back on itself, or in other words, each incident ray is normal to the mirror surface, avoiding the polarization effects due to high angles of incidence. A schematic diagram is shown in Figure 5-7.

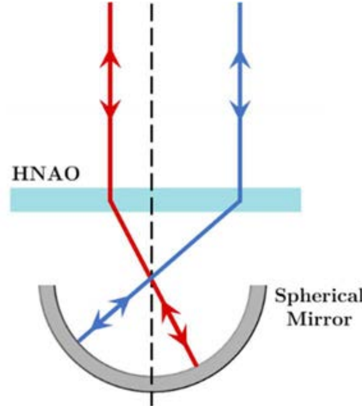

Figure 5-7. Schematic diagram of the spherical mirror and the high numerical aperture objective (HNAO). Each incident ray is reflected back in the same direction when the focal point of the HNAO coincides with the center of the spherical mirror.

By using the optimized Mueller polarimeter, the polarization changes introduced by the *double-pass* through the HNAO and by the spherical mirror reflection can be measured. Taking into account the normal reflection at the spherical mirror (see Eq. (4.10)) that gives the Mueller matrix for a mirror at normal incidence, $\boldsymbol{M}_{\mathrm{mirror}}$, is valid for all the $\boldsymbol{k}_i$, and the Mueller matrix of the system can be expressed as

$$\boldsymbol{M} = \boldsymbol{M}_{ob} \cdot \boldsymbol{M}_{\mathrm{mirror}} \cdot \boldsymbol{M}_{of} \tag{5.6}$$

where $\boldsymbol{M}_{ob}$ and $\boldsymbol{M}_{of}$ are the Mueller matrices of the HNAO in single-pass in the backward and forward directions, respectively. We have considered that the Mueller matrices in the forward and the backward directions are equal $\left(\boldsymbol{M}_o = \boldsymbol{M}_{ob} = \boldsymbol{M}_{of}\right)$ [125] and the Mueller matrix of the HNAO in *single-pass* is the one of an isotropic linear dichroic retarder [124, 125]. Therefore, Eq. (5.6) is rewritten as

$$\boldsymbol{M} = \boldsymbol{M}_{\mathrm{mirror}} \cdot \boldsymbol{M}_o^2 \tag{5.7}$$

and

$$\boldsymbol{M}_o^2 = \boldsymbol{M}_{\mathrm{mirror}}^{-1} \cdot \boldsymbol{M} \tag{5.8}$$

The square root of the Mueller matrix image $\boldsymbol{M}_o$ can be calculated by using numerical methods implemented into MATLAB (see Ref. [186]). Figure 5-8 (a) shows the measured Mueller matrix image of the whole system ($\boldsymbol{M}$ in Eq. (5.6)), while Figure 5-8 (b) shows the calculated Mueller matrix image of the HNAO ($\boldsymbol{M}_o$).

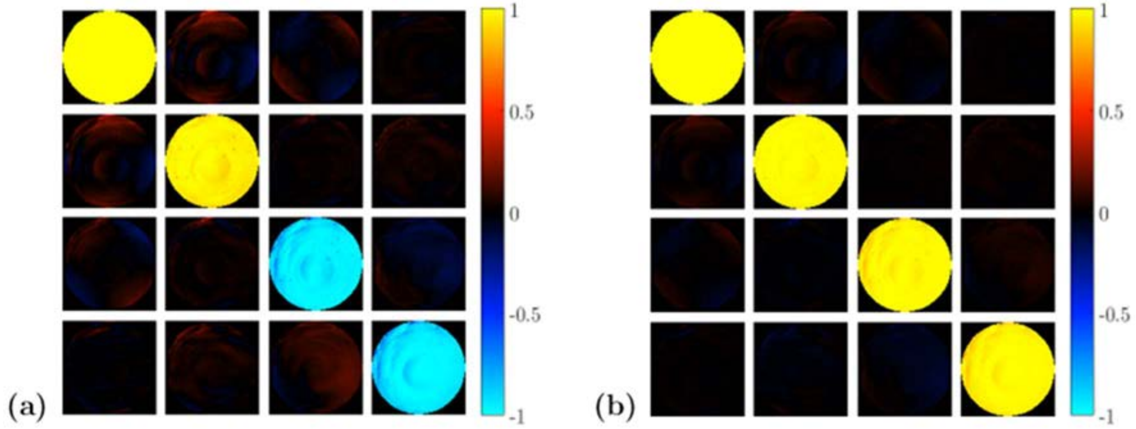

Figure 5-8. (a) Measured Mueller matrix of the HNAO-spherical mirror system (Matrix $\boldsymbol{M}$ in Eq. (5.6)). Light has passed twice through the high numerical aperture objective (in the backward and forward directions). (b) Mueller matrix image of the high numerical aperture objective (M_o).

By using the Lu-Chipman decomposition [111, 177], explained in section 5.2.2, the Mueller matrices of the equivalent retarder, diattenuator and depolarizer can be calculated from the matrix $\boldsymbol{M}_o$ of the HNAO. Figure 5-9 (a), Figure 5-10 (a) and Figure 5-11 (a) shows the obtained results for the equivalent diattenuation, retardance and depolarization matrices, respectively. They result in three quasi-diagonal matrices close to the identity. The results obtained from this decomposition conclude that the chosen high numerical aperture objective does not introduce important changes in the polarization of the incident and reflected beams. To quantitatively show that the three matrix images represented in Figure 5-9 (a), Figure 5-10 (a) and Figure 5-11 (a) are close to the identity matrix, we have calculated the horizontal cross-sections of all of them (see Figure 5-9 (b), Figure 5-10 (b) and Figure 5-11 (b)).

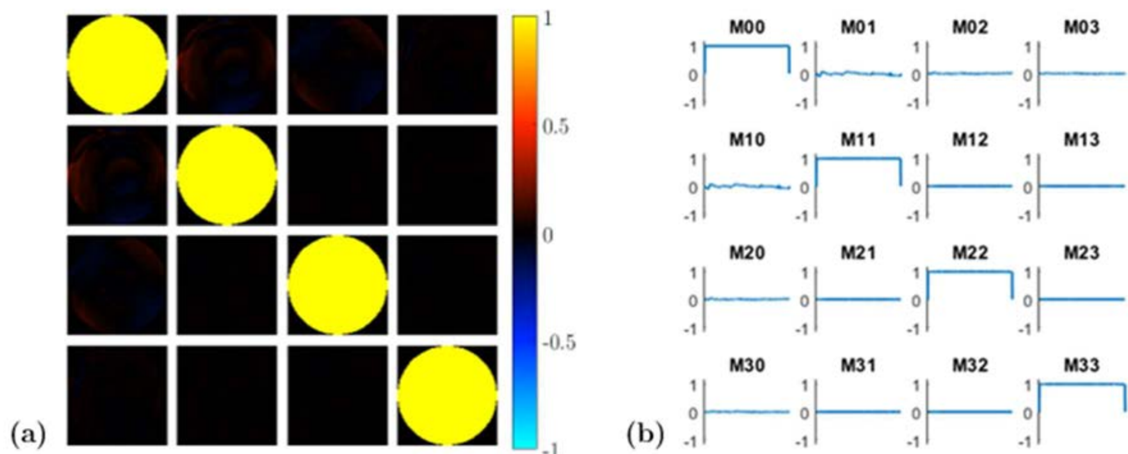

Figure 5-9. (a) Diattenuation matrix image after Lu-Chipman decomposition of the Mueller matrix image of the high numerical aperture objective shown in Figure 5-8; and (b) cross-section of the diattenuation matrix image.

From Figure 5-9 (b), Figure 5-10 (b) and Figure 5-11 (b), we can conclude that the high numerical aperture objective does not introduce notable polarization effects that can affect the experimental Mueller matrix images. In fact, the Mean Absolute Error between the identity matrix and any single diattenuation, retardance and depolarization matrices are $E_{\text{diattenation}} = 0.0032$, $E_{\text{retardance}} = 0.0031$, and $E_{\text{depolarization}} = 0.0023$, respectively.

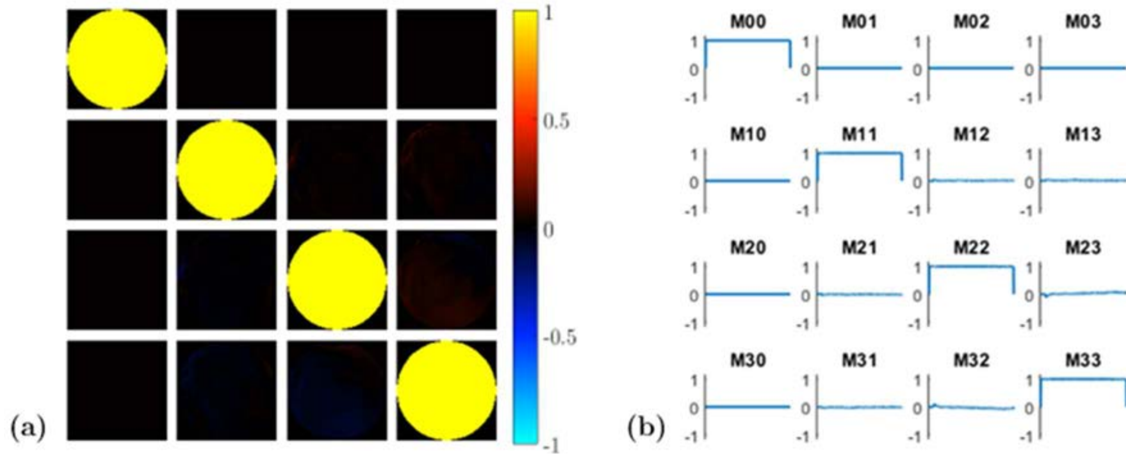

Figure 5-10. (a) Retardance matrix image after Lu-Chipman decomposition of the Mueller matrix image of the high numerical aperture objective shown in Figure 5-8. (b) cross-section of the retardance matrix image.

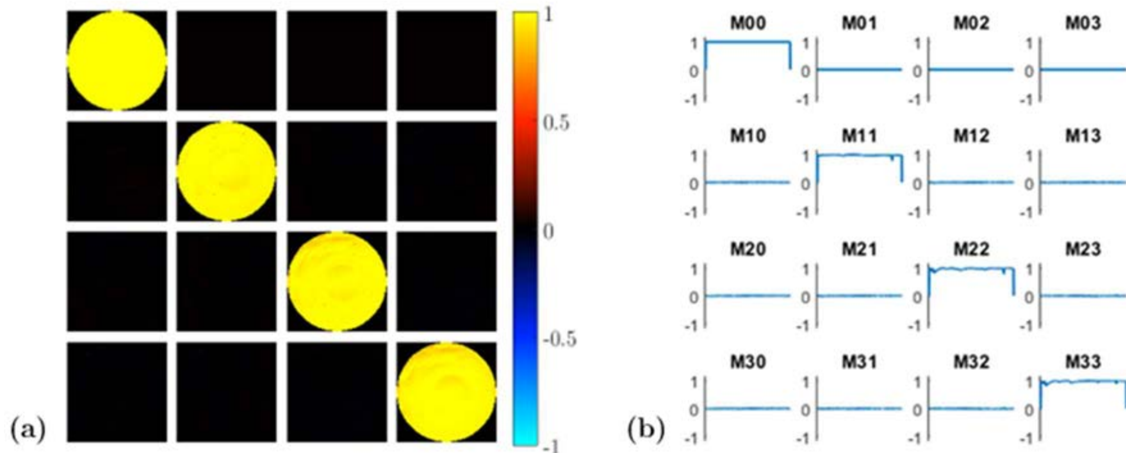

Figure 5-11. (a) Depolarization matrix image after Lu-Chipman decomposition of the Mueller matrix image of the high numerical aperture objective shown in Figure 5-8. (b) cross-section of the depolarization matrix image.

5.3.2 High *NA* Objective alignment concerns

Once the HNAO is calibrated, the specimens are placed on the sample positioning system. The goniometers and the translation platforms are used to align the sample surface in such a way that the light beam is reflected back parallel to the incident beam (see Figure 4-8), while the *K6XS* holder is used to align the HNAO (see Figure 4-6). Note that by using an objective with a high numerical aperture implies that any small angular

misalignment is magnified. To show the importance of this effect, Figure 5-12 demonstrates how the Mueller matrix image of a glass sample appears when the high *NA* objective is misaligned (Figure 5-12 (a)) and carefully aligned (Figure 5-12 (b)).

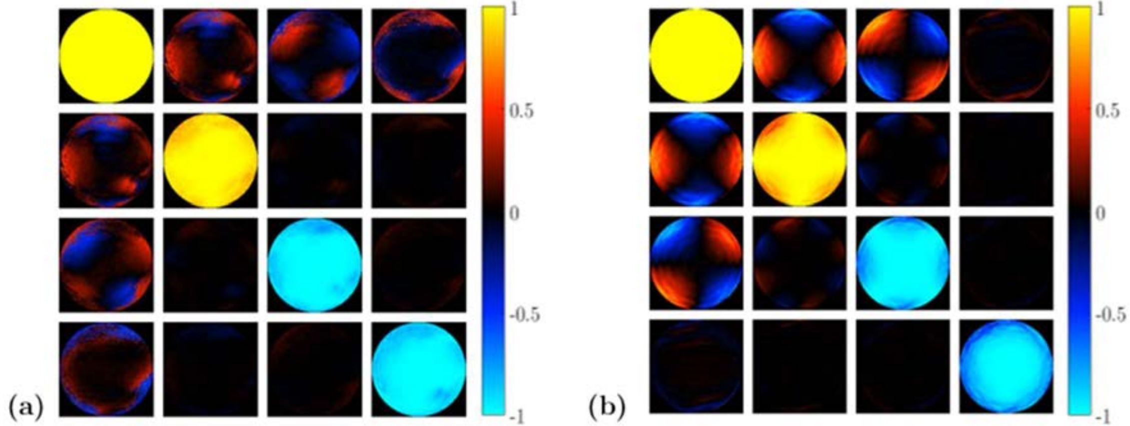

Figure 5-12. (a) Misaligned; and (b) aligned Mueller matrix images of a glass sample after covariance and depolarization filtering process.

In addition, the sample must be positioned at the focal plane of the high numerical aperture objective (2 *mm*). It is important to remark that if the sample is not at the right axial distance, the measured Mueller matrix image will present modifications from the expected simulation, with modulations due to diffraction effects, and the measured $\boldsymbol{k}_r$ do not coincide with the expected ones. To show this critical dependence of the Mueller matrix images with the axial position of the sample, we performed the following experiment. By moving the motorized translation stage of the sample positioning system (see Figure 4-8), the distance from the focal plane to the sample surface can be accurately changed (as sketched in the scheme given in Figure 5-13 (j)). Under this scenario, we measured a set of experimental Mueller matrix images corresponding to different sample-HNAO axial distances. The obtained results are given in Figure 5-13 (a) - (i). In particular, between each consecutive Mueller matrix image in Figure 5-13 there is a tiny space increment of the sample position of 5 μm. As was expected, different reflected beam spot dimensions, due to axial displacement of the sample, imply a significant variation of the Mueller matrix pattern size. In addition, different diffractive effects can also be observed in some Mueller coefficients, depending on the axial position of the sample.

We obtain the right size Mueller matrix image when the sample is placed at the focal plane of the HNAO and the incident and the reflected beams are overlapped, as can be seen in Figure 5-14 (a). Otherwise the size of the reflected beam over the front lens of the HNAO is going to be smaller (or bigger) than the desired (see Figure 5-14 (b)), producing different Mueller matrix pattern sizes shown in Figure 5-13 (a) - (i), and modifying the value for the maximum azimuthal angle of incidence, $\theta_{i,\max}$.

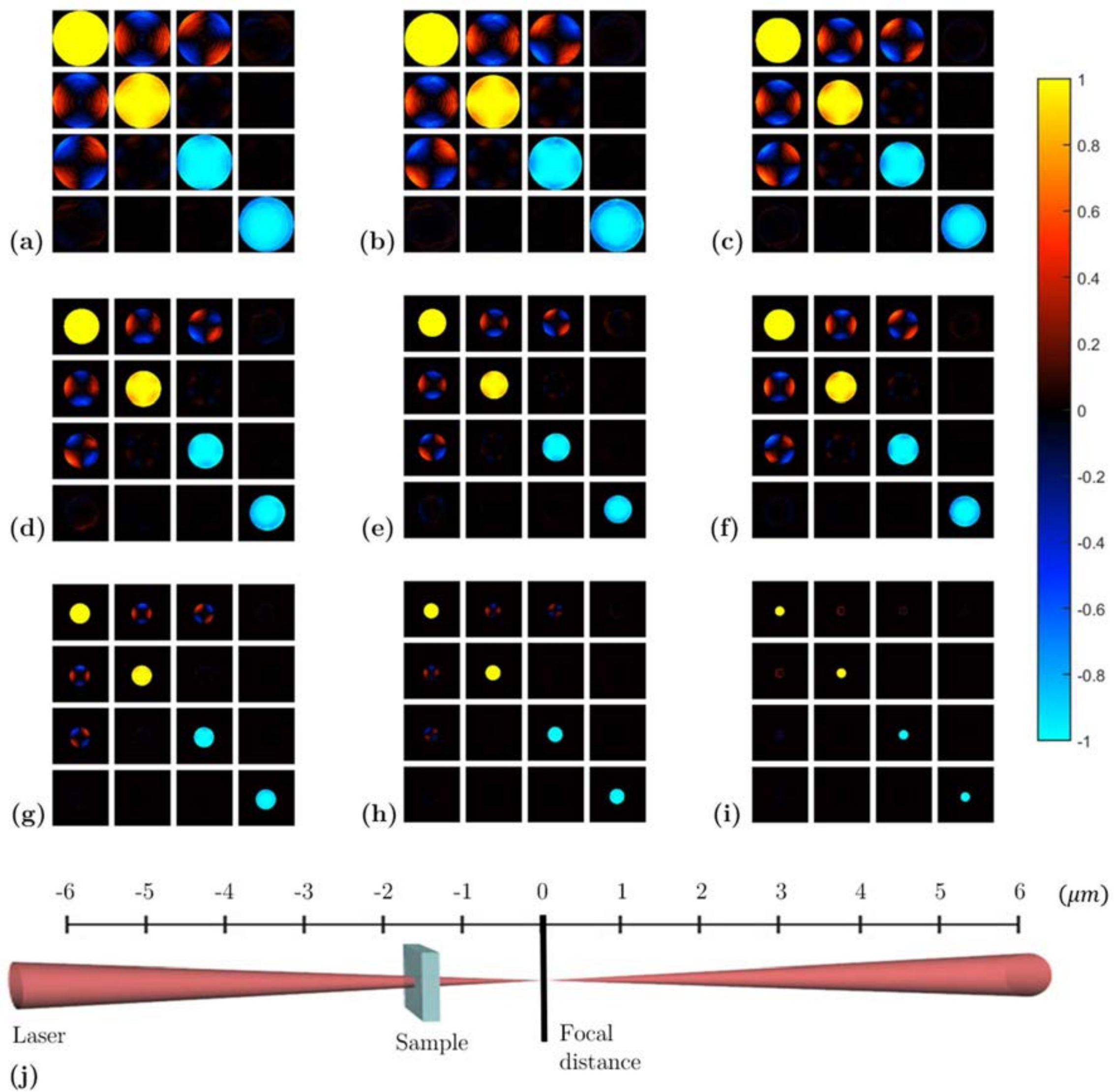

Figure 5-13. (a) – (i) Mueller matrix images of a glass sample at different sample-HNAO distances; and (j) scheme of the displacement of the sample to find the focal distance of the HNAO.

As a consequence of this critical dependence of Mueller images with the axial position of the sample, an experimental method must be applied to place the sample at the proper distance from the HNAO. In this sense, a lens system was included in the instrumentation to find the position where the sample is at the focal plane of the high *NA* objective. The used optical system makes a real image of the focal spot of the HNAO over the CMOS camera. When the sample is exactly placed at the focal plane of the microscope, the image of the spot recorded by the camera is well-defined. Out of this position, certain defocusing is observed, and the spot is blurred and its size increases. Therefore, the spot focalization can be used as criteria to discriminate, to certain extent, the proper z-plane of the sample. Once the sample is set to the proper position, the lens system can be removed to perform the angle-resolved Mueller matrix measures in Fourier space. Taking into account that we are working with high numerical aperture objectives and the spot size at its focal plane is

very small, the additional optical system has to magnify the size of the image over the CMOS camera. In other words, if the image of the spot is small, it is complicated to appreciate when the sample surface is placed at the focal point of the HNAO.

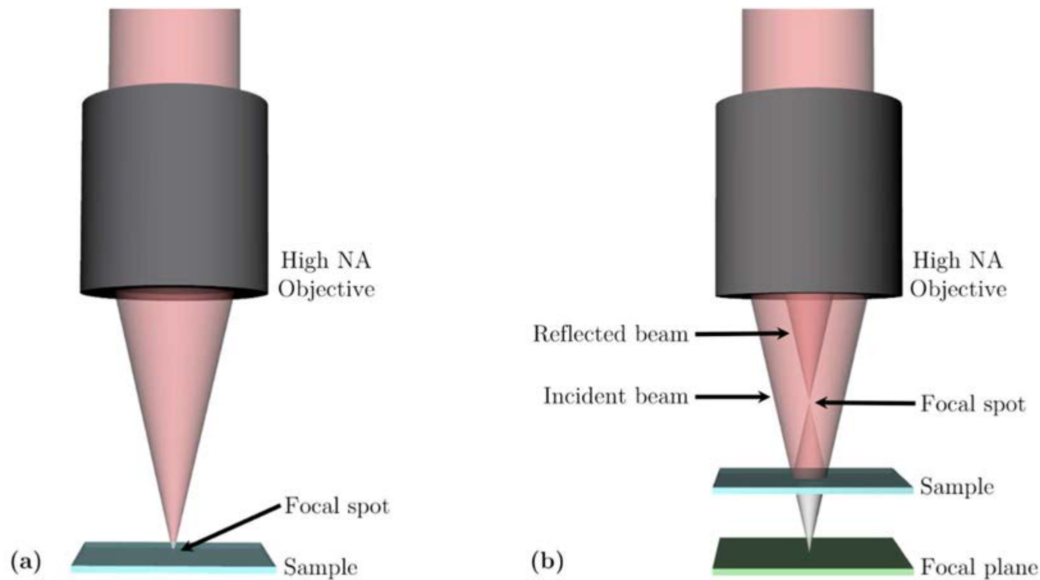

Figure 5-14. Sample placed at: (a) the focal plane of the high numerical aperture (NA) objective (z = z (focal distance)), the incident and reflected beams are overlapped. (b) z < z (focal distance), the incident beam does not focus over the sample, thus the reflected beam does not overlap the incident beam.

When the system is considered to be aligned and the sample is placed at the focal plane of the HNAO, the characteristic Mueller matrix of the sample can be measured. As an example, we follow with the study of the glass sample. The obtained experimental Mueller image of this glass specimen at the proper axial position is filtered and processed to improve the experimental results (section 5.2). Figure 5-15 shows the significant difference between the Mueller matrix image before and after the filtering process produced by depolarization and noise.

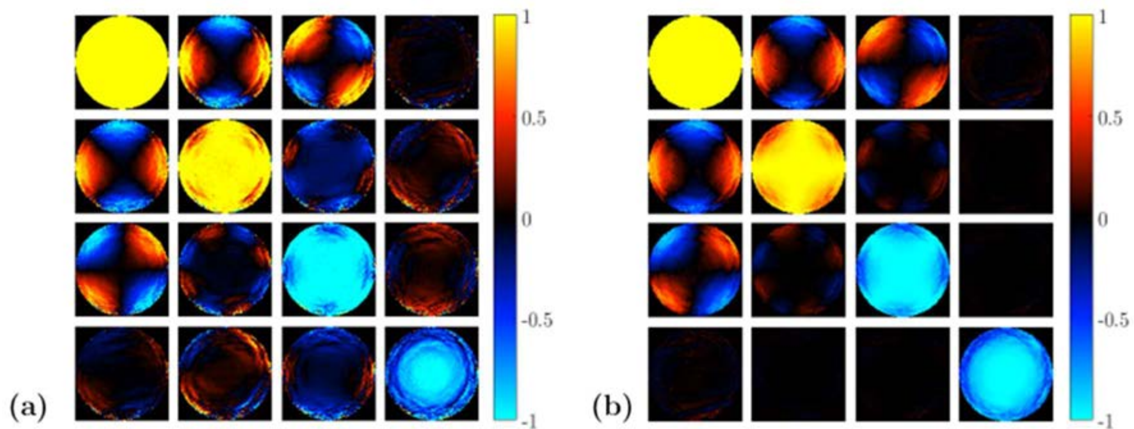

Figure 5-15. Experimental Mueller matrix images of a planar glass sample (a) before the filtering process; and (b) after the covariance and depolarization filtering processes.

It should be mentioned that although the sample and the HNAO look well-aligned, some parts of the designed prototype are placed manually, and they are very difficult to properly align. Consequently, any experimental Mueller matrix image (for example Figure 5-12 (b) and Figure 5-13 (a)) may be slightly different than the simulated matrices (see Figure 3-18). In both experimental figures, Figure 5-12 (b) and Figure 5-13 (a), some distorted Mueller matrix elements can be observed. They are mainly due to:

- Very small set-up misalignments.
- The size of the incident Gaussian beam (bigger/smaller than the HNAO aperture), and the corresponding diffractive effects.
- The sample is not perfectly placed at the focal plane of the high numerical aperture objective.
- The reflected beam is formed by a combination of multiple unwanted reflections coming from different parts of the sample.
- The sample axially moves during the measuring time as a consequence of the vibration produced by the CMOS camera cooling fan. It can also move due to an uncontrollable very smooth movement of the sample positioning system due to an adjustment of the screws position. These two kinds of displacements, that are negligible in low aperture situations, have to be controlled in measures with high numerical aperture objectives.

Because of the combination of all these effects, the measured patterns of the angle-resolved Mueller matrix images are not identical to the simulated data, presenting small distortions in the experimental result. However, we can consider that the measured images, after the filtering process, are close to the expected values, so the optical parameters can be approximately calculated using the optimization program.

5.3.3 Correlation between model parameters

The optimization program calculates the desired optical parameters of samples by using some estimation from previous knowledge of the sample (see section 3.5). A set of lower and upper bounds on the unknown variables as well as an initial estimation of the parameters used to simulate an initial theoretical Mueller matrix image are introduced into the optimization program to obtain the best-fit results. In addition, some termination tolerances are fixed on the function value (Eq. (3.18)) and on the studied parameters, so that fitting program finalizes in a local minimum that satisfies the constrains and the tolerances.

Those parameters which produce the best fit of the model are assumed to be the solution for the optical constants of samples. However, from a previous set of measures done at our laboratory, we have concluded that the parameters obtained with the optimization program were not, in all cases, the actual ones. We found that there are correlations between some model parameters, i.e., certain variables are highly dependent, in such a way that multiple

combination of parameters lead to different local minimum and different solutions being distant from the actual parameters are obtained. In this respect, the mathematical model presented in Chapter 2 and Chapter 3 constitutes a proper approximation to the physical reality of samples, as provided by the simulations of artificial samples and the proper identification of the physical parameters. However, when dealing with experimental Mueller matrices, experimental errors added to the Mueller matrices, whose origin was discussed in previous sub-sections, move away the experimental Mueller matrix image from the real Mueller matrix of the sample, and the correlation issue becomes critical. The solution lies in eliminating these observed correlations to properly calculate the refractive indices.

Note that when two or more model parameters are correlated, a high degree of correlation adds difficulty in finding these parameters [110]. In addition, depending on the starting points and constrains of these parameters, an acceptable figure of merit can be obtained for a wide range of values of the correlated parameters.

To get the best and real solution when the set of parameters are dependent, it is appropriate to optimize one parameter at a time and to run the optimization program using different initial guess values and constrains. Comparing the function value *MSE* (Eq. (3.18)), the desired parameters are those that have a lower local minimum objective function value. In our case, when the sample is uniaxial anisotropic, there are eight fit parameters $((x_0, y_0), \varepsilon_0, \theta_{i,\max}, \theta_c, \phi_c, n_e$ and $n_o)$ to be calculated. On the other hand, when the sample is isotropic, there are just five unknown parameters $((x_0, y_0), \varepsilon_0, \theta_{i,\max}$ and $n)$. However, not all of them are highly correlated. Along the next sections, we have studied the correlation relations between parameters, and which ones are the most critical to accurately calculate the refractive indices of samples.

Next sub-sections show some materials that have been measured in our laboratory. The following 4×4 Mueller matrix elements were normalized with respect to the first element M_{00} that represents the total intensity of light reflected by the sample. Then, they were filtered, and their depolarization contribution was removed. In this way, the Mueller matrix images shown in following sub-sections are filtered angle-resolved Mueller matrices, which were used to obtain the optical parameters of samples. Furthermore, the absolute error of the measured Mueller matrices and the best-fit parameters Mueller matrix images are given as well.

5.3.4 Mueller matrix images of unknown samples

To evaluate if the conoscopic Mueller microscope is able to characterize different samples (isotropic, anisotropic, planar, non-planar, liquid, solid, etc.), we measure the angle-resolved Mueller matrices of different materials. The refractive indices of studied samples were previously measured by using a commercial Abbe refractometer (*Carl Zeiss Abbe Refractometer, Number 323245*), see section 1.2.2, as a reference value, and both values were compared.

a) Olive oil

Olive oil is an isotropic dense liquid. Its normalized angle-resolved Mueller matrix measured with our conoscopic Mueller microscope is shown in Figure 5-16. The obtained Mueller matrix image is off-centered and it presents some anomalies due to small vibrations of olive oil produced by the CMOS camera cooling fan during measuring time. We have chosen to measure this dense liquid because it is less sensitive to vibrations than other liquid samples, as water.

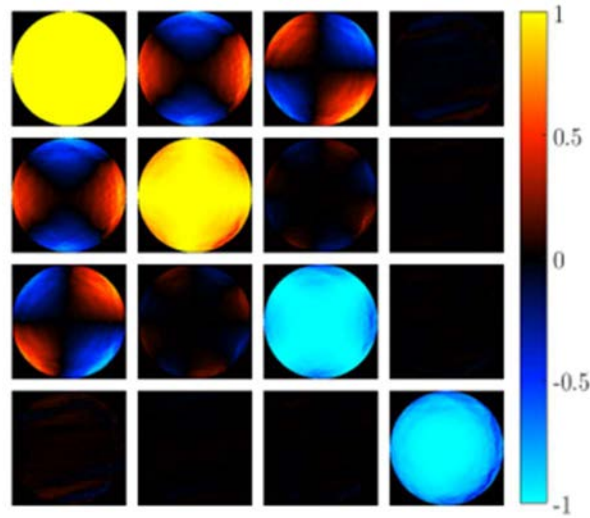

Figure 5-16. Experimental Mueller matrix image of olive oil.

As was explained in previous sections, there are strong correlations between n and $\theta_{i,\max}$ parameters. This existing correlation makes optical parameters calculation more difficult. To quantitatively probe the correlation between n and $\theta_{i,\max}$, we have change the optimization program in such a way that it calculates the refractive index related to the Mueller matrix image in Figure 5-16, but in this case, by fixing the value of $\theta_{i,\max}$. Then, this has been repeated for different values of $\theta_{i,\max}$ into a range (from 48.0º to 48.9º in steps of 0.1º). Figure 5-17 shows the best-fit refractive indices (Figure 5-17 (a)) and the obtained *MSE* function (Figure 5-17 (b)) for the stated maximum angles of incidence range. From both graphics we can conclude that if n or $\theta_{i,\max}$ are not fixed, the optimization routine will give a RI smaller than its real value, satisfying the condition of minimizing *MSE*. But, when the maximum angle of incidence is fixed, the program can calculate the actual optical parameters. In this sense, it is interesting to accurately measure $\theta_{i,\max}$ before using the optimization program. In this way, we can break the mathematical correlation between n and $\theta_{i,\max}$, and thus, to accurately find the characteristic optical parameters of samples, in this particular case, of olive oil.

Furthermore, we have analyzed the dependence of the best-fit refractive index on the optimization routine initial parameters and constrains. By repeating the iterative routine several times, each time changing the initial parameters values, the best-fit refractive index is always the same, even if the fixed initial values are very different than the expected.

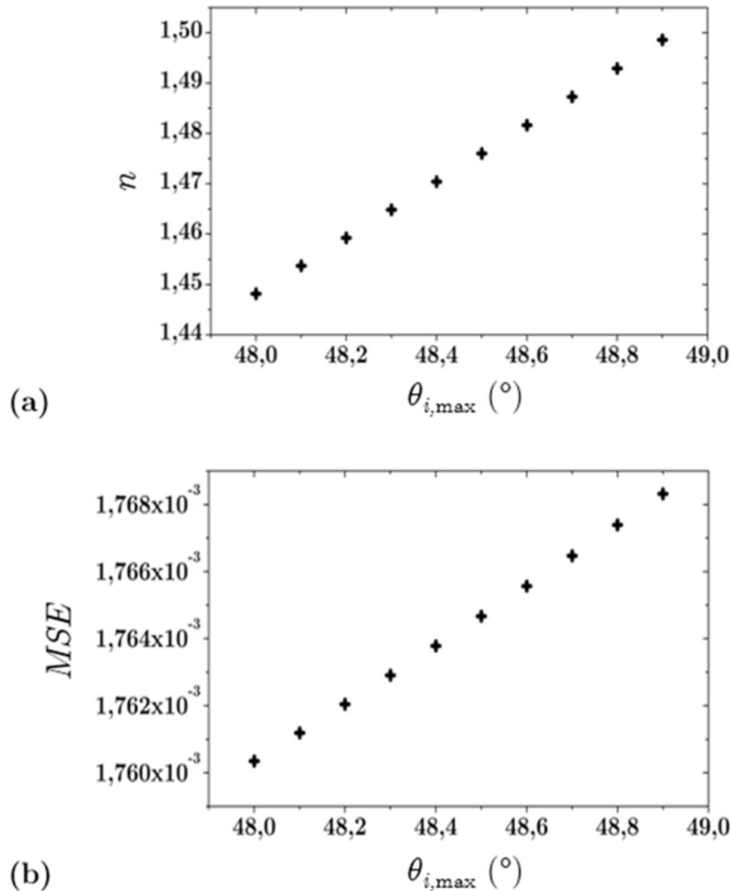

Figure 5-17. (a) Refraction index (n); and (b) Mean Squared Error (*MSE*) as a function of $\theta_{i,\max}$ (°) for olive oil.

In addition, we have observed that the center of the image (x_0, y_0) and the azimuthal rotation ε_0 are not correlated, and their values are not altered even if n and $\theta_{i,\max}$ change. As an example of this situation, Figure 5-18 shows the values for x_0 (red crosses), y_0 (black plus signs) and ε_0 (blue asterisks) as a function of $\theta_{i,\max}$. A very small fluctuation can be appreciated (a center position deviation lower than one pixel, while the total number of pixels is 980×980 *pixels*, and around one degree for the azimuthal angle), but their best-fit values do not show an increasing or decreasing trend. A similar fluctuation, always smaller than 1 pixel for the centered of the image and 1° for the rotation, is obtained for the rest of analyzed isotropic and uniaxial anisotropic samples. Thus, we can consider that the center of the image position and the rotation angle are well found without any correlation.

By using the Abbe refractometer, the RI of our olive oil sample was measured, obtaining n_{oil} =1.469. From graph Figure 5-17 (a), we can extract the best-fit refractive index and the corresponding maximum angle of incidence, being closer to the refractive index of olive oil measured with our Abbe refractometer (see Table 5-1).

Parameters	n	$\theta_{i,\max}$ (°)
Best-fit values	1.470	48. 4°

Table 5-1. Best-fit values corresponding to olive oil.

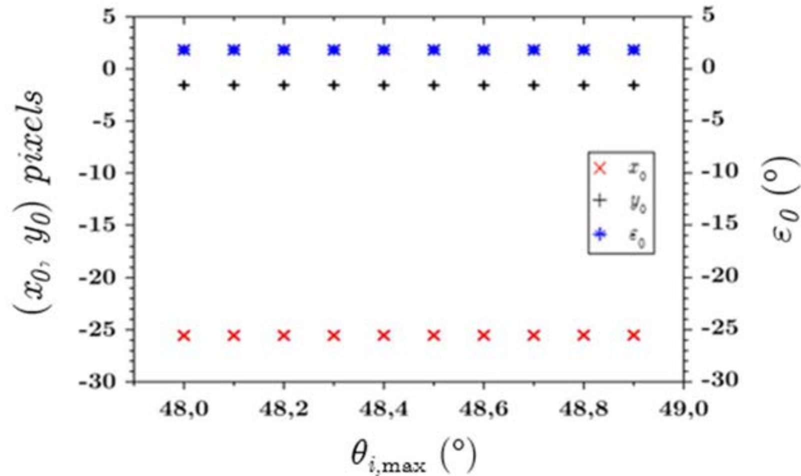

Figure 5-18. Bets-fit center of the image (x_0, y_0) and best-fit rotation angle (ε_0) as a function of the maximum angle of incidence ($\theta_{i,\max}$ (°)) for olive oil. Red crosses indicate x_0 values, black plus signs are y_0 and blue asterisks are ε_0.

The simulated Mueller matrix image for the best-fit parameters is shown in Figure 5-19 (a). Furthermore, Figure 5-19 (b) shows the square of the difference between the simulated (from best-fit values) and experimental Mueller matrix images ($(M_{\text{sim}} - M_{\text{exp}})^2$). Let us call it squared absolute error (*SAE*). We can observe that the SAE per pixel increases for higher angles of incidence i.e., close to the edge of the high numerical aperture objective. Thus, edge angles of incidence seem to provide more critical information.

The averaged *SAE* per pixel of the Mueller matrix images is equal to 0.0019.

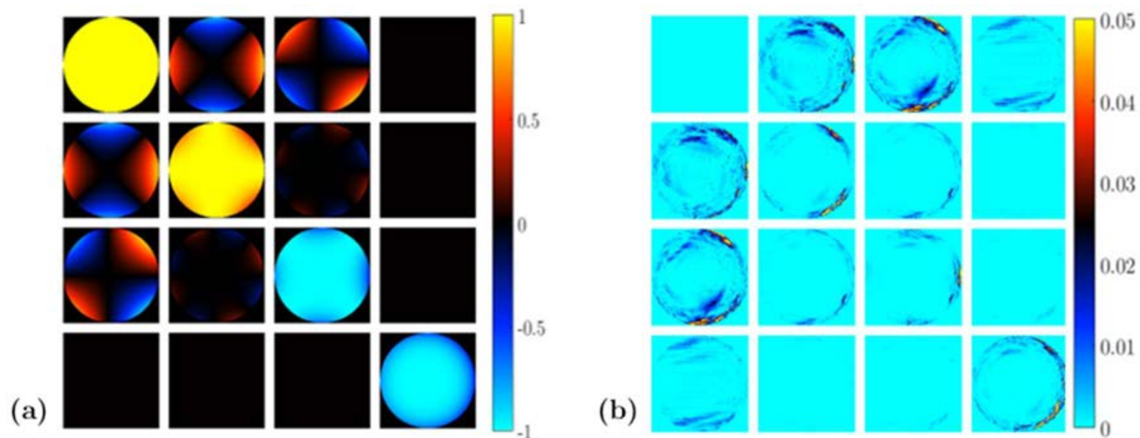

Figure 5-19. (a) Simulation of the Mueller matrix image of olive oil by using the best-fit parameters found from the optimization program. (b) Squared absolute error per pixel between experimental and simulated Mueller matrix images.

b) Distilled water

The normalized measured Mueller matrix image of distilled water is shown in Figure 5-20. As can be seen, the experimental image of distilled water presents more anomalies than

the olive oil image (see Figure 5-16) that are due to the lower density of water, which implies that the vibrations of water during measuring time are greater than for olive oil.

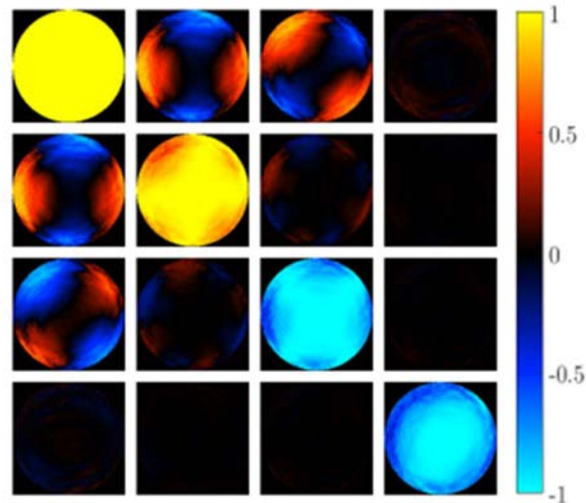

Figure 5-20. Mueller matrix image of distilled water measured with our conoscopic Mueller microscope.

The strong correlation existing between n and $\theta_{i,\max}$ is confirmed. We have set different maximum angles of incidence and the corresponding best-fit refractive indices have been obtained from the optimization program. The obtained refractive indices and *MSE* values were plotted and can be seen in Figure 5-21 (a) and (b), respectively. As in the olive oil case, we can conclude that if n or $\theta_{i,\max}$ are not fixed, the optimization routine will give a refraction index smaller than the real one, minimizing the *MSE* value.

The RI of distilled water, measured by using the Abbe refractometer, was found to be $n = 1.333$. From data in Figure 5-21 (a), we obtain the best-fit n (that closer to the refractive index of distilled water measured by the Abbe refractometer) and its respective maximum angle of incidence. Obtained results are shown in Table 5-2. The best-fit maximum angle of incidence for water is close to that obtained for the oil case, so we obtain a consistent result. The small difference obtained for the $\theta_{i,\max}$ value ($>1°$), for the oil and water cases, may be related with the experimental quality of the Mueller images, degraded to certain extend due to liquid vibrations, but it is mainly related with the position of both samples with respect to the HNAO. Both samples are not exactly at the focal plane, and thus, the corresponding maximum angle of incidence is slightly different.

Parameters	n	$\theta_{i,\max}$ (°)
Best-fit values	1.3333	49.34°

Table 5-2. Best-fit values corresponding to distilled water.

The simulated Mueller matrix image for the obtained best-fit parameters is shown in Figure 5-22 (a). In addition, Figure 5-22 (b) shows a pixelated image of *SAE* between corresponding pixels of the experimental Mueller and the simulated Mueller matrix images. We can observe that the values of *SAE* image for distilled water are greater than those for olive oil (Figure 5-19 (b)) due to experimental errors, related to unavoidable small waves

on its surface originated by mechanical vibrations introduced by the CMOS camera and sample holder.

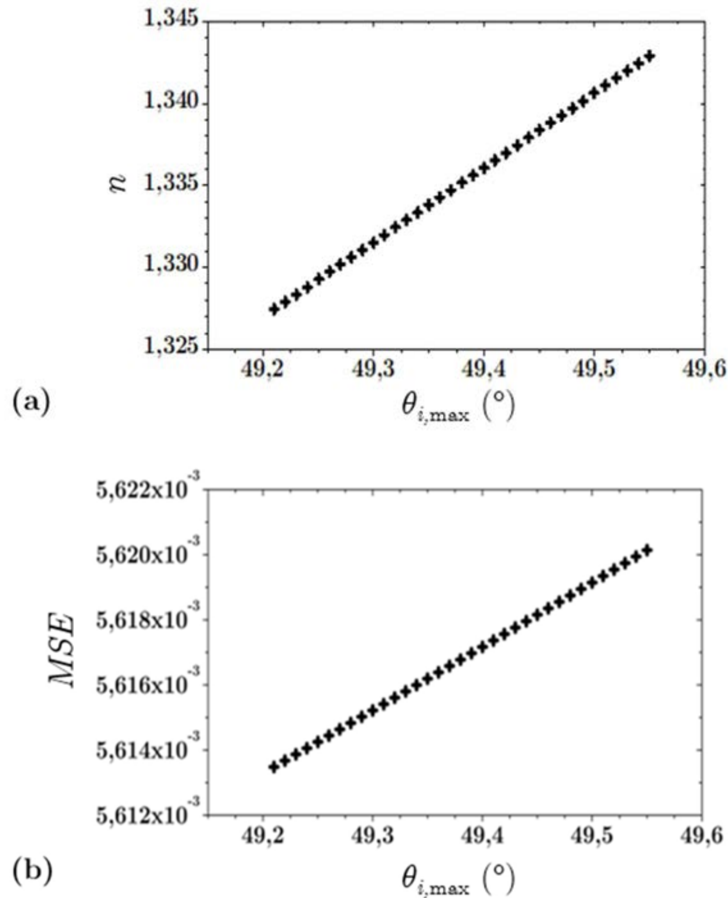

Figure 5-21. (a) Refraction index (n) and (b) Mean Squared Error (MSE) as a function of $\theta_{i,\max}$ (°) for distilled water.

The averaged SAE per pixel of Figure 5-22 (b) is 0.00455, which is bigger than the obtained for olive oil.

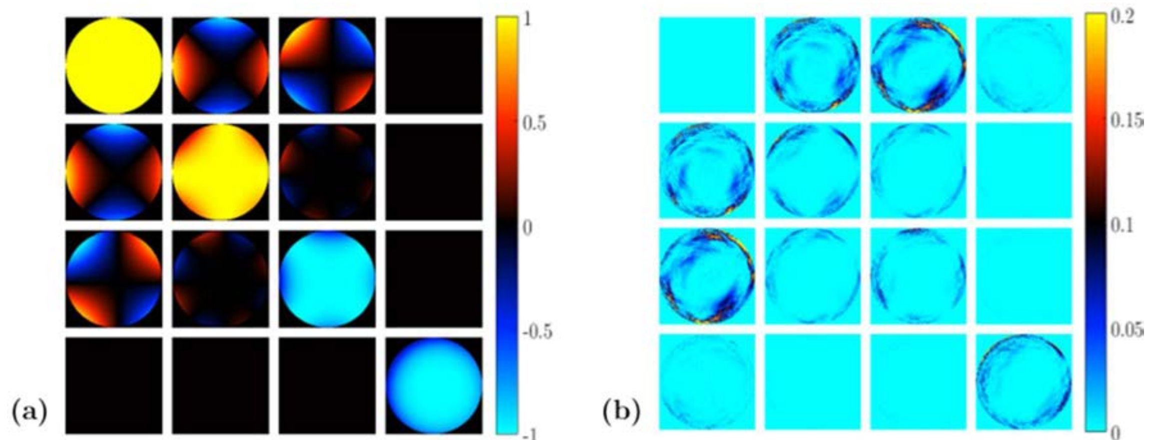

Figure 5-22. (a) Simulation of the Mueller matrix image of distilled water using the best-fit parameters found from the optimization program. (b) Squared absolute error per pixel between experimental and simulated Mueller matrix images of distilled water shown in Figure 5-20.

c) Plastic material

We have also measured the Mueller matrix image of a planar plastic material previously characterized by our Abbe refractometer ($n = 1.582$). The obtained experimental Mueller matrix image is shown in Figure 5-23. This angle-resolved Mueller matrix is clearer than the two previous ones. The main reason is that the oscillation waves are avoided when we are working with solid samples.

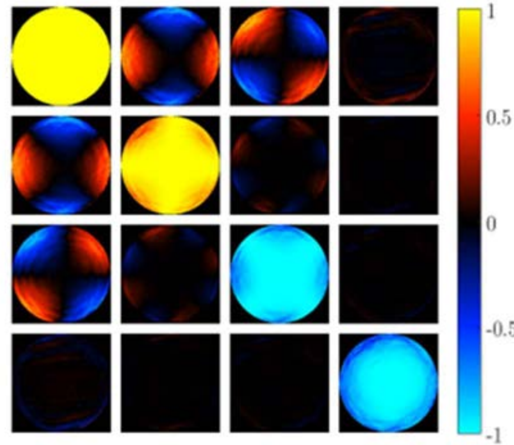

Figure 5-23. Experimental Mueller matrix image of a planar plastic material with $n = 1.582$.

Repeating the process followed for olive oil and water, the characteristic parameters of the Mueller matrix image are obtained into a range of angles of incidence we selected (the choice was made based on previous knowledge acquired with oil and sample liquids). Under this scenario, the optimization routine developed in MATLAB provided the best-fit data. The corresponding refractive index and the Mean Squared Error values are shown in Figure 5-24 as a function of the maximum angle of incidence.

Table 5-3 gives the best-fit refractive index closer to the value measured with the Abbe refractometer ($n_{\mathrm{Abbe}} = 1.582$) and its respective maximum angle of incidence. The obtained $\theta_{i,\max}$ is similar to the olive oil and water, but not exactly the same. Taking into account that the maximum angle of incidence is independent of the material under study, its value has to be the same for all characterized samples. As in the previous characterized specimens, we are not able to accurately determine the focal plane position required to overlap the incident and reflected cones. For this reason, the $\theta_{i,\max}$ obtained for the plastic does not exactly coincide with the other sample values. An alternative method has to be used to set the axial position of the sample with high precision, in order to improve the accuracy of the method.

Parameters	n	$\theta_{i,\max}$ (°)
Best-fit values	1.583	50.30°

Table 5-3. Best-fit values corresponding to a plastic material found from the optimization routine.

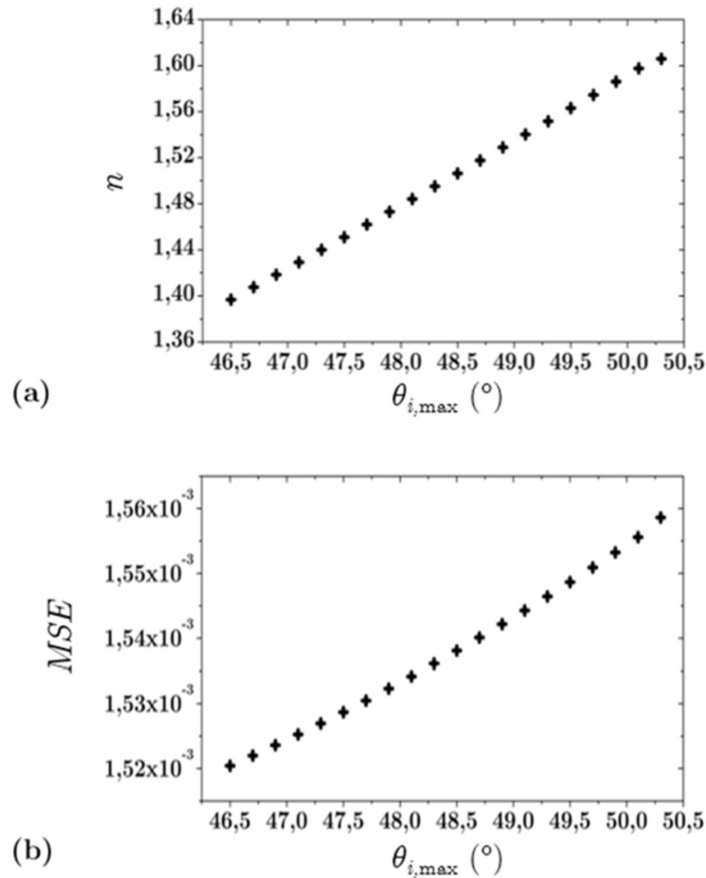

Figure 5-24. (a) Refractive index and (b) Mean Squared Error (*MSE*) as a function of the maximum angle of incidence $\theta_{i,\max}$ $(^{\circ})$ for a planar plastic sample.

From the best-fit values of Figure 5-23, calculated by the optimization routine, we have simulated the best-fit Mueller matrix image that is shown in Figure 5-25 (a). The pixel-by-pixel *SAE*, given in Figure 5-25 (b), is calculated to observe the largest errors between angle-resolved Mueller matrices. The larger errors are once again at the highest incident angles. The averaged *SAE* per pixel of Figure 5-25 (b) is 0.00169. As expected, the error for this plastic material is smaller than for water or olive oil.

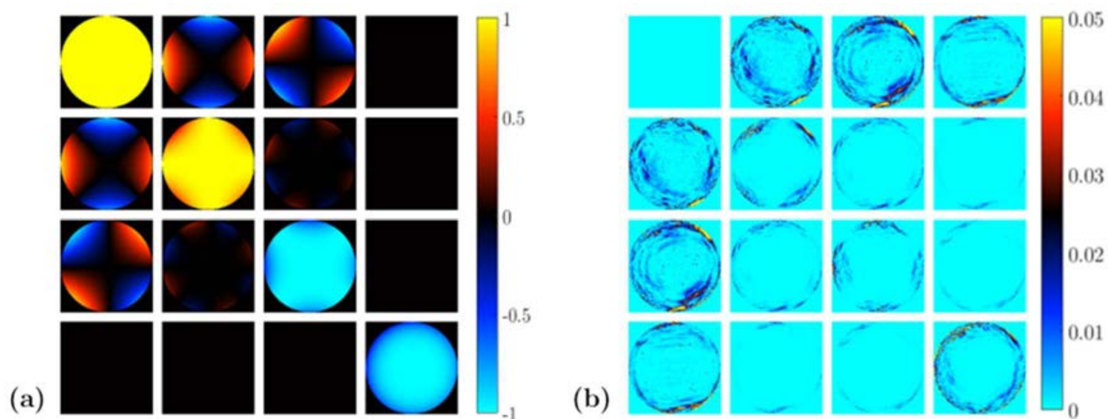

Figure 5-25. (a) Simulated Mueller matrix image from best-fit values calculated with the optimization routine. (b) Squared absolute error per pixel between the measured Mueller matrix image (shown in Figure 5-23) and the simulated Mueller matrix for a planar plastic material.

5.3.5 Mueller matrix images of well-known glass prisms

The theoretical optical parameters used to know the accuracy of our conoscopic Mueller microscope in section 5.3.4 are estimated from literature and from our Abbe refractometer (that works with white light). In this sense, the refractive indices of the used samples can vary a little from the expected values due to the used wavelength. For this reason, two well-known isotropic samples, calibrated for the used λ, were used to study the conoscopic Mueller microscope developed during this thesis. The two glass prisms labeled as 4705 and 4903 (see Figure 5-26) were calibrated for different wavelengths by the Physikalisch-Technische Bundesanstalt (PTB) in Germany, in order to have both samples accurately characterized. The RIs for our used wavelength ($\lambda = 635\ nm$) are given in Table 5-4.

Our goal is to use both calibrated prisms to accurately calculate the maximum angle of incidence of the system, in order to fix it when launching the optimization routine with unknown samples (i.e., to break the correlation between $\theta_{i,\max}$ and n parameters). Note that $\theta_{i,\max}$ is independent of the material under study, as long as the sample is placed at the focal plane. Once the maximum angle of incidence is well-known, the refractive index can be obtained. In this sense, we have measured the Mueller matrix images of both prims, and then, the best-fit parameters were calculated by fixing their particular RIs values calculated by the PTB. The obtained results are presented in the following sub-sections.

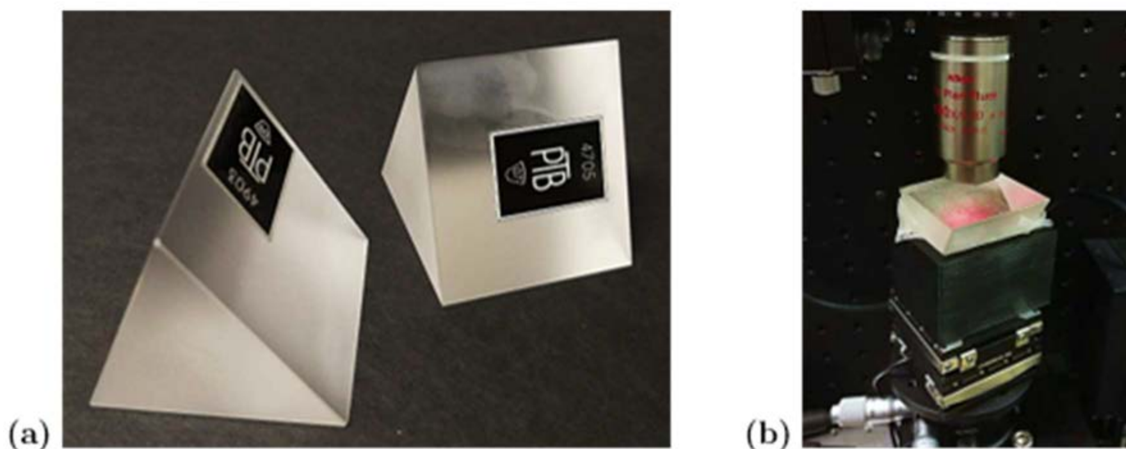

Figure 5-26. (a) Well-known isotropic prisms calibrated by PTB (Physikalisch-Technische Bundesanstalt) and (b) one of the prisms placed on the sample positioning system at the focal plane of the high *NA* objective.

	Wavelength $\lambda = 635\ nm$	
Samples	Prism 4705	Prism 4903
n	1.514913	1.456871

Table 5-4. Data for the two isotropic prisms calibrated by the PTB in Germany for the same wavelength than the used in the set-up.

a) Prism 4903

The normalized measured Mueller matrix image of prism 4903 is shown in Figure 5-27. As in the previous analyzed samples, one can observe noise introduced by the CMOS camera originated by vibrations produced by the cooling fan during the Mueller matrix image measuring time.

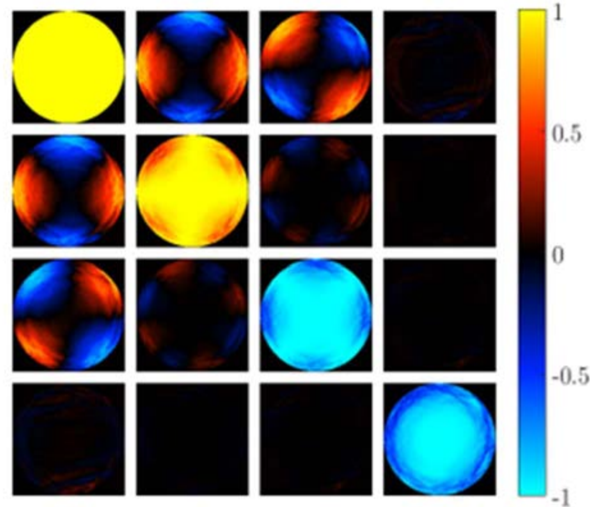

Figure 5-27. Measured Mueller matrix image of the glass prism 4903. The experimental image was filtered, and the depolarization was removed.

In section 5.3.3, we proved how the refractive index of samples and the maximum angle of incidence are mathematically correlated. As the two parameters are completely dependent, the optimization program may obtain a combination of these parameters that result into a local minimum different than the desired. Fitting the five unknown parameters; (x_0, y_0), ε_0, $\theta_{i,\max}$ and n, the best-fit refractive index found from the optimization routine is smaller than $n = 1.35$, i.e., the obtained result is quite different from the calibration value given by PTB (see Table 5-4). In this respect, we have decided to use the experimental Mueller matrix shown in Figure 5-27 and the refractive index of the well-calibrated glass prism (given in Table 5-4) to calculate the maximum angle of incidence of the HNAO. As has been demonstrated in Figure 5-18, the center of the image (x_0, y_0) and its rotation angle, ε_0, are not strongly correlated. Thus, by fixing n to the PTB value, the maximum angle of incidence can be obtained from the optimization program. Table 5-5 gives the obtained result, which corresponds to a *SAE* per pixel of 0.0026.

Parameters	n	$\theta_{i,\max}$ (°)
PTB values	1.456871	–
Best-fit values	1.456871	49.351446°

Table 5-5. Best-fit maximum angle of incidence for the Mueller matrix image of prism 4903 shown in Figure 5-27.

Simulated Mueller matrix image of the 4903 prism obtained from the best-fit data provide by the optimization program, when the RI is fixed to the PTB value, is shown in Figure 5-28 (a) and the *SAE* per pixel is graphically represented in Figure 5-28 (b).

To validate the measured $\theta_{i,\max}$, we have set a range of incident angles around the maximum angle of incidence retrieved by using the calibration 4903 prism, i.e., data given in Table 5-5 and the corresponding refraction indices have been calculated with the optimization routine. and the corresponding refraction indices have been calculated with the optimization routine. Figure 5-29 shows the refractive index n and its respective merit function value (*MSE*) as a function of the maximum angle of incidence.

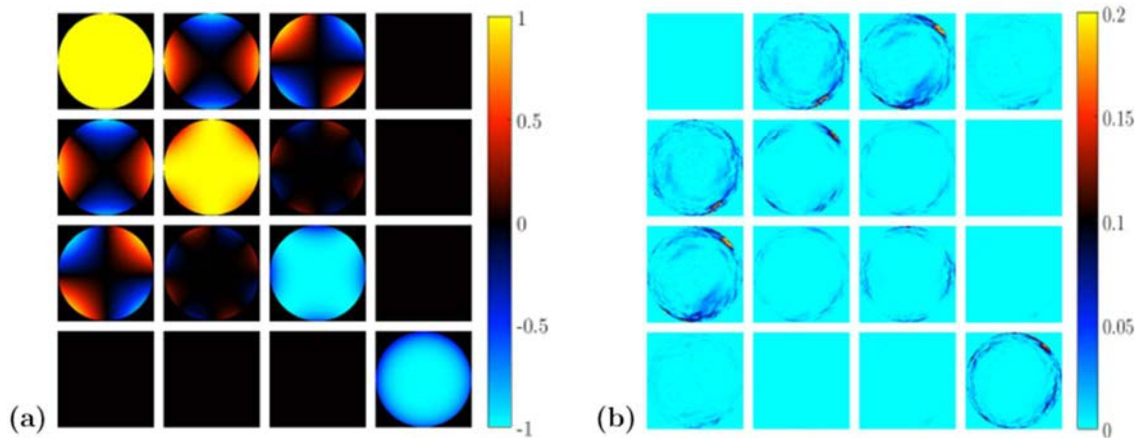

Figure 5-28. (a) Simulated Mueller matrix image obtained for a refractive index of $n = 1.456871$. (b) Representation of the squared absolute error per pixel between the experimental and the simulated Mueller matrix images of the 4903 glass prism.

Note that although the measured Mueller matrix image (see Figure 5-28) presented some experimental distortions (e.g., diffraction patterns are observed, the M_{03} and M_{30} coefficients are not zero), if the maximum angle of incidence is well-known, the refractive index can be accurately found, as correlation constrains are eliminated.

Therefore, this well-calibrated sample can be a reference to obtain the maximum angle of incidence, allowing us to fix it to break correlations. Nevertheless, although this method arises as a nice approximation to estimate the maximum angle of incidence, its value may slightly vary when a new sample has to be measured, especially because of concerns with regard to the sample axial position. This may reduce the final accuracy of the method for the RI measurement. In particular, if the sample is not perfectly well-placed at the focal plane of the HNAO, the size of different experimental Mueller matrix images slightly varies (see Figure 5-13), so it does the maximum incident angle. For this reason, we select a Region of Interest (ROI) at the experimental Mueller images by setting a circular mask (values are set to zero out of the circle) that fixes an incident angle between 48.5° and 50.3°, this allowing us to avoid, local minimums far away for the actual solution.

By taking into account the discussion above-provided, we want to emphasize that the precision of the method can be highly increased by devising some instrumental method able to place the samples surfaces with larger precision at the focal plane of the HNAO. In section 5.4, some possible methods to achieve this situation are proposed. Note that once the samples are perfectly placed at the microscope objective focal plane, corresponding

maximum angle of incidence is already known thanks to the calibration procedure conducted with the 4903 prism.

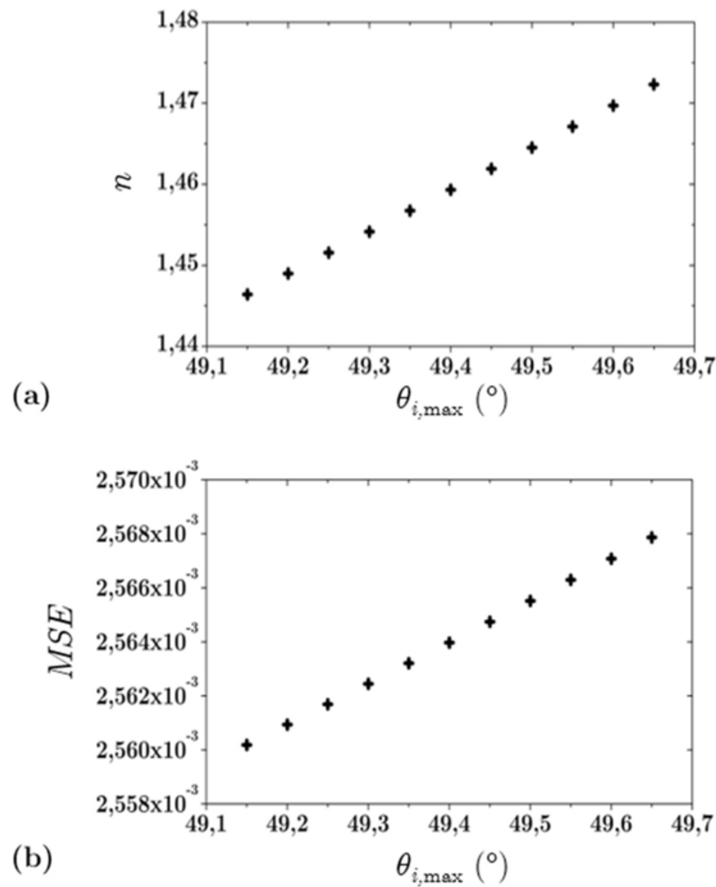

Figure 5-29. (a) Refraction index (*n*); and (b) Mean Squared Error (*MSE*) as a function of the maximum angle of incidence $\theta_{i,\max}$ (°) for the glass prism 4903.

It is important to note that when $\theta_{i,\max}$ value is fixed to that one given by the prims calibration (Table 5-5), the corresponding best-fit refractive index is very close to the value provided by the PTB (see Table 5-6), the method providing a RI measure with an accuracy at the forth decimal.

Parameters	n	$\theta_{i,\max}$ (°)
PTB values	1.456871	–
Best-fit values	1.456739	49.35°
Difference	0.000132	–

Table 5-6. Best-fit parameters for prism 4903 measured in reflection.

b) Prism 4705

The Mueller matrix image of the prism 4705 is measured by using our conoscopic Mueller microscope (see Figure 5-30)

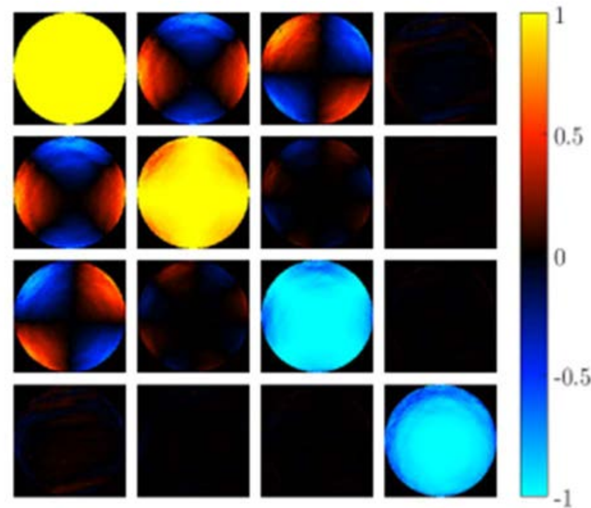

Figure 5-30. Measured Mueller matrix image of the Prism 4705.

The optimization program was used to find the best-fit values for prism 4705 for different maximum angles of incidence. Figure 5-31 shows the obtained n and *MSE*.

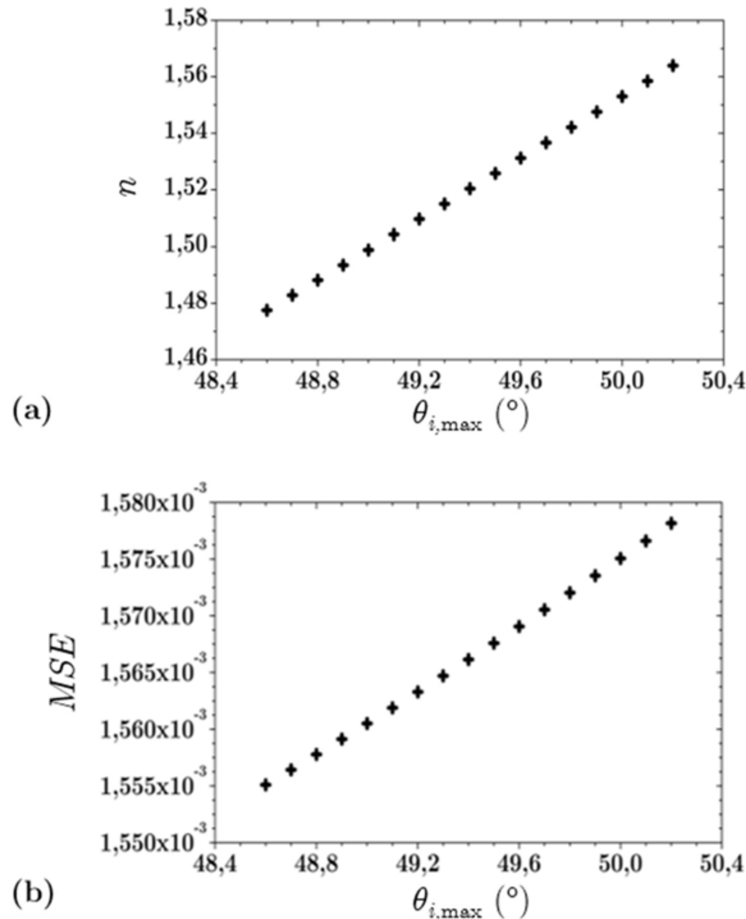

Figure 5-31. (a) Refraction index (n); and (b) Mean Squared Error (*MSE*) as a function of the maximum angle of incidence, $\theta_{i,\max}$ (°), for the well-known glass prism 4705.

By fixing the refractive index value of the 4705 prism, calibrated by the PTB (see Table 5-4), the maximum angle of incidence for the measured Mueller matrix image is obtained

from the optimization program. Results are given in Table 5-7. By comparing the maximum angles of incidence obtained for the 4903 (Table 5-6) and 4705 (Table 5-7) prisms, a small difference of 0.024º is obtained, mainly related with the system uncertainty in the axial positioning of samples.

Parameters	n	$\theta_{i,\max}$ (º)
PTB values	1.514913	–
Best-fit values	1.514913	49.374°

Table 5-7. Best-fit maximum angle of incidence for the Mueller matrix image of prism 4705 shown in Figure 5-30.

The simulated Mueller matrix image for the 4705 prism obtained from the best-fit parameters in Table 5-7 can be observed in Figure 5-32 (a) and a graphical representation of the pixel-by-pixel *SAE* is shown in Figure 5-32 (b).

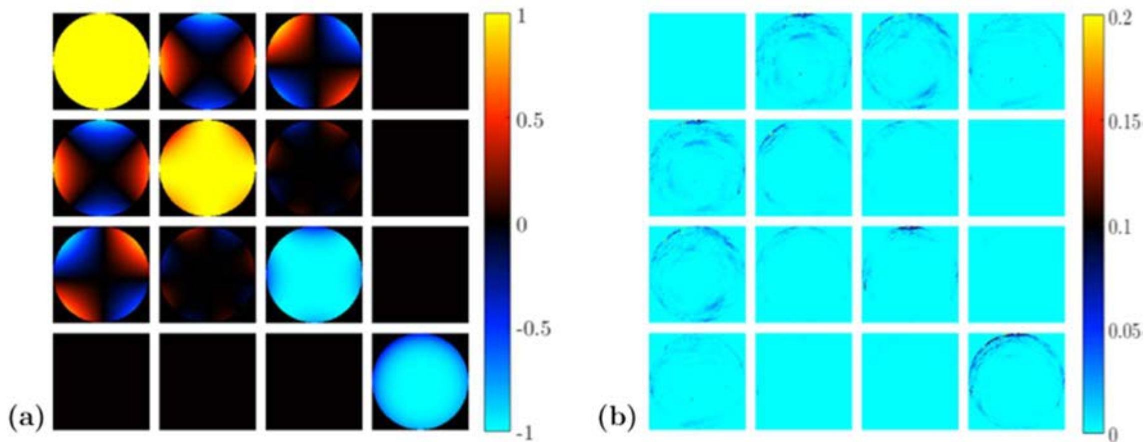

Figure 5-32. (a) Simulated Mueller Matrix image from best-fit values. (b) Squared absolute error between the experimental Mueller matrix (shown in Figure 5-30) and the simulated Mueller matrix, both for the prism 4705.

5.3.6 Non-planar surfaces

Once the performance of the conoscopic Mueller microscope and the method accuracy have been thoroughly analyzed to the characterization of planar samples, we tested the capability of the method to measure samples with arbitrary shape surfaces. In particular, to show the ability of the proposed conoscopic Mueller microscope to measure non-planar surfaces, two new samples were measured in our laboratory. An isotropic curved sample (glass bottle) and a uniaxial anisotropic mineral (quartz).

a) Glass bottle sample

We have used a glass bottle as an isotropic sample with non-planar surface because its surface is smooth but curved. The resulting Mueller matrix image can be seen in Figure 5-

33. We have demonstrated that, as the focused spot of the HNAO is smaller than the curvature surface of the sample, the surface at this scale can be considered planar and the Mueller matrix image of a glass bottle is similar to the angle-resolved Mueller matrix of a planar surface of glass.

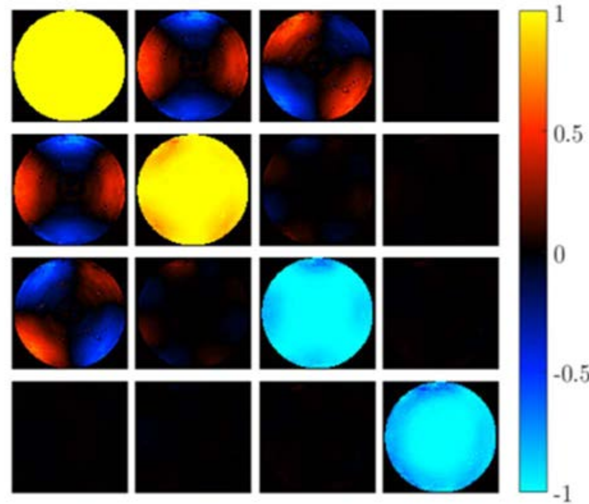

Figure 5-33. Measured Mueller matrix image of a curved glass bottle (isotropic sample).

To prevent of being redundant, in this subsection only qualitative analysis is provided (experimental Mueller matrix images). However, we have also conducted the calculation of the optical parameters in the same way than in previous sections. We reached the same conclusions, i.e., optical parameters in the optical model are strongly correlated, so accurate measurements of the refractive index are only achieved with a previous knowledge of the actual $\theta_{i,\max}$ for the particular sample axial position. By knowing the maximum incident angle value, the actual RI value is achieved, independently of the sample surface shape.

b) Quartz sample

To show the applicability of our conoscopic Mueller microscope, we have also measured a rough material. In this case, the sample is quartz (n_o = 1.5425 and n_e = 1.5516); i.e., a uniaxial anisotropic material. Its rough surface is clearly appreciated in Figure 5-34.

After placing the sample surface at the HNAO focal plane, we have measured the Mueller matrix image of the rough quartz. The resulting image is shown in Figure 5-35.

The same conclusions are reached for quartz, i.e., correlations constrain the method accuracy. In this particular case, more correlations between parameters are observed because of the larger number of parameters in the model (n_e, n_o, θ_c and ϕ_c) if comparing with the isotropic case. Therefore, further studies are needed to break correlations and expand the method accuracy.

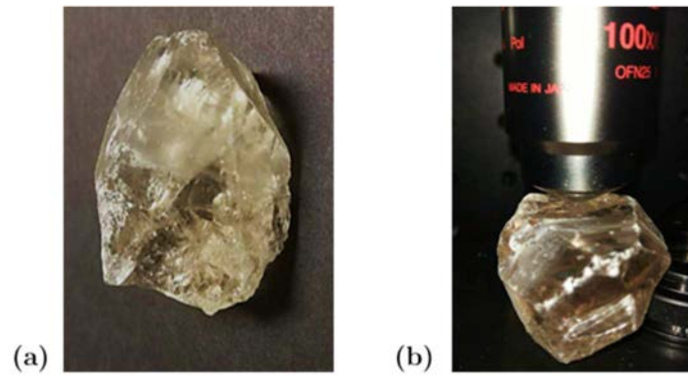

Figure 5-34. (a) Rough quartz crystal; and (b) Quartz placed in the sample positioning system.

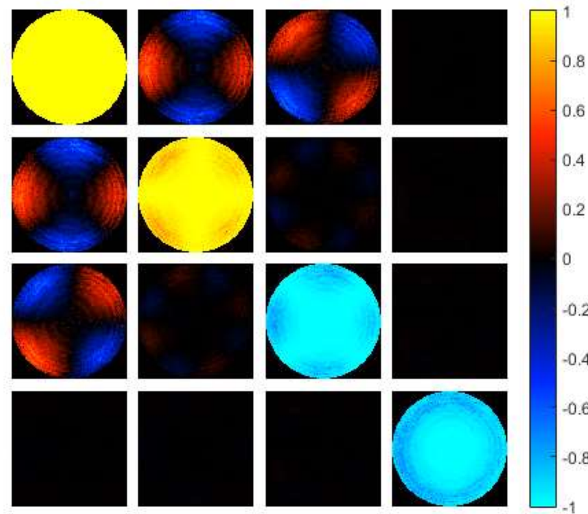

Figure 5-35. Measured Mueller matrix image of a rough quartz crystal.

5.4 Discussion and perspectives

In this chapter we have seen that the Mueller matrix image of any sample regardless of its curvature can be measured by using our developed conoscopic Mueller microscope. In this sense, we have measured angle-resolved Mueller matrices for different kinds of samples such as flat and non-planar surfaces, liquids and solids, isotropic and uniaxial anisotropic materials, among others. The obtained patterns for this numerical aperture are similar to the simulated ones described in Chapter 3. However, the proposed set-up is a first prototype that needs certain improvements. In this section, we suggest some changes that can be implemented to improve the final result. We think that the designed microscope clearly demonstrates the potential of angle-resolved Mueller matrices as a refractive index characterization tool. Nevertheless, some further improvements have to be done on the design of the instrument itself to make it even reliable and more accurate.

First, we have seen the importance of placing the sample surface at the focal plane of the high numerical aperture objective. The actual prototype does not exactly focus the incident beam on the sample surface, which results in different sizes of the Mueller matrix

image. The used method presents the problem that the image of the spot on the CMOS camera is small and it is complicated to appreciate when the sample surface is perfectly placed at the focal point of the HNAO. In this sense, a better way to ensure the optimal placement of samples at the focal plane is needed to obtain higher accuracy measures.

Our proposal is to readapt our conoscopic Mueller microscope into a confocal microscope [187–189] similar to the shown in Figure 5-36. Confocal optical microscopy is a spatial filtering technique used for increasing the contrast of microscope images eliminating out-of-focus light. It works on a simple principle, light from the focal point of the HNAO is imaged on a small pinhole, making these two points confocal, i.e., by using an additional microscope objective and a pinhole (PH) (see Figure 5-36) the volume observed with the CMOS camera is restricted. Under this scenario, a sample surface that is not placed at the focal plane of the HNAO will not completely illuminate all the pinhole. Hence, the PH prevents reflected light from planes different than the plane of focus from reaching the CMOS camera. By moving the sample parallel to the optical axis of the HNAO, only when reflected light passes through the pinhole, the sample surface is placed at the right position. Furthermore, a confocal configuration avoids undesired reflections produced by different sample layers, thus the Mueller matrix image will be clearer.

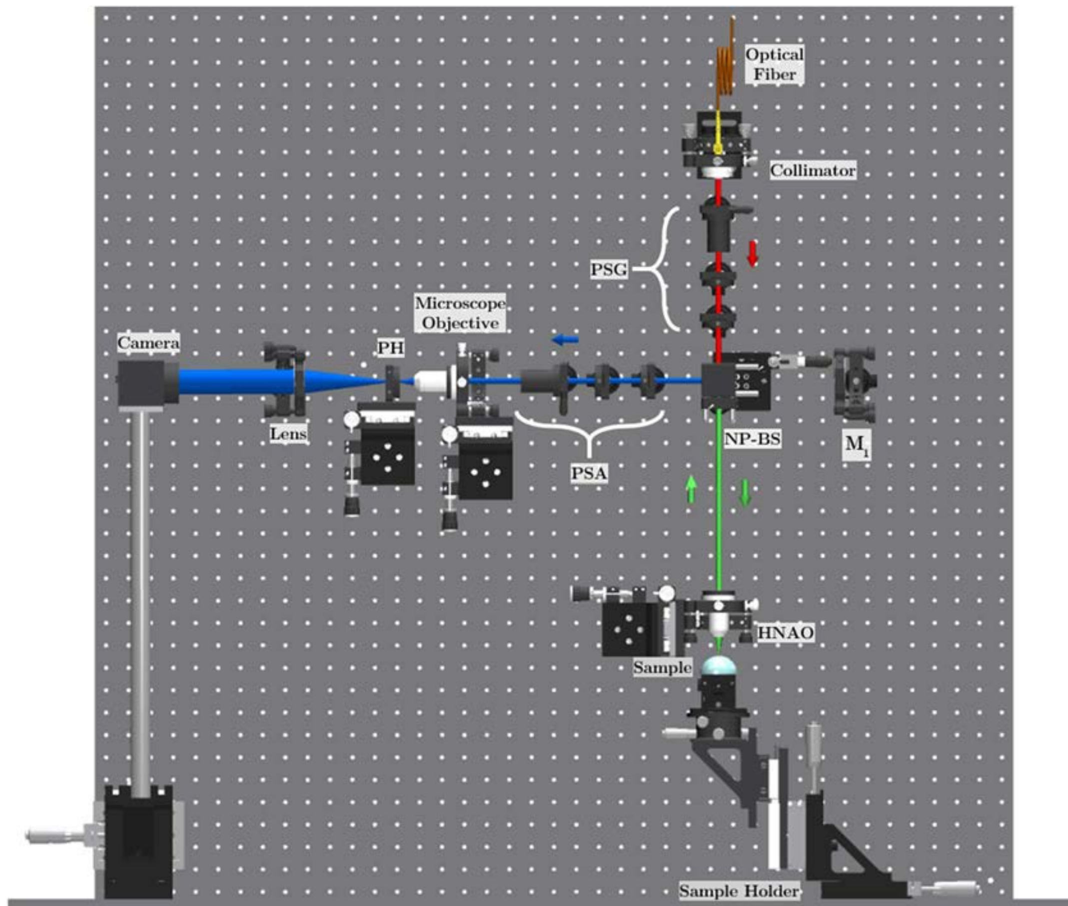

Figure 5-36. Scheme of the confocal Mueller microscope. The set-up is similar to the conoscopic Mueller microscope shown in Figure 4-1. A microscope objective, a pinhole (PH) and a lens are introduced in the set-up to convert our proposed Mueller microscope into a confocal microscope.

On the other hand, to reduce the correlation between parameters when the optimization program calculates the best-fit refractive index, we need to know the maximum angle of incidence that is imaged on the CMOS camera. The proposed confocal configuration also allows to find $\theta_{i,\max}$. When the surface of the well-calibrated prisms is placed at the right focal plane, the Mueller patterns will have the exact size and hence, the same maximum angle of incidence. Consequently, by fixing the refractive indices of the prism samples in the iterative optimization program, the maximum angle of incidence can be calculated from their experimental Mueller matrix images. In both cases the best-fit $\theta_{i,\max}$ has to be equal, although their refractive indices are different. Then, the best-fit RI of any other sample can be calculated by measuring its characteristic Mueller matrix image and by fixing the previously calculated best-fit $\theta_{i,\max}$ in the optimization program.

In literature, we can find other techniques that allows us to characterize and understand the physical properties of materials avoiding the correlation between parameters. Refs. [190] and [110] propose a procedure to increase, not only the angles of incidence usually performed by moving arms, but also the number of used wavelengths in ellipsometric measures, providing more information on the optical parameters. In our case, each point of our measured Mueller matrix image corresponds to an angle of incidence that illuminates a pixel of our CMOS camera, and this angular distribution is independent of the used wavelength. So, the use of diverse wavelengths results in different Mueller patterns, because of the dependence of the refractive index with λ, but the distribution of the angles of incidence will be always the same. Thus, using several wavelengths and a sample with its refractive indices well-calibrated for each λ, we will obtain larger redundancy data for the of maximum angle of incidence determination.

A different method is proposed in Ref. [125] to measure $\theta_{i,\max}$. They place well-known gratings, whose refractive indices and pitches are well-characterized, in the focal plane of the HNAO and then, they analyze the position of different diffraction orders, with respect to the zero order. The maximum angle of incidence is obtained from

$$\theta_{i,\max} = \arcsin\left(n \frac{\lambda \cdot R}{\Lambda \cdot d} \right) \tag{5.9}$$

where R is the radius of the image corresponding to the maximum aperture, d the shift (in pixels) between the orders (see Figure 5-37), and Λ the pitch of the grating.

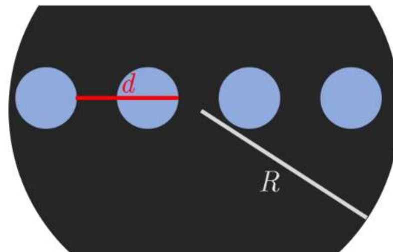

Figure 5-37. Scheme of four diffraction orders of a grating. d is the shift between orders and R is the radius of the image corresponding to the maximum aperture.

Finally, we propose to expand the theoretical model to anisotropic biaxial crystals. In such a way, any dielectric material can be optically characterized by using the conoscopic Mueller microscope. We also propose to readapt the set-up, similar to the microscopes shown in Refs. [120, 191], to measure Mueller matrix images also in transmission mode.

Chapter 6 Conclusions

A conoscopic Mueller microscope working in reflection was designed, implemented and applied for the first time to measure the refractive indices of dielectric isotropic samples and uniaxial anisotropic crystals, with planar or non-planar surfaces. First, a mathematical model was developed to determine the angle-resolved Mueller matrix image of the microscope back focal plane. The model parameters of interest were studied by performing a collection of simulations, and we analyzed the viability of the method by measuring the characteristics of different artificial samples. Then, a conoscopic microscope within a complete Mueller matrix polarimeter was designed and experimentally implemented. After being calibrated and tested by measuring different well-known polarimetric samples, the experimental angle-resolved Mueller matrices of different isotropic and anisotropic materials were measured. By fitting the optical parameters of the theoretical model with the experimental data, the optical characteristics of different samples were determined by minimizing a merit function based on the Mean Squared Error (*MSE*) minimization. The method shown the potential of being used for the characterization of isotropic and anisotropic samples, both presenting planar or non-planar surfaces, and in solid and liquid phases.

As the proposed instrument performs the measurements into a reflective configuration, it could be used to characterize optical elements already integrated in optical systems, this kind of samples being impossible to be studied with other existing metrological techniques. In this last chapter we summarize the main results presented in this thesis (section 6.1) and we outline possible future perspectives of the instrumentation (section 6.2), to enhance its efficiency in samples characterization.

6.1 Summary and conclusions

We emphasize the following main conclusions from each chapter:

6.1.1 Mathematical formalism

Our study in Chapter 2 was meant to review some preliminary concepts required to physically describe the conoscopic Mueller microscope developed in our laboratory. Starting with Maxwell's equations, we have developed a mathematical formalism able to describe an electromagnetic plane wave at the interface of an isotropic sample (air) in contact with a uniaxial anisotropic crystal. Both media were considered dielectric and non-absorbing.

The mathematical model was proposed to describe the wave vectors and the polarization states of the incident, reflected and refracted waves as a function of the wavelength, the angle of incidence, the amplitude and phase of the incident beam, and the refractive indices (ordinary and extraordinary) and the orientation of the optical axis of the uniaxial anisotropic sample. Then, the Fresnel coefficients in reflection and in transmission were obtained, allowing us to easily relate the reflected (or transmitted) electromagnetic fields with the incident one.

The Jones matrix formalism was also introduced as a form of express the polarization changes produced by an isotropic-uniaxial anisotropic interface. Finally, from the obtained Jones matrix, the equivalent Mueller matrix of the uniaxial anisotropic sample was also calculated.

6.1.2 Mueller conoscopy

In the first part of Chapter 3 we have generalized the Jones matrix obtained in Chapter 2 to describe the changes of the electromagnetic fields produced when light passes through a high numerical aperture objective (HNAO). When a set of planar electromagnetic waves passes through a HNAO, the incident light is bent with multiple angles of incidence forming a cone of light. In this manner, we are able to instantaneously generate a large number of wave vectors. At the same time, the polarization of each generated wave-vector changes as a function of the polar and azimuthal angles of incidence. Considering both effects, we have recalculated the Jones and the Mueller matrices in order to express them as a function of azimuthal and polar angles of incidence. In addition, both matrices were represented, in the incident plane coordinate system, that changes with the azimuth, and also in the laboratory coordinate system, that is fixed, to take into account the polarization changes produced by the HNAO. The differences between both coordinate systems were presented for isotropic and uniaxial anisotropic crystals.

From this extension of the mathematical model, we have proposed to build a conoscopic microscope working in reflection by using a high numerical aperture objective that illuminates the sample surface and, at the same time, collects the reflected beam. In this sense, by using the mathematical formalism described in Chapter 2 and Chapter 3, the optical parameters of the sample could be obtained from the angle-resolved Mueller matrix image, where each point of the measured Mueller matrix image is associated to a particular pair of angles of incidence (azimuthal and polar angles), and thus, to a polarization change.

The polarimetric measurement matrix principle used to acquire the Mueller matrix image, and the errors introduced by the polarimetric system, were also explained. We proposed to use six polarizing generators and six analyzers to measure the Mueller matrix image. The optimized configuration for generating and analyzing an arbitrary polarization state was a regular polyhedron with six vertices inscribed in the Poincaré sphere, to achieve the minimum possible condition number of $CN = \sqrt{3}$.

Once the Mueller matrix was described in the laboratory coordinate system, we simulated several scenarios to analyze the viability of the proposed conoscopic Mueller microscope. In this sense, objectives with different NA and multiple samples with various refractive indices were studied. In particular, we have demonstrated that higher numerical apertures provide more significant sample information. For small variations of the incident angle when being above of $\theta_{i,\max} > 50^{\circ}$, one could clearly see how Mueller matrix coefficients sharply vary, as the system is close to the Brewster angle of the material. In addition, significant differences were observed in the Mueller matrix images of uniaxial anisotropic and isotropic specimens meaning that we could perfectly design a conoscopic Mueller microscope for refractive index characterization.

The last part of this chapter describes the method developed in order to obtain the refractive indices of materials comparing experimental and theoretical Mueller matrix images. An iterative optimization routine was created based on the minimization of the Mean Squared Error (MSE) function. The idea was to compare each point of the predicted and experimental Mueller matrix images, varying a set of unknown parameters (the refractive indices, the orientation of the sample, $\theta_{i,\max}$, and the center and any rotation of the image). When the MSE was minimized, we considered that the desired values were found. For that purpose, a previous knowledge of the material under study might allow to constrain the unknown parameters. The validity of this method was studied by using artificial Mueller matrix images, simulating experimental Mueller matrix images (e.g. rotated, displaced, with noise, etc.).

6.1.3 Experimental implementation of our conoscopic Mueller microscope

The conoscopic Mueller microscope built in this work uses a high numerical aperture objective (HNAO) to highly focus the incident light beam on the sample surface and to collect the reflected beam, allowing us to simultaneously illuminate the specimen with a large number of angles of incidence without involving any moving arms in the system (this avoiding the consequent positioning errors). In Chapter 4, we have described the experimental implementation of our conoscopic Mueller microscope and the calibration process followed.

The first subsections provided the description of the set-up as well as each used optical element. We have divided the whole system in four different parts that were described in detail in section 4.1:

- Illumination arm: formed by a diode laser ($\lambda = 635\ nm$), a collimator and polarization state generator (PSG) able to generate collimated input light beams with controlled polarization.

- Detector arm: consists of a polarization state analyzer (PSA) and a CMOS camera. It analyzes the polarization changes of the reflected beam caused by the sample. From the intensity images obtained with this instrumental block, we were able to calculate the experimental Mueller matrix image. Compared with other systems, the fact of including a PSG and a PSA in our system which are based on liquid crystal displays, allows us the generation and detection of polarization states without the requirement of mechanical movements.

- High numerical aperture focusing system: focuses the incident beam and, at the same time, collects the reflected cone of light by using a high numerical aperture objective (HNAO). Once the reflected beam was collimated, an achromatic non-polarizing beam-splitter cube (NP-BS) steered it to the detector arm. The fact of using a HNAO in our system, allows us instantaneously performing angle-resolved measures of the Mueller matrix, avoiding moving parts and thus, positioning errors.

- Sample Positioning System: formed by a sample holder, a pair of goniometers and translation platforms. The designed holder allows both to place the sample at the high *NA* objective focal plane and to accurately align the sample surface perpendicularly to the optical axis of the HNAO.

The used microscope objective has a *NA* of 0.90 and a long working distance of 1 *mm*. Consequently, the resulting focalization spot was small enough to approximate the studied surfaces as locally planar. Note that as we are using a high *NA*, this implies that any small deviation of the light path, when it passed through any slightly misaligned optical element, becomes critical due to the high magnification of the system. For this reason, the whole conoscopic Mueller microscope was designed to be able to correct any possible small misalignment. This was achieved by allowing us to shift in different directions and/or rotate in different angles each one of the optical elements in our set-up. Furthermore, we have taken into account that our microscope would measure the angle-resolved Mueller matrix of different specimens. Therefore, the HNAO was chosen to not introduce polarization modifications to the involved beams.

As stated above, the developed microscope worked as a Mueller image polarimeter. To include the polarimetric information to the angle-resolved system, the microscope includes a PSG and PSA systems to generate and analyze different polarization states. Both optical devices consisted of a linear polarizer and two liquid crystal displays (as linear variable retarders) oriented at 45° one to each other.

The designed set-up theoretically enabled us to measure the angle-resolved Mueller matrix of samples for all azimuth angles (from 0° to 360°) and for angles of incidence from 0° to 64° (approx.). Nevertheless, the incident collimated beam was measured by using the

knife-edge technique, obtaining a beam diameter smaller than the aperture of the HNAO. Thus, the maximum angle of incidence was smaller than the predicted value (around 50°). Apart from the *NA* of the microscope objective, to measure a large number of angles of incidence, we have used a CMOS camera with high-resolution (2048 × 2048 *pixels*). It was also important to use a camera with high dynamic range to have greater range of measured intensities.

The alignment procedure followed to build the whole system was detailed in this chapter. Moreover, the calibration method applied to characterize the beam-splitter, the CMOS camera and the PSG and PSA systems were discussed at the end of this chapter. From the obtained results, we observed polarimetric effects introduced by the NP-BS. Consequently, both PSG and PSA were calibrated together with the NP-BS to consider these effects when the Mueller matrix images were measured (i.e., the polarimetric effects of the beam-splitter are included in the polarimetric matrices describing the input polarizations set for the PSG and the polarization analyzers set for the PSA). To verify the optimized performance of the system, in terms of noise amplification from intensity images to the obtained experimental angle-resolved Mueller matrices, the condition number for the PSG and PSA systems (including the BS effects) were measured, obtaining respectively $CN(\text{PSG}) = 1.76$ and the $CN(\text{PSA}) = 1.78$, these values being close to the optimum theoretical minimum $CN = \sqrt{3}$.

6.1.4 Results

First, the Mueller polarimeter was experimentally tested by measuring in reflection different well-known polarizing samples (e.g. mirror, polarizer, quarter waveplate, etc.), and an excellent agreement between experimental and theoretical values were obtained. The maximum error in the Mueller matrices was smaller than 0.78%, and could be due not only to the calibration of the PSG and PSA, but also to effects of small misalignments present in polarizing elements (mostly in their orientation), no ideal optical samples, etc. In addition, we have observed condensate droplets inside the CMOS camera protector glass. These droplets are due to the condensation of air that enters inside the protector glass and cannot be removed. Although we observed that the image degradation related to the droplets do not affect too much the recorded intensity images, their effects had to be considered.

For this reason, to reduce the impact of these undesirable effects in the experimental Mueller image, some filtering techniques were described and implemented. The covariance filtering method was used to eliminate noise in the measured image and to obtain a physically realizable Mueller matrix, and the Lu-Chipman decomposition was used to remove depolarization effects.

Next, we have experimentally characterized the high numerical aperture objective. This was done by using a spherical mirror specially designed to avoid the polarization effects of high angles of incidence. When placing the mirror at the proper distance from the HNAO,

each ray in the incident cone is reflected normal to the mirror surface. Under this scheme, the characteristic Mueller matrix of the HNAO was obtained. We have observed that the retardance, diattenuation and depolarization introduced by the used HNAO were negligible.

Once the whole microscope was completely calibrated, different isotropic and uniaxial anisotropic samples were measured, observing that the experimental angle-resolved Mueller matrix images were in agreement to those simulated in Chapter 3. However, the measured experimental images presented certain deviation from the simulated images, whose origin was mainly due to instrumental errors, and that were not fully corrected by the applied filtering process. In particular, these deviations from the theoretical images are introduced by small misalignments of the HNAO, sample oscillations produced by the cooler fan of the CMOS camera during the measuring time, diffractive effects related to aperture sizes, small displacements of the sample holder related to screws spatial relaxations, etc.

The developed optimization program was used to calculate refractive indices of different samples by fitting the theoretical optical parameters of the developed model with experimental angle-resolved Mueller matrices. First, liquids and planar samples were characterized (olive oil, water, and plastics). From these first results, we have concluded that there exists a high correlation between $\theta_{i,\max}$ and RI parameters, whereas the center and the rotation of the image were independent parameters. Furthermore, we have observed that by setting the correct value for the maximum angle of incidence, the calculated values for the refractive indices agree with the expected values. Therefore, an external measure of the $\theta_{i,\max}$ value is required to properly measure the RI of samples.

Afterwards, we measured two reference samples to further test our developed method. We used planar glass samples which were previously accurately calibrated by the Physikalisch-Technische Bundesanstalt (PTB) in Germany by using the minimum deviation method and were accurately characterized for our used wavelength ($\lambda = 635\ nm$) Comparing the results obtained from both glass prisms, we confirmed the necessity of an external and accurate determination of the experimental maximum angle of incidence parameter, as the axial position of the sample affected the value of $\theta_{i,\max}$, and therefore, the value of the obtained RI. As a consequence, only by accurately setting the proper value of the experimental $\theta_{i,\max}$, a good agreement was obtained between the RI values provided by the PTB and by our proposed method. As logical, the correct experimental value for maximum angle of incidence was that set when the measured samples were exactly placed at the focal plane of the HNAO (i.e., $\theta_{i,\max} \sim 49.5^{\circ}$). However, note that by changing from sample to sample in a chain procedure, an associated error to the axial position of the samples may be added, this being crucial for the RI determination of the samples, due to the above-stated correlations.

Under this scenario, we have proposed some changes in the experimental instrumentation that can be implemented to place the sample at the right position as well as to improve the quality of the recorded image. These modifications were discussed in section 5.4.

Finally, to prove the practical applicability of this conoscopic Mueller microscope, the Mueller matrix images of curved glass and rough quartz samples were measured and shown. Considering the capacity of our instrument to determine angular-resolved Mueller matrix images of those samples, we demonstrate that our developed microscope can be suitable to optically characterize non-planar surfaces in reflection.

6.2 Proposal for future research

- The mathematical formalism explained in Chapter 2 can be expanded to anisotropic biaxial crystals. Thus, any dielectric material could be optically characterized by using the conoscopic Mueller microscope.
- To convert the conoscopic Mueller microscope in a reflection confocal microscope. In this sense, light that returns to the system from layers different than the sample surface will be blocked (or almost blocked) by the confocal aperture. When information coming from different sample depths is incoherently added at the detector, non-desired depolarization contributions may be added at the final Mueller matrix images. Therefore, the confocal configuration will reduce depolarization content in Mueller matrix images. More importantly, the confocal configuration also allows that only those samples exactly placed at the back focal plane of the HNAO can be measured, this guaranteeing a fixed ($\theta_{i,\max}$) for all the samples.
- To implement an experimental method able to accurately measure the maximum angle of incidence ($\theta_{i,\max}$), in order to fix this value in the mathematical model, and thus, to reduce correlations between parameters. As was explained in Chapter 5, the characteristic optical parameters of the sample can be obtained when the maximum angle of incidence is accurately known a priori.
- The optimization program can also be reviewed to include different optimization routines and to improve its calculation speed.
- The conoscopic Mueller microscope can be readapted to work in transmission by properly adding a second high numerical aperture objective. Accordingly, thin layers can be measured in both, reflection and transmission configurations. The transmission configuration could also be used to determine other properties of samples, as their thickness. Moreover, the model has to be expanded to describe the characteristic Mueller matrix of isotropic or anisotropic samples at the back focal plane of the second HNAO.
- The system could also be adapted to work for different wavelengths. Although the refraction index may change for different wavelengths due to dispersion of light, the ($\theta_{i,\max}$) remains constant for all wavelengths, as ($\theta_{i,\max}$) is not an intrinsic property of samples but of the optical system. Therefore, by imposing this condition, in addition to the angle-resolved redundancy data, a more efficient data fitting could be achieved.

List of acronyms

Acronym	**Meaning**
CN	Condition Number
HNAO	High Numerical Aperture Objective
LP	Linear Polarizer
MAE	Mean Absolute Error
MSE	Mean Squared Error
NA	Numerical Aperture
PSA	Polarization State Generator
PSG	Polarization State Analyzer
RI	Refractive index
SAE	Squared Absolute Error
SoP	State of Polarization

Bibliography

[1] E. Hecht. *Optics. 4th Ed.* Addison-Wesley (2001).

[2] M. Born, and E. Wolf. *Principles of optics: Electromagnetic Theory of Propagation, Interference and Diffraction of Light. 7th Ed.* Cambridge University Press (1999).

[3] J. Sun, S.J. Lee, L. Wu, M. Sarntinoranont, and H. Xie. *Refractive index measurement of acute rat brain tissue slices using optical coherence tomography.* Opt. Express **20** (2), pp. 1084–1095 (2012).

[4] D. Maciel, S.P. Veres, H.J. Kreuzer, and L. Kreplak. *Quantitative phase measurements of tendon collagen fibres.* J. Biophotonics **10** (1), pp. 111–117 (2017).

[5] J. Binding, J. Ben Arous, J.-F. Léger, S. Gigan, C. Boccara, and L. Bourdieu. *Brain refractive index measured in vivo with high-NA defocus-corrected full-field OCT and consequences for two-photon microscopy.* Opt. Express **19** (6), pp. 4833–4847 (2011).

[6] Y. Park, M. Diez-Silva, G. Popescu, G. Lykotrafitis, W. Choi, M.S. Feld, and S. Suresh. *Refractive index maps and membrane dynamics of human red blood cells parasitized by Plasmodium falciparum.* Proc. Natl. Acad. Sci. **105** (37), pp. 13730–13735 (2008).

[7] J. Yoon, K. Kim, H. Park, C. Choi, S. Jang, and Y. Park. *Label-free characterization of white blood cells by measuring 3D refractive index maps.* Biomed. Opt. Express **6** (10), pp. 3865–3875 (2015).

[8] M. Schürmann, J. Scholze, P. Müller, C.J. Chan, A.E. Ekpenyong, K.J. Chalut, and J. Guck. *Refractive index measurements of single, spherical cells using digital holographic microscopy*, in *Methods in cell biology*, vol. 125, pp. 143–159 (2015).

[9] P.Y. Liu, L.K. Chin, W. Ser, H.F. Chen, C.-M. Hsieh, C.-H. Lee, K.-B. Sung, T.C. Ayi, P.H. Yap, B. Liedberg, K. Wang, T. Bourouina, and Y. Leprince-Wang. *Cell refractive index for cell biology and disease diagnosis: past, present and future.* Lab Chip **16** (4), pp. 634–644 (2016).

[10] B. Rappaz, P. Marquet, E. Cuche, Y. Emery, C. Depeursinge, and P.J. Magistretti. *Measurement of the integral refractive index and dynamic cell morphometry of living cells with digital holographic microscopy.* Opt. Express **13** (23), pp. 9361–9373 (2005).

[11] Z. Wang, G. Popescu, K. V. Tangella, and A. Balla. *Tissue refractive index as marker of disease.* J. Biomed. Opt. **16** (11) (2011).

[12] W.M. bin M. Yunus, and A. bin A. Rahman. *Refractive index of solutions at high concentrations.* Appl. Opt. **27** (16), pp. 3341–3343 (1988).

[13] J.S. Buckley. *Predicting the Onset of Asphaltene Precipitation from Refractive Index Measurements*. Energy Fuels **13** (2), pp. 328–332 (1999).

[14] J. Babul, and E. Stellwagen. *Measurement of protein concentration with interferences optics*. Anal. Biochem. **28**, pp. 216–221 (1969).

[15] P. Strop, and A.T. Brunger. *Refractive index-based determination of detergent concentration and its application to the study of membrane proteins*. Protein Sci. **14**, pp. 2207–2211 (2005).

[16] M.J. Iqbal, and M.A. Chaudhry. *Thermodynamic study of three pharmacologically significant drugs: Density, viscosity, and refractive index measurements at different temperatures*. J. Chem. Thermodyn. **41** (2), pp. 221–226 (2009).

[17] M. Ebert, S. Weinbruch, P. Hoffmann, and H.M. Ortner. *The chemical composition and complex refractive index of rural and urban influenced aerosols determined by individual particle analysis*. Atmos. Environ. **38** (38), pp. 6531–6545 (2004).

[18] H. Horvath, and R.J. Charlson. *The Direct Optical Measurement of Atmospheric Air Pollution*. Am. Ind. Hyg. Assoc. J. **30** (5), pp. 500–509 (1969).

[19] L.G. Thompson. *Study of the Effect of Pollutants on the Index of Refraction*. Appl. Opt. **10** (3), pp. 677–678 (1971).

[20] R. Camezon. *Brix determining apparatus*. US 6135319A (1999).

[21] V. Fedele. *Universal refractometer apparatus and method*. US 8239144B2 (2010).

[22] Y.-L. Yeh. *Real-time measurement of glucose concentration and average refractive index using a laser interferometer*. Opt. Lasers Eng. **46** (9), pp. 666–670 (2008).

[23] D. Yoder-Short. *Interferometric measurement of glucose by refractive index determination*. US 5168325A (1992).

[24] M.D. Dyar, M.E. Gunter, and D. Tasa. *Mineralogy and optical mineralogy*. Mineralogical Society of America (2008).

[25] F.D. Bloss. *Optical crystallography*. Mineralogical Society of America (1999).

[26] M.P. Jones. *Applied mineralogy: a quantitative approach*. Graham & Trotman (1987).

[27] R.C. Faust. *Refractive Index Determinations by the Central Illumination (Becke Line) Method*. Proc. Phys. Soc. Sect. B **68** (12), pp. 1081–1094 (1955).

[28] C.W. Correns, and J. Zemann. *Introduction to Mineralogy: Crystallography and Petrology. 2nd Ed.* Springer-Berlin Heidelberg (1969).

[29] B.E. Sørensen. *A revised Michel-Lévy interference colour chart based on first-principles calculations*. Eur. J. Mineral. **25** (1), pp. 5–10 (2013).

[30] V.G. Feklichev, and B.V. Rassadin. *Diagnostic constants of minerals*. CRC Press (1992).

[31] F.D. Bloss. *Optical Crystallography Simplified - The spindle stage: Principles and Practice*. Mineralogical Society of America (2017).

[32] S. Mukherjee. *Applied mineralogy : applications in industry and environment*. Springer Netherlands (2011).

[33] W.D. Nesse. *Introduction to optical mineralogy. 3rd Ed.* Oxford University Press (2004).

[34] A. Kuske, and G.S. Robertson. *Photoelastic stress analysis*. John Wiley & Sons (1974).

[35] J.F. Orr, and J.B. Finlay. *Photoelastic stress analysis*, in *Optical measurement methods in biomechanics*, Springer, pp. 1–16 (1997).

[36] A.R. Lang. *Causes of Birefringence in Diamond*. Nature **213**, pp. 248–251 (1967).

[37] D. Howell. *Strain-induced birefringence in natural diamond: a review*. Eur. J. Mineral. **24** (4), pp. 575–585 (2012).

[38] Y. Ju, Z. Zheng, H. Xie, J. Lu, L. Wang, and K. He. *Experimental Visualisation Methods for Three-Dimensional Stress Fields of Porous Solids*. Exp. Tech. **41** (4), pp. 331–344 (2017).

[39] T.D. Pallicity, A.-T. Vu, K. Ramesh, P. Mahajan, G. Liu, and O. Dambon. *Birefringence measurement for validation of simulation of precision glass molding process*. J. Am. Ceram. Soc. **100** (10), pp. 4680–4698 (2017).

[40] K. Ramesh, and V. Ramakrishnan. *Digital photoelasticity of glass: A comprehensive review*. Opt. Lasers Eng. **87**, pp. 59–74 (2016).

[41] K. Ramesh, M.P. Hariprasad, and S. Bhuvanewari. *Digital photoelastic analysis applied to implant dentistry*. Opt. Lasers Eng. **87**, pp. 204–213 (2016).

[42] I.A. Takacs, A.I. Botean, M. Hardau, and S. Chindris. *Displacement-stress Distribution in a Femoral Bone by Optical Methods*. Procedia Technol. **19**, pp. 901–908 (2015).

[43] G.P. Agrawal. *Fiber-optic communication systems. 3rd Ed.* John Wiley & Sons (2002).

[44] I.P. Kaminow, T. Li, and A.E. Willner. *Optical fiber telecommunications VI. A, Components and subsystems. 6th Ed.* Academic Press (2013).

[45] B. Lee. *Review of the present status of optical fiber sensors*. Opt. Fiber Technol. **9** (2), pp. 57–79 (2003).

[46] K.T. V. Grattan, and B.T. Meggitt (eds.). *Optical Fiber Sensor Technology*. Springer US, Boston, MA (1999).

[47] W.-S. Tsai, B.-J. Huang, and F.-W. Sheu. *Improvement of refractive index profiling of a small-core single-mode fiber under partially coherent light excitation*. Opt. Commun. **336**, pp. 88–92 (2015).

[48] M. Spier. *Injection molding process*. US 3950483A (1974).

[49] Hermann P. Weber. *Apparatus for injection molding lenses*. US 4008031A (1975).

[50] A.Y. Yi, and A. Jain. *Compression Molding of Aspherical Glass Lenses-A Combined Experimental and Numerical Analysis*. J. Am. Ceram. Soc. **88** (3), pp. 579–586 (2005).

[51] M. Vandenberg. *Compression molding of optical lenses*. US 6521146B1 (2000).

[52] K.-M. Tsai. *Effect of injection molding process parameters on optical properties of lenses*. Appl. Opt. **49** (31), pp. 6149 (2010).

[53] A. Guevara-Morales, and U. Figueroa-López. *Residual stresses in injection molded products*. J. Mater. Sci. **49** (13), pp. 4399–4415 (2014).

[54] S.-C. Chen, Y.-C. Chen, H.-S. Peng, and L.-T. Huang. *Simulation of injection-compression molding process, Part 3: Effect of process conditions on part birefringence*. Adv. Polym. Technol. **21** (3), pp. 177–187 (2002).

[55] S. Singh. *Refractive Index Measurement and its Applications*. Phys. Scr. **65** (2), pp. 167–180 (2002).

[56] W.L. Bond. *Measurement of the Refractive Indices of Several Crystals*. J. Appl. Phys. **36** (5), pp. 1674–1677 (1965).

[57] D. Tentori, and J.R. Lerma. *Refractometry by minimum deviation: accuracy analysis*. Opt. Eng. **29** (2), pp. 160–168 (1990).

[58] V.G. Plotnichenko, and V.O. Sokolov. *Influence of absorption on the refractive index determination accuracy by the minimum deviation method*. Appl. Opt. **57** (4), pp. 639–647 (2018).

[59] B.M. Pixton, and J.E. Greivenkamp. *Automated measurement of the refractive index of fluids*. Appl. Opt. **47** (10), pp. 1504–1509 (2008).

[60] L.W. Tilton. *Testing and Accurate Use of Abbe-Type Refractometers*. J. Opt. Soc. Am. **32** (7), pp. 371–381 (1942).

[61] H.M. Heinemann. *Measurement of the Refractive Index and Dispersion of an Unpolished Sample on an Abbe Refractometer*. Appl. Opt. **9** (11), pp. 2586–2587 (1970).

[62] K. Kuhler, E.L. Dereniak, and M. Buchanan. *Measurement of the index of refraction of the plastic Phenoxy PKFE*. Appl. Opt. **30** (13), pp. 1711–1714 (1991).

[63] I. Haller, H.A. Huggins, and M.J. Freiser. *On the Measurement of Indices of Refraction of Nematic Liquids*. Mol. Cryst. Liq. Cryst. **16** (1–2), pp. 53–59 (1972).

[64] J. Räty, and K.E. Peiponen. *Inverse Abbe-method for observing small refractive index changes in liquids*. Talanta **137**, pp. 143–147 (2015).

[65] J. Rheims, J. Köser, and T. Wriedt. *Refractive-index measurements in the near-IR using an Abbe refractometer*. Meas. Sci. Technol. **8** (6), pp. 601–605 (1997).

[66] P.P. Herrmann. *Determination of thickness, refractive index, and dispersion of waveguiding thin films with an Abbe refractometer*. Appl. Opt. **19** (19), pp. 3261–3262 (1980).

[67] A. García-Valenzuela, and H. Contreras-Tello. *Optical model enabling the use of Abbe-type refractometers on turbid suspensions*. Opt. Lett. **38** (5), pp. 775–777 (2013).

[68] Atago. (Jul. 2018). *Abbe refractometers*, retrieved from http://www.atago.net/.

[69] G.H. Meeten. *Refractive index errors in the critical-angle and the Brewster-angle methods applied to absorbing and heterogeneous materials*. Meas. Sci. Technol. **8** (7), pp. 728–733 (1997).

[70] M.A. Jeppesen, and A.M. Taylor. *Thickness and Refractive Index Measurement of a Lamina with a Michelson Interferometer*. J. Opt. Soc. Am. **56** (4), pp. 451–455 (1966).

[71] J.J. Fendley. *Measurement of refractive index using a Michelson interferometer*. Phys. Educ. **17**, pp. 209–211 (1982).

[72] A.C.P. Rocha, J.R. Silva, S.M. Lima, L.A.O. Nunes, and L.H.C. Andrade. *Measurements of refractive indices and thermo-optical coefficients using a white-light Michelson interferometer*. Appl. Opt. **55** (24), pp. 6639–6643 (2016).

[73] D.J. Bang, Y. Kim, Y. Kim, M.-J. Kim, and K.H. Kim. *Simultaneous measurement of group and phase refractive indices and physical thickness of transparent plates with low coherence Fabry–Perot interferometry*. Appl. Opt. **57** (16), pp. 4428–4433 (2018).

[74] J.J. Lunazzi, and M. Garavaglia. *Fabry-Perot laser interferometry to measure refractive index or thickness of transparent materials*. J. Phys. E. **6** (3), pp. 237–

240 (1973).

[75] J.T. Dong, F. Ji, H.J. Xia, Z.J. Liu, T.D. Zhang, and L. Yang. *Angle-resolved spectral Fabry–Pérot interferometer for single-shot measurement of refractive index dispersion over a broadband spectrum.* Meas. Sci. Technol. **29** (1) (2018).

[76] K. Betzler, A. Grone, N. Schmidt, and P. Voigt. *Interferometric measurement of refractive indices.* Rev. Sci. Instrum. **59** (4), pp. 652–653 (1988).

[77] S.H. Kim, S.H. Lee, J.I. Lim, and K.H. Kim. *Absolute refractive index measurement method over a broad wavelength region based on white-light interferometry.* Appl. Opt. **49** (5), pp. 910–914 (2010).

[78] H. El-Kashef, G.E. Hassan, and I. El-Ghazaly. *Mach–Zehnder optical system as a sensitive measuring instrument.* Appl. Opt. **33** (16), pp. 3540–3544 (1994).

[79] H. Maruyama, S. Inoue, T. Mitsuyama, M. Ohmi, and M. Haruna. *Low-coherence interferometer system for the simultaneous measurement of refractive index and thickness.* Appl. Opt. **41** (7), pp. 1315–1322 (2002).

[80] T. Fukano, and I. Yamaguchi. *Simultaneous measurement of thicknesses and refractive indices of multiple layers by a low-coherence confocal interference microscope.* Opt. Lett. **21** (23), pp. 1942–1944 (1996).

[81] S. Kim, J. Na, M.J. Kim, and B.H. Lee. *Simultaneous measurement of refractive index and thickness by combining low-coherence interferometry and confocal optics.* Opt. Express **16** (8), pp. 5516–5526 (2008).

[82] D. Francis, H.D. Ford, and R.P. Tatam. *Spectrometer-based refractive index and dispersion measurement using low-coherence interferometry with confocal scanning.* Opt. Express **26** (3), pp. 3604–6317 (2018).

[83] H. Fujiwara. *Spectroscopic ellipsometry: principles and applications.* John Wiley & Sons (2007).

[84] R.M.A. Azzam, and N.M. Bashara. *Ellipsometry and polarized light.* North-Holland (1977).

[85] E. Garcia-Caurel, R. Ossikovski, M. Foldyna, A. Pierangelo, B. Drévillon, and A. De Martino. *Advanced Mueller Ellipsometry Instrumentation and Data Analysis*, in *Ellipsometry at the Nanoscale*, Springer-Verlag Berlin Heidelberg, pp. 31–143 (2013).

[86] H. Arwin, M. Poksinski, and K. Johansen. *Total internal reflection ellipsometry: principles and applications.* Appl. Opt. **43** (15), pp. 3028–3036 (2004).

[87] G.E. Jellison. *The calculation of thin film parameters from spectroscopic ellipsometry data.* Thin Solid Films **290–291**, pp. 40–45 (1996).

[88] R.J. King, and M.J. Downs. *Ellipsometry applied to films on dielectric substrates.* Surf. Sci. **16**, pp. 288–302 (1969).

[89] D. Ngo, H. Liu, N. Sheth, R. Lopez-Hallman, N.J. Podraza, M. Collin, S. Gin, and S.H. Kim. *Spectroscopic ellipsometry study of thickness and porosity of the alteration layer formed on international simple glass surface in aqueous corrosion conditions.* npj Mater. Degrad. **2** (20), pp. 1–9 (2018).

[90] A. De Martino, E. Garcia-Caurel, J.-P. Gaston, and L. Yan. *Application of Spectroscopic Ellipsometry and Mueller Ellipsometry to Optical Characterization.* Appl. Spectrosc. **67** (1), pp. 1–21 (2013).

[91] H. Arwin. *Application of ellipsometry techniques to biological materials.* Thin Solid Films **519** (9), pp. 2589–2592 (2011).

[92] H. Arwin. *Ellipsometry on thin organic layers of biological interest: characterization and applications*. Thin Solid Films **377–378**, pp. 48–56 (2000).

[93] H. Elwing. *Protein absorption and ellipsometry in biomaterial research*. Biomaterials **19** (4–5), pp. 397–406 (1998).

[94] E.A. Irene. *Applications of spectroscopic ellipsometry to microelectronics*. Thin Solid Films **233** (1–2), pp. 96–111 (1993).

[95] P. Nestler, and C.A. Helm. *Determination of refractive index and layer thickness of nm-thin films via ellipsometry*. Opt. Express **25** (22), pp. 27077–27085 (2017).

[96] M. Gilliot, A. Hadjadj, and J. Martin. *Luminescence and ellipsometry investigations of annealing effects on nano-granular ZnO*. J. Lumin. **192**, pp. 25–32 (2017).

[97] C.A. Fenstermaker, and F.L. McCrackin. *Errors arising from surface roughness in ellipsometric measurement of the refractive index of a surface*. Surf. Sci. **16**, pp. 85–96 (1969).

[98] M.W. Williams. *Depolarization and cross polarization in ellipsometry of rough surfaces*. Appl. Opt. **25** (20), pp. 3616–3623 (1986).

[99] P. Yeh. *Optical Waves in Layered Media*. John Wiley & Sons (1988).

[100] F.E. Veiras, M.T. Garea, and L.I. Perez. *Wide angle conoscopic interference patterns in uniaxial crystals*. Appl. Opt. **51** (15), pp. 3081–3090 (2012).

[101] S. V. Shatalin, R. Juskaitis, J.B. Tan, and T. Wilson. *Reflection conoscopy and micro-ellipsometry of isotropic thin film structures*. J. Microsc. **179** (3), pp. 241–252 (1995).

[102] B.L. Van Horn, and H.H. Winter. *Conoscopic Measurement of Birefringence and Orientation in Biaxially Stretched Polymer Films and Sheets*. Macromolecules **36** (22), pp. 8513–8521 (2003).

[103] A.R. MacGregor. *Method for computing homogeneous liquid-crystal conoscopic figures*. J. Opt. Soc. Am. A **7** (3), pp. 337–347 (1990).

[104] B.L. Van Horn, and H.H. Winter. *Analysis of the conoscopic measurement for uniaxial liquid-crystal tilt angles*. Appl. Opt. **40** (13), pp. 2089–2094 (2001).

[105] J.-K. Song, J.K. Vij, and B.K. Sadashiva. *Conoscopy of chiral smectic liquid crystal cells*. J. Opt. Soc. Am. A. Opt. Image Sci. Vis. **25** (7), pp. 1820–1827 (2008).

[106] P. Yeh. *Extended Jones matrix method*. J. Opt. Soc. Am. **72** (4), pp. 507–513 (1982).

[107] C. Gu, and P. Yeh. *Extended Jones Matrix-Method. II*. J. Opt. Soc. Am. A Opt. Image Sci. Vis. **10** (5), pp. 966–973 (1993).

[108] M. Mansuripur. *Analysis of multilayer thin-film structures containing magneto-optic and anisotropic media at oblique incidence using 2×2 matrices*. J. Appl. Phys. **67** (10), pp. 6466–6475 (1990).

[109] R.F. Spanier, R.G. Wolf, R.M.H. Loiterman, and Mitchell E. *Simultaneous multiple angle/multiple wavelength ellipsometer and method*. US 5166752A (1990).

[110] T.E. Jenkins. *Multiple-angle-of-incidence ellipsometry*. J. Phys. D. Appl. Phys. **32** (9), pp. R45–R56 (1999).

[111] D.H. Goldstein. *Polarized light. 2nd Ed.* CRC Press (2011).

[112] R.A. Chipman. *Polarimetry*, in *Handbook of Optics: Devices, measurements, and properties*, McGraw-Hill (1995).

[113] J.N. Hilfiker, B. Johs, C.M. Herzinger, J.F. Elman, E. Montbach, D. Bryant, and

P.J. Bos. *Generalized spectroscopic ellipsometry and Mueller-matrix study of twisted nematic and super twisted nematic liquid crystals*. Thin Solid Films **455–456**, pp. 596–600 (2004).

[114] N. Hong, R.A. Synowicki, and J.N. Hilfiker. *Mueller matrix characterization of flexible plastic substrates*. Appl. Surf. Sci. **421**, pp. 518–528 (2017).

[115] N.A. Beaudry, Y. Zhao, and R.A. Chipman. *Dielectric tensor measurement from a single Mueller matrix image*. J. Opt. Soc. Am. A **24** (3), pp. 814–824 (2007).

[116] P.K. Smith. *Characterizing dielectric tensors of anisotropic materials from a single measurement*. PhD thesis, The University of Arizona (2013).

[117] J.J. Stamnes. *Waves in Focal Regions: Propagation, Diffraction and Focusing of Light, Sound and Water Waves*. CRC Press (1986).

[118] P.R.T. Munro, and P. Török. *Properties of high-numerical-aperture Mueller-matrix polarimeters*. Opt. Lett. **33** (21), pp. 2428–2430 (2008).

[119] M. Mansuripur. *Classical optics and its applications. 2nd Ed.* Cambridge University Press (2009).

[120] O. Arteaga, S.M. Nichols, and J. Antó. *Back-focal plane Mueller matrix microscopy: Mueller conoscopy and Mueller diffractrometry*. Appl. Surf. Sci. **421** (Part B), pp. 702–706 (2017).

[121] B.H. Ibrahim, S. Ben Hatit, and A. de Martino. *Angle resolved Mueller polarimetry with a high numerical aperture and characterization of transparent biaxial samples*. Appl. Opt. **48** (27), pp. 5025–5034 (2009).

[122] C.T. Samlan, and N.K. Viswanathan. *Field-controllable Spin-Hall Effect of Light in Optical Crystals: A Conoscopic Mueller Matrix Analysis*. Sci. Rep. **8** (2002), pp. 1–10 (2018).

[123] O. Arteaga, M. Baldrís, J. Antó, A. Canillas, E. Pascual, and E. Bertran. *Mueller matrix microscope with a dual continuous rotating compensator setup and digital demodulation*. Appl. Opt. **53** (10), pp. 2236–2245 (2014).

[124] S. Ben Hatit. *Polarimétrie de Mueller résolue en angle*. PhD thesis, Ecole Polytechnique X (2009).

[125] C. Fallet. *Angle resolved Mueller polarimetry, applications to periodic structures*. PhD thesis, Ecole Polytechnique X (2011).

[126] A. Peinado, A. Lizana, A. Turpin, I. Estévez, C. Iemmi, T.K. Kalkanjiev, J. Mompart, and J. Campos. *Snapshot polarimeter based on the conical refraction phenomenon*. Proc. SPIE 9526, Model. Asp. Opt. Metrol. V, **952616** (2015).

[127] M.H. Smith, J.B. Woodruff, and J.D. Howe. *Beam wander considerations in imaging polarimetry*. **3754**, pp. 50–54 (1999).

[128] A. Peinado. *Design of polarimeters based on liquid crystals and biaxial crystals for polarization metrology*. PhD thesis, Universitat Autònoma de Barcelona (2014).

[129] A. de Martino, E. Garcia-Caurel, B. Laude, and B. Drévillon. *General methods for optimized design and calibration of Mueller polarimeters*. Thin Solid Films **455–456**, pp. 112–119 (2004).

[130] A. de Martino, Y.-K. Kim, E. Garcia-Caurel, B. Laude, and B. Drévillon. *Optimized Mueller polarimeter with liquid crystals*. Opt. Lett. **28** (8), pp. 616–618 (2003).

[131] F. Goudail, P. Terrier, Y. Takakura, L. Bigué, F. Galland, and V. DeVlaminck. *Target detection with a liquid-crystal-based passive Stokes polarimeter*. Appl. Opt. **43** (2), pp. 274–282 (2004).

[132] D.J. Griffiths. *Introduction to Electrodynamics. 3rd Ed.* Prentice Hall (1999).

[133] A. Yariv, and P. Yeh. *Optical waves in crystals: propagation and control of laser radiation.* John Wiley & Sons (1984).

[134] T. Scharf. *Polarized Light in Liquid Crystals and Polymers.* John Wiley & Sons (2006).

[135] K.K. Sharma. *Optics: principles and applications.* Elsevier (2006).

[136] F.H. Yu, and H.S. Kwok. *Comparison of extended Jones matrices for twisted nematic liquid-crystal displays at oblique angles of incidence.* J. Opt. Soc. Am. A **16** (11), pp. 2772–2780 (1999).

[137] H. Goldstein, C.P. Poole, and J.L. Safko. *Classical mechanics. 3rd Ed.* Addison Wesley (2001).

[138] J. Lekner. *Optical properties of a uniaxial layer.* Pure Appl. Opt. J. Eur. Opt. Soc. Part A **3** (5), pp. 821–837 (1994).

[139] P. Yeh, and C. Gu. *Optics of liquid crystal displays.* John Wiley & Sons (1999).

[140] Z. Zhang, and H.J. Caulfield. *Reflection and refraction by interfaces of uniaxial crystals.* Opt. Laser Technol. **28** (7), pp. 549–553 (1996).

[141] A. Lien. *Extended Jones matrix representation for the twisted nematic liquid-crystal display at oblique incidence.* Appl. Phys. Lett. **57** (26), pp. 2767–2769 (1990).

[142] A. Lien. *A detailed derivation of extended jones matrix representation for twisted nematic liquid crystal displays.* Liq. Cryst. **22** (2), pp. 171–175 (1997).

[143] M. Schubert, B. Rheinländer, J. a. Woollam, B. Johs, and C.M. Herzinger. *Extension of rotating-analyzer ellipsometry to generalized ellipsometry: determination of the dielectric function tensor from uniaxial TiO2.* J. Opt. Soc. Am. A **13** (4), pp. 875–883 (1996).

[144] R.M.A. Azzam, and N.M. Bashara. *Application of generalized ellipsometry to anisotropic crystals.* J. Opt. Soc. Am. **64** (2), pp. 128–133 (1974).

[145] G. James, D. Witten, T. Hastie, and R. Tibshirani. *An Introduction to Statistical Learning with Applications in R.* Springer-Verlag New York (2013).

[146] E. Garcia-Caurel, A. de Martino, and B. Drévillon. *Spectroscopic Mueller polarimeter based on liquid crystal devices.* Thin Solid Films **455–456**, pp. 120–123 (2004).

[147] B. Johs, J.A. Woollam, C.M. Herzinger, J.N. Hilfiker, R.A. Synowicki, and C.L. Bungay. *Overview of variable-angle spectroscopic ellipsometry (VASE): II. Advanced applications.* Proc. SPIE 10294, Opt. Metrol. A Crit. Rev. **1029404** (1999).

[148] S. Ben Hatit, M. Foldyna, A. de Martino, and B. Drévillon. *Angle-resolved mueller polarimeter using a microscope objective.* Phys. Status Solidi Appl. Mater. Sci. **205** (4), pp. 743–747 (2008).

[149] D. Lara, and C. Dainty. *Axially resolved complete mueller matrix confocal microscopy.* Appl. Opt. **45** (9), pp. 1917–1930 (2006).

[150] M. Mansuripur. *Abbe's Sine Condition.* Opt. Photonics News **9** (2), pp. 56–60 (1998).

[151] M. Gu, P.C. Ke, and X.S. Gan. *Trapping force by a high numerical-aperture microscope objective obeying the sine condition.* Rev. Sci. Instrum. **68** (10), pp. 3666–3668 (1997).

[152] P. Török, and F.-J. Kao. *Optical imaging and microscopy : techniques and advanced systems. 2nd Ed.* Springer-Verlag Berlin Heidelberg (2007).

[153] T. Baldacchini. *Three-dimensional microfabrication using two-photon polymerization: fundamentals, technology, and applications. 1st Ed.* William Andrew (2015).

[154] J.A. Haigh, Y. Kinebas, and A.J. Ramsay. *Inverse conoscopy: a method to measure polarization using patterns generated by a single birefringent crystal.* Appl. Opt. **53** (2), pp. 184–188 (2014).

[155] M. Shribak. *Polarization aberrations caused by differential transmission and phase shift in high-numerical-aperture lenses: theory, measurement, and rectification.* Opt. Eng. **41** (5), pp. 943–954 (2002).

[156] K.M. Twietmeyer, and R.A. Chipman. *Optimization of Mueller matrix polarimeters in the presence of error sources.* Opt. Express **16** (15), pp. 11589–11603 (2008).

[157] E. Garcia-Caurel, A. Lizana, G. Ndong, B. Al-Bugami, C. Bernon, E. Al-Qahtani, F. Rengnez, and A. de Martino. *Mid-infrared Mueller ellipsometer with pseudo-achromatic optical elements.* Appl. Opt. **54** (10), pp. 2776–2785 (2015).

[158] J.S. Tyo. *Design of optimal polarimeters: maximization of signal-to-noise ratio and minimization of systematic error.* Appl. Opt. **41** (4), pp. 619–630 (2002).

[159] A. Peinado, A. Lizana, J. Vidal, C. Iemmi, and J. Campos. *Optimization and performance criteria of a Stokes polarimeter based on two variable retarders.* Opt. Express **18** (10), pp. 9815–9830 (2010).

[160] M.N. Polyanskiy. (Aug. 2018). *Refractive index database*, retrieved from https://refractiveindex.info/.

[161] J. Ralph, and K. Ralph. (Feb. 2018). *The gemstone and gemology information website*, retrieved from https://www.gemdat.org/.

[162] B.D. Fahlman. *Materials Chemistry. 1st Ed.* Springer Netherlands (2011).

[163] D.H. Goldstein. *Mueller matrix dual-rotating retarder polarimeter.* Appl. Opt. **31** (31), pp. 6676–6683 (1992).

[164] D.S. Sabatke, M.R. Descour, E.L. Dereniak, W.C. Sweatt, S.A. Kemme, and G.S. Phipps. *Optimization of retardance for a complete Stokes polarimeter.* Opt. Lett. **25** (11), pp. 802–804 (2000).

[165] J.L. Pezzaniti, and R.A. Chipman. *Mueller matrix imaging polarimetry.* Opt. Eng. **34** (6), pp. 1558–1568 (1995).

[166] M.H. Smith. *Optimization of a dual-rotating-retarder Mueller matrix polarimeter.* Appl. Opt. **41** (13), pp. 2488–2493 (2002).

[167] A. Peinado, A. Lizana, and J. Campos. *Optimization and tolerance analysis of a polarimeter with ferroelectric liquid crystals.* Appl. Opt. **52** (23), pp. 5748–5757 (2013).

[168] E. Compain, and B. Drévillon. *High-frequency modulation of the four states of polarization of light with a single phase modulator.* Rev. Sci. Instrum. **69** (4), pp. 1574–1580 (1998).

[169] Y. Liu, G.A. Jones, Y. Peng, and T.H. Shen. *Generalized theory and application of Stokes parameter measurements made with a single photoelastic modulator.* J. Appl. Phys. **100** (6), pp. 35371–35377 (2006).

[170] J. Lee, J. Koh, and R.W. Collins. *Dual rotating-compensator multichannel ellipsometer: Instrument development for high-speed Mueller matrix spectroscopy of*

surfaces and thin films. Rev. Sci. Instrum. **72** (3), pp. 1742–1754 (2001).

[171] L. Broch, A. En Naciri, and L. Johann. *Systematic errors for a Mueller matrix dual rotating compensator ellipsometer*. Opt. Express **16** (12), pp. 8814–8824 (2008).

[172] Thorlabs. (Sep. 2018). *Thorlabs, Inc. - Your Source for Fiber Optics, Laser Diodes, Optical Instrumentation and Polarization Measurement & Control*, retrieved from https://www.thorlabs.com/.

[173] J.A. Kurvits, M. Jiang, and R. Zia. *Comparative analysis of imaging configurations and objectives for Fourier microscopy*. J. Opt. Soc. Am. A **32** (11), pp. 2082–2092 (2015).

[174] J.M. Khosrofian, and B.A. Garetz. *Measurement of a Gaussian laser beam diameter through the direct inversion of knife-edge data*. Appl. Opt. **22** (21), pp. 3406–3410 (1983).

[175] M. González-Cardel, P. Arguijo, and R. Díaz-Uribe. *Gaussian beam radius measurement with a knife-edge: a polynomial approximation to the inverse error function*. Appl. Opt. **52** (16), pp. 3849–3855 (2013).

[176] M.A. de Araújo, R. Silva, E. de Lima, D.P. Pereira, and P.C. de Oliveira. *Measurement of Gaussian laser beam radius using the knife-edge technique: improvement on data analysis*. Appl. Opt. **48**, pp. 393–396 (2009).

[177] S.-Y. Lu, and R.A. Chipman. *Interpretation of Mueller matrices based on polar decomposition*. J. Opt. Soc. Am. A **13** (5), pp. 1106–1113 (1996).

[178] R.M.A. Azzam, I.M. Elminyawi, and A.M. El-Saba. *General analysis and optimization of the four-detector photopolarimeter*. J. Opt. Soc. Am. A **5** (5), pp. 681–689 (1988).

[179] J. Fade, S. Panigrahi, A. Carré, L. Frein, C. Hamel, F. Bretenaker, H. Ramachandran, and M. Alouini. *Long-range polarimetric imaging through fog*. Appl. Opt. **53** (18), pp. 3854–3865 (2014).

[180] J.J. Gil. *Characteristic properties of Mueller matrices*. J. Opt. Soc. Am. A **17** (2), pp. 328–334 (2000).

[181] A. Aiello, G. Puentes, and J.P. Woerdman. *Linear optics and quantum maps*. Phys. Rev. A **76** (032323), pp. 1–12 (2007).

[182] J.J. Gil. *Polarimetric characterization of light and media*. Eur. Phys. J. Appl. Phys. **40** (1), pp. 1–47 (2007).

[183] S.R. Cloude. *Conditions For The Physical Realisability Of Matrix Operators In Polarimetry*. Proc. SPIE 1166, Polariz. Considerations Opt. Syst. II **1166** (1990).

[184] J.J. Gil. *On optimal filtering of measured Mueller matrices*. Appl. Opt. **55** (20), pp. 5449–5455 (2016).

[185] F. Stabo-Eeg. *Development of instrumentation for Mueller matrix ellipsometry*. PhD thesis, Norwegian University of Science and Technology (2009).

[186] G.R. Lindfield, and J.E.T. Penny. *Numerical methods using MATLAB. 3rd Ed.* Academic Press (2012).

[187] M. Marvin. *Microscopy apparatus*. US 69510757A (1961).

[188] M. Marvin. *Memoir on inventing the confocal scanning microscope*. Scanning (1988).

[189] R.H. Webb. *Confocal optical microscopy*. Reports Prog. Phys. **59**, pp. 427–471 (1996).

[190] G.H. Bu-Abbud, N.M. Bashara, and J.A. Woollam. *Variable wavelength, variable angle ellipsometry including a sensitivities correlation test*. Thin Solid Films **138** (1), pp. 27–41 (1986).

[191] H.E. Keller. *Proper Alignment of the Microscope*. Methods Cell Biol. **81**, pp. 43–53 (2007).